

# **Spectroscopic and Computational Studies of the Physical Properties and Reactivities of Peroxomanganese(III) Complexes**

By

Copyright © 2011

**Robert A. Geiger**

Submitted to the graduate degree program in Chemistry and the Graduate Faculty of the  
University of Kansas in partial fulfillment of the requirements for the degree of Doctor of  
Philosophy

---

Chairperson: Dr. Timothy A. Jackson

---

Dr. David Weis

---

Dr. Heather Desaire

---

Dr. Jennifer S. Laurence

---

Dr. Michael A. Johnson

Date Defended: May 12<sup>th</sup>, 2012

The Dissertation Committee for Robert A. Geiger certifies that this is the approved version of the following thesis:

**Spectroscopic and Computational Studies of the Physical Properties and  
Reactivities of Peroxomanganese(III) Complexes**

---

Chairperson: Dr. Timothy A. Jackson

Date approved: May 12<sup>th</sup>, 2012

## **Spectroscopic and Computational Studies of the Physical Properties and Reactivities of Peroxomanganese(III) Complexes**

Robert A. Geiger

Under the supervision of Assistant Professor Timothy A. Jackson at the University of Kansas

A wide range of  $\text{Mn}^{\text{III}}$  intermediates were generated and studied using various spectroscopic techniques, including electronic absorption, magnetic circular dichroism (MCD), variable-temperature, variable-field (VTVH) MCD, electron paramagnetic resonance (EPR), and X-ray absorption. Computational methods, such as density functional theory (DFT), time-dependent DFT (TD-DFT), and multi-reference ab initio calculations, were used to complement and aid in the interpretation of the spectroscopic data. Specifically, this combined spectroscopic/computational approach was employed to systematically investigate the geometric and electronic structure of a series of peroxomanganese(III) ( $\text{Mn}^{\text{III}}\text{-O}_2$ ) intermediates supported by tridentate, tetradentate, and pentadentate ligands. This work has afforded new insight into the steric and electronic effects of the supporting ligand on the physical properties and reactivity of manganese species. The most significant results made in these studies are summarized below.

$\text{Mn}^{\text{III}}\text{-O}_2$  adducts have been postulated as important intermediates in small molecule oxidation catalysts and manganese containing enzymes. A series of tetradentate dipyrityl- (or diquinolinylnyl-) diazacycloalkane ligands were synthesized to systematically probe the effects of steric and electronic perturbations on the properties of  $\text{Mn}^{\text{II}}$  and  $\text{Mn}^{\text{III}}\text{-O}_2$  complexes. In the initial study, a set of four  $[\text{Mn}^{\text{II}}(\text{L}^7\text{py}_2^{\text{R}})]^{2+}$  complexes, supported by the tetradentate 1,4-bis(2-pyridylmethyl)-1,4-diazepane ligand and derivatives with pyridine substituents in the five (R = 5-Br) and six-positions (R = 6-Me and 6-MeO), were synthesized. Treatment of these  $\text{Mn}^{\text{II}}$  precursors with  $\text{H}_2\text{O}_2$  or  $\text{KO}_2$  at  $-40\text{ }^\circ\text{C}$  resulted in the formation of  $\text{Mn}^{\text{III}}\text{-O}_2$  complexes

$[\text{Mn}^{\text{III}}(\text{O}_2)(\text{L}^7\text{py}_2^{\text{R}})]^+$  differing only in the identity of the pyridine ring substituent. The electronic structures of two of these complexes,  $[\text{Mn}^{\text{III}}(\text{O}_2)(\text{L}^7\text{py}_2^{\text{H}})]^+$  and  $[\text{Mn}^{\text{III}}(\text{O}_2)(\text{L}^7\text{py}_2^{6\text{-Me}})]^+$ , were examined with our combined spectroscopic/computational approach. While these complexes exhibit similar ground state parameters, their low-temperature MCD spectra revealed significant shifts in electronic transition energies that are correlated to differences in Mn–O<sub>2</sub> interactions among these complexes. These results indicate that the  $[\text{Mn}^{\text{III}}(\text{O}_2)(\text{L}^7\text{py}_2^{\text{H}})]^+$  complex exhibits symmetric Mn–O<sub>peroxo</sub> bond lengths, consistent with a side-on bound peroxo ligand. In contrast, the peroxo ligand of the  $[\text{Mn}^{\text{III}}(\text{O}_2)(\text{L}^7\text{py}_2^{6\text{-Me}})]^+$  complex is bound in a more end-on fashion, with asymmetric Mn–O<sub>peroxo</sub> distances. This difference in binding mode can be rationalized either in terms of the greater electron-donating abilities of the methyl-appended pyridines or by steric interactions between the peroxo ligand with the substituent at the six position.

To distinguish between steric and electronic effects, additional  $\text{Mn}^{\text{II}}$  complexes were generated with pyridine derivatives with substituents in the four-position (R = 4-Me and 4-Cl), with different numbers of atoms in the diazacycloalkane backbone (n = 6, 7, 8), and with the type of N-ligand donor changed from a pyridine to a quinoline ligand. Spectroscopic analysis of these  $\text{Mn}^{\text{III}}\text{-O}_2$  intermediates revealed a significant shift in the lowest-energy electronic transition when a bulky functional group is on the six position of the pyridine rings. These results indicate that the  $\text{Mn}^{\text{III}}\text{-O}_2$  complexes lacking substituents at the six positions of the pyridine rings ( $\text{L}^7\text{py}_2^{\text{H}}$ ,  $\text{L}^8\text{py}_2^{\text{H}}$ ,  $\text{L}^7\text{py}_2^{4\text{-Me}}$  and  $\text{L}^7\text{isoq}_2$ ) exhibit symmetric Mn–O<sub>peroxo</sub> bond lengths, consistent with a side-on bound peroxo ligand. The peroxo ligand of the complexes with a substituent at the six position ( $\text{L}^7\text{py}_2^{6\text{-Me}}$ ,  $\text{L}^7\text{q}_2$ , and  $\text{L}^8\text{py}_2^{6\text{-Me}}$ ) exhibit asymmetric Mn–O<sub>peroxo</sub> bond lengths, consistent with a more end-on bound peroxo ligand. This difference in binding mode can be rationalized by steric clash of the peroxo ligand with the 6-substituent at the six positions.

To determine the effects of small ligand perturbations on the reactivity of the peroxo group, the more thermally stable  $\text{Mn}^{\text{III}}\text{-O}_2$  complexes were reacted with cyclohexanecarboxaldehyde, a model substrate used to probe the relative nucleophilicities of peroxo metal species. Surprisingly, the rate of deformylation did not correlate with the expected nucleophilicity of the  $\text{Mn}^{\text{III}}\text{-O}_2$  unit, as the inclusion of methyl substituents on the pyridines affords slower deformylation rates. It was proposed that adding methyl-substituents to the pyridines, or increasing the number of carbons on the diazacycloalkane backbone, sterically hinders nucleophilic attack of the peroxo ligand on the carbonyl carbon of the aldehyde.

With small ligand perturbations causing large modulations of the  $\text{Mn-O}_{\text{peroxo}}$  bond lengths, additional  $\text{Mn}^{\text{III}}\text{-O}_2$  complexes, supported by aminopyridyl pentadentate ligands, were evaluated in collaboration with Dr. Elodie Anxolabéhère-Mallart (*Laboratoire d'Electrochimie Moléculaire, Université Paris*). Two  $\text{Mn}^{\text{III}}\text{-O}_2$  complexes supported by pentadentate ligands, *N*-methyl-*N,N',N'*-tris(2-pyridylmethyl)ethane-1,2-diamine ( $\text{mL}_5^{2-}$ ) and *N*-methyl-*N,N',N'*-tris((1-methylimidazolyl)methyl)ethane-1,2-diamine ( $\text{ImL}_5^{2-}$ ) were examined with the spectroscopic/computational method to probe the geometric and the electronic structure. The electronic absorption spectra of these  $\text{Mn}^{\text{III}}\text{-O}_2$  complexes (intense broad feature in the range of 15 000  $\text{cm}^{-1}$  to 18 000  $\text{cm}^{-1}$  with a weak shoulder at  $\sim 23\,000\text{ cm}^{-1}$ ) are uniquely different compared to analogous tetradentate ligands (weak broad feature  $\sim 15\,500\text{ cm}^{-1}$  with an intense absorption feature at  $\sim 22\,000\text{ cm}^{-1}$ ). The combined spectroscopic/computational approach was allowed for unambiguous assignment of the structure of these complexes because, although several  $\text{Mn}^{\text{III}}\text{-O}_2$  binding modes are possible, each mode should have a unique set of spectral properties. The possible modes are either a seven-coordinate, side-on  $\text{Mn}^{\text{III}}\text{-O}_2$  species; a six-coordinate, end on  $\text{Mn}^{\text{III}}\text{-O}_2$  species; or a six-coordinate, side-on  $\text{Mn}^{\text{III}}\text{-O}_2$  adduct with a

dissociated N donor from the ligand. This spectroscopic/computational approach revealed that  $\text{Mn}^{\text{III}}\text{-O}_2$  complexes supported by pentadentate ligands are stabilized by a six-coordinate environment, with one of the pyridine/imidazole groups dissociated and with a side-on peroxo binding mode.

With the observed trend that  $\text{Mn}^{\text{III}}\text{-O}_2$  adducts are stabilized by a six-coordinate environment, an additional  $\text{Mn}^{\text{III}}\text{-O}_2$  complex supported by a tridentate ligand was synthesized to evaluate its coordination environment and its electronic structure. A bulky scorpionate-based ligand, tris(3,5-diphenylpyrazolyl)borate ( $\text{Tp}^{\text{Ph}_2}$ ) was designed to stabilize a  $\text{Mn}^{\text{III}}\text{-O}_2$  complex at room temperature. We proposed that the bulky phenyl groups should shield the peroxo ligand and may form a weak hydrogen bonding network, thereby stabilizing a  $\text{Mn}^{\text{III}}\text{-O}_2$  intermediate, allowing for characterization by XRD, which the instability of the other intermediates had precluded. The  $\text{Mn}^{\text{II}}$  XRD structure revealed a six coordinate complex with the  $\text{Tp}^{\text{Ph}_2}$  ligand in a facially coordinating geometry, with three solvent molecules completing the coordination sphere. Treatment of this  $\text{Mn}^{\text{II}}$  complex with  $\text{H}_2\text{O}_2$  or  $\text{KO}_2$  at room temperature resulted in the formation of a  $\text{Mn}^{\text{III}}\text{-O}_2$  complex that is stable for several days at ambient conditions. The increase stability allowed for the isolation of single needle crystals for XRD analysis. The XRD structure confirmed the assignment of this species as a  $\text{Mn}^{\text{III}}\text{-O}_2$  adduct (Mn-O and O-O of 1.86 and 1.43 Å) and revealed a distorted six-coordinate octahedral complex with one solvent molecule completing the coordination sphere. The geometric and electronic structure of this  $\text{Mn}^{\text{III}}\text{-O}_2$  complex was characterized by using the combined spectroscopic/computational approach.

## ACKNOWLEDGEMENTS

Professor Jackson, I would like to say thank you for mentoring me and helping me become the scientist that I am today. You have always had an open door, no matter what the reason was. I am grateful and proud to be your first graduate student. My experiences have allowed me to learn and experience every single aspect of developing a research group. You have a great ability in understanding someone's weakness and turning it into one of their strengths. I wish you and the group continued success in the future.

Dr. Swarup Chattopadhyay, thank you for getting my first project going. You helped me build a sound structure to my graduate career. You showed me that research could be exciting and also rewarding, even if it was a 24 hour kinetics experiment. You told me I could relax and grab a beer while the UV-Vis did all the work. I wish you the best of success at the University of Kalyani in West Bengal, India.

Jackson group, I watched the group grow from one graduate student to six graduate students. You all have become great friends of mine and made working in the Laboratory exciting. Amanda, thank you for helping me with all the different biological aspects, your wiliness to help, and all the good food! James, I loved to hear all the different and crazy ideas you had and all the different practical jokes you pulled on me. Domenick, thank you for being my go-to guy in lab; you were a great person to bounce ideas back and forth on. Kevin and Gayan, thank you two for taking over and expanding on my graduate work. I wish all of you great success for the rest of your graduate and professional careers. Try not to give Tim any more gray hair; I have already given him plenty!

Sammy, you have been a great friend and roommate. From the first time I met you on recruiting weekend, I knew we could be great friends. Thank you for being there for me for my whole graduate career. I wish you great success in your professional career.

I thank Professor Elodie Anxolabéhère-Mallart and her graduate students for supplying the pentadentate  $\text{Mn}^{\text{II}}$  complexes. I thank Dr. Victor Day for solving all my crystal structures in a timely manner. I thank Dr. Frank Neese for use of his ORCA program. I also thank my committee, for taking their time to participate in my oral exam and in my final defense.

I thank my brother, sisters, family, and friends for your love and support. You didn't always understand what I was doing, but you were always interested. I thank my parents for supporting my decision to move half-way across the country and inspiring me to do the best I can. Most importantly, I thank my soon-to-be wife and fiancée Jillian. You have put up with many late and stressful nights, but no matter what you always had confidence in me doing well.



**TABLE OF CONTENTS****page**

Abstract	iii-vi
Acknowledgments	vii-viii
Table of Contents	ix-x
List of Figures	xi-xiv
List of Tables	xv-xiix
List of Schemes	xx
Abbreviations and Acronyms	xxi-xxiii

**Chapter 1. Peroxomanganese(III): An Overview**

1.1 Introduction	2-3
1.2 Manganese containing enzymes that react with O <sub>2</sub> and its reduced derivatives	3-4
1.3 Small-Molecule Manganese Catalysts	5-6
1.4 Peroxomanganese(III) Complexes	6-8
1.5 Combined Spectroscopic and Computational Approach	9-10
1.6 Validation of Analytical Approach	10-14
1.7 References	14-16

**Chapter 2. Spectroscopic and Computational Studies of Peroxomanganese(III) Complexes Supported by Tetradentate Aminopyridyl Ligands**

2.1 Introduction	18-19
2.2 Results and Discussion	19-40
2.3 Summary	40-42
2.4 Material and Methods	42-47
2.5 Supporting Information	47-55
2.6 References	55-57

**Chapter 3. Nucleophilic Reactivity of a Series of Peroxomanganese(III) Complexes Supported by Tetradentate Aminopyridyl Ligands**

3.1 Introduction	59-62
3.2 Results and Discussion	62-72
3.3 Summary	72
3.4 Material and Methods	73-78
3.5 Supporting Information	78-85
3.6 References	85-86

**Chapter 4. Steric and Electronic Influences on the Structures of Peroxomanganese(III) Complexes Supported by Tetradentate Ligands**

4.1 Introduction	88-89
4.2 Results and Discussion	89-96
4.3 Summary	97

4.4 Material and Methods	97-100
4.5 References	100-101
<b>Chapter 5. Geometric and Electronic Structures of Peroxomanganese(III) Complexes Supported by Pentadentate Amino-pyridine and -imidazole Ligands</b>	
5.1 Introduction	103-107
5.2 Results and Analysis	108-125
5.3 Discussion	126-130
5.4 Material and Methods	130-132
5.5 References	132-135
<b>Chapter 6. Geometric and Electronic Structure of a Peroxomanganese(III) Complex Supported by a Scorpionate Ligand</b>	
6.1 Introduction	137-138
6.2 Results and Discussion	139-149
6.3 Summary	150
6.4 Material and Methods	150-153
6.5 References	153-155
<b>Appendix</b>	156-217

<b>List of Figures</b>	<b>page</b>
Figure 1.1. Active site for Manganese Superoxide Dismutase	4
Figure 1.2. Molecular structures of $\text{Mn}^{\text{III}}\text{-O}_2$ adducts characterized by XRD	7
Figure 1.3. Electronic absorption and MCD spectroscopies of $[\text{Mn}^{\text{III}}(\text{O}_2)(\text{TMC})]^+$	11
Figure 1.4. DFT-Optimized model of $[\text{Mn}^{\text{III}}(\text{O}_2)(\text{TMC})]^+$	13
Figure 1.5. Electronic absorption and TD-DFT spectra	14
Figure 2.1. ORTEP diagrams of $[\text{Mn}^{\text{II}}(\text{L}^7\text{py}_2^{\text{R}})]^{2+}$ R = H, 5-Br, 6-Me, and 6-MeO	21
Figure 2.2. Electronic absorption of $[\text{Mn}^{\text{III}}(\text{O}_2)(\text{L}^7\text{py}_2^{\text{R}})]^+$ R = H, 5-Br, 6-Me, and 6-MeO	27
Figure 2.3. Electronic absorption and MCD spectra of $[\text{Mn}^{\text{III}}(\text{O}_2)(\text{L}^7\text{py}_2^{\text{H}})]^+$	30
Figure 2.4. Electronic absorption and MCD spectra of $[\text{Mn}^{\text{III}}(\text{O}_2)(\text{L}^7\text{py}_2^{6\text{-Me}})]^+$	32
Figure 2.5. DFT-Optimized Model of $[\text{Mn}^{\text{III}}(\text{O}_2)(\text{L}^7\text{py}_2^{\text{H}})]^+$	35
Figure 2.6. MO Diagram of $[\text{Mn}^{\text{III}}(\text{O}_2)(\text{L}^7\text{py}_2^{\text{R}})]^+$ R=H and 6-Me	36
Figure 2.7. Surface contour plots of the spin-up Mn $d_{xy}$ and $\text{O}_2 \pi_{\text{op}}^*$ MOs	37
Figure 2.8. Simulated absorption spectra of $[\text{Mn}^{\text{III}}(\text{O}_2)(\text{L}^7\text{py}_2^{\text{R}})]^+$ R = H and 6-Me	39
Figure 3.1. ORTEP diagrams of $[\text{Mn}^{\text{II}}(\text{L}^n\text{py}_2^{\text{R}})]^{2+}$ n = 6, 7, and 8 R = H, 6-Me, and 4-Me	64
Figure 3.2. Electronic absorption of $[\text{Mn}^{\text{II}}(\text{L}^n\text{py}_2^{\text{R}})]^{2+}$ n = 6, 7, and 8 R = H, 6-Me, and 4-Me	66
Figure 3.3. Electronic absorption spectrum of CCA Reaction of $[\text{Mn}^{\text{III}}(\text{O}_2)(\text{L}^7\text{py}_2^{\text{H}})]^+$	69
Figure 3.4. Hammett correlation plot of benzaldehydes deformylation	71
Figure 3.5. Space filling models of $[\text{Mn}^{\text{III}}(\text{O}_2)(\text{L}^7\text{py}_2^{\text{R}})]^+$ R = H, 6-Me, and 4-Me	72
Figure 4.1. OTREP diagrams and space filling models of $[\text{Mn}^{\text{II}}(\text{L}^7\text{py}_2^{4\text{-Cl}})](\text{OTf})$ and of $[\text{Mn}^{\text{II}}(\text{L}^7\text{isoq}_2)](\text{OTf})$	90
Figure 4.2. Electronic absorption spectra of $[\text{Mn}^{\text{III}}(\text{O}_2)(\text{L}^7\text{py}_2^{\text{R}})]^+$ (R = H, 4-Cl, 4-Me, and 6-Me), $[\text{Mn}^{\text{III}}(\text{O}_2)(\text{L}^7\text{q}_2)]^+$ , and $[\text{Mn}^{\text{III}}(\text{O}_2)(\text{L}^7\text{isoq}_2)]^+$	91

Figure 4.3.	MCD spectra of $[\text{Mn}^{\text{III}}(\text{O}_2)(\text{L}^7\text{py}_2^{\text{R}})]^+$ R = H, 4-Me, and 6-Me	93
Figure 4.4.	MCD spectra of $[\text{Mn}^{\text{III}}(\text{O}_2)(\text{L}^7\text{q}_2)]^+$ and $[\text{Mn}^{\text{III}}(\text{O}_2)(\text{L}^7\text{isoq}_2)]^+$	94
Figure 4.5.	MCD spectra of $[\text{Mn}^{\text{III}}(\text{O}_2)(\text{L}^7\text{py}_2^{\text{R}})]^+$ R = H, 4-Me, and 4-Cl	95
Figure 4.6.	Lowest <i>d-d</i> transition energy versus average Mn-O <sub>peroxo</sub> computed bond distance	96
Figure 5.1.	Reported mononuclear Mn <sup>III</sup> -O <sub>2</sub> adducts	105
Figure 5.2.	Active sites of Mn <sup>II</sup> SOD and the HPCA adduct of Mn <sup>II</sup> MndD	106
Figure 5.3.	Electronic absorption spectra of $[\text{Mn}^{\text{III}}(\text{O}_2)(\text{mL}_5^2)]^+$ and $[\text{Mn}^{\text{III}}(\text{O}_2)(\text{imL}_5^2)]^+$	108
Figure 5.4.	Absorption spectra of $[\text{Mn}^{\text{III}}(\text{O}_2)(\text{imL}_5^2)]^+$ from 280 K – 150 K	110
Figure 5.5.	Absorption and 4.5 K, 7 T MCD spectra of $[\text{Mn}^{\text{III}}(\text{O}_2)(\text{mL}_5^2)]^+$ and $[\text{Mn}^{\text{III}}(\text{O}_2)(\text{imL}_5^2)]^+$	111
Figure 5.6.	VTVH MCD data collected for $[\text{Mn}^{\text{III}}(\text{O}_2)(\text{mL}_5^2)]^+$	114
Figure 5.7.	Hypothetical structures of $[\text{Mn}^{\text{III}}(\text{O}_2)(\text{mL}_5^2)]^+$ complexes developed using DFT computations	117
Figure 5.8.	Experimental electronic absorption spectrum of $[\text{Mn}^{\text{III}}(\text{O}_2)(\text{mL}_5^2)]^+$ and TD-DFT-computed absorption spectra for $[\text{Mn}^{\text{III}}(\text{O}_2)(\text{mL}_5^2)\text{-N}(4)]^+$ and $[\text{Mn}^{\text{III}}(\text{O}_2)(\text{mL}_5^2)\text{-N}(3)]^+$	120
Figure 5.9.	Experimental electronic absorption spectrum of $[\text{Mn}^{\text{III}}(\text{O}_2)(\text{mL}_5^2)]^+$ and SORCI-computed absorption spectra for $[\text{Mn}^{\text{III}}(\text{O}_2)(\text{NH}_3)_4\text{-N}(4)]^+$ and $[\text{Mn}^{\text{III}}(\text{O}_2)(\text{NH}_3)_4\text{-N}(3)]^+$	122
Figure 5.10.	Schematic molecular orbital splitting diagram for $[\text{Mn}^{\text{III}}(\text{O}_2)(\text{mL}_5^2)\text{-N}(3)]^+$	124
Figure 5.11.	Molecular structures for $[\text{Mn}^{\text{III}}(\text{O}_2)(\text{imL}_5^2)\text{-N}(3)]^+$ and $[\text{Mn}^{\text{III}}(\text{O}_2)(\text{N4py})\text{-N}(2)]^+$ developed using DFT computations	126
Figure 6.1.	ORTEP diagram and space filling model of $[\text{Mn}^{\text{II}}(\text{Tp}^{\text{Ph}_2})(\text{DMF})_3](\text{OTf})$	139
Figure 6.2.	Electronic absorption spectra of $[\text{Mn}^{\text{II}}(\text{Tp}^{\text{Ph}_2})(\text{DMF})_3](\text{OTf})$ and $[\text{Mn}^{\text{III}}(\text{O}_2)(\text{Tp}^{\text{Ph}_2})(\text{THF})]$	141

Figure 6.3. X-band EPR spectra of $[\text{Mn}^{\text{II}}(\text{Tp}^{\text{Ph}_2})(\text{DMF})_3](\text{OTf})$ and $[\text{Mn}^{\text{III}}(\text{O}_2)(\text{Tp}^{\text{Ph}_2})(\text{THF})]$	141
Figure 6.4. ORTEP diagram and space filling models of $[\text{Mn}^{\text{III}}(\text{O}_2)(\text{Tp}^{\text{Ph}_2})(\text{THF})]$	143
Figure 6.5. Electronic absorption and MCD spectra of $[\text{Mn}^{\text{III}}(\text{O}_2)(\text{Tp}^{\text{Ph}_2})(\text{THF})]$	144
Figure 6.6. VTVH MCD data collected for $[\text{Mn}^{\text{III}}(\text{O}_2)(\text{Tp}^{\text{Ph}_2})(\text{THF})]$	145
Figure 6.7. DFT-Optimized Model of $[\text{Mn}^{\text{III}}(\text{O}_2)(\text{Tp}^{\text{Ph}_2})(\text{THF})]$	146
Figure 6.8. Molecular orbital energy-level diagram for $[\text{Mn}^{\text{III}}(\text{O}_2)(\text{Tp}^{\text{Ph}_2})(\text{THF})]$	147
Figure 6.9. Surface contour plots of the spin-up Mn dxz and Mn dxy MOs for $[\text{Mn}^{\text{III}}(\text{O}_2)(\text{Tp}^{\text{Ph}_2})(\text{THF})]$	148
Figure 6.10. Experimental absorption spectra and simulated absorption spectra of $[\text{Mn}^{\text{III}}(\text{O}_2)(\text{Tp}^{\text{Ph}_2})(\text{THF})]$	149
Figure A.2.1. Molecular structures of isomers of $[\text{Mn}^{\text{III}}(\text{O}_2)(\text{L}^7\text{py}_2^{\text{H}})]^+$ based on BP86 DFT geometry optimizations	170
Figure A.2.2. Space filling models of $[\text{Mn}^{\text{II}}(\text{L}^7\text{py}_2^{\text{R}})]^{2+}$ R = H, 5-Br, 6-Me, and 6-MeO	170
Figure A.2.3. ESI-MS data for $[\text{Mn}^{\text{III}}(\text{O}_2)(\text{L}^7\text{py}_2^{\text{H}})]^+$ prepared with $\text{H}_2^{16}\text{O}_2$ and $\text{H}_2^{18}\text{O}_2$	171
Figure A.2.4. Simulated VTVH MCD curves for 90 % z polarization and 99 % z polarization	171
Figure A.2.5. Simulated absorption spectra for models of $[\text{Mn}^{\text{III}}(\text{O}_2)(\text{L}^7\text{py}_2^{\text{H}})]^+$ where the O-O bond lengths are systematically varied from 1.42 to 1.48 Å	172
Figure A.2.6. Simulated absorption spectra for models of $[\text{Mn}^{\text{III}}(\text{O}_2)(\text{L}^7\text{py}_2^{\text{H}})]^+$ where the Mn-O bond lengths are systematically varied from 1.88 to 1.82 Å	172
Figure A.3.1. Space filling models of $[\text{Mn}^{\text{II}}(\text{L}^6\text{py}_2^{\text{H}})(\text{NCMe})_3](\text{ClO}_4)_2$ , $[\text{Mn}^{\text{II}}(\text{L}^7\text{py}_2^{\text{H}})(\text{CH}_3\text{CN})_3](\text{ClO}_4)_2$ , $[\text{Mn}^{\text{II}}(\text{L}^7\text{py}_2^{6\text{-Me}})(\text{ClO}_4)(\text{CH}_3\text{CN})](\text{ClO}_4)_2$ , $[\text{Mn}^{\text{II}}(\text{L}^7\text{py}_2^{4\text{-Me}})(\text{OTf})_2]$ , $[\text{Mn}^{\text{II}}(\text{L}^7\text{q}_2)(\text{ClO}_4)_2]$ , $[\text{Mn}^{\text{II}}(\text{L}^7\text{py}_2^{6\text{-MeO}})(\text{ClO}_4)_2]$ , $[\text{Mn}^{\text{II}}(\text{L}^8\text{py}_2^{\text{H}})(\text{ClO}_4)_2]$ , and $[\text{Mn}^{\text{II}}(\text{L}^8\text{py}_2^{6\text{-Me}})(\text{OTf})_2]$	178
Figure A.4.1. Electronic absorption and MCD spectra of $[\text{Mn}^{\text{III}}(\text{O}_2)(\text{L}^7\text{py}_2^{4\text{-Me}})]^+$	185
Figure A.4.2. Electronic absorption and MCD spectra of $[\text{Mn}^{\text{III}}(\text{O}_2)(\text{L}^7\text{iso-q}_2)]^+$	185

Figure A.4.3. Electronic absorption and MCD spectra of $[\text{Mn}^{\text{III}}(\text{O}_2)(\text{L}^7\text{q}_2)]^+$	186
Figure A.4.4. Electronic absorption and MCD spectra of $[\text{Mn}^{\text{III}}(\text{O}_2)(\text{L}^7\text{py}_2^{4-\text{Cl}})]^+$	186
Figure A.5.1. Absorption intensity of $[\text{Mn}^{\text{III}}(\text{O}_2)(\text{ImL}_5^2)]^+$ at $17\,036\text{ cm}^{-1}$ as a function of temperature	203
Figure A.5.2. VTVH MCD data collected for $[\text{Mn}^{\text{III}}(\text{O}_2)(\text{mL}_5^2)]^+$	203
Figure A.5.3. Contour plot of $\chi^2$ values as a function of ZFS parameters $D$ and $E/D$ for $[\text{Mn}^{\text{III}}(\text{O}_2)(\text{mL}_5^2)]^+$ at $26\,667$ and $30\,800\text{ cm}^{-1}$	204
Figure A.5.4. Contour plot of $\chi^2$ values as a function of ZFS parameters $D$ and $E/D$ for $[\text{Mn}^{\text{III}}(\text{O}_2)(\text{ImL}_5^2)]^+$ at $16\,700$ and $25\,600\text{ cm}^{-1}$	204
Figure A.5.5. Relative energy, Mn-O and O-O bond lengths, and Mn-N(1) bond lengths as a function of the Mn-O distance for $[\text{Mn}^{\text{III}}(\text{O}_2)(\text{mL}_5^2)]^+$	205
Figure A.5.6. Total energy and Mn-O and O-O bond lengths as a function of the Mn-N(1) distance of $[\text{Mn}^{\text{III}}(\text{O}_2)(\text{mL}_5^2)]^+$	206
Figure A.5.7. TD-DFT-computed electronic absorption spectra for $[\text{Mn}^{\text{III}}(\text{O}_2)(\text{mL}_5^2)\text{-N}(4)]^+$ and $[\text{Mn}^{\text{III}}(\text{O}_2)(\text{mL}_5^2)\text{-N}(3)]^+$	206
Figure A.5.8. Total energy of $[\text{Mn}^{\text{III}}(\text{O}_2)(\text{ImL}_5^2)\text{-N}(3)]^+$ as a function of Mn-N(1) distance and TD-DFT-computed absorption spectra for $[\text{Mn}^{\text{III}}(\text{O}_2)(\text{ImL}_5^2)\text{-N}(3)]^+$	207
Figure A.6.1. Surface contour plots of the spin-up Mn d-MOs for $[\text{Mn}^{\text{III}}(\text{O}_2)(\text{Tp}^{\text{Ph,Me}})(\text{THF})]$	215

<b>List of Tables</b>	<b>page</b>
Table 1.1. Selected manganese containing enzymes	3
Table 2.1. Bond Lengths of $[\text{Mn}^{\text{II}}(\text{L}^7\text{py}_2^{\text{R}})]^{2+}$ R = H, 5-Br, 6-Me, and 6-MeO	22
Table 2.2. Properties of $[\text{Mn}^{\text{III}}(\text{O}_2)(\text{L}^7\text{py}_2^{\text{R}})]^+$ R = H, 5-Br, 6-Me, and 6-MeO	29
Table 2.3. Bond Lengths of Optimized Models of $[\text{Mn}^{\text{III}}(\text{O}_2)(\text{L}^7\text{py}_2^{\text{R}})]^+$ R = H and 6-Me	35
Table 3.1. Bond Lengths of $[\text{Mn}^{\text{II}}(\text{L}^n\text{py}_2^{\text{R}})]^{2+}$ n = 6,7, and 8 R = H, 6-Me, and 4-Me	65
Table 3.2. Properties of Peroxomanganese(III) Complexes	67
Table 3.3. Second-Order-Rate Constants for CCA Deformylation	70
Table 4.1. Bond Lengths of $[\text{Mn}^{\text{II}}(\text{L}^7\text{py}_2^{\text{R}})]^{2+}$ R = H, 4-Me, and 4-Cl	90
Table 4.2. Properties of $[\text{Mn}^{\text{III}}(\text{O}_2)(\text{L}^7\text{py}_2^{\text{R}})]^+$ (R = H, 4-Cl, 4-Me, and 6-Me), $[\text{Mn}^{\text{III}}(\text{O}_2)(\text{L}^7\text{q}_2)]^+$ , and $[\text{Mn}^{\text{III}}(\text{O}_2)(\text{L}^7\text{isoq}_2)]^+$	91
Table 4.3. Energy of band 1 compared to average Mn-O <sub>peroxo</sub> bond length from DFT computations	95
Table 5.1. Energies and oscillator strengths of electronic transitions for $[\text{Mn}^{\text{III}}(\text{O}_2)(\text{imL}_5^2)]^+$ and $[\text{Mn}^{\text{III}}(\text{O}_2)(\text{mL}_5^2)]^+$	112
Table 5.2. Axial ( <i>D</i> ) and Rhombic ( <i>E/D</i> ) Zero-Field Splitting Parameters for Peroxomanganese(III) Complexes	115
Table 5.3. Relative Energies and Mn-Ligand Bond Lengths for Four Hypothetical Models of $[\text{Mn}^{\text{III}}(\text{O}_2)(\text{mL}_5^2)]^+$	118
Table 5.4. Energies and Compositions of the Mn 3d-based MOs from B3LYP Spin-Unrestricted DFT Computations for $[\text{Mn}^{\text{III}}(\text{O}_2)(\text{mL}_5^2)]^+$	123
Table 6.1. Selected Bond Lengths and Angles for $[\text{Mn}^{\text{II}}(\text{Tp}^{\text{Ph}_2})(\text{DMF})_3](\text{OTf})$	140
Table 6.2. Selected Bond Lengths and for reported Mn <sup>III</sup> -O <sub>2</sub> complexes	142
Table 6.3. Selected Bond Lengths and for reported $[\text{Mn}^{\text{III}}(\text{O}_2)(\text{Tp}^{\text{Ph}_2})(\text{THF})]$	143

Table A.2.1. Crystal Data and Structure Refinement for $[\text{Mn}^{\text{II}}(\text{L}^7\text{py}_2^{\text{H}})(\text{NCCH}_3)_3](\text{ClO}_4)_2$	157
Table A.2.2. Crystal Data and Structure Refinement for $[\text{Mn}(\text{L}^7\text{py}_2^{5\text{-Br}})(\text{ClO}_4)(\text{CH}_3\text{COCH}_3)](\text{ClO}_4)$	158
Table A.2.3. Crystal Data and Structure Refinement for $[\text{Mn}(\text{L}^7\text{py}_2^{6\text{-Me}})(\text{ClO}_4)(\text{NCCH}_3)](\text{ClO}_4)$	159
Table A.2.4. Crystal Data and Structure Refinement for $[\text{Mn}(\text{L}^7\text{py}_2^{6\text{-MeO}})(\text{ClO}_4)(\text{NCCH}_3)](\text{ClO}_4)$	160
Table A.2.5. Selected Bond Lengths (Å) and Angles (°) for Low-Occupancy Forms of $[\text{Mn}^{\text{II}}(\text{L}^7\text{py}_2^{\text{H}})(\text{NCCH}_3)_3](\text{ClO}_4)_2$ and $[\text{Mn}(\text{L}^7\text{py}_2^{5\text{-Br}})(\text{ClO}_4)(\text{CH}_3\text{COCH}_3)](\text{ClO}_4)$	161
Table A.2.6. Cartesian coordinates for DFT energy-minimized model of $[\text{Mn}^{\text{III}}(\text{O}_2)(\text{L}^7\text{py}_2^{\text{H}})]^+$ (isomer <b>P</b> ).	162-163
Table A.2.7. Cartesian coordinates for DFT energy-minimized model of $[\text{Mn}^{\text{III}}(\text{O}_2)(\text{L}^7\text{py}_2^{\text{H}})]^+$ (isomer <b>E</b> ).	163-164
Table A.2.8. Cartesian coordinates for DFT energy-minimized model of $[\text{Mn}^{\text{III}}(\text{O}_2)(\text{L}^7\text{py}_2^{6\text{-Me}})]^+$ .	164-165
Table A.2.9. Room-temperature effective magnetic moments ( $\mu_{\text{eff}}$ BM) for $[\text{Mn}^{\text{II}}(\text{L}^7\text{py}_2^{\text{R}})]^{2+}$ R = H, 6-Me, 6-MeO, and 5-Br complexes	165
Table A.2.10. Electronic transition energies, oscillator strengths, and bandwidths from Gaussian deconvolutions for $[\text{Mn}^{\text{III}}(\text{O}_2)(\text{L}^7\text{py}_2^{\text{H}})]^+$	165
Table A.2.11. Electronic transition energies, oscillator strengths, and bandwidths from Gaussian deconvolutions of $[\text{Mn}^{\text{III}}(\text{O}_2)(\text{L}^7\text{py}_2^{\text{H}})]^+$	166
Table A.2.12. Energies and Compositions of the O 2p-based MOs and the Mn 3d-based MOs Based on Spin-Unrestricted B3LYP DFT Computations of $[\text{Mn}^{\text{III}}(\text{O}_2)(\text{L}^7\text{py}_2^{\text{H}})]^+$	166
Table A.2.13. TD-DFT Calculated Energies, Percent Contributions from Dominant One-electron Excitations, and Oscillator Strengths for the Major Electronic Transitions of $[\text{Mn}^{\text{III}}(\text{O}_2)(\text{L}^7\text{py}_2^{\text{H}})]^+$	167-168
Table A.2.14. TD-DFT Calculated Energies, Percent Contributions from Dominant One-electron Excitations, and Oscillator Strengths for the Major Electronic Transitions of $[\text{Mn}^{\text{III}}(\text{O}_2)(\text{L}^7\text{py}_2^{6\text{-Me}})]^+$	168-169



Table A.2.15. Energies and Compositions of the O 2p-based MOs and the Mn 3d-based MOs Based on Spin-Unrestricted B3LYP DFT Computations of $[\text{Mn}^{\text{III}}(\text{O}_2)(\text{L}^7\text{py}_2^{6\text{-Me}})]^+$	169
Table A.3.1. Crystal data and structure refinement for $[\text{Mn}(\text{L}^6\text{py}_2)(\text{NCCCH}_3)_3][\text{ClO}_4]_2$	173
Table A.3.2. Crystal data and structure refinement for $[\text{Mn}(\text{L}^7\text{py}_2^{4\text{-Me}})(\text{OTf})_2]$	174
Table A.3.3. Crystal data and structure refinement for $[\text{Mn}(\text{L}^7\text{q}_2)(\text{ClO}_4)_2]$	175
Table A.3.4. Crystal data and structure refinement for $[\text{Mn}(\text{L}^8\text{py}_2^{\text{H}})(\text{ClO}_4)_2]$	176
Table A.3.5. Crystal data and structure refinement for $[\text{Mn}(\text{L}^8\text{py}_2^{6\text{-Me}})(\text{OTf})_2]$	177
Table A.3.6. Cartesian coordinates for DFT optimized model of $[\text{Mn}^{\text{III}}(\text{O}_2)(\text{L}^7\text{py}_2^{\text{H}})]^+$	179-180
Table A.3.7. Cartesian coordinates for DFT optimized model of $[\text{Mn}^{\text{III}}(\text{O}_2)(\text{L}^7\text{py}_2^{6\text{-Me}})]^+$	180-181
Table A.3.8. Cartesian coordinates for DFT optimized model for $[\text{Mn}^{\text{III}}(\text{O}_2)(\text{L}^7\text{py}_2^{4\text{-Me}})]^+$	181-182
Table A.4.1. Crystal data and structure refinement for $[\text{Mn}(\text{L}^7\text{py}_2^{4\text{-Cl}})(\text{OTf})_2]$	183
Table A.4.2. Crystal data and structure refinement for $[\text{Mn}(\text{L}^7\text{isoq}_2)(\text{OTf})_2]$	184
Table A.4.3. Cartesian coordinates for DFT optimized model of $[\text{Mn}^{\text{III}}(\text{O}_2)(\text{L}^7\text{py}_2^{\text{H}})]^+$	187-188
Table A.4.4. Cartesian coordinates for DFT optimized model of $[\text{Mn}^{\text{III}}(\text{O}_2)(\text{L}^7\text{py}_2^{6\text{-Me}})]^+$	188-189
Table A.4.5. Cartesian coordinates for DFT optimized model for $[\text{Mn}^{\text{III}}(\text{O}_2)(\text{L}^7\text{py}_2^{4\text{-Me}})]^+$	189-190
Table A.4.6. Cartesian coordinates for DFT optimized model for $[\text{Mn}^{\text{III}}(\text{O}_2)(\text{L}^7\text{q}_2)]^+$	190-191
Table A.4.7. Cartesian coordinates for DFT optimized model for $[\text{Mn}^{\text{III}}(\text{O}_2)(\text{L}^7\text{isoq}_2)]^+$	191-193
Table A.4.8. Cartesian coordinates for DFT optimized model for $[\text{Mn}^{\text{III}}(\text{O}_2)(\text{L}^7\text{py}_2^{4\text{-Cl}})]^+$	193-194

Table A.5.1. Cartesian coordinates for DFT energy minimized $[\text{Mn}^{\text{III}}(\text{O}_2)(\text{mL}_5^2)\text{-N}(1)]^+$ model	194-195
Table A.5.2. Cartesian coordinates for DFT energy minimized $[\text{Mn}^{\text{III}}(\text{O}_2)(\text{mL}_5^2)\text{-N}(4)]^+$ model	195-196
Table A.5.3. Cartesian coordinates for DFT energy minimized $[\text{Mn}^{\text{III}}(\text{O}_2)(\text{mL}_5^2)\text{-N}(3)]^+$ model	197-198
Table A.5.4. Cartesian coordinates for DFT energy minimized $[\text{Mn}^{\text{III}}(\text{O}_2)(\text{ImL}_5^2)\text{-N}(1)]^+$ model	198-199
Table A.5.5. Cartesian coordinates for DFT energy minimized $[\text{Mn}^{\text{III}}(\text{O}_2)(\text{ImL}_5^2)\text{-N}(4)]^+$ model	199-200
Table A.5.6. Cartesian coordinates for DFT energy minimized $[\text{Mn}^{\text{III}}(\text{O}_2)(\text{ImL}_5^2)\text{-N}(3)]^+$ model	200-202
Table A.5.7. Gaussian fitting parameters	202
Table A.5.8. Transition Polarizations and ZFS Parameters determined from fits of VTVH MCD Data Collected for $[\text{Mn}^{\text{III}}(\text{O}_2)(\text{mL}_5^2)]^+$ and $[\text{Mn}^{\text{III}}(\text{O}_2)(\text{imL}_5^2)]^+$	202
Table A.5.9. Metric parameters for $\text{ImL}_5^2$ structures from surface scan	203
Table A.6.1. Crystal data and structure refinement for $[\text{Mn}(\text{Tp}^{\text{Ph}_2})(\text{DMF})_3](\text{OTf})$ .	208
Table A.6.2. Crystal data and structure refinement for $[\text{Mn}(\text{O}_2)(\text{Tp}^{\text{Ph}_2})(\text{THF})]$	209
Table A.6.3. Cartesian coordinates for DFT energy minimized $[\text{Mn}^{\text{III}}(\text{O}_2)(\text{Tp}^{\text{Ph}_2})(\text{THF})]$ model.	210-212
Table A.6.4. Cartesian coordinates for DFT energy minimized $[\text{Mn}^{\text{III}}(\text{O}_2)(\text{Tp}^{\text{Ph,Me}})(\text{THF})]$ model	212-214
Table A.6.5. Energies and Compositions of the O 2p-based MOs and the Mn 3d-based MOs Based on Spin-Unrestricted B3LYP DFT Computations for $[\text{Mn}^{\text{III}}(\text{O}_2)(\text{Tp}^{\text{Ph}_2})]^+$ .	214
Table A.6.6. TD-DFT Calculated Energies, Percent Contributions from Dominant One-electron Excitations, and Oscillator Strengths for the Major Electronic Transitions of $[\text{Mn}^{\text{III}}(\text{O}_2)(\text{Tp}^{\text{Ph,Me}})]^+$	216
Table A.6.7. Electronic transition energies, oscillator strengths, and bandwidths from Gaussian deconvolutions of absorption and MCD data of $[\text{Mn}^{\text{III}}(\text{O}_2)(\text{Tp}^{\text{Ph}_2})(\text{THF})]$	217

Table A.6.6. Metric parameters for $[\text{Mn}^{\text{III}}(\text{O}_2)(\text{Tp}^{\text{Ph}_2})(\text{THF})]$ from DFT optimized geometry	217
--	-----

<b>List of Schemes</b>	<b>page</b>
Scheme 1.1. Peroxide-shunt pathway of the heme paradigm	5
Scheme 1.2. Spectroscopic/computational Approach	9
Scheme 1.3. Reaction landscape for $[\text{Mn}^{\text{III}}(\text{O}_2)(\text{TMC})]^+$	10
Scheme 2.1. Ligands used for $\text{H}_2\text{O}_2$ activation	25
Scheme 3.1. Metal Complexes that Reacted with CCA in Aldehyde Deformylation	60
Scheme 3.2. Ligands Used to supporting $\text{Mn}^{\text{III}}\text{-O}_2$ Complexes	62
Scheme 3.3. Reaction Scheme for the Formation of $\text{Mn}^{\text{III}}\text{-O}_2$ Complexes	67
Scheme 4.1. $\text{L}^7\text{py}_2^{\text{R}}$ ( $\text{R} = \text{H}, 4\text{-Me}, 4\text{-Cl}, \text{and } 6\text{-Me}$ ), $\text{L}^7\text{q}_2$ , and $\text{L}^7\text{isoq}_2$ ligands used to support $\text{Mn}^{\text{III}}\text{-O}_2$ complexes	89
Scheme 5.1. $\text{mL}_5^2$ and $\text{imL}_5^2$ ligands and the $[\text{Mn}^{\text{II}}(\text{mL}_5^2)(\text{ClO}_4)]^+$ reaction landscape with $\text{H}_2\text{O}_2$	107
Scheme 6.1 $\text{Tp}^{\text{Ph}_2}$ ligand	138

## ABBREVIATIONS AND ACRONYMS

Abs	Absorption
BPMEN	<i>N,N'</i> -dimethyl- <i>N,N'</i> -bis(2-pyridylmethyl)-1,2-ethane diamine
BPMCNC	<i>N,N'</i> -dimethyl- <i>N,N'</i> -bis(2-pyridylmethyl)-1,2-cyclohexanediamine)
CCA	cyclohexanecarboxaldehyde
CD	circular dichroism
CI	configuration interaction
CT	charge transfer
DFT	density functional theory
EDDM	electron density difference map
EPR	electron paramagnetic resonance
HF	high-field, high-frequency
HOMO	highest occupied molecular orbital
INDO/S	intermediate neglect of differential overlap/spectroscopic parameterization
L <sup>6</sup> py <sub>2</sub> <sup>H</sup>	1,4-bis(2-pyridinylmethyl)piperazine
L <sup>7</sup> py <sub>2</sub> <sup>H</sup>	1,4-bis(2-pyridylmethyl)-1,4-diazepane
L <sup>7</sup> py <sub>2</sub> <sup>5-Br</sup>	1,4-bis(5-bromo-2-pyridylmethyl)-1,4-diazepane
L <sup>7</sup> py <sub>2</sub> <sup>4-Me</sup>	1,4-bis(4-methyl-2-pyridylmethyl)-1,4-diazepane
L <sup>7</sup> py <sub>2</sub> <sup>4-Cl</sup>	1,4-bis(4-chloro-2-pyridylmethyl)-1,4-diazepane
L <sup>7</sup> py <sub>2</sub> <sup>6-MeO</sup>	1,4-bis(6-methoxy-2-pyridylmethyl)-1,4-diazepane
L <sup>7</sup> py <sub>2</sub> <sup>6-Me</sup>	1,4-bis(6-methyl-2-pyridylmethyl)-1,4-diazepane
L <sup>7</sup> q <sub>2</sub>	1,4-bis(2-quinolinylmethyl)-1,4-diazepane
L <sup>7</sup> isoq <sub>2</sub>	1,4-bis(2-isoquinolinylmethyl)-1,4-diazepane
L <sup>8</sup> py <sub>2</sub> <sup>H</sup>	1,5-bis(2-pyridylmethyl)-1,5-diazacyclooctane

$L^8py_2^{6-Me}$	1,5-bis((6-methyl-2-pyridyl)methyl)-1,5-diazacyclooctane
LF	ligand field
LMCT	ligand-to-metal charge transfer
LUMO	lowest unoccupied molecular orbital
MCD	magnetic circular dichroism
$mL_5^2$	<i>N</i> -methyl- <i>N,N',N'</i> -tris(2-pyridylmethyl)ethane-1,2-diamine
MnCAT	manganese catalase
MadD	manganese dependent catechol oxygenase
MnRNR	manganese ribonucleotide reductases
MnSOD	manganese superoxide dismutase
$Mn^{III}-O_2$	peroxomanganese(III) adduct
MO	molecular orbital
OEC	Oxygen Evolving Complex
OxOx	Oxalate Oxidase
$pz^{iPr_2}$	3,5-isopropylpyrazole
NIR	near-infrared
NMR	nuclear magnetic resonance
rR	resonance Raman
RT	room temperature
ROS	reactive oxygen species
SCF	self-consistent field
SOD	superoxide dismutase
SOMO	singly occupied molecular orbital
TACN	triazocyclononane

TMC	tetramethylcyclam
Tp <sup>iPr2</sup>	hydrotris(3,5-diisopropylpyrazol-1-yl)borate
Tp <sup>Ph2</sup>	hydrotris(3,5-diphenylpyrazol-1-yl)borate
Tp <sup>Ph,Me</sup>	hydrotris(3-phenyl-5-methyl-pyrazol-1-yl)borate
TPP	tetraphenylporphyrin
TD	time-dependent
UV	ultraviolet
VTVH	variable temperature, variable field
XRD	X-ray diffraction
ZFS	zero-field splitting

## **Chapter 1**

### **Peroxomanganese(III) Adducts: An Overview**



## 1.1 Introduction.

Manganese interacts with molecular oxygen and its reduced derivatives to produce an assortment of manganese oxygen adducts that are of relevance as catalytic intermediates in biological and synthetic systems.<sup>1</sup> These intermediates differ in terms of the oxidation states of the manganese center and the identity of the oxygen species. For mononuclear systems, these intermediates include, but are not limited to, superoxomanganese(III)  $[\text{Mn}^{\text{III}}\text{-O}_2]^{-2+}$  and peroxomanganese(III)  $[\text{Mn}^{\text{III}}\text{-O}_2^{2-}]^+$  adducts.<sup>2</sup> These adducts may undergo either one-electron homolytic or two-electron heterolytic O-O bond cleavage to form potent oxidants, either with a terminal oxo ligand with a multiple bond to a single manganese center ( $\text{Mn}=\text{O}^{2-}$ ) or with an oxo that is bridged to multiple manganese centers ( $\text{Mn-O}^{2-}\text{-Mn}$ ).<sup>3</sup> Understanding the physical and reactivity properties of these manganese–oxygen species is important because of their relevance to a variety of synthetic manganese-based catalysts that use molecular oxygen or  $\text{H}_2\text{O}_2$  for oxygenation reactions, as well as several manganese-containing enzymes, such as Mn-superoxide dismutase (MnSOD), Mn-catalase (MnCAT), Mn-ribonucleotide reductases (MnRNR), and Mn-dependent catechol oxygenase (MndD).

With regards to synthetic Mn catalysts, the majority of reported work to date has focused on the initial  $\text{O}_2$ -binding steps and the reactivity of high-valent oxomanganese species,<sup>4-7, 16-19</sup> which are likely the end products of  $\text{O}_2$  activation. Comparatively little is known concerning intermediate steps in  $\text{O}_2$  (and  $\text{H}_2\text{O}_2$ ) activation and the steric or electronic effect of the coordination environment on the peroxo and superoxo ligand binding mode. In turn, a better understanding of the mechanism of these enzymes, including the role of  $\text{Mn}^{\text{III}}\text{-O}_2$  intermediates, would help in the rational design of catalysts. Employing environmentally-friendly manganese complexes and clean,  $\text{O}_2$ -derived oxidants in a manner inspired by Nature would overcome

current challenges in industrial catalysis including the use of expensive precious metals, and high temperature and pressures, poor atom economy, and non-environmentally friendly oxidants.

## 1.2 Manganese containing enzymes that react with O<sub>2</sub> and its reduced derivatives.

Manganese enzymes that react with molecular oxygen and its reduced derivatives play indispensable biological roles; including detoxification of reactive oxygen species (ROS),<sup>8,9</sup> oxalate degradation<sup>10</sup>, hydroxylation of aromatic substrates<sup>11</sup>, the conversion of ribonucleotides to deoxynucleotides<sup>12,13</sup>, and the formation of O<sub>2</sub> from H<sub>2</sub>O<sup>14</sup> (Table 1.1). The active sites of these enzymes feature Mn<sup>II</sup> centers bound to histidines and carboxylate ligands (see Figure 1.1 for the active site of MnSOD).

**Table 1.1.** Selected manganese containing enzymes

Enzyme	Substrate Activity
Mn-Superoxide Dismutase (MnSOD)	O <sub>2</sub> <sup>•-</sup> disproportionation
Mn-Catalase (MnCAT)	H <sub>2</sub> O <sub>2</sub> disproportionation
Mn-Ribonucleotide Reductase (MnRNR)	Conversion of ribo- to deoxyribonucleotides with HO <sub>2</sub> <sup>-</sup>
Mn-dependant Catechol Oxygenase (MndD)	Oxidation of aromatics with O <sub>2</sub>
Oxygen Evolving Complex (OEC)	Formation of O <sub>2</sub> from H <sub>2</sub> O
Oxalate Oxidase (OxOx)	Conversion of oxalate to formate with O <sub>2</sub>

The mechanisms of these manganese containing enzymes have been the subject of scrutiny for several decades, but the overall manganese-oxygen reaction landscape for these systems is still incompletely understood, in part because the rapid kinetics of these enzymes hampers the detection of catalytic intermediates.<sup>11,15</sup>

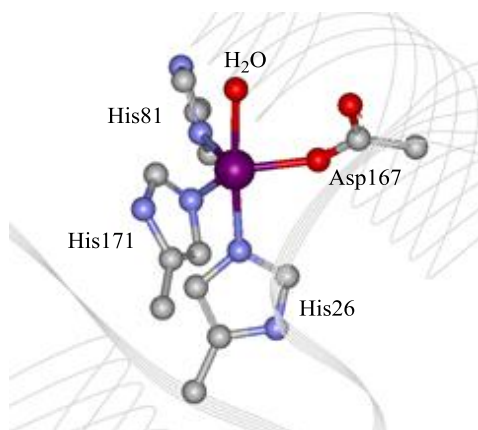


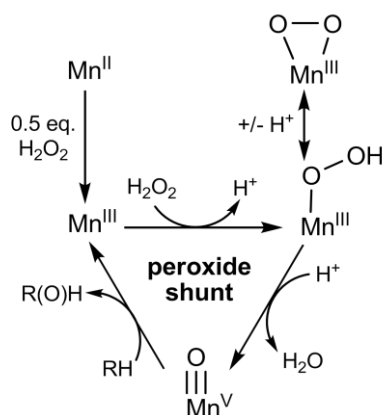
**Figure 1.1.** Active site for Manganese Superoxide Dismutase.

Recently, there have been several reports that support superoxo- and peroxo-manganese adducts are key intermediates for Mn-containing enzymes. A superoxomanganese(III) adduct was observed in single-turnover electron paramagnetic resonance (EPR) experiments on the dioxygen-activating manganese enzyme homoprotocatechuate dioxygenase MndD.<sup>15</sup> A bacterial isoform of Mn-RNR, an enzyme that catalyzes the reduction of ribonucleotides to form deoxyribonucleotides, reacts with only hydroperoxyl anion or superoxide ( $O_2^{\cdot-}$ ) and not with molecular oxygen, which is required for Fe-RNR, further supporting the importance of understanding these  $Mn^{III}$ -peroxo and -superoxo intermediates.<sup>12</sup> MnSOD utilizes a mononuclear Mn active site to disproportionate  $O_2^{\cdot-}$  and MnCat employs a dinuclear Mn active site to dismutate  $H_2O_2$ , both providing defense against ROS.<sup>8,16,17</sup> Manganese hydroperoxo intermediates have been proposed as a key intermediate for both of these enzymes,<sup>8,9</sup> but no intermediates have been spectroscopically characterized. However, it has been shown that under high concentrations of superoxide, MnSOD shows the accumulation of an off-pathway species with absorption features resembling a  $Mn^{III}$ - $O_2$  adduct.<sup>18,19</sup> This accumulation of this  $Mn^{III}$ - $O_2$  adduct suggests that it is possible for a peroxo intermediate to be stabilized by a Mn-containing enzyme although the biological relevance is unclear in this system.

### 1.3 Small-Molecule Manganese Catalysts.

The rising cost of precious metal catalysts (*i.e.* Ir, Pt, and Pd) has brought attention to the use of more inexpensive metals, such as Fe and Mn, in industrial catalysis.<sup>16</sup> Manganese-based catalysts have been reported to undergo catalytic oxygenation reactions, such as olefin epoxidation, C-H bond hydroxylation, and alcohol oxidation.<sup>16-19</sup> These catalysts facilitate

**Scheme 1.1**



oxidation reactions using environmentally friendly and atom-economical oxidants such as molecular oxygen or  $\text{H}_2\text{O}_2$ .<sup>20-23</sup> When  $\text{H}_2\text{O}_2$  is the oxidant, it is generally assumed that the  $\text{H}_2\text{O}_2$  activation follows the peroxide-shunt pathway of the heme paradigm (Scheme 1.1), where 0.5 equivalents of  $\text{H}_2\text{O}_2$  initiate the cycle by oxidizing the  $\text{Mn}^{\text{II}}$  ion to  $\text{Mn}^{\text{III}}$ . Then  $\text{H}_2\text{O}_2$  binds to the  $\text{Mn}^{\text{III}}$  ions, forming a  $\text{Mn}^{\text{III}}\text{-O}_2$  adduct that is in acid base equilibrium with a  $\text{Mn}^{\text{III}}\text{-OOH}$  adduct. This  $\text{Mn}^{\text{III}}\text{-O}_2$  species can undergo two electron heterolytic O-O bond cleavage giving a potent oxomanganese(V) oxidant. High-valent oxomanganese species have been experimentally characterized, but are conventionally produced using other oxidants such as peracetic acid and iodosylbenzene.<sup>24-30</sup>

The heme paradigm for  $\text{H}_2\text{O}_2$  activation is supported by the observation that carboxylic acids promote the formation of high-valent Mn-oxo species.<sup>31</sup> Carboxylic acid additives could

serve as a general Brønsted acid and protonate the  $\text{Mn}^{\text{III}}\text{-OOH}$  adduct and promote heterolytic O-O bond cleavage (Scheme 1.1).<sup>31,32</sup> However, it has been observed that less acidic acid additives lead to more active catalysts, challenging this model. In addition, several recent reports have identified species other than  $\text{Mn=O}$  adducts as active oxidants. In particular,  $\text{Mn}^{\text{IV}}\text{-OOH}$  and  $\text{Mn}^{\text{V}}\text{-iodoarene}$  species have been postulated as active oxidant of olefin epoxidation reactions.<sup>1</sup> The full potential of these manganese/ $\text{H}_2\text{O}_2$  catalysts has not yet been realized because the mechanism of these systems is poorly understood and the effect of the coordination environment on the activation of  $\text{O}_2$  (and  $\text{H}_2\text{O}_2$ ) has not yet be determined.

#### 1.4 Peroxomanganese(III) Complexes.

To date, a variety of synthetic  $\text{Mn}^{\text{III}}\text{-O}_2$  species have been reported,<sup>33-39</sup> and these have typically been generated by treating  $\text{Mn}^{\text{II}}$  precursors with  $\text{H}_2\text{O}_2$  or  $\text{KO}_2$ . In only one case has  $\text{O}_2$  been used as oxidant.<sup>35</sup> Because of their limited thermal stabilities and high reactivities, low temperatures ( $<0^\circ\text{C}$ ) are often required to stabilize these intermediates. X-ray diffraction (XRD) structures for the more stable complexes have revealed O-O bond lengths ranging from 1.40 – 1.43 Å,<sup>36-39</sup> firmly establishing the peroxo assignment. The Mn-O bond lengths vary from 1.841 to 1.901 Å, similar to  $\text{Mn}^{\text{III}}\text{-OH}$  distances found in synthetic complexes and Mn enzymes.<sup>40</sup> The longer Mn-O bond lengths ( $\sim 1.89$  Å) were observed for adducts reported by the groups of Valentine and Nam, who respectively used the dianionic TPP (TPP = tetraphenylporphyrin) and neutral TMC (TMC = tetramethylcyclam) ligands that both provide four, nearly coplanar, N donors (Figure 1.2).<sup>37,39</sup>  $\text{Mn}^{\text{III}}\text{-O}_2$  species supported by the facially coordinating, monoanionic  $\text{Tp}^{\text{iPr}}$  ( $\text{Tp}^{\text{iPr}}$  = tris(3,5-diisopropylpyrazolyl)borate) ligand show a degree of variation in Mn-O bond lengths (1.84 – 1.88 Å), with the longer distances attributed to H-bonding interactions proposed to have a stabilizing effect on the  $\text{Mn}^{\text{III}}\text{-O}_2$  unit.<sup>36,38</sup> The thermal stabilities of these

complexes vary remarkably, with the  $\text{Mn}^{\text{III}}\text{-O}_2$  adducts of TMC and  $\text{mL}_5^2$  ( $\text{mL}_5^2 = N\text{-methyl-}N,N',N'\text{-tris(2-pyridylmethyl)ethane-1,2-diamine}$ ) providing the extremes with room temperature half-lives of  $\sim 5$  hours and  $\sim 30$  minutes, respectively. The unusual stability of the TMC complex was attributed to steric crowding around the peroxo group from the  $N\text{-methyl}$  substituents of the TMC macrocycle (Figure 1.2).

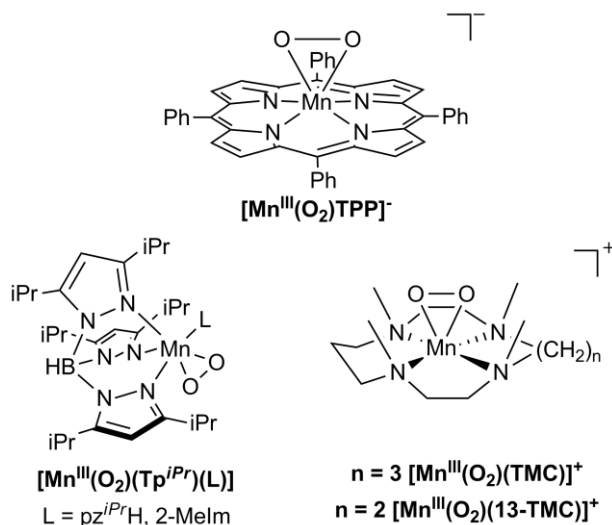


**Figure 1.2.** Representations of the molecular structures of  $\text{Mn}^{\text{III}}\text{-O}_2$  adducts characterized by X-ray crystallography.<sup>36-39,41</sup>

Characteristic spectroscopic features of  $\text{Mn}^{\text{III}}\text{-O}_2$  complexes include weak absorption bands in the visible region, the energies and intensities of which are dependent on the supporting ligands. For example,  $\text{Mn}^{\text{III}}\text{-O}_2$  adducts of the  $\text{Tp}^{\text{iPr}}$  and  $\text{mL}_5^2$  ligands show one prominent band centered at  $\sim 560 - 590$  nm with more intense features at  $< 400$  nm.<sup>33,37</sup> The corresponding TMC complex displays two bands of differing intensities at  $\sim 630$  and  $453$  nm.<sup>37</sup> Given their low intensities, these bands likely arise from  $\text{Mn}^{\text{III}}$   $d\text{-}d$  transitions, though it should be noted that weak charge-transfer (CT) bands are observed for  $\text{Fe}^{\text{III}}\text{-O}_2$  adducts at  $\sim 700$  nm ( $\epsilon \sim 500 \text{ M}^{-1}\text{cm}^{-1}$ ).<sup>42</sup> Resonance Raman (rR) experiments exciting into the visible bands of  $\text{Mn}^{\text{III}}\text{-O}_2$

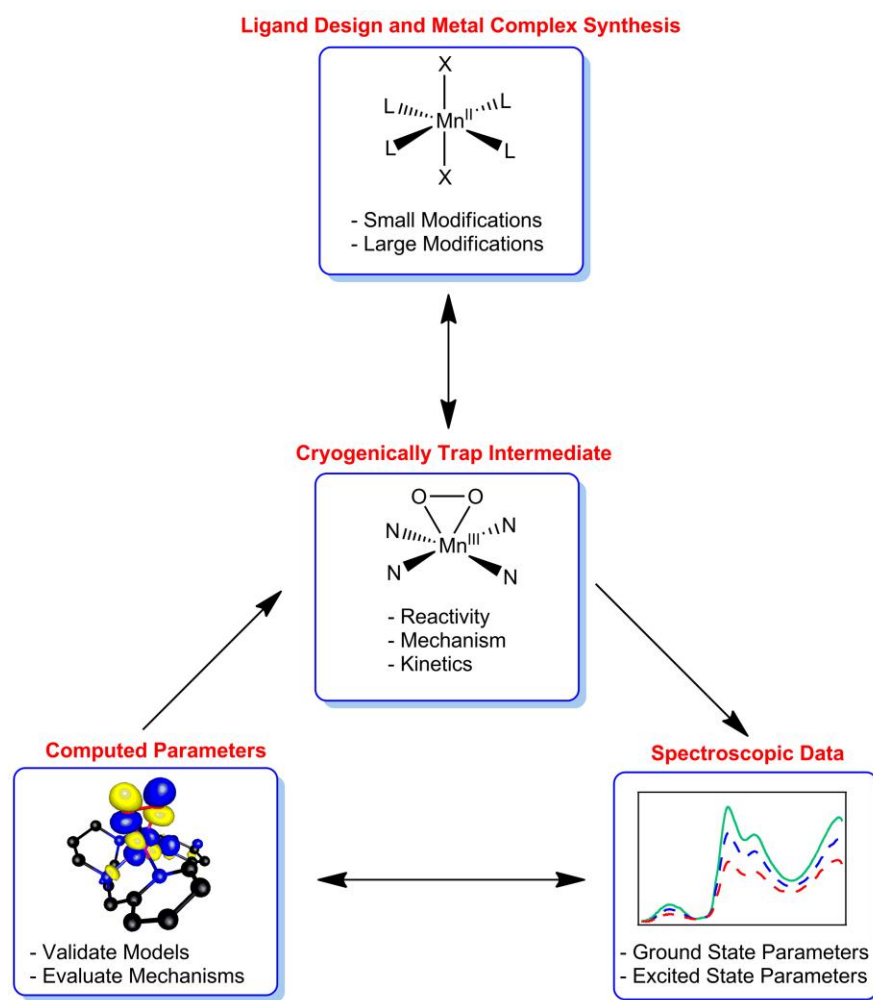
O<sub>2</sub> adducts have not yet permitted observation of the O–O or Mn–O stretching modes,<sup>33,37</sup> consistent with the assignment of these bands as *d-d* transitions. This is in contrast to peroxoiron(III) complexes that are quite amenable to interrogation using rR spectroscopy. IR spectroscopy was used to obtain  $\nu_{\text{O-O}}$  frequencies for four Mn<sup>III</sup>–O<sub>2</sub> adducts, which fall within the narrow range of  $\sim 885 - 896 \text{ cm}^{-1}$ . These frequencies are blue-shifted by  $\sim 70 \text{ cm}^{-1}$  compared to those of high-spin Fe<sup>III</sup>–O<sub>2</sub> adducts,<sup>42</sup> suggesting a stronger O–O bond in the Mn<sup>III</sup>–O<sub>2</sub> adducts. Lack of corresponding information regarding the Mn–O<sub>peroxo</sub> bond strength represents a crucial gap in knowledge, as a comparison of the relative Mn–O and O–O bond strengths is expected to be of key importance in understanding the reactivities of these complexes.

Reactivity studies of Mn<sup>III</sup>–O<sub>2</sub> adducts have shown that the peroxo ligand is nucleophilic, but not as much as corresponding peroxoiron(III) adducts.<sup>43</sup> A characteristic reaction is the deformylation of aldehydes, as demonstrated for the [Mn<sup>III</sup>(O<sub>2</sub>)(TMC)]<sup>+</sup> and [Mn<sup>III</sup>(O<sub>2</sub>)(H<sub>3</sub>bupa)]<sup>–</sup> complexes.<sup>35,37</sup> Studies of a series of [Mn<sup>III</sup>(O<sub>2</sub>)(13-TMC)(X)]<sup>+</sup> complexes, where the axial ligand X = CN<sup>–</sup>, NCS<sup>–</sup>, CF<sub>3</sub>CO<sub>2</sub><sup>–</sup>, and N<sub>3</sub><sup>–</sup>, and the control complex with no axial ligand, revealed that the identity of the axial ligand can affect the rate of aldehyde deformylation by nearly three orders of magnitude.<sup>41</sup> It was proposed that strongly electron-donating *trans* ligands convert the side-on peroxo ligand to a more end-on geometry, with nonequivalent Mn–O<sub>peroxo</sub> bond lengths. While the reactivities of Mn<sup>III</sup>–O<sub>2</sub> complexes have been the subject of several in-depth studies, the electronic structure and the effect of the supporting ligand on the electronic structure of these complexes have remained comparatively unexplored.

## 1.5 Combined Spectroscopic and Computational Approach.

The majority of  $\text{Mn}^{\text{III}}\text{-O}_2$  adducts reported to date are too unstable to be characterized using XRD, but these complexes display the most intriguing reactivities. To address this gap in knowledge, a combined spectroscopic and computational approach was developed to obtain experimentally validated structures in the absence of XRD data. This method consists of four

Scheme 1.2



major steps: i) design and synthesis of  $\text{Mn}^{\text{II}}$  precursors, ii) use of cryogenic techniques to generate and trap  $\text{Mn}^{\text{III}}\text{-O}_2$  adducts, iii) determination of spectroscopic parameters for the  $\text{Mn}^{\text{III}}\text{-O}_2$  adducts, and iv) development of hypothetical structures using density functional theory

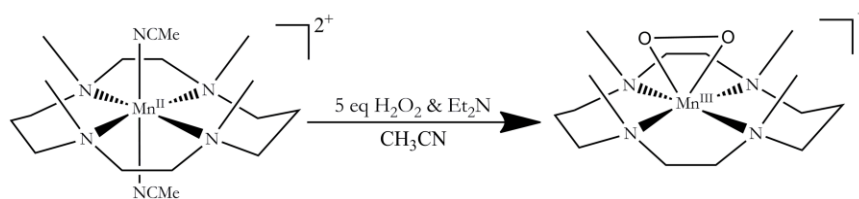


(DFT). The geometry optimized models were used to evaluate the validity of proposed structures by comparing computed and experimental spectroscopic parameters (Scheme 1.2). Prior to this work, this combined spectroscopic and computational method had not been employed in studying  $\text{Mn}^{\text{III}}\text{-O}_2$  systems. To validate this approach, it was first applied to a crystallographically-characterized  $\text{Mn}^{\text{III}}\text{-O}_2$  complex,  $[\text{Mn}^{\text{III}}(\text{O}_2)(\text{TMC})]^+$ , as discussed below.

### 1.6 Validation of Combined Spectroscopic and Computational Approach.

Because  $[\text{Mn}^{\text{III}}(\text{O}_2)(\text{TMC})]^+$  is one of the more stable  $\text{Mn}^{\text{III}}\text{-O}_2$  complexes, with a half-life of five hours at room temperature and a reported XRD structure, it is an ideal system to use to validate our combined spectroscopic and computational approach. The XRD structure of this complex revealed an O–O bond length of 1.40 Å and symmetric Mn–O bond lengths with distances of 1.88 Å.<sup>37</sup> Electrospray ionization mass spectrometry (ESI-MS) and electronic absorption spectroscopy was used to further characterize the  $[\text{Mn}^{\text{III}}(\text{O}_2)(\text{TMC})]^+$  complex. The electronic absorption spectrum showed an intense band at  $\sim 22\,000\text{ cm}^{-1}$  and a broad band at  $\sim 15$

**Scheme 1.3**



$900\text{ cm}^{-1}$  (Figure 1.3A). ESI-MS displayed a prominent ion peak consistent with a  $[\text{Mn}^{\text{III}}(\text{O}_2)(\text{TMC})]^+$  complex (reported for  $\text{M}^+$  ( $[\text{Mn}^{\text{III}}(\text{O}_2)(\text{TMC})](\text{OTf})$ ) $^+$  343.1 m/z requires:  $\text{M}^+$ , 343.2 m/z). When  $\text{H}_2^{18}\text{O}_2$  was used to form the  $\text{Mn}^{\text{III}}\text{-O}_2$  complex, the ESI-MS parent ion peak exhibited a four-mass-unit increase, indicating that the bound  $\text{O}_2$  unit was derived from  $\text{H}_2\text{O}_2$ . (reported for  $\text{M}^+$  ( $[\text{Mn}^{\text{III}}(^{18}\text{O}_2)(\text{TMC})](\text{OTf})$ ) $^+$  347.1 m/z requires:  $\text{M}^+$ , 347.2 m/z).

The TMC ligand was purchased from Sigma-Aldrich and used without further purification. The  $[\text{Mn}^{\text{II}}(\text{TMC})](\text{OTf})_2$  complex was synthesized following the reported procedure.<sup>37</sup> Upon addition of 5 equivalents of  $\text{H}_2\text{O}_2$  and 0.5 equivalents of triethylamine (TEA) to colorless solution of  $[\text{Mn}^{\text{II}}(\text{TMC})](\text{OTf})_2$ , the forest green product  $[\text{Mn}^{\text{III}}(\text{O}_2)(\text{TMC})]^+$  was formed (Scheme 1.3). This species displayed an electronic absorption spectrum virtually indistinguishable from the published spectrum (Figure 1.3A).<sup>37</sup>

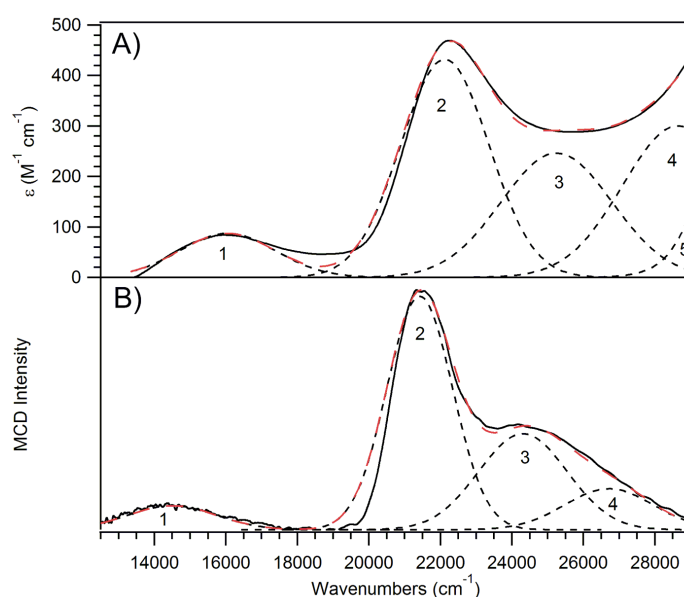


**Figure 1.3.** A) 293 K electronic absorption and B) 4.5 K, 7 T MCD spectra of  $[\text{Mn}^{\text{III}}(\text{O}_2)(\text{TMC})]^+$ . Individual Gaussian curves (black dotted lines) and their sums (red dashed lines) obtained from iterative fits of these data sets are displayed on their respective spectra. Conditions: Absorption data were collected for a 2.5 mM sample in  $\text{CH}_3\text{CN}$ . MCD data were collected for a 10 mM frozen glass sample in ethanol.

MCD spectroscopy was used to further characterize the  $[\text{Mn}^{\text{III}}(\text{O}_2)(\text{TMC})]^+$  complex. Figure 1.3 shows the 298 K absorption and 4.5 K, 7 T MCD spectra of  $[\text{Mn}^{\text{III}}(\text{O}_2)(\text{TMC})]^+$ . The two prominent absorption bands at  $\sim 15\,900$  and  $\sim 22\,000\text{ cm}^{-1}$  correspond to positive features in the MCD spectrum, and an additional positive band at  $\sim 24\,360\text{ cm}^{-1}$  is also resolved. An iterative Gaussian deconvolution of the absorption and MCD data sets reveals a total of four electronic transitions from  $12\,500$  to  $29\,000\text{ cm}^{-1}$ . For high-spin  $d^4$   $\text{Mn}^{\text{III}}$  complexes, a total of

four spin-allowed  $\text{Mn}^{\text{III}}$   $d-d$  transitions are expected in the near-IR to near-UV region. With no additional electronic features being observed down to  $9\,000\text{ cm}^{-1}$ , band 1 can be assigned as the lowest-energy  $d-d$  transition. For typical six-coordinate  $\text{Mn}^{\text{III}}$  complexes, this band is observed at  $\sim 10\,000\text{ cm}^{-1}$ , and reflects the splitting of the  $e_g$ -derived orbitals (traditionally  $d_z^2$  and  $d_{x^2-y^2}$ ), using the symmetry notation from the  $O_h$  point group. This transition is shifted to higher energy by  $\sim 5\,000\text{ cm}^{-1}$  for  $[\text{Mn}^{\text{III}}(\text{O}_2)(\text{TMC})]^+$ , indicating an unusual electronic structure, likely due to the presence of the peroxo ligand. Assignments for bands 2 - 4 are unclear given that none of these bands appear to be selectively enhanced in the MCD spectrum and cannot be unambiguously assigned as  $d-d$  transitions. Time-dependent-DFT computations were performed to aid in assigning these transitions as well as to determine if this computational method could be used to reproduce the electronic transition energies and intensities for a well-defined system.

A DFT-optimized model was developed to compare calculated bond lengths to the reported crystal structure. The *ORCA* 2.7 software package was used for all DFT computations.<sup>40</sup> An initial model of  $[\text{Mn}^{\text{III}}(\text{O}_2)(\text{TMC})]^+$  was built using the X-ray coordinates of the reported  $\text{Mn}^{\text{III}}$  complex. The geometry optimized model of this metal complex was converged to the  $S = 2$  spin state. These calculations employed the Becke-Perdew (BP86) functional<sup>44,45</sup> and the SVP (Ahlichs split valence polarized)<sup>46,47</sup> basis set with the SV/J auxiliary basis set for all atoms except for manganese, nitrogen, and oxygen, where the larger TZVP (Ahlichs triple- $\zeta$  valence polarized)<sup>44</sup> basis set in conjunction with the TZV/J auxiliary basis set were used. The resolution of identity (RI) approximation, developed by Neese,<sup>45</sup> was used for all calculations. Solvation effects associated with acetonitrile (dielectric constant  $\epsilon = 36.6$ ) were incorporated using COSMO, as implemented in *ORCA*.<sup>46</sup> The optimized structure displays a six-coordinate Mn center with side-on peroxo ligand, as shown in Figure 1.4.

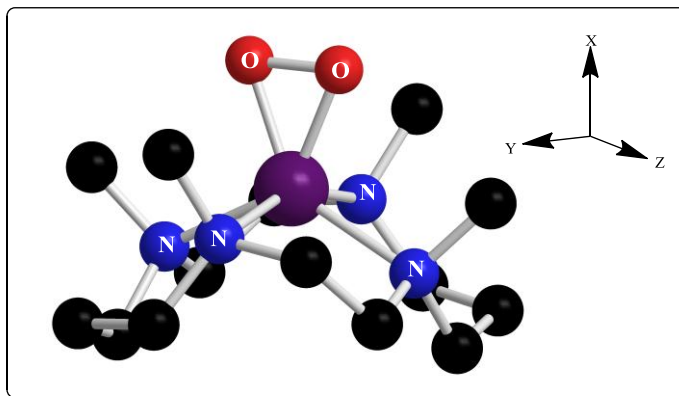


**Figure 1.4.** DFT-Optimized Model of  $[\text{Mn}^{\text{III}}(\text{O}_2)(\text{TMC})]^+$

The nitrogen atoms of the supporting TMC ligand form the base of a square plane that sits below the  $\text{Mn}^{\text{III}}\text{--O}_2$  unit. The O-O bond length is 1.43 Å and the Mn-O bond length is 1.87 Å, which is remarkably comparable to those reported in the XRD structure (Mn-O 1.88 Å and O-O 1.40 Å).

Using the DFT optimized model, the electronic transition energies and intensities were computed using the TD-DFT method<sup>48-50</sup> within the Tamm-Dancoff approximation.<sup>51,52</sup> These calculations employed the B3LYP functional,<sup>53-55</sup> and TZVP (Mn, N, and O) and SVP (C and H) basis sets. In this calculation, 40 excited states were calculated by including all one-electron excitations within an energy window of  $\pm 3$  Hartrees with respect to the HOMO/LUMO energies. The TD-DFT computed absorption spectrum for  $[\text{Mn}^{\text{III}}(\text{O}_2)(\text{TMC})]^+$  is strikingly similar to the experimental spectrum (Figure 1.5), with a slight blue shift of  $\sim 2\,000\text{ cm}^{-1}$  when compared to experimental data, which is within the error of the TD-DFT method.<sup>55</sup> Bands 1 and 2 ( $16\,820\text{ cm}^{-1}$  and  $24\,790\text{ cm}^{-1}$ , figure 1.5B, respectively) are predicted as  $d_{x^2-y^2} \rightarrow d_{yz}$  and  $d_z \rightarrow d_{yz}$  transitions, respectively. Band 3 ( $28\,680\text{ cm}^{-1}$ , Figure 1.5) is predicted as a peroxo-to- $\text{Mn}^{\text{III}}$  charge transfer (CT) transition ( $\text{O}_2 \rightarrow \text{Mn } d_{xz}$ ). At higher energy, the TD-DFT calculations predict additional peroxo-to- $\text{Mn}^{\text{III}}$  CT transitions (band 4,  $33\,631\text{ cm}^{-1}$ ) as well as the remaining

two  $d-d$  bands ( $34\,160$  and  $38\,930\text{ cm}^{-1}$ ). This combined spectroscopic/computational method has proved to be well suited for the study of the electronic and geometric structure of  $\text{Mn}^{\text{III}}\text{-O}_2$  complexes and it is thus warranted to apply this technique in the characterization of complexes for which structural information is lacking.

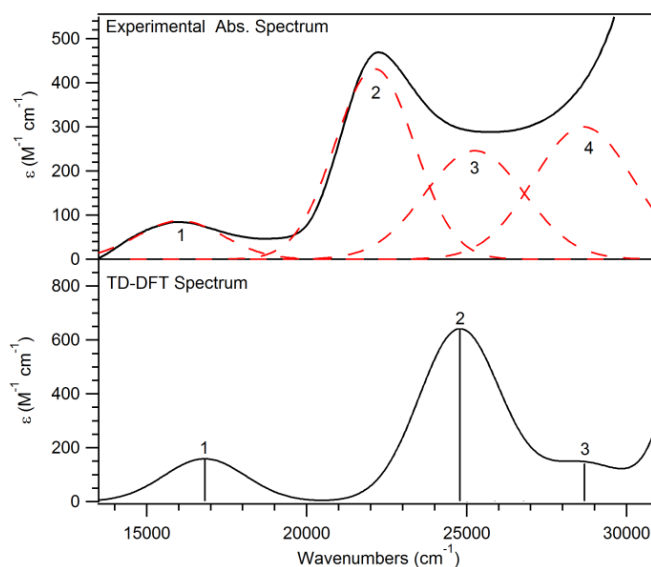


**Figure 1.5.** Top: 293 K electronic absorption spectra of  $[\text{Mn}^{\text{III}}(\text{O}_2)(\text{TMC})]^+$ . Individual Gaussian curves (black dotted lines) obtained from iterative fits of these data sets are displayed on their respective spectra. Conditions: Absorption data were collected for a 2.5 mM sample in  $\text{CH}_3\text{CN}$ . Bottom: Simulated absorption spectra of  $[\text{Mn}^{\text{III}}(\text{O}_2)(\text{TMC})]^+$  based on TD-DFT computations employing the B3LYP functional. Sticks mark the position of individual electronic transitions.

## 1.7 References.

- (1) Song, W. J.; Sun, Y. J.; Choi, S. K.; Nam, W. *Chem. Eur. J* **2006**, 2006, 130.
- (2) Vaska, L. *Acc. Chem. Res.* **1975**, 9, 175.
- (3) Betley, T. A.; Surendranath, Y.; Childress, M. V.; Alliger, G. E.; Fu, R.; Cummins, C. C.; Nocera, D. G. *Phil. Trans. R. Soc. B* **2008**, 363, 1293.
- (4) Goldberg, D. P. *Acc. Chem. Res.* **2007**, 40, 626.
- (5) Gross, Z.; Golubkov, G.; Simkhovich, L. *Angew. Chem. Int. Ed.* **2000**, 39, 4045.
- (6) Popescu, D.-L.; Chanda, A.; Stadler, M.; Tiago de Oliveira, F.; Ryabov, A. D.; Münck, E.; Bominaar, E. L.; Collins, T. J. *Coord. Chem. Rev.* **2008**, 252, 2050.
- (7) Song, W. J.; Seo, M. S.; DeBeerGeorge, S.; Ohta, T.; Song, R.; Kang, M. J.; Tosha, T.; Kitagawa, T.; Solomon, E. I.; Nam, W. *J. Am. Chem. Soc.* **2007**, 129, 1268.
- (8) Wu, A. J.; Penner-Hahn, J. E.; Pecoraro, V. L. *Chem. Rev.* **2004**, 104, 903.
- (9) Miller, A. F. *Superoxide processing*, In *Comprehensive Coordination Chemistry II*; Elsevier Ltd: Oxford, UK., 2004.

- (10) Svedružić, D.; Jónsson, S.; G., T. C.; Reinhardt, L. A.; Ricagno, S.; Lindqvist, Y.; Richards, N. G. *J. Arch. Biochem. Biophys* **2005**, *433*, 176.
- (11) Emerson, J. P.; Kovaleva, E. G.; Farquhar, E. R.; Lipscomb, J. D.; Que, L. J. *Proc. Natl. Acad. Sci.* **2008**, *105*, 74347.
- (12) Cotruvo, J. A.; Stubbe, J. *Biochemistry* **2010**, *49*, 1297.
- (13) Willing, A.; Follmann, H.; Auling, G. *Eur. J. Biochem.* **1988**, *170*, 603.
- (14) Pecoraro, V. L.; Hsieh, W. Y. *Inorg. Chem* **2008**, *47*, 1765.
- (15) Gunderson, W. A.; Zatsman, A. I.; Emerson, J. P.; Farquhar, E. R.; Que, L.; Lipscomb, J. D.; Hendrich, M. P. *J. Am. Chem. Soc.* **2008**, *130*, 14465.
- (16) Edwards, R. A.; Baker, H. M.; Whittaker, M. M.; Whittaker, J. W.; Jameson, G. B.; Baker, E. N. *J. Bio. Chem.* **1998**, *278*, 21483.
- (17) Ludwig, M. L.; Metzger, A. L.; Patridge, K. A.; Stallings, W. C. *J. Biol. Inorg. Chem.* **1991**, *3*.
- (18) Bull, C.; Niederhoffer, E. C.; Yoshida, T.; Fee, J. A. *J. Am. Chem. Soc.* **1991**, *113*, 4069.
- (19) Ludwig, M. L.; Metzger, A. L.; Patridge, K. A.; Stallings, W. C. *J. Mol. Biol* **1991**, *219*, 335.
- (20) Sibbons, K.; Shastri, K.; Watkinson, M. *Dalton Trans.* **2006**, *2006*, 645.
- (21) Hage, R.; Lienke, A. *J. Mol. Catal. A: Chem* **2006**, *251*, 150.
- (22) Hage, R.; Lienke, A. *Chem. Rev.* **2006**, *105*, 1565.
- (23) Hage, R.; Iburg, J. E.; Kerschner, J.; Koek, J. H.; Lempers, E. L. M.; Martens, R. J.; Racherla, U. S.; Russell, S. W.; Swarthoff, T.; Van Vliet, M. R. P.; Warnaar, J. B.; Wolf, L. v. d.; Krijnen, B. *Nature* **1994**, *369*, 637.
- (24) Gross, Z.; Golubkov, G.; Simkhovich, L. *Angew. Chem. Int. Ed.* **2000**, *39*, 4045.
- (25) Goldberg, D. P. *Acc. Chem. Res.* **2007**, *40*, 626.
- (26) Popescu, D. L.; Chanda, A.; Stadler, M.; Tiago de Oliveira, F.; Ryabov, A. D.; Münck, E.; Bominaar, E. L.; Collins, T. J. *Coord. Chem. Rev.* **2008**, *252*, 2050.
- (27) Song, W. J.; Seo, M. S.; DeBeerGeorge, S.; Ohta, T.; Song, R.; Kang, M. J.; Tosha, T.; Kitagawa, T.; Solomon, E. I.; Nam, W. *J. Am. Chem. Soc.* **2007**, *129*, 1268.
- (28) MacDonnell, F. M.; Fackler, N. L. P.; Stern, C.; O'Halloran, T. V. *J. Am. Chem. Soc.* **1994**, *116*, 7431.
- (29) Jin, N.; Groves, J. T. *J. Am. Chem. Soc.* **1999**, *121*.
- (30) Groves, J. T.; Lee, J.; Marla, S. S. *J. Am. Chem. Soc.* **1997**, *119*, 6269.
- (31) Lane, B. S.; Burgess, K. *Chem. Rev.* **2003**, *103*, 2457.
- (32) Mansuy, D. *Chem. Rev.* **1993**, *105*, 1565.
- (33) Groni, S.; Blain, G.; Guillot, R.; Policar, C.; Anxolabéhère-Mallart, E. *Inorg. Chem.* **2007**, *46*, 1951.
- (34) Groni, S.; Dorlet, P.; Blain, G.; Bourcier, S.; Guillot, R.; Anxolabéhère-Mallart, E. *Inorg. Chem.* **2008**, *47*, 3166.
- (35) Shook, R. L.; Gunderson, W. A.; Greaves, J.; Ziller, J. W.; Hendrich, M. P.; Borovik, A. S. *J. Am. Chem. Soc.* **2008**, *130*, 8888.
- (36) Kitajima, N.; Komatsuzaki, H.; Hikichi, S.; Osawa, M.; Moro-oka, Y. *J. Am. Chem. Soc.* **1994**, *116*, 11596.
- (37) Seo, M. S.; Kim, J. Y.; Annaraj, J.; Kim, Y.; Lee, Y.-M.; Kim, S.-J.; Kim, J.; Nam, W. *Angew. Chem. Int. Ed.* **2007**, *46*, 377.
- (38) Singh, U. P.; Sharma, A. K.; Hikichi, S.; Komatsuzaki, H.; Moro-oka, Y.; Akita, M. *Inorg. Chim. Acta* **2006**, *359*, 4407.

- (39) VanAtta, R. B.; Strouse, C. E.; Hanson, L. K.; Valentine, J. S. *J. Am. Chem. Soc.* **1987**, *109*, 1425.
- (40) Jackson, T. A.; Brunold, T. C. *Acc. Chem. Res.* **2004**, *37*, 461.
- (41) Annaraj, J.; Cho, J.; Lee, Y.-M.; Kim, S. Y.; Latifi, R.; de Visser, S. P.; Nam, W. *Angew. Chem. Int. Ed.* **2009**, *48*, 4150.
- (42) Costas, M.; Mehn, M. P.; Jensen, M. P.; Que, L. J. *Chem. Rev.* **2004**, *104*, 939.
- (43) Sisemore, M. F.; Selke, M.; Burstyn, J. N.; Valentine, J. S. *Inorg. Chem.* **1997**, *36*, 979.
- (44) Becke, A. D. *J. Chem. Phys.* **1986**, *84*, 4524.
- (45) Perdew, J. P. *Physical Review B* **1986**, *33*, 8822.
- (46) Schäfer, A.; Horn, H.; Ahlrichs, R. *J. Chem. Phys.* **1992**, *97*, 2571.
- (47) Schäfer, G.; Huber, C.; Ahlrichs, R. *J. Chem. Phys.* **1994**, *100*, 5829.
- (48) Bauernschmitt, R.; Ahlrichs, R. *Chem. Phys. Lett.* **1996**, *256*, 454.
- (49) Casida, E. M.; Jamorski, C.; Casida, K. C.; Salahub, D. R. *J. Chem. Phys.* **1998**, *108*, 4439.
- (50) Stratman, R. E.; Scuseria, G. E.; Frisch, M. J. *J. Chem. Phys.* **1998**, *109*, 8218.
- (51) Hirata, S.; Head-Gordon, M. *Chem. Phys. Lett.* **1999**, *302*, 375.
- (52) Hirata, S.; Head-Gordon, M. *Chem. Phys. Lett.* **1999**, *314*, 291.
- (53) Becke, A. D. *J. Chem. Phys.* **1993**, *98*, 1372.
- (54) Becke, A. D. *J. Chem. Phys.* **1993**, *98*, 5648.
- (55) Lee, C.; Yang, W.; Parr, R. G. *Phys. Rev. B* **1988**, *37*, 785.

## Chapter 2

### **Spectroscopic and Computational Studies of Peroxomanganese(III) Complexes Supported by Tetradentate Aminopyridyl Ligands**

This work has been published under the following: Geiger R. A.; Chattopadhyay S.; Day V. W.; Jackson T. A.; A Series of Peroxomanganese(III) Complexes Supported by Tetradentate Aminopyridyl Ligands: Detailed Spectroscopic and Computational Studies; *J. Am. Chem. Soc.* **2010**, 132, 2821-2831



## 2. 1 Introduction.

Manganese centers that react with oxygen and its reduced derivatives play important roles in biological systems, including the detoxification of superoxide and hydrogen peroxide and the bioremediation of aromatics.<sup>1-5</sup> Such manganese centers are also of interest for synthetic applications, as they have been shown to mediate useful oxygenation reactions, including olefin epoxidation, C–H bond hydroxylation, and alcohol oxidation.<sup>6-9</sup> While the elucidation of the mechanisms of these systems remains the subject of much current work, the importance of peroxo-level intermediates has been underscored by several reports. For example, the enzyme manganese superoxide dismutase (MnSOD), which functions to disproportionate superoxide to dioxygen and water, forms a product-inhibited complex under high superoxide concentrations that has been proposed as a peroxomanganese(III) adduct.<sup>10-11</sup> With respect to synthetic manganese catalysts that activate hydrogen peroxide, (hydro)peroxomanganese intermediates are often proposed to precede high-valent oxomanganese adducts invoked as active oxidants.<sup>6,9</sup> Alternatively, in some cases, peroxomanganese intermediates have been proposed as the active species for substrate oxidation.<sup>12</sup> Thus, fundamental studies of peroxomanganese(III) intermediates should advance the current level of understanding of manganese centers important in biological and synthetic systems.

In this chapter we report the generation and characterization of four peroxomanganese(III) adducts supported by derivatives of the linear tetradentate  $L^7py_2^R$  ( $L^7py_2 = 1,4\text{-bis}(2\text{-pyridylmethyl})\text{-}1,4\text{-diazepane}$ ) ligands that differ only with respect to the identity of pyridine ring substituents ( $R = H, 5\text{-Br}, 6\text{-Me}, \text{ and } 6\text{-MeO}$ ). X-ray diffraction (XRD), ESI-MS, and  $^1H\text{-NMR}$  experiments have been used to characterize the solid-state and solution properties

of the corresponding manganese(II) precursors. For all complexes, the XRD structures show the  $L^7py_2^R$  ligand bound in a *trans* conformation, which we propose plays an important role in governing the reactivity of these complexes with hydrogen peroxide. The four peroxomanganese(III) complexes  $[Mn^{III}(O_2)(L^7py_2^H)]^+$ ,  $[Mn^{III}(O_2)(L^7py_2^{5-Br})]^+$ ,  $[Mn^{III}(O_2)(L^7py_2^{6-Me})]^+$ ,  $[Mn^{III}(O_2)(L^7py_2^{6-MeO})]^+$  were generated using cryogenic techniques and characterized by ESI-MS and electronic absorption spectroscopy. The electronic structures of the  $[Mn^{III}(O_2)(L^7py_2^H)]^+$  and  $[Mn^{III}(O_2)(L^7py_2^{6-Me})]^+$  complexes were investigated in more detail using low-temperature magnetic circular dichroism (MCD), and variable-temperature, variable-field (VTVH) MCD spectroscopies. Whereas fits of VTVH MCD data collected for these samples revealed similar ground-state zero-field splitting parameters, the electronic absorption and MCD spectra display key differences in *d-d* and charge-transfer transition energies, indicating structural and/or electronic perturbations among these complexes. Using a framework provided by density functional theory (DFT) computations; these spectroscopic perturbations were related to differences in  $Mn^{III}-O_2$  bonding among these complexes. Specifically, these data suggest that the presence of electron-rich substituents support more asymmetric (*i.e.*, more end-on) peroxo ligands. Together, these combined experimental and theoretical studies provide the first detailed investigation of the electronic structures of peroxomanganese(III) adducts and offer a basis for correlating spectroscopic features with  $Mn^{III}-O_2$  bonding.

## 2.2 Results and Discussion.

**2.2.1 Structures and Physical Properties of  $[Mn^{II}(L^7py_2^R)](ClO_4)_2$  Complexes.** Figure 2.1 displays ORTEP diagrams for the four manganese(II) complexes  $[Mn^{II}(L^7py_2^H)(NCMe)_3](ClO_4)_2$  (**1-H**),  $[Mn^{II}(L^7py_2^{5-Br})(OCMe_2)(ClO_4)](ClO_4)$  (**1-Br**),  $[Mn^{II}(L^7py_2^{6-Me})(NCMe)(ClO_4)](ClO_4)$  (**1-**

**Me**), and  $[\text{Mn}^{\text{II}}(\text{L}^7\text{py}_2^{6\text{-MeO}})(\text{ClO}_4)_2]$  (**1-MeO**). Selected bond distances and angles are given in the Table 2.1. The amine nitrogens (N3 and N4; see Figure 2.1) of the **1-H** and **1-Br** complexes are seen to be linked by a high-occupancy (~80%) pair of ethylene and propylene chains and a pair of low-occupancy chains (~20%) chains, consistent with cocrystallization of two different conformations of the metal complex that have virtually identical sizes and shapes. Metric parameters for the high-occupancy species are displayed in Table 2.1, whereas corresponding parameters for the low-occupancy species are included in Supporting Information. Importantly, the metric parameters among these complexes are comparable. For the **1-MeO** complex, the Mn atom lies along a crystallographic  $C_2$  axis, and thus the respective pyridine nitrogens, amine nitrogens, and perchlorate groups are symmetry related (Table 2.1).

For each of the four **1-R** complexes shown in Figure 2.1, the linear, tetradentate  $\text{L}^7\text{py}_2^{\text{R}}$  ligand is bound in the *trans* configuration, as opposed to the *cis-α* or *cis-β* isomers. This observed configuration creates two *trans* coordination sites occupied by solvent and/or perchlorate ligands (X1 and X2; see Figure 2.1). In the cases of **1-H** and **1-Br**, a seventh ligand is bound in the equatorial plane and flanked by the pyridine rings of the  $\text{L}^7\text{py}_2^{\text{H}}$  and  $\text{L}^7\text{py}_2^{5\text{-Br}}$  ligands. For all complexes, the  $\text{Mn}^{\text{II}}$ –ligand bond lengths range from ~2.1 to 2.5 Å, expected distances for high-spin Mn(II) centers.

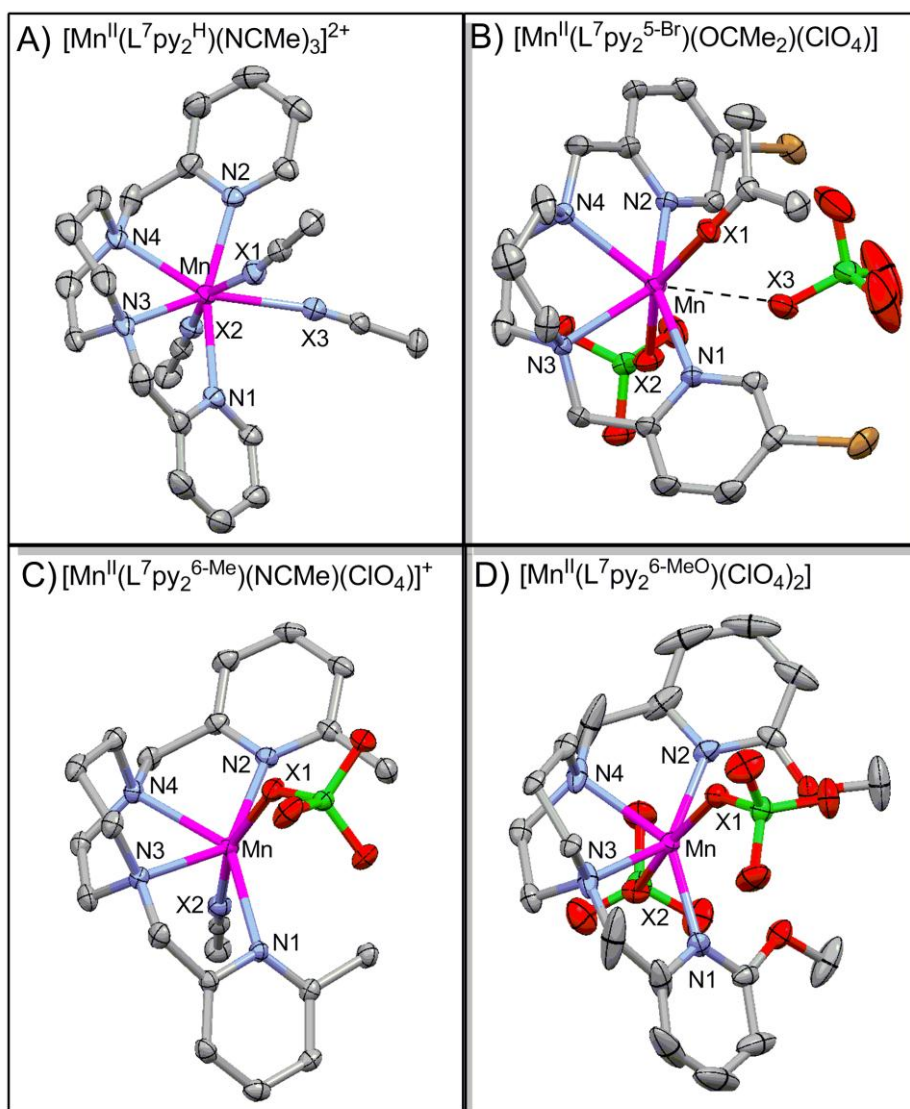


**Figure 2.1.** ORTEP diagrams of A)  $[\text{Mn}^{\text{II}}(\text{L}^7\text{py}_2^{\text{H}})(\text{NCMe})_3](\text{ClO}_4)_2$  (**1-H**), B)  $[\text{Mn}^{\text{II}}(\text{L}^7\text{py}_2^{5\text{-Br}})(\text{OCMe}_2)(\text{ClO}_4)](\text{ClO}_4)$  (**1-Br**), C)  $[\text{Mn}^{\text{II}}(\text{L}^7\text{py}_2^{6\text{-Me}})(\text{NCMe})(\text{ClO}_4)](\text{ClO}_4)$  (**1-Me**), and D)  $[\text{Mn}^{\text{II}}(\text{L}^7\text{py}_2^{6\text{-MeO}})(\text{ClO}_4)_2]$  (**1-MeO**) showing 50% probability thermal ellipsoids. Hydrogen atoms and non-coordinating perchlorate counter anions have been removed for clarity. Significant interatomic distances and angles are listed in Table 2.1.

**Table 2.1.** Selected Bond Lengths (Å) and Angles (°) for Complexes **1-H**, **1-Br**, **1-Me**, and **1-MeO**.

Complex <b>1-H</b>			
Mn-N(1)	2.306(3)	N(1)-Mn-N(2)	158.8(1)
Mn-N(2)	2.308(2)	N(1)-Mn-N(3)	72.0(1)
Mn-N(3)	2.369(3)	N(2)-Mn-N(4)	71.4(1)
Mn-N(4)	2.357(2)	N(3)-Mn-N(4)	67.4(1)
Mn-X(1)	2.268(2)	X(1)-Mn-X(2)	160.0(1)
Mn-X(2)	2.311(2)	X(1)-Mn-X(3)	79.5(1)
Mn-X(3)	2.478(2)	X(2)-Mn-X(3)	80.8(1)
Complex <b>1-Br</b>			
Mn-N(1)	2.262(3)	N(1)-Mn-N(2)	154.1(1)
Mn-N(2)	2.285(3)	N(1)-Mn-N(3)	73.6(1)
Mn-N(3)	2.323(4)	N(2)-Mn-N(4)	71.2(1)
Mn-N(4)	2.341(3)	N(3)-Mn-N(4)	68.9(1)
Mn-X(1)	2.200(2)	X(1)-Mn-X(2)	154.2(1)
Mn-X(2)	2.292(2)	X(1)-Mn-X(3)	80.8(1)
Mn...X(3)	2.679(3)	X(2)-Mn-X(3)	74.1(1)
Complex <b>1-Me</b>			
Mn-N(1)	2.284(2)	N(1)-Mn-N(2)	143.34(7)
Mn-N(2)	2.284(2)	N(1)-Mn-N(3)	76.32(7)
Mn-N(3)	2.306(2)	N(2)-Mn-N(4)	75.02(7)
Mn-N(4)	2.285(2)	N(3)-Mn-N(4)	69.50(7)
Mn-X(1)	2.212(2)	X(1)-Mn-X(2)	161.91(7)
Mn-X(2)	2.280(2)		
Complex <b>1-MeO</b>			
Mn-N(1)/N(2)	2.176(2)	N(1)-Mn-N(2)	142.1(1)
Mn-N(3)/N(4)	2.308(2)	N(1)-Mn-N(3)	75.7(1)
Mn-X(1)/X(2)	2.278(2)	N(3)-Mn-N(4)	70.3(1)
		X(1)-Mn-X(2)	173.1(1)

Differences in the crystallographic structures of these  $\text{Mn}^{\text{II}}$  complexes can be attributed to the distinct steric and electronic influences caused by the pyridine substituents.  $\text{Mn}^{\text{II}}$  complexes can exist in a variety of geometries, including six-, seven-, and eight-coordinate forms.<sup>47-48</sup> The **1-H** complex containing the sterically unencumbered  $\text{L}^7\text{py}_2^{\text{H}}$  ligand displays a seven-coordinate  $\text{Mn}^{\text{II}}$  ion in a distorted pentagonal bipyramidal geometry. The tetradentate  $\text{L}^7\text{py}_2^{\text{H}}$  ligand defines the equatorial plane, though this plane is quite ruffled; the mean deviation of the nitrogen atoms from this plane is 0.747 Å. The seven coordinate structure is completed by three MeCN solvent molecules occupying a meridional plane. The equatorial acetonitrile ligand (labeled X3 in Figure 2.2) displays a weak interaction with the  $\text{Mn}^{\text{II}}$  center ( $\text{Mn}^{\text{II}}\text{--NCMe}$  distance of 2.479 Å), and the  $\text{Mn}\text{--NCMe}$  vector roughly bisects the two  $\text{Mn}\text{--N}_{\text{amine}}$  bonds. The  $\text{Mn}^{\text{II}}$  center of the **1-Br** complex is likewise seven-coordinate, with a weakly associated perchlorate anion in the equatorial plane ( $\text{Mn}\text{--OCIO}_3$  distance of 2.679 Å). Because this complex was crystallized in acetone/ether, an axially bound acetone ligand is observed rather than an MeCN ligand.

Unlike **1-H** and **1-Br**, the **1-Me** and **1-MeO** complexes are six-coordinate in the solid state structures (Figure 2.1), which is likely due to both electronic and steric effects. This reduced coordination number could be attributed to the greater electron-donating abilities of the methyl- and methoxy-appended pyridine ligands, as these electron-donating functionalities will reduce the Lewis acidity of the  $\text{Mn}^{\text{II}}$  center and could be expected to support a complex with a lower coordination number when compared with complexes supported by the  $\text{L}^7\text{py}_2^{\text{H}}$  and  $\text{L}^7\text{py}_2^{5-\text{Br}}$  ligands. In support, it was recently reported that the coordination number of  $\text{Mn}^{\text{III}}$  Schiff base complexes can be controlled by the presence or absence of electron-withdrawing  $\text{--CF}_3$  groups on the ligand.<sup>49</sup> Specifically, six-coordinate  $\text{Mn}^{\text{III}}$  complexes were observed in complexes with  $\text{--CF}_3$  groups, whereas five-coordinate complexes were evident when these groups were absent. For **1-**

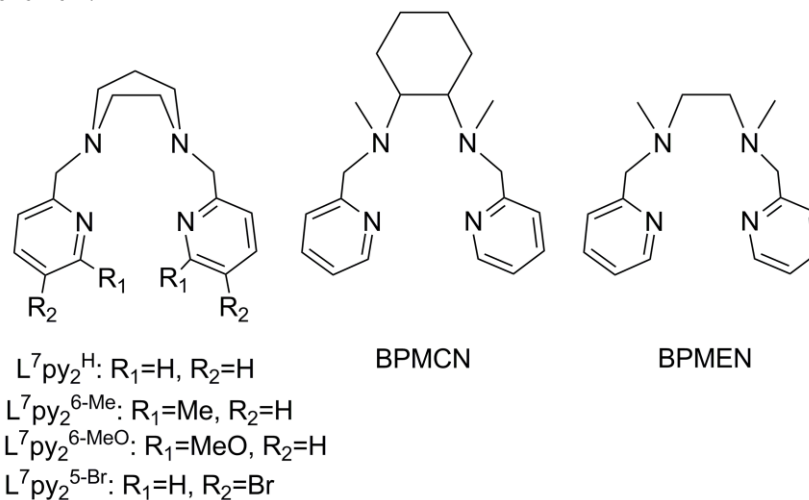
**Me** and **1-MeO**, the steric bulk of the methyl and methoxy substituents would additionally be expected to block the binding of a seventh ligand between the two pyridine rings (see Figure A.2.2 for a comparison of the space filling diagrams of the **1-R** complexes). It is quite likely that both steric and electronic effects contribute to the lower coordination number of the **1-Me** and **1-MeO** complexes.

The solution structures of these  $\text{Mn}^{\text{II}}$  salts were probed using electrospray ionization mass spectrometry (ESI-MS) and magnetic experiments. In all ESI-MS experiments, prominent ion peaks corresponding to a cationic mononuclear species. Specifically,  $\{\text{Mn}^{\text{II}}(\text{L}^7\text{py}_2^{\text{R}})(\text{ClO}_4)\}^+$  ions were observed at  $m/z = 436.0707$  (**1-H**),  $593.8927$  (**1-Br**),  $464.1023$  (**1-Me**), and  $496.0899$  (**1-MeO**). In addition, the spin states of the  $\text{Mn}^{\text{II}}$  complexes in deuterated MeCN solution were probed using the  $^1\text{H}$ -NMR method of Evans.<sup>25</sup> Analysis of the  $^1\text{H}$ -NMR data revealed room-temperature effective magnetic moments of  $\sim 5.80 - 6.1$  BM (Table A.2.9), consistent with theoretical values expected for high-spin manganese(II) systems ( $\mu_{\text{eff}} = 5.92$  BM).

It is informative to discuss the structures of these  $\text{Mn}^{\text{II}}$  complexes within the context of previously reported structures that feature other linear, tetradentate ligands (Scheme 2.1), such as BPMEN (BPMEN = *N,N'*-dimethyl-*N,N'*-bis(2-pyridylmethyl)-1,2-ethane diamine) and BPMCN (BPMCN = *N,N'*-dimethyl-*N,N'*-bis(2-pyridylmethyl)-1,2-cyclohexanediamine). The  $[\text{Mn}^{\text{II}}(\text{BPMEN})\text{Cl}_2]$  and  $[\text{Mn}^{\text{II}}(R,R\text{-BPMCN})(\text{CF}_3\text{SO}_3)_2]$  complexes both display the ligands bound in the *cis*- $\alpha$  conformation,<sup>50-51</sup> with the respective chloride and triflate anions *cis* to one another and *trans* to the amine nitrogens. The presence of these *cis* labile binding sites has been proposed to be important for catalytic epoxidation reactions involving peracetic acid as terminal oxidant.<sup>51-52</sup> Presumably, these *cis* labile sites also contribute to the facile formation of bis( $\mu$ -

oxo)-bridged dimers for the  $\text{Mn}_2(\text{III,III})$ ,  $\text{Mn}_2(\text{III,IV})$  and  $\text{Mn}_2(\text{IV,IV})$  forms of these complexes.<sup>50,53-58</sup> In contrast, the *trans* orientations observed for the **1-R** complexes with the pyridyl-appended diazacycloalkane  $\text{L}^7\text{py}_2^{\text{R}}$  ligands (figure 2.1), are consistent with the observations of Que and Halfen, who reported the  $\text{L}^7\text{py}_2^{\text{H}}$  ligand bound in a *trans* fashion for  $\text{Cu}^{\text{II}}$  and  $\text{Fe}^{\text{II}}$  complexes.<sup>59-61</sup> An exception to these observations is the recent report of  $\text{Fe}^{\text{III}}$  complexes of the  $\text{L}^7\text{py}_2^{\text{H}}$  ligand bound in the *cis-β* orientation.<sup>26</sup> We attribute this difference to the fact that this complex was co-crystallized with a bidentate tetrachlorocatecholate ligand, which, because of its structural rigidity, cannot bind in a bidentate fashion if the  $\text{L}^7\text{py}_2^{\text{H}}$  ligand is in a *trans*-conformation. Thus, while the  $\text{L}^7\text{py}_2^{\text{R}}$  ligands are flexible in their binding modes, the *trans*-conformation appears to be preferred, in contrast to that reported for the similar BPMEN and BPMCN ligands.

Scheme 2.1



**2.2.2 Characterization of  $[\text{Mn}^{\text{III}}(\text{O}_2)(\text{L}^7\text{py}_2^{\text{R}})]^+$  Intermediates.** The absorption spectra of acetonitrile solutions of all **1-R** complexes are featureless below 300 nm. This is expected, as the *d-d* transitions for these high-spin  $\text{Mn}^{\text{II}}$  centers are all spin-forbidden, and no charge transfer



(CT) transitions involving the pyridine and amine ligands are anticipated in the visible region. When 5 equivalents of H<sub>2</sub>O<sub>2</sub> and 0.5 equivalents of triethylamine are added to a 2.5 mM solution of [Mn<sup>II</sup>(L<sup>7</sup>py<sub>2</sub><sup>H</sup>)]<sup>2+</sup> in MeCN at -40 °C, a forest green intermediate (**2-H**) is formed. The absorption spectrum of **2-H** is characterized by a prominent absorption band at 445 nm and a weaker, broader band at 590 nm ( $\epsilon = 280$  and  $120 \text{ M}^{-1}\text{cm}^{-1}$ , respectively, Figure 2.2, top). The formation of these absorption bands upon addition of H<sub>2</sub>O<sub>2</sub> is consistent with oxidation of the Mn<sup>II</sup> ion, as complexes with higher oxidation state Mn centers (*i.e.*, Mn<sup>III</sup> and Mn<sup>IV</sup>) commonly display absorption bands in the visible region. While **2-H** is stable at -40 °C for several hours, the  $t_{1/2}$  at 0 °C is approximately 15 minutes. Due to this thermal instability, we have not been able to prepare crystals of **2-H** suitable for XRD experiments. Accordingly, we used ESI-MS to aid in defining the molecular composition of **2-H**. The ESI-MS spectrum of **2-H** exhibits a prominent ion peak at  $m/z = 369.1121$ , whose mass and isotope pattern corresponds to the [Mn<sup>III</sup>(O<sub>2</sub>)(L<sup>7</sup>py<sub>2</sub><sup>H</sup>)]<sup>+</sup> cation (calculated 369.1123) (Figure A.2.2). When **2-H** is generated with isotopically labeled H<sub>2</sub><sup>18</sup>O<sub>2</sub>, the major ion peak upshifts by four mass units to  $m/z = 373.1157$ , indicating that the oxygen atoms of **2-H** derive from hydrogen peroxide. An alternative route for forming **2-H** was achieved by treating the corresponding Mn<sup>II</sup> complex with 1 equivalent KO<sub>2</sub> in the presence of 18-Crown-6 in MeCN at -40 °C. Identical absorption and ESI-MS data are obtained regardless of whether H<sub>2</sub>O<sub>2</sub>/Et<sub>3</sub>N or KO<sub>2</sub> are used to form **2-H**. This latter route has the advantage that H<sub>2</sub>O and base are not introduced into the reaction mixture.

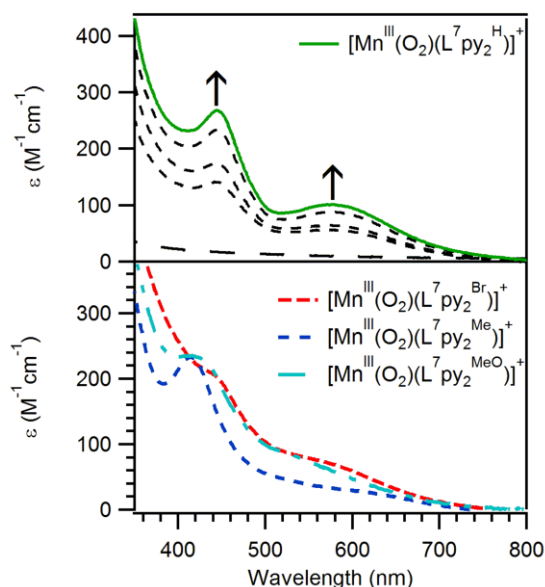


**Figure 2.2.** Top: Formation of  $[\text{Mn}^{\text{III}}(\text{O}_2)(\text{L}^7\text{py}_2^{\text{H}})]^+$  following the addition of 5 equivalents  $\text{H}_2\text{O}_2$  and 0.5 equivalents triethylamine to  $[\text{Mn}^{\text{II}}(\text{L}^7\text{py}_2^{\text{H}})]^{2+}$  in MeCN at  $-40^\circ\text{C}$ . Bottom: Electronic absorption spectra of  $[\text{Mn}^{\text{III}}(\text{O}_2)(\text{L}^7\text{py}_2^{5-\text{Br}})]^+$ ,  $[\text{Mn}^{\text{III}}(\text{O}_2)(\text{L}^7\text{py}_2^{6-\text{Me}})]^+$ , and  $[\text{Mn}^{\text{III}}(\text{O}_2)(\text{L}^7\text{py}_2^{6-\text{MeO}})]^+$  at  $-40^\circ\text{C}$  in MeCN.

The absorption spectrum of **2-H** (Figure 2.2, top) bears a striking resemblance to that reported for the crystallographically characterized complex  $[\text{Mn}^{\text{III}}(\text{O}_2)(\text{TMC})]^+$ , which displayed an intense absorption band at 453 nm with a broader band at 630 nm ( $\epsilon = 490$  and  $120 \text{ M}^{-1}\text{cm}^{-1}$ , respectively).<sup>17</sup> The spectral similarities between these complexes, along with our ESI-MS data for **2-H**, lead us to conclude that **2-H** likewise contains a six-coordinate  $\text{Mn}^{\text{III}}$  center with a peroxo ligand bound in a side-on  $\eta^2$  fashion. Further confirmation for the  $\text{Mn}^{\text{III}}$  oxidation state is provided by VTVH MCD data described in the following section. The observation that peroxomanganese(III) complex **2-H** can be formed using either  $\text{H}_2\text{O}_2$  or  $\text{KO}_2$  as oxidant parallels that reported for  $[\text{Mn}^{\text{III}}(\text{O}_2)(\text{Me-TPEN})]^+$ .<sup>13-14</sup> The observed reactivity of **1-H** with  $\text{H}_2\text{O}_2$  is in contrast to that observed when  $\text{Mn}^{\text{II}}$  salts of BPMEN and BPMCN are treated with  $\text{H}_2\text{O}_2$ , as oxo-

bridged dimers were reported in those cases.<sup>55,58,62</sup> We attribute this difference in reactivity to the *trans* binding mode of the  $L^7py_2^R$  ligands (Figure 2.1) that presumably disfavors dimerization.

When **1-Br**, **1-Me**, and **1-MeO** are treated either with  $H_2O_2$  in the presence of base, or with  $KO_2$ , new chromophoric species (**2-R**) are observed (Figure 2.2 and Table 2.2). While intermediate **2-Br** displays  $\lambda_{max}$  values virtually identical to those of **2-H**, both **2-Me** and **2-MeO** display a blue-shift of the prominent absorption band to ~410 nm and a broadening of the lower-energy feature. In all cases these species are all less stable than **2-H** (Table 2.2). **2-Br** and **2-Me** display half-lives at 0 °C of 3 and 6 minutes, respectively. Intermediate **2-MeO** is significantly more unstable, exhibiting a half-life at -40 °C of 6 minutes. ESI-MS experiments performed for **2-Br** and **2-Me** reveal prominent ion peaks with  $m/z$  values consistent with cationic mononuclear  $[Mn^{III}(O_2)(L^7py_2^R)]^+$  complexes ( $R = 5-Br$  and  $6-Me$ ) that all up-shift by four  $m/z$  units when these samples are prepared with isotopically labeled  $H_2^{18}O_2$ . Owing to its instability, we were unable to obtain ESI-MS data for **2-MeO**, but, on the basis of the similarities between the absorption spectra of **2-Me** and **2-MeO**, we likewise propose that **2-MeO** is a peroxomanganese(III) adduct.

Thus, by using the series of  $L^7py_2^R$  ligands, we have prepared a set of four peroxomanganese(III) complexes that differ solely with regard to the identity of pyridine ring substituents. The differences in optical properties of these complexes, **2-H** and **2-Br** on the one hand, and **2-Me** and **2-MeO** on the other (Table 2.2), are indicative of structural and/or electronic perturbations caused by the different steric and electronic properties of the supporting ligand. To evaluate the origins of these perturbations in more detail, magnetic circular dichroism

(MCD) spectroscopy was used to evaluate the excited- and ground-state properties of **2-H** and **2-Me**.

**Table 2.2.** Properties of Peroxomanganese(III) Complexes.

	$\lambda_{\text{max}}$ (nm) ( $\epsilon$ ( $\text{M}^{-1}\text{cm}^{-1}$ ))	$t_{1/2}$ at 0 °C	$D$ ( $\text{cm}^{-1}$ )	$E/D$
<b>2-H</b>	445 (280)	15 min	-2	0.13
	590 (120)			
<b>2-Br</b>	445 (220)	3 min	ND <sup>a</sup>	ND <sup>a</sup>
	589 (90)			
<b>2-Me</b>	415 (280)	6 min	-3	0.05
	~620 (80)			
<b>2-</b>	416 (250)	~seconds <sup>b</sup>	ND <sup>a</sup>	ND <sup>a</sup>
<b>MeO</b>	~560 (80)			

<sup>a</sup>Not determined. <sup>b</sup>This complex displays a  $t_{1/2}$  of 6 minutes at -40 °C.

**2.2.3 MCD and VTVH MCD Spectroscopy.** Figure 2.3 shows the 233 K absorption and 4.5 K, 7 T MCD spectra of **2-H** plotted in wavenumbers ( $\text{cm}^{-1}$ ). The two prominent absorption bands at  $\sim 16\,000$  and  $\sim 22\,220\text{ cm}^{-1}$  correspond to positive features in the MCD spectrum, and an additional band at  $\sim 24\,430\text{ cm}^{-1}$  is also resolved. An iterative Gaussian deconvolution of the absorption and MCD data sets reveals a total of six electronic transitions from  $14\,000$  to  $30\,000\text{ cm}^{-1}$  (Table A.2.10). No additional features were observed down to  $9\,000\text{ cm}^{-1}$  using either absorption or MCD spectroscopies. Given the low symmetry anticipated for **2-H**, four spin-allowed  $\text{Mn}^{\text{III}}$   $d-d$  bands are expected in the near-IR to near-UV region. Band 1 can be assigned as the lowest-energy  $d-d$  transition, which for high-spin  $\text{Mn}^{\text{III}}$  complexes corresponds to an intra- $e_g$  transition, using the symmetry labels from the parent octahedral point group. For six-

coordinate manganese(III) complexes this band is typically observed at  $\sim 10\,000\text{ cm}^{-1}$  and is a consequence of the Jahn-Teller splitting of the  $e_g$  orbitals.<sup>63</sup> Thus, the lowest energy  $d-d$  band of **2-H** (band 1; Figure 2.3) is shifted to higher energy by  $\sim 6\,000\text{ cm}^{-1}$  relative to the majority of six-coordinate manganese(III) complexes, indicating an unusual electronic structure likely due to the presence of the peroxo ligand. Band 3 is assigned as the second  $\text{Mn}^{\text{III}}$   $d-d$  transition, as it is weak in the absorption spectrum but carries significant MCD intensity. Assignments for bands 2 and 4 - 6 are unclear given that none of these bands appear to be selectively enhanced in the MCD spectrum, and thus are not able to be readily assigned as  $d-d$  bands. Further complicating the assignment of these transitions is the fact that, on the basis of analogy with peroxoiron(III) systems, peroxo-to-manganese(III) charge-transfer (CT) transitions are anticipated in the visible region.<sup>22,64</sup> As discussed below, TD-DFT computations were performed to aid in assigning these transitions.

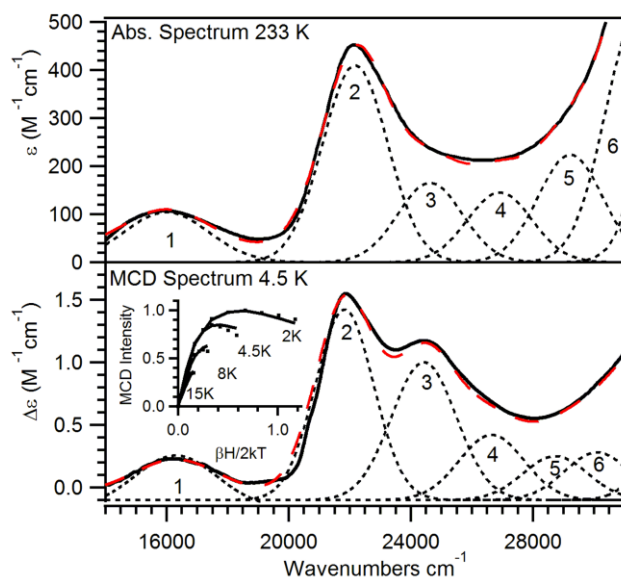


**Figure 2.3.** 233 K electronic absorption (top) and 4.5 K, 7 T MCD (bottom) spectra of  $[\text{Mn}^{\text{III}}(\text{O}_2)(\text{L}^7\text{py}_2\text{H})]^+$  (**2-H**). Individual Gaussian curves (black dotted lines) and their sums (red dashed lines) obtained from iterative fits of these data sets are displayed on their respective spectra. Inset: Experimental VTVH MCD data collected at  $21\,872\text{ cm}^{-1}$  for **2-H** ( $\cdots$ ) and theoretical fit ( $\text{—}$ ) using the following parameters:  $D = -2.00$ ,  $E/D = 0.130$ ,  $g_{\text{iso}} = 2.00$ , and 4 %

*x*, 5% *y*, and 91% *z* polarization. Conditions: Absorption data were collected for a 2.5 mM sample in CH<sub>3</sub>CN. MCD data were collected for a 10 mM frozen glass sample in butyronitrile.

To assess the effects of changing the properties of the L<sup>7</sup>py<sub>2</sub><sup>R</sup> ligand on electronic structure, low-temperature MCD data were also collected for **2-Me** (Figure 2.4, bottom). Similar to that observed for **2-H**, the major absorption bands of **2-Me** are retained in the MCD spectrum, but additional features are also apparent. Most notably, a lower energy band at ~13 500 cm<sup>-1</sup> is resolved, and bands 3 and 5 are significantly more prominent in the MCD spectrum (Figure 2.4). An iterative Gaussian deconvolution of the absorption and MCD spectra of **2-Me** reveals a total of seven transitions from 12 000 to 30 000 cm<sup>-1</sup> (Table A.2.11). Because of their relatively large MCD-to-absorption intensity ratios, bands 1, 3, and 5 are assigned as Mn<sup>III</sup> *d-d* bands. In contrast, bands 2, 4, and 6, which carry moderate absorption intensities are comparatively weaker in the MCD spectrum, suggesting that these bands are charge-transfer in origin. When compared to **2-H**, the most notable difference for **2-Me** is the ~2 500 cm<sup>-1</sup> red-shift of the lowest-energy *d-d* band (band 1). Importantly, this large shift is not evident from inspection of the corresponding absorption spectra. It is, however, readily appreciated when the MCD data sets are compared, illustrating the power of MCD spectroscopy to probe peroxomanganese(III) adducts.

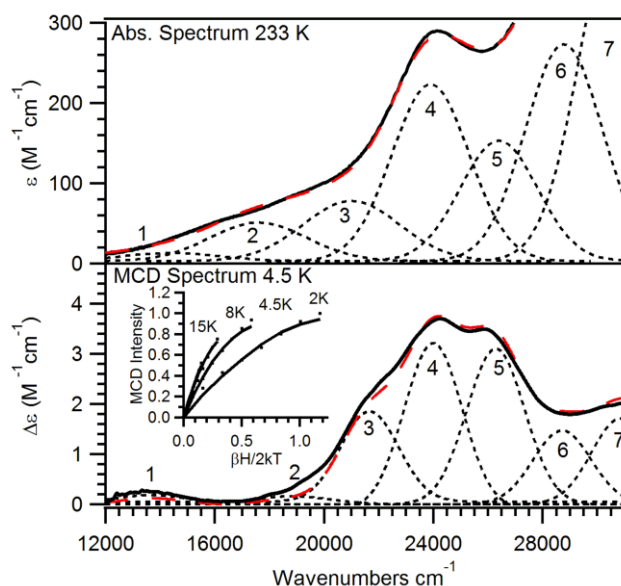


**Figure 2.4.** 233 K electronic absorption (top) and 4.5 K, 7 T MCD (bottom) spectra of  $[\text{Mn}^{\text{III}}(\text{O}_2)(\text{L}^7\text{py}_2^{6\text{-Me}})]^+$  (**2-Me**). Individual Gaussian curves (black dotted lines) and their sums (black dashed lines) obtained from iterative fits of these data sets are displayed on their respective spectra. Inset: Experimental VTVH MCD data collected at 24 150  $\text{cm}^{-1}$  for **2-Me** (···) and theoretical fit (—) using the following parameters:  $D = -3.00$ ,  $E/D = 0.05$ ,  $g_{\text{iso}} = 2.00$ , and 0.001%  $x$ , 0.002%  $y$ , and 99.997%  $z$  polarization. Conditions: Absorption data were collected for a 2.5 mM sample in  $\text{CH}_3\text{CN}$ . MCD data were collected for a 10 mM frozen glass sample in butyronitrile.

While our analysis of the absorption and MCD spectra of **2-H** and **2-Me** provides transitions energies and intensities, it does not afford insight into the ground-state properties of these complexes. Accordingly, variable-temperature, variable-field (VTVH) MCD spectroscopy was used to probe both the ground-state zero field splitting (ZFS) parameters and transition polarizations.<sup>29,65</sup>

VTVH MCD curves obtained for **2-H** at 21 872  $\text{cm}^{-1}$  (Figure 2.3; inset) are nested; *i.e.*, higher temperature curves saturate more rapidly than lower temperature curves, indicating that the  $\text{Mn}^{\text{III}}$  ion is subject to a moderate ZFS. Notably, the addition of a methyl group onto the  $\text{L}^7\text{py}_2$  ligand framework significantly alters the VTVH saturation behavior of the MCD signal (cf. Figures 2.3 and 2.4; insets). Specifically, the VTVH MCD signals for **2-Me** saturate more

slowly with increased field. Because neither transition polarizations nor ZFS parameters are known for **2-H** and **2-Me**, the VTVH MCD data sets for these species were systematically fit to extract these parameters. In this procedure,  $D$  and  $E/D$  were varied from  $-3$  to  $3\text{ cm}^{-1}$  and from  $0$  to  $0.3$  in increments of  $0.5$  and  $0.05\text{ cm}^{-1}$ , respectively. Transition-moment products (*i.e.*,  $M_{xy}$ ,  $M_{xz}$ ,  $M_{yz}$ ) were optimized to fit the experimental data for a given set of  $D$  and  $E/D$  values. The goodness of fit was assessed by the  $\chi^2$  value; where  $\chi^2$  is the sum of the squares of the differences between experimental and fit data sets. The best fits were obtained assuming an  $S = 2$  spin state, further confirming our assignment of **2-H** and **2-Me** as high-spin  $\text{Mn}^{\text{III}}$  complexes. Excellent fits for **2-H** and **2-Me** ( $\chi^2 < 0.12$ ) were obtained with  $D$  values of  $-2.0$  and  $-3.0\text{ cm}^{-1}$  and  $E/D$  values of  $0.13$  and  $0.05\text{ cm}^{-1}$ , respectively (Figures 2.3 and 2.4; insets). The observation that both complexes have axial ZFS parameters of the same sign (*i.e.*,  $D < 0\text{ cm}^{-1}$ ) implies that these species have similar orbital ground states. Because of the similarities in the  $D$  and  $E/D$  values, the transition polarizations were examined to understand the different nesting behavior of **2-H** and **2-Me**. Both transitions are highly  $z$ -polarized ( $> 90\%$ ); however, the data for **2-H** and **2-Me** are best fit with  $90\%$  and  $99\%$   $z$ -polarization, respectively. To explore whether this  $9\%$  change in polarization could account completely for the different nesting behaviors, we simulated VTVH MCD data for  $D$  and  $E/D$  values of  $-3.0$  and  $0.05$ , respectively, but with  $z$ -polarizations of  $90$  and  $99\%$ . It is evident from the resulting traces (Figure A.2.4) that this small change in  $z$ -polarization can greatly affect the nesting behavior of these systems.

Taken together, the results of the MCD and VTVH-MCD experiments reveal that the ground- and excited-state properties of **2-Me** compare favorably with those of **2-H**, consistent with the similar structures expected for these peroxomanganese(III) complexes. Nonetheless



shifts in electronic transition energies indicate that the electronic structure of the  $\text{Mn}^{\text{III}}\text{-O}_2$  unit is influenced by the presence of pyridine ring substituents. In order to correlate these spectral shifts with changes in the geometric and electronic structure of the  $\text{Mn}^{\text{III}}\text{-O}_2$  unit caused by ligand perturbations, density functional theory (DFT) and time dependent-DFT (TD-DFT) calculations were performed on models of **2-H** and **2-Me**.

**2.2.4 DFT-Optimized Geometries.** Important metric parameters of our DFT-optimized models of **2-H** and **2-Me** are collected in Table 2.3. In both cases, the optimized structures display six-coordinate  $\text{Mn}^{\text{III}}$  centers with side-on peroxo ligands, as shown for **2-H** in Figure 2.5. The nitrogen atoms of the supporting  $\text{L}^7\text{py}_2^{\text{H}}$  ligand forms the base of a square plane that sits below the  $\text{Mn}^{\text{III}}\text{-O}_2$  unit. Importantly, the computed O–O and Mn–O distances fall within the ranges observed for crystallographically characterized peroxomanganese(III) complexes (the experimental distances are 1.40 – 1.43 Å and 1.84 – 1.90 Å, respectively).<sup>16-19,21</sup> However, while the model of **2-H** has relatively symmetric Mn–O bond lengths of  $1.870 \pm 0.005$  Å, **2-Me** exhibits asymmetric Mn–O distances of 1.91 and 1.87 Å (Table 2.3). We attribute this to the great electron-donating ability of the  $\text{L}^7\text{py}_2^{6\text{-Me}}$  ligand that reduces the Lewis acidity of the  $\text{Mn}^{\text{III}}$  center in **2-Me**. This observation is thus potentially related to the difference in coordination number observed for the corresponding  $\text{Mn}^{\text{II}}$  complexes, **1-H** and **1-Me**, that respectively displayed seven- and six-coordinate  $\text{Mn}^{\text{II}}$  centers (Figure 2.2). Notably, Nam and co-workers recently proposed that the presence of electron-donating ligands *trans* to the peroxo unit in  $\text{Mn}^{\text{III}}\text{-O}_2$  species leads to more end-on-like peroxo ligands with asymmetric Mn–O bond lengths.<sup>21</sup> Our computations lend further credence to this proposal and additionally predict that *cis* ligands can have a similar effect.

**Table 2.3.** Metal-Ligand Bond Lengths (Å) for  $[\text{Mn}^{\text{III}}(\text{O}_2)(\text{L}^7\text{py}_2^{\text{H}})]^+$  and  $[\text{Mn}^{\text{III}}(\text{O}_2)(\text{L}^7\text{py}_2^{6\text{-Me}})]^+$  Complexes Based on BP86 DFT Geometry Optimizations

	$[\text{Mn}^{\text{III}}(\text{O}_2)(\text{L}^7\text{py}_2^{\text{H}})]^+$	$[\text{Mn}^{\text{III}}(\text{O}_2)(\text{L}^7\text{py}_2^{6\text{-Me}})]^+$
Mn–O <sup>A</sup>	1.874	1.907
Mn–O <sup>B</sup>	1.867	1.866
O <sup>A</sup> –O <sup>B</sup>	1.444	1.452
Mn–N1	2.215	2.296
Mn–N2	2.108	2.177
Mn–N3	2.212	2.147
Mn–N4	2.283	2.279

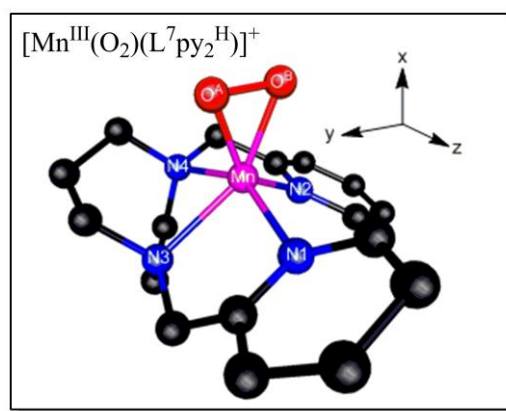


**Figure 2.5.** DFT-Optimized Model of  $[\text{Mn}^{\text{III}}(\text{O}_2)(\text{L}^7\text{py}_2^{\text{H}})]^+$  (**2-H**).

The Mn *d* orbital splitting patterns of **2-H** and **2-Me** are shown in Figure 2.6. For these calculations, we have used a coordinate system with the *z*-axis perpendicular to the  $\text{Mn}^{\text{III}}\text{--O}_2$  unit and the *x*-axis bisecting the O–O bond (see Figure 2.5). With this coordinate system, the Mn  $d_{xy}$  and  $d_z^2$  MOs are the  $\sigma$ -type orbitals (*i.e.*, the  $e_g$  set), whereas the  $d_{x^2-y^2}$ ,  $d_{xz}$ , and  $d_{yz}$  MOs are the  $\pi$ -type orbitals (*i.e.*, the  $t_{2g}$  set). Using the commonly accepted hole formalism, the  $(d_{yz})^1(d_{x^2-y^2})^1(d_{xz})^1(d_z^2)^1(d_{xy})^0$  configurations predicted for both **2-H** and **2-Me** give rise to  $d_{xy}$  orbital ground states. The similar ground states predicted for these complexes are consistent with the observation that VTVH MCD data collected for **2-H** and **2-Me** are both best fit with  $D < 0 \text{ cm}^{-1}$ .

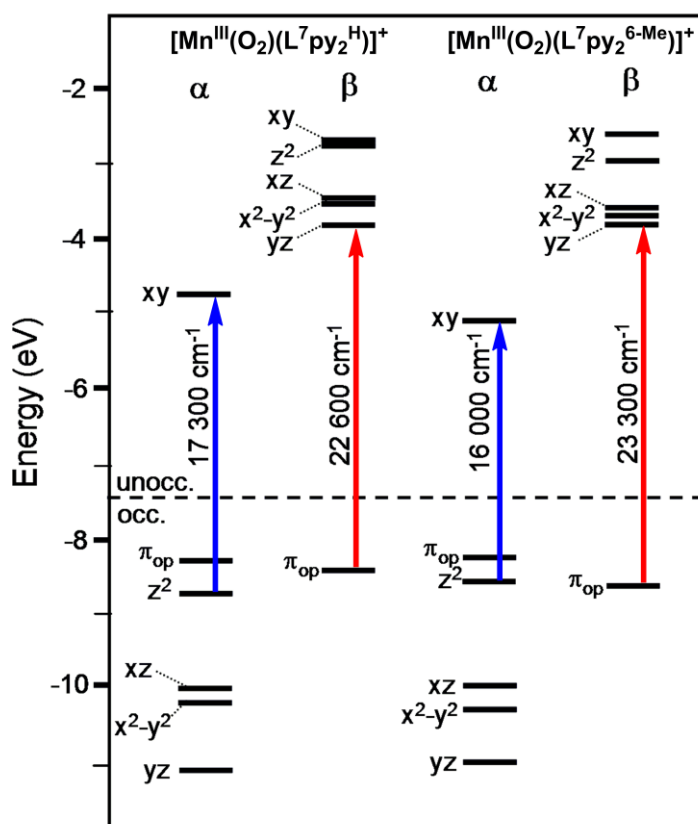


**Figure 2.6.** Molecular orbital (MO) energy-level diagrams for  $[\text{Mn}^{\text{III}}(\text{O}_2)(\text{L}^7\text{py}_2^{\text{H}})]^+$  (**2-H**; left) and  $[\text{Mn}^{\text{III}}(\text{O}_2)(\text{L}^7\text{py}_2^{6\text{-Me}})]^+$  (**2-Me**; right) complexes obtained from spin-unrestricted DFT calculations. MOs are labeled according to their principal contributors. For clarity only  $\text{Mn}^{\text{III}}$  d-based and  $\text{O}_2$   $\pi_{\text{op}}^*$ -based MOs are included. TD-DFT computed transition energies of prominent electronic transitions are also displayed.

**2.2.5 Electronic Structure and Spectral Assignments for 2-H.** Before comparing the electronic structures in detail, the bonding description afforded by DFT computations performed for **2-H** will be briefly summarized in order to provide a framework for understanding perturbations caused by the more side-on bound peroxo ligand in **2-Me**. The bonding in side-on peroxometal adducts is dominated by a  $\sigma$ -interaction involving the Mn  $d_{xy}$  orbital and the in-plane peroxo  $\pi$ -antibonding orbital ( $\pi_{\text{ip}}^*$ ), as discussed previously for peroxoiron(III) complexes.<sup>64</sup> A plot of the Mn  $d_{xy}$  MO for **2-H** is shown in Figure 2.7 (right). The strength of the Mn– $\text{O}_2$   $\sigma$ -interaction is evidenced by the relatively high percentage of peroxo character

(~48%) in this MO. We note that, because  $\text{Mn}^{\text{III}}$  is a  $d^4$  ion, this  $\text{Mn}-\text{O}_{\text{peroxo}}$   $\sigma$ -antibonding orbital is doubly-unoccupied. This is in contrast to corresponding high-spin  $\text{Fe}^{\text{III}}-\text{O}_2$  systems ( $d^5$ ) where the related MO is half-filled. This difference in occupancy of the metal-peroxo  $\sigma$ -antibonding orbital could account for the fact that  $\text{Fe}^{\text{III}}-\text{O}_{\text{peroxo}}$  bond lengths in side-on peroxoiron(III) complexes<sup>22</sup> are, on average, longer than  $\text{Mn}^{\text{III}}-\text{O}_{\text{peroxo}}$  distances.<sup>16-18,21</sup>

In contrast to the high covalency of the  $\text{Mn } d_{xy}$  MO, the  $d_z^2$  MO of **2-H** carries only ~5% peroxo character and is predominantly  $\text{Mn}-\text{L}^7\text{py}_2$   $\sigma$ -antibonding (Table A.2.12). The  $t_{2g}$ -derived orbitals are involved in  $\pi$ -interactions with both the peroxo ligand and the  $\pi^*$  orbitals of the pyridine rings of the  $\text{L}^7\text{py}_2^{\text{H}}$  ligand. These  $\pi$ -interactions are rather weak and account for the small energy splitting observed for these MOs (Figure 2.5). Also included among the frontier orbitals of **2-H** are the doubly-occupied out-of-plane peroxo  $\pi$ -antibonding orbital ( $\pi_{\text{op}}^*$ ). This is the highest-occupied MO for **2-H** and carries a small percentage of  $\text{Mn } d_{yz}$  character (Figure 2.7, left), representing a weak  $\text{Mn}-\text{O}_2$   $\pi$ -interaction. To correlate this electronic structure description with the spectroscopic data collected for **2-H**, we next performed TD-DFT computations to predict electronic transition energies.

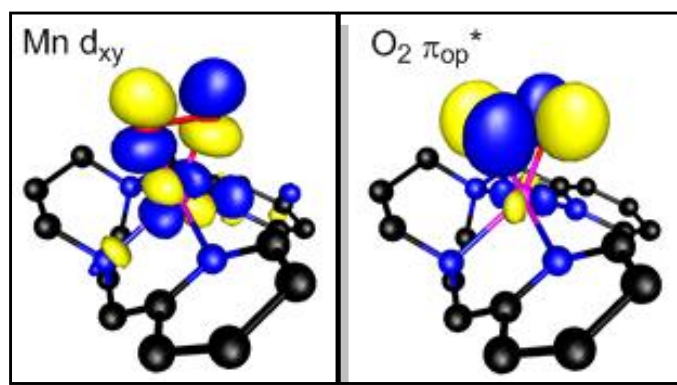


**Figure 2.7.** Surface contour plots of the spin-up Mn  $d_{xy}$  (left) MOs and O<sub>2</sub>  $\pi_{op}^*$  (right).

The TD-DFT computed absorption spectrum for **2-H** shown in Figure 2.8 (top) is strikingly similar to the experimental spectrum (Figure 2.2). A low-intensity band is predicted at 17 300  $\text{cm}^{-1}$  (band *i*; Figure 2.8) that is in good agreement with the experimental feature at  $\sim 16\,000\text{ cm}^{-1}$  (band 1; Figure 4). Band *i* is due solely to the Mn  $d_z^2 \rightarrow d_{xy}$  transition (Table A.2.13), which is the lowest-energy  $d-d$  transition. Because the acceptor orbital for this transition is the Mn–O<sub>2</sub>  $\sigma$ -antibonding MO, the relatively high energy of this transition compared to that of other six-coordinate Mn<sup>III</sup> complexes can be attributed to the strong  $\sigma$ -covalency of the Mn–O<sub>peroxo</sub> bonds that destabilizes the  $d_{xy}$  MO. The higher-energy absorption band computed for **2-H** (band *ii*; Figure 2.8), which corresponds well with the experimental band at 22 200  $\text{cm}^{-1}$  (band 2; Figure 2.4), is due to a weak peroxo-to-Mn<sup>III</sup> charge transfer (CT) transition (O<sub>2</sub>  $\pi_{op}^* \rightarrow$  Mn  $d_{yz}$ ). The low intensity of this CT band (experimental  $\epsilon \approx 500\text{ M}^{-1}\text{cm}^{-1}$ ) is due to the fact that the acceptor MO (Mn  $d_{yz}$ ) has very little peroxo character. In addition to allowing us to assign the major features in the absorption spectrum of **2-H**, the TD-DFT calculations allow us to make assignments for additional bands resolved in the low-temperature MCD spectrum. Specifically band 3 (Figure 2.4) can be assigned as the second Mn  $d-d$  transition ( $d_{xz} \rightarrow d_{xy}$ ), which is predicted at  $\sim 24\,600\text{ cm}^{-1}$ . This corroborates our initial assignment of band 3 as a  $d-d$  transition

based on its enhanced intensity in the MCD spectrum (Figure 2.4). At higher-energy, the TD-DFT calculations predict additional peroxo-to-Mn<sup>III</sup> CT transitions as well as the remaining two *d-d* bands (Table A.2.13).

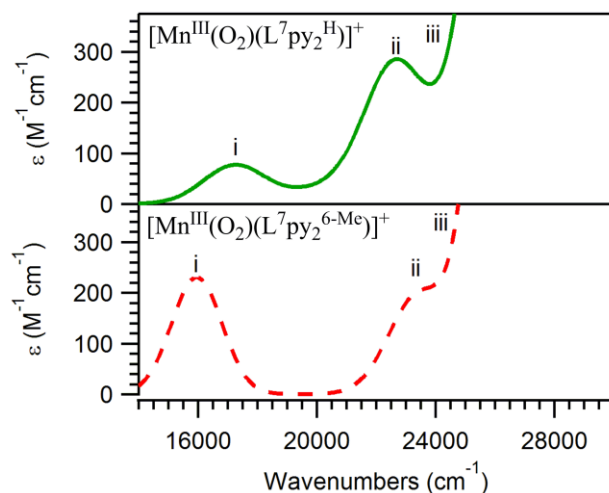


**Figure 2.8.** Simulated absorption spectra of [Mn<sup>III</sup>(O<sub>2</sub>)(L<sup>7</sup>py<sub>2</sub><sup>H</sup>)]<sup>+</sup> (**2-H**; top) and [Mn<sup>III</sup>(O<sub>2</sub>)(L<sup>7</sup>py<sub>2</sub><sup>6-Me</sup>)]<sup>+</sup> (**2-Me**; bottom) based on TD-DFT computations employing the B3LYP functional.

**2.2.6 Electronic Structure and Spectral Assignments for 2-Me.** The asymmetric Mn–O<sub>2</sub> bond lengths observed for **2-Me** attenuates the  $\sigma$ -interaction between the Mn *d*<sub>xy</sub> and O<sub>2</sub>  $\pi_{ip}^*$  orbitals. This causes a reduction of the energy splitting between the spin-up *d*<sub>xy</sub> and *d*<sub>z</sub><sup>2</sup> MOs (Figure 2.6). Consequently, the *d*<sub>z</sub><sup>2</sup> → *d*<sub>xy</sub> transition is predicted at lower energy in the TD-DFT computed spectrum for **2-Me** (Figure 2.8), reproducing the experimentally observed red-shift of this band when compared with **2-H**. The origin of this spectral shift is the more end-on binding mode of the peroxo ligand in **2-Me**. Further, these data suggest that there is a correlation between the energy of the *d*<sub>z</sub><sup>2</sup> → *d*<sub>xy</sub> transition and the Mn–O bond length.

The longer Mn–O bond lengths in **2-Me** are accompanied by a small elongation (0.01 Å) of the O–O distance compared with **2-H** (Table 2.3). This elongation stabilizes the spin-down

$\text{O}_2 \pi_{\text{op}}^*$  orbitals (Figure 2.6). As these are the donor orbitals for the prominent  $\text{O}_2 \pi_{\text{op}}^* \rightarrow \text{Mn } d_{yz}$  transition, this stabilization causes a shift of this band to higher energy. To assess if this is a general trend, we systematically elongated the O–O bond for **2-H** and computed absorption spectra for these models. The results of these calculations show that lengthening the O–O bond leads to a steady blue-shift of the  $\text{O}_2 \pi_{\text{op}}^* \rightarrow \text{Mn } d_{yz}$  transition energy (Figure A.2.13). Thus, the spectral perturbations of **2-Me** relative to **2-H** can both be explained by a more end-on binding mode of the peroxo ligand in the former complex that perturbs the energies of the Mn- and  $\text{O}_2$ -based MOs that are involved in the dominant electronic transitions.

### 2.3 Summary.

A detailed understanding of the pathways by which biological and synthetic Mn centers activate dioxygen and hydrogen peroxide requires fundamental studies of potential intermediates involved in these processes. This chapter describes the generation and characterization of a set of peroxomanganese(III) adducts supported by tetradentate  $\text{L}^7\text{py}_2^{\text{R}}$  ligands with a range of steric and electronic properties. X-ray crystal structures of the corresponding  $\text{Mn}^{\text{II}}$  complexes indicate that in all cases the  $\text{L}^7\text{py}_2^{\text{R}}$  ligands bind in the *trans* conformation. Importantly, this *trans* binding mode appears to favor the formation of mononuclear peroxomanganese(III) adducts over oxo-bridged dimers, at least at low temperature, as the latter species have been previously observed for similar ligand sets that coordinate Mn centers to give *cis- $\alpha$*  complexes.<sup>55,58,62</sup>

While it has been known for some time that the electronic absorption spectra of peroxomanganese(III) adducts are affected by the nature of the supporting ligand, the results reported herein offer evidence that these spectral signatures can be related to certain features of  $\text{Mn}^{\text{III}}\text{--O}_2$  bonding. Specifically, we propose that the lowest-energy *d-d* band should be a marker

of the strength of the Mn–O<sub>peroxo</sub>  $\sigma$ -interaction, with lower-energy bands signifying weaker Mn–O<sub>peroxo</sub> bonds or peroxo ligands bound in a more side-on fashion. This correlation is possible because the acceptor orbital for this electronic transition is the Mn–O<sub>2</sub>  $\sigma$ -antibonding MO. Indeed, when the Mn–O distances of **2-H** are systematically varied from 1.82 to 1.88 Å, the TD-DFT-computed energy of the  $d_z^2 \rightarrow d_{xy}$  transition decreases from 18 200 to 17 000 cm<sup>-1</sup> in a fairly linear fashion (Figure A.2.5). Moreover, this model is consistent with the observation that Mn<sup>III</sup>–O<sub>2</sub> complexes supported by the Tp<sup>iPr</sup> ligand exhibit higher energy electronic transitions (~560 nm; 17 900 cm<sup>-1</sup>) and shorter Mn–O bonds (~1.85 Å),<sup>16,18</sup> relative to the [Mn(O<sub>2</sub>)(TMC)]<sup>+</sup> and [Mn(O<sub>2</sub>)(13-TMC)]<sup>+</sup> complexes that respectively display lower energy bands at 630 and 615 nm (15 900 and 16 260 cm<sup>-1</sup>) and longer Mn–O distances (1.884 and 1.859 Å).<sup>17,21</sup> In addition, this model lends credence to the proposal that the product-inhibited complex observed for MnSOD is a peroxomanganese(III) adduct with relatively long, asymmetric Mn–O<sub>peroxo</sub> bond lengths, as this complex exhibits a low-energy absorption band at 650 nm (15 400 cm<sup>-1</sup>). One caveat of this proposal is that this transition energy will be modulated by interactions with the supporting ligand, as the donor orbital is the Mn-ligand  $\sigma^*$  MO. Further, we emphasize that, in some cases, the combined use of absorption and MCD spectroscopy appears will be required for identifying the lowest energy  $d-d$  band, because  $d-d$  bands are selectively enhanced in low-temperature MCD spectra. This is exemplified by **2-Me**, where the low energy band 1 is completely obscured in the electronic absorption spectrum but clearly evident in the low-temperature MCD spectrum (Figure 2.4).

Taken together, these results show that the electron-donating properties of supporting ligands are able to modulate the peroxo binding mode in Mn<sup>III</sup>–O<sub>2</sub> complexes, with electron-rich



ligands supporting more asymmetric Mn–O<sub>peroxo</sub> bonds. Thus, the use of electron-rich supporting ligands could provide a route to peroxo ligands primed for further activation.<sup>21</sup> For nonheme iron systems, it is well established that side-on peroxoiron(III) centers are relatively unreactive, whereas end-on hydroperoxo- and alkylperoxoiron(III) complexes have been proposed to undergo O–O cleavage reactions to afford high-valent oxoiron intermediates.<sup>22</sup> Whether this reactivity pattern can be generally applied to manganese systems has yet to be determined.

## 2.4 Materials and Methods.

**2.4.1 Materials.** All chemicals obtained from commercial vendors were ACS reagent-grade or better and were used as received. All solvents were dried by routine techniques under an inert argon atmosphere.<sup>24</sup> Unless otherwise stated, manipulations of Mn<sup>II</sup> complexes were carried out under argon using a glovebox or Schlenck techniques.

**2.4.2 Instrumentation.** <sup>1</sup>H-NMR spectra were obtained on a Bruker DRX 400 MHz NMR spectrometer. Electronic absorption spectra were recorded on a Cary 50 Bio spectrophotometer (Varian) interfaced with a Unisoku cryostat (USP-203-A). Mass spectrometry experiments were performed using an LCT Primers MicroMass Electrospray-ionization time of flight instrument. Magnetic circular dichroism (MCD) spectra were collected on a spectropolarimeter (Jasco J-815) interfaced with a magnetocryostat (Oxford Instruments SM-4000-8) capable of horizontal fields up to 8 T. Elemental analyses were performed by Chemisar Laboratories, Inc. (Ontario, Canada). Solution magnetic moments of [Mn(L<sup>7</sup>py<sub>2</sub><sup>R</sup>)](ClO<sub>4</sub>)<sub>2</sub> complexes were determined by the <sup>1</sup>H-NMR method of Evans in CD<sub>3</sub>CN at 298 K.<sup>25</sup>

**2.4.3 Ligand Synthesis.** 1,4-bis(2-pyridylmethyl)-1,4-diazepane ( $L^7py_2^H$ ) and 1,4-bis(6-methyl-2-pyridylmethyl)-1,4-diazepane ( $L^7py_2^{6-Me}$ ) were prepared by a previously reported reductive amination procedure, where homopiperazine is reacted with 2-pyridinecarboxaldehyde and 6-methyl-2-pyridinecarboxaldehyde, respectively.<sup>26</sup> The ligands 1,4-bis(5-bromo-2-pyridylmethyl)-1,4-diazepane ( $L^7py_2^{5-Br}$ ) and 1,4-bis(6-methoxy-2-pyridylmethyl)-1,4-diazepane ( $L^7py_2^{6-MeO}$ ) were prepared following the same procedure using 5-bromo-2-pyridinecarboxaldehyde and 6-methoxy-2-pyridinecarboxaldehyde, respectively. <sup>1</sup>H-NMR data (400 MHz) for  $L^7py_2^{5-Br}$  and  $L^7py_2^{6-MeO}$  are as follows:  $L^7py_2^{5-Br}$  ( $CDCl_3$ ;  $\delta$ ) = 8.61 (s, 2H), 7.80 (d, 2H,  $J_{HH}$ =20.12), 7.42 (d, 2H,  $J_{HH}$ =8.28), 3.78 (s, 4H), 2.79 (m, 8H), 1.84 (m, 2H);  $L^7py_2^{6-MeO}$  ( $CDCl_3$ ;  $\delta$ ) = 7.55 (m, 2H), 7.04 (d, 2H,  $J_{HH}$ =7.16), 6.60 (d, 2H,  $J_{HH}$ =8.16), 3.93 (s, 6H), 3.77 (s, 4H), 2.84 (m, 8H), 1.87 (m, 2H).

**2.4.4 Preparation of  $[Mn(L^7py_2^R)](ClO_4)_2$  Complexes.** *Caution! While no problems were encountered during this work, care should always be taken when handling perchlorate salts of metal complexes because of the possibility of explosion.*  $[Mn(L^7py_2^R)](ClO_4)_2$  complexes were synthesized in excellent yields (~85%) by reacting  $L^7py_2^R$  ( $R = H, 5-Br, 6-Me, 6-MeO$ ) ligands with  $Mn(ClO_4)_2$  in acetonitrile (MeCN) solution in 1:1 molar ratio. Details of a representative preparation are as follows. To a stirred solution of 82 mg (0.323 mmol)  $Mn(ClO_4)_2$  in 10 mL of MeCN was added 100 mg (0.322 mmol)  $L^7py_2^{6-Me}$  in 10 mL MeCN. The yellow solution was stirred overnight, evaporated under reduced pressure, and the solid thus obtained was dried in vacuo. Recrystallization of the crude solid from MeCN/diethyl ether afforded 155 mg (85%) of  $[Mn(L^7py_2^{6-Me})](ClO_4)_2$  as nearly colorless crystals. Electrospray ionization-mass spectrometry (ESI-MS) was used to explore liquid-state composition of the purified  $[Mn(L^7py_2^R)](ClO_4)_2$  complexes in MeCN solution. ESI-MS data are as follows:  $\{[Mn(L^7py_2^H)](ClO_4)^+\}$   $m/z =$

436.0707 (calc 436.0710),  $\{[\text{Mn}(\text{L}^7\text{py}_2^{5\text{-Br}})](\text{ClO}_4)^+\}$   $m/z = 593.8927$  (calc 593.8900),  $\{[\text{Mn}(\text{L}^7\text{py}_2^{6\text{-Me}})](\text{ClO}_4)_2^+\}$   $m/z = 464.1023$  (calc 464.1023),  $\{[\text{Mn}(\text{L}^7\text{py}_2^{6\text{-MeO}})](\text{ClO}_4)_2^+\}$   $m/z = 496.0899$  (calc 496.0921).

**2.4.5 X-ray Crystallography.** Single crystals of  $[\text{Mn}(\text{L}^7\text{py}_2^{6\text{-Me}})(\text{CH}_3\text{CN})(\text{ClO}_4)](\text{ClO}_4)$  and  $[\text{Mn}(\text{L}^7\text{py}_2^{6\text{-MeO}})(\text{ClO}_4)_2]$  were grown by vapor diffusion of ether into MeCN solutions of the complexes at room temperature. Single crystals of  $[\text{Mn}(\text{L}^7\text{py}_2^{\text{H}})(\text{CH}_3\text{CN})_3](\text{ClO}_4)_2$  were grown by a similar vapor-diffusion method at  $-20\text{ }^\circ\text{C}$ . Single crystals of  $[\text{Mn}(\text{L}^7\text{py}_2^{5\text{-Br}})(\text{OCMe}_2)(\text{ClO}_4)](\text{ClO}_4)$  were grown by vapor diffusion of ether into an acetone solution of the complex at room temperature. Data collection and refinement parameters are summarized in Tables A.2.1 – A.2.4.

For each sample, a full hemisphere of diffracted intensities was measured for a single-domain specimen using graphite-monochromated  $\text{MoK}\alpha$  radiation ( $\lambda = 0.71073\text{ \AA}$ ) on a Bruker SMART APEX CCD Single Crystal Diffraction System.<sup>27</sup> X-rays were provided by a fine-focus sealed X-ray tube operated at 45 kV and 35 mA. Lattice constants were determined with the Bruker SAINT software package. The Bruker software package SHELXTL was used to solve the structure using “direct methods” techniques. All stages of weighted full-matrix least-squares refinement were conducted using  $F_o^2$  data with the SHELXTL Version 6.10 software package.<sup>28</sup> Experimental descriptions of XRD data collection and analysis for specific samples is included in Supporting Information.

**2.4.6 In Situ Preparation of Peroxomanganese(III) Complexes.** The green peroxomanganese(III) intermediates  $[\text{Mn}^{\text{III}}(\text{O}_2)(\text{L}^7\text{py}_2^{\text{R}})]^+$  ( $\text{R} = \text{H}, 6\text{-Me}, 5\text{-Br}, \text{ and } 6\text{-MeO}$ ) were formed by treating an acetonitrile solution of  $[\text{Mn}^{\text{II}}(\text{L}^7\text{py}_2^{\text{R}})](\text{ClO}_4)_2$  with 5 equivalents of  $\text{H}_2\text{O}_2$

and 0.5 equivalents of triethylamine at  $-40\text{ }^{\circ}\text{C}$ . The formation of the  $[\text{Mn}^{\text{III}}(\text{O}_2)(\text{L}^7\text{py}_2^{\text{R}})]^+$  complexes was evident from the appearance of characteristic bands in the electronic absorption spectra and supported by ESI-MS data (*vide infra*). These intermediates could also be prepared using  $\text{KO}_2$  as oxidant. For these reactions, a stock solution of  $\text{KO}_2$  was made by dissolving 1:5  $\text{KO}_2$ :18-Crown-6 (mol:mol) in acetonitrile. Treatment of an acetonitrile solution of  $[\text{Mn}^{\text{II}}(\text{L}^7\text{py}_2^{\text{R}})](\text{ClO}_4)_2$  with 1 equivalent of  $\text{KO}_2$ :18-Crown-6 at  $-40\text{ }^{\circ}\text{C}$  resulted in the formation of the  $[\text{Mn}^{\text{III}}(\text{O}_2)(\text{L}^7\text{py}_2^{\text{R}})]^+$  complexes.

**2.4.7 Magnetic Circular Dichroism Experiments.** 10 mM frozen glass samples of  $[\text{Mn}^{\text{III}}(\text{O}_2)(\text{L}^7\text{py}_2^{\text{H}})]^+$  and  $[\text{Mn}^{\text{III}}(\text{O}_2)(\text{L}^7\text{py}_2^{6\text{-Me}})]^+$  were prepared in butyronitrile at  $-40^{\circ}\text{C}$ . Butyronitrile was used instead of MeCN, as the former produces an optical-quality glass upon freezing. We concluded that the solvent switch did not affect the composition of  $[\text{Mn}^{\text{III}}(\text{O}_2)(\text{L}^7\text{py}_2^{\text{H}})]^+$ , as absorption spectra of  $[\text{Mn}^{\text{III}}(\text{O}_2)(\text{L}^7\text{py}_2^{\text{H}})]^+$  in MeCN and butyronitrile are virtually identical. Once formation of the peroxomanganese(III) species was complete (as monitored by UV-visible spectroscopy), the samples were cooled to  $-80^{\circ}\text{C}$ , transferred to pre-cooled MCD cells, and flash-frozen in liquid  $\text{N}_2$ . To assess sample purity, ESI-MS experiments were performed on the remainder of the solution sample. The obtained MCD spectra were measured in mdeg ( $\theta$ ) and converted to  $\Delta\epsilon$  ( $\text{M}^{-1}\text{cm}^{-1}$ ) using the standard conversion factor  $\Delta\epsilon = \theta/(32980 \cdot c \cdot d)$ , where  $c$  is the concentration of the sample and  $d$  is the path length. MCD spectra were collected at 2, 4, 8, and 15 K for positive and negative field strengths of 1 to 7 T in 1 T increments. VTVH data were fit using the general method developed by Neese and Solomon.<sup>29</sup> Fits were performed for an  $S = 2$  system with isotropic  $g$ -values of 2.00. Using a previously

described protocol,<sup>30</sup> zero-field splitting (ZFS) parameters  $D$  and  $E/D$  were systematically varied while the transition moment products were optimized for a given set of ZFS parameters.

**2.4.8 Density Functional Theory Computations.** The *ORCA* 2.7 software package was used for all DFT computations.<sup>31</sup> Initial models of  $[\text{Mn}^{\text{III}}(\text{O}_2)(\text{L}^7\text{py}_2^{\text{R}})]^+$  ( $\text{R} = \text{H}$  and 6-Me) were built using the X-ray coordinates of the corresponding manganese(II) complexes and adding side-on peroxo ligands. Geometry optimizations for models of  $[\text{Mn}^{\text{III}}(\text{O}_2)(\text{L}^7\text{py}_2^{\text{R}})]^+$  complexes were converged to the  $S = 2$  spin state and employed the Becke-Perdew (BP86) functional,<sup>32-33</sup> the SV(P) (Ahlrichs split valence polarized) basis with the SV/C auxiliary basis for all atoms except for manganese, nitrogen, and oxygen, where the larger TZVP (Ahlrichs triple- $\zeta$  valence polarized) basis in conjunction with the TZV/J auxiliary basis were used.<sup>34-35</sup> These calculations employed the resolution of identity (RI) approximation developed by Neese.<sup>36</sup> Solvation effects associated with acetonitrile (dielectric constant  $\epsilon = 36.6$ ) were incorporated using COSMO, as implemented in *ORCA*.<sup>37</sup> The propyl and ethyl linkers in the diazacycloalkane fragment of the  $\text{L}^7\text{py}_2^{\text{R}}$  ligands create two different faces when this ligand is bound in a *trans* geometry, as observed for the  $\text{Mn}^{\text{II}}$  complexes (*vide infra*). Therefore, in constructing our computational models of  $[\text{Mn}^{\text{III}}(\text{O}_2)(\text{L}^7\text{py}_2^{\text{R}})]^+$ , we considered two isomers for the simplest  $[\text{Mn}^{\text{III}}(\text{O}_2)(\text{L}^7\text{py}_2^{\text{H}})]^+$  complex, where the peroxo ligand is adjacent to either the propyl (**P**) or ethyl (**E**) linkers (see Figure 2.10). The **P** isomer is predicted to be lower energy than the **E** isomer by only ~1 kcal/mol, which is well within the error expected for DFT calculations.<sup>38</sup> In addition, the TD-DFT computed absorption spectra of isomers **P** and **E** are essentially identical, indicating that these nearly isoenergetic isomers are expected to display very similar optical properties. Accordingly, we only considered isomer **P** in our analysis, under the assumption that, while there

may likely be two isomers present in experimental samples of  $[\text{Mn}^{\text{III}}(\text{O}_2)(\text{L}^7\text{py}_2^{\text{H}})]^+$ , these isomers will have virtually identical geometric and electronic structures. The coordinates of all DFT energy-minimized models presented in this study are included as Supporting Information (Tables A.2.6 – A.2.8).

Electronic transition energies and intensities were computed for  $[\text{Mn}^{\text{III}}(\text{O}_2)(\text{L}^7\text{py}_2^{\text{H}})]^+$  and  $[\text{Mn}^{\text{III}}(\text{O}_2)(\text{L}^7\text{py}_2^{6\text{-Me}})]^+$  using the time-dependent (TD)-DFT method<sup>39-41</sup> within the Tamm-Dancoff approximation.<sup>42-43</sup> These calculations employed the B3LYP functional,<sup>44-46</sup> and TZVP (Mn, N, and O) and SVP (C and H) basis sets. In each calculation, 40 excited states were calculated by including all one-electron excitations within an energy window of  $\pm 3$  Hartrees with respect to the HOMO/LUMO energies. Isosurface plots of molecular orbitals and electron density difference maps (EDDMs) were generated using the gOpenMol program using isodensity values of 0.05 and 0.02  $\text{b}^{-3}$ , respectively.

## 2.5 Supporting Information.

### 2.5.1 Specific Details of XRD Data Collection and Analysis for

$[\text{Mn}^{\text{II}}(\text{L}^7\text{py}_2^{\text{H}})(\text{NCMe})_3](\text{ClO}_4)_2$  (**1-H**). Colorless plate-shaped crystals of  $[\text{Mn}(\text{N}_4\text{C}_{17}\text{H}_{22})(\text{NCCH}_3)_3][\text{ClO}_4]_2$  are, at 100(2) K, triclinic, space group  $\text{P}\bar{1} - \text{C}_i^1$  (No. 2)<sup>66</sup> with  $\mathbf{a} = 10.458(1) \text{ \AA}$ ,  $\mathbf{b} = 11.979(1) \text{ \AA}$ ,  $\mathbf{c} = 12.977(1) \text{ \AA}$ ,  $\alpha = 91.148(1)^\circ$ ,  $\beta = 97.368(1)^\circ$ ,  $\gamma = 111.967(1)^\circ$ ,  $V = 1491.2(2) \text{ \AA}^3$  and  $Z = 2$  formula units  $\{\text{d}_{\text{calcd}} = 1.469 \text{ g/cm}^3$ ;  $\mu_{\text{a}}(\text{MoK}\alpha) = 0.68 \text{ mm}^{-1}\}$ . A full hemisphere of diffracted intensities (1850 10-second frames with a  $\omega$  scan width of  $0.30^\circ$ ) was measured for a single-domain specimen using graphite-monochromated MoK $\alpha$  radiation ( $\lambda = 0.71073 \text{ \AA}$ ) on a Bruker SMART APEX CCD Single Crystal Diffraction System.<sup>67</sup>

X-rays were provided by a fine-focus sealed X-ray tube operated at 45kV and 35mA. Lattice constants were determined with the Bruker SAINT software package using peak centers for 5826 reflections. A total of 17596 integrated reflection intensities having  $2\theta(\text{MoK}\alpha) < 61.05^\circ$  were produced using the Bruker program SAINT;<sup>68</sup> 8675 of these were unique and gave  $R_{\text{int}} = 0.037$  with a coverage which was 95.2% complete. The data were corrected empirically for variable absorption effects using equivalent reflections; the relative transmission factors ranged from 0.898 to 1.000. The Bruker software package SHELXTL was used to solve the structure using “direct methods” techniques. All stages of weighted full-matrix least-squares refinement were conducted using  $F_o^2$  data with the SHELXTL Version 6.10 software package.<sup>69</sup>

Once all of the anticipated nonhydrogen atoms for the  $\text{Mn}(\text{N}_4\text{C}_{17}\text{H}_{22})^{2+}$  moiety were located and refined, nitrogen atoms N(2) and N(3) were seen to be linked by a high-occupancy (81% of the time) pair of ethylene and propylene chains and a pair of low-occupancy (19% of the time) chains. This is consistent with cocrystallization of two different conformations for the metal complex that have virtually identical sizes and shapes. These characteristics allow the two conformations to occupy the same portion of the unit cell and give disorder of the type observed. The structure was therefore refined with “whole molecule disorder” restraints for the  $\text{Mn}(\text{N}_4\text{C}_{17}\text{H}_{22})^{2+}$  unit: two moieties having identical atom-to-atom connectivities were restrained to have the same covalent bond lengths and angles for their nonhydrogen atoms. The final structural model incorporated anisotropic thermal parameters for all nonhydrogen atoms of the major “cation” and the Mn atom of the minor “cation”. All carbon and nitrogen atoms of the minor cation were included in the structural model with isotropic thermal parameters that were allowed to vary. Both  $[\text{ClO}_4]^-$  anions are also disordered and their Cl and O atoms were modeled with “whole molecule disorder” restraints. Both anions have two slightly different orientations

in the lattice about a nearly common position for the Cl atom. The major orientation is occupied 58% of the time for the first anion and 69% of the time for the second anion.

Methyl groups for the three coordinated acetonitrile molecules were incorporated into the structural model as rigid groups (using idealized  $sp^3$ -hybridized geometry and a C-H bond length of 0.98 Å) that were allowed to rotate about their C-C bonds. The remaining hydrogen atoms were included in the structural model as idealized atoms (assuming  $sp^2$ - or  $sp^3$ -hybridization of the carbon atoms and C-H bond lengths of 0.95 – 0.99 Å) “riding” on their respective carbon atoms. The isotropic thermal parameters of all idealized hydrogen atoms were fixed at values 1.2 (nonmethyl) or 1.5 (methyl) times the equivalent isotropic thermal parameter of the carbon atom to which they are covalently bonded.

A total of 559 parameters were refined using 92 restraints, 8675 data and weights of  $w = 1 / [\sigma^2(F^2) + (0.0548 P)^2]$ , where  $P = [F_o^2 + 2F_c^2] / 3$ . Final agreement factors at convergence are:  $R_1$ (unweighted, based on F) = 0.047 for 6645 independent absorption-corrected “observed” reflections having  $2\theta(\text{MoK}\alpha) < 61.05^\circ$  and  $I > 2\sigma(I)$ ;  $R_1$ (unweighted, based on F) = 0.065 and  $wR_2$ (weighted, based on  $F^2$ ) = 0.112 for all 8675 independent absorption-corrected reflections having  $2\theta(\text{MoK}\alpha) < 61.05^\circ$ . The largest shift/s.u. was 0.002 in the final refinement cycle. The final difference map had maxima and minima of 0.41 and -0.32  $e^-/\text{\AA}^3$ , respectively.

**2.5.2 Specific Details of XRD Data Collection and Analysis for  $[\text{Mn}^{\text{II}}(\text{L}^7\text{py}_2^{5-}\text{Br})(\text{OCMe}_2)(\text{ClO}_4)](\text{ClO}_4)$  (1-Br).** Yellow-brown rectangular-parallelepiped shaped crystals of  $[\text{Mn}(\text{N}_4\text{C}_{17}\text{H}_{20}\text{Br}_2)(\text{ClO}_4)-(\text{CH}_3\text{COCH}_3)](\text{ClO}_4)$  are, at 100(2) K, monoclinic, space group  $P2_1/c - C_{2h}^5$  (No. 14)<sup>66</sup> with  $a = 9.801(1)$  Å,  $b = 17.980(1)$  Å,  $c = 15.157(1)$  Å,  $\beta = 96.511(1)^\circ$ ,  $V =$



2653.8(2) Å<sup>3</sup> and  $Z = 4$  formula units  $\{d_{\text{calcd}} = 1.882 \text{ g/cm}^3; \mu_a(\text{MoK}\alpha) = 3.767 \text{ mm}^{-1}\}$ . A full hemisphere of diffracted intensities (1850 40-second frames with a  $\omega$  scan width of 0.30°) was measured for a single-domain specimen using graphite-monochromated MoK $\alpha$  radiation ( $\lambda = 0.71073 \text{ Å}$ ) on a Bruker SMART APEX CCD Single Crystal Diffraction System.<sup>67</sup> X-rays were provided by a fine-focus sealed x-ray tube operated at 45kV and 35mA. Lattice constants were determined with the Bruker SAINT software package using peak centers for 6351 reflections. A total of 30806 integrated reflection intensities having  $2\theta(\text{MoK}\alpha) < 61.04^\circ$  were produced using the Bruker program SAINT;<sup>68</sup> 7991 of these were unique and gave  $R_{\text{int}} = 0.042$  with a coverage which was 98.7% complete. The data were corrected empirically for variable absorption effects using equivalent reflections; the relative transmission factors ranged from 0.758 to 1.000. The Bruker software package SHELXTL was used to solve the structure using “direct methods” techniques. All stages of weighted full-matrix least-squares refinement were conducted using  $F_o^2$  data with the SHELXTL Version 6.10 software package.<sup>69</sup>

Once all of the anticipated nonhydrogen atoms for the  $\text{Mn}(\text{N}_4\text{C}_{17}\text{H}_{20}\text{Br}_2)$  moiety were located and refined, nitrogen atoms N(2) and N(3) were seen to be linked by a high-occupancy (78% of the time) pair of ethylene and propylene chains and a pair of low-occupancy (22% of the time) chains. This is consistent with cocrystallization of two different conformations for the metal complex that have virtually identical sizes and shapes. These characteristics allow the two conformations to occupy the same portion of the unit cell and give disorder of the type observed. The structure was therefore refined with “whole molecule disorder” restraints for the  $\text{Mn}(\text{N}_4\text{C}_{17}\text{H}_{20}\text{Br}_2)$  unit: two moieties having identical atom-to-atom connectivities were restrained to have the same covalent bond lengths and angles for their nonhydrogen atoms. The

final structural model incorporated anisotropic thermal parameters for all nonhydrogen atoms of both “molecules”. Mild restraints were placed on the anisotropic thermal parameters for the following 4 atoms of the minor (occupied 22% of the time) orientation for the  $\text{Mn}(\text{N}_4\text{C}_{17}\text{H}_{20}\text{Br}_2)$  moiety: N(24), C(23), C(26) and C(31). The  $[\text{ClO}_4]^-$  counterion is also disordered. It has two orientations about the Cl(2)-O(21) bond; the major orientation is occupied 74% of the time and the minor orientation is occupied 26% of the time.

Both methyl groups for the coordinated acetone molecule were incorporated into the structural model as rigid groups (using idealized  $\text{sp}^3$ -hybridized geometry and a C-H bond length of 0.98 Å) that were allowed to rotate about their C-C bonds. The remaining hydrogen atoms were included into the structural model as idealized atoms (assuming  $\text{sp}^2$ - or  $\text{sp}^3$ -hybridization of the carbon atoms and C-H bond lengths of 0.95 – 0.99 Å) “riding” on their respective carbon atoms. The isotropic thermal parameters of all idealized hydrogen atoms were fixed at values 1.2 (nonmethyl) or 1.5 (methyl) times the equivalent isotropic thermal parameter of the carbon atom to which they are covalently bonded.

A total of 590 parameters were refined using 102 restraints, 7991 data and weights of  $w = 1 / [\sigma^2(F^2) + (0.0437 P)^2 + 0.9585 P]$ , where  $P = [F_o^2 + 2F_c^2] / 3$ . Final agreement factors at convergence are:  $R_1$ (unweighted, based on F) = 0.040 for 6166 independent absorption-corrected “observed” reflections having  $2\theta(\text{MoK}\alpha) < 61.04^\circ$  and  $I > 2\sigma(I)$ ;  $R_1$ (unweighted, based on F) = 0.060 and  $wR_2$ (weighted, based on  $F^2$ ) = 0.091 for all 7991 independent absorption-corrected reflections having  $2\theta(\text{MoK}\alpha) < 61.04^\circ$ . The largest shift/s.u. was 0.001 in the final refinement cycle. The final difference map had maxima and minima of 0.79 and -0.49  $\text{e}^-/\text{\AA}^3$ , respectively.

**2.5.3 Specific Details of XRD Data Collection and Analysis for  $[\text{Mn}^{\text{II}}(\text{L}^7\text{py}_2^{6-\text{Me}})(\text{NCMe})(\text{ClO}_4)](\text{ClO}_4)$  (1-Me).** Colorless crystals of  $[\text{Mn}(\text{N}_4\text{C}_{19}\text{H}_{26})(\text{NCCH}_3)(\text{ClO}_4)](\text{ClO}_4)$  are, at 100(2) K, monoclinic, space group  $\text{P2}_1/\text{c} - \text{C}_{2\text{h}}^5$  (No. 14)<sup>66</sup> with  $\mathbf{a} = 18.169(2) \text{ \AA}$ ,  $\mathbf{b} = 9.879(1) \text{ \AA}$ ,  $\mathbf{c} = 14.545(2) \text{ \AA}$ ,  $\beta = 104.277(2)^\circ$ ,  $V = 2530.1(6) \text{ \AA}^3$  and  $Z = 4$  formula units  $\{\text{d}_{\text{calcd}} = 1.589 \text{ g/cm}^3$ ;  $\mu_{\text{a}}(\text{MoK}\alpha) = 0.789 \text{ mm}^{-1}\}$ . A full hemisphere of diffracted intensities (1850 10-second frames with a  $\omega$  scan width of  $0.30^\circ$ ) was measured for a single-domain specimen using graphite-monochromated  $\text{MoK}\alpha$  radiation ( $\lambda = 0.71073 \text{ \AA}$ ) on a Bruker SMART APEX CCD Single Crystal Diffraction System.<sup>67</sup> X-rays were provided by a fine-focus sealed x-ray tube operated at 45kV and 35mA. Lattice constants were determined with the Bruker SAINT software package using peak centers for 5833 reflections. A total of 23041 integrated reflection intensities having  $2\theta((\text{MoK}\alpha)) < 58.39^\circ$  were produced using the Bruker program SAINT;<sup>68</sup> 6423 of these were unique and gave  $R_{\text{int}} = 0.054$  with a coverage which was 93.8% complete. The data were corrected empirically for variable absorption effects using equivalent reflections; the relative transmission factors ranged from 0.901 to 1.000. The Bruker software package SHELXTL was used to solve the structure using “direct methods” techniques. All stages of weighted full-matrix least-squares refinement were conducted using  $F_o^2$  data with the SHELXTL Version 6.10 software package.<sup>69</sup>

The final structural model incorporated anisotropic thermal parameters for all nonhydrogen atoms and isotropic thermal parameters for all hydrogen atoms. All hydrogen atoms were located in a difference Fourier and included in the structural model as independent isotropic atoms whose parameters were allowed to vary in least-squares refinement cycles. A total of 450 parameters were refined using no restraints, 6423 data and weights of  $w = 1/[\sigma^2(F^2)]$

+ (0.0496  $P$ )<sup>2</sup>], where  $P = [F_o^2 + 2F_c^2] / 3$ . Final agreement factors at convergence are:  $R_1$ (unweighted, based on  $F$ ) = 0.048 for 5263 independent absorption-corrected “observed” reflections having  $2\theta(\text{MoK}\alpha) < 58.39^\circ$  and  $I > 2\sigma(I)$ ;  $R_1$ (unweighted, based on  $F$ ) = 0.062 and  $wR_2$ (weighted, based on  $F^2$ ) = 0.107 for all 6423 independent absorption-corrected reflections having  $2\theta(\text{MoK}\alpha) < 58.39^\circ$ . The largest shift/s.u. was 0.001 in the final refinement cycle. The final difference map had maxima and minima of 0.82 and -0.50  $e^-/\text{\AA}^3$ , respectively.

**2.5.1 Specific Details of XRD Data Collection and Analysis for  $[\text{Mn}^{\text{II}}(\text{L}^7\text{py}_2^{6-\text{MeO}})(\text{ClO}_4)_2] \cdot (\text{1-MeO})$ .** Colorless rectangular-parallelepiped shaped crystals of  $[\text{Mn}(\text{N}_4\text{C}_{19}\text{H}_{28}\text{O}_2)(\text{ClO}_4)_2]$  are, at 100(2) K, monoclinic, space group  $\text{C2/c} - \text{C}_{2h}^6$  (No. 15)<sup>66</sup> with  $\mathbf{a} = 13.631(1) \text{ \AA}$ ,  $\mathbf{b} = 10.755(1) \text{ \AA}$ ,  $\mathbf{c} = 17.202(2) \text{ \AA}$ ,  $\beta = 109.022(1)^\circ$ ,  $V = 2384.0(4) \text{ \AA}^3$  and  $Z = 4$  molecules { $d_{\text{calcd}} = 1.667 \text{ g/cm}^3$ ;  $\mu_a(\text{MoK}\alpha) = 0.842 \text{ mm}^{-1}$ }. A full hemisphere of diffracted intensities (1850 10-second frames with an  $\omega$  scan width of  $0.30^\circ$ ) was measured for a single-domain specimen using graphite-monochromated  $\text{MoK}\alpha$  radiation ( $\lambda = 0.71073 \text{ \AA}$ ) on a Bruker SMART APEX CCD Single Crystal Diffraction System.<sup>67</sup> X-rays were provided by a fine-focus sealed x-ray tube operated at 45kV and 35mA. Lattice constants were determined with the Bruker SAINT software package using peak centers for 7461 reflections. A total of 10685 integrated reflection intensities having  $2\theta(\text{MoK}\alpha) < 58.19^\circ$  were produced using the Bruker program SAINT;<sup>3</sup> 2995 of these were unique and gave  $R_{\text{int}} = 0.057$  with a coverage which was 93.6% complete. The data were corrected empirically for variable absorption effects using equivalent reflections; the relative transmission factors ranged from 0.815 to 1.000. The Bruker software package SHELXTL was used to solve the structure using “direct methods” techniques. All stages of weighted full-matrix least-squares refinement were conducted using  $F_o^2$  data with the SHELXTL Version 6.10

software package.<sup>69</sup>

The Mn atom was seen to lie on the crystallographic  $C_2$  axis at (0, y, ¼) in the unit cell. The molecule was therefore statistically disordered about this axis and this was consistent with cocrystallization of two different conformations for the metal complex that have virtually identical sizes and shapes. The difference between the two “disordered” conformations of the molecule principally involved interchanging alkyl chain linkers between N(2) and its  $C_2$ -related atom. Since this does not alter the gross shape and size of the molecule, the two conformations can occupy the same portion of the unit cell and give disorder of the type observed. Carbon atom C(7) appeared to have a position common to both orientations of the ethylene and propylene chain linkers; it was therefore included in the structural model with an occupancy factor of 1.00. The remaining carbon atoms in these chains were included in the structural model with occupancy factors of 0.50.

The methoxy methyl group was incorporated into the structural model as a rigid group (using idealized  $sp^3$ -hybridized geometry and a C-H bond length of 0.98 Å) that was allowed to rotate about its O-C bond. The remaining hydrogen atoms were included in the structural model as idealized atoms (assuming  $sp^2$ - or  $sp^3$ -hybridization of the carbon atoms and C-H bond lengths of 0.95 – 0.99 Å) “riding” on their respective carbon atoms. The isotropic thermal parameters of all idealized hydrogen atoms were fixed at values 1.2 (nonmethyl) or 1.5 (methyl) times the equivalent isotropic thermal parameter of the carbon atom to which they are covalently bonded.

A total of 178 parameters were refined using no restraints, 2995 data and weights of  $w = 1 / [\sigma^2(F^2) + (0.0388 P)^2 + 9.449 P]$ , where  $P = [F_o^2 + 2F_c^2] / 3$ . Final agreement factors at convergence are:  $R_1$ (unweighted, based on F) = 0.053 for 2948 independent absorption-corrected

“observed” reflections having  $2\theta(\text{MoK}\alpha) < 58.19^\circ$  and  $I > 2\sigma(I)$ ;  $R_1(\text{unweighted, based on } F) = 0.054$  and  $wR_2(\text{weighted, based on } F^2) = 0.126$  for all 2995 independent absorption-corrected reflections having  $2\theta(\text{MoK}\alpha) < 58.19^\circ$ . The largest shift/s.u. was 0.000 in the final refinement cycle. The final difference map had maxima and minima of 0.69 and  $-0.67 \text{ e}^-/\text{\AA}^3$ , respectively.

## 2.6 References.

- (1) Emerson, J. P.; Kovaleva, E. G.; Farquhar, E. R.; Lipscomb, J. D.; Que, L., Jr. *Proc. Natl. Acad. Sci. USA* **2008**, *105*, 7347-7352.
- (2) Grove, L. E.; Brunold, T. C. *Comments Inorg. Chem.* **2008**, *29*, 134-168.
- (3) Gunderson, W. A.; Zatsman, A. I.; Emerson, J. P.; Farquhar, E. R.; Que, L.; Lipscomb, J. D.; Hendrich, M. P. *J. Am. Chem. Soc.* **2008**, *130*, 14465-14467.
- (4) Miller, A.-F. *Curr. Opin. Chem. Biol.* **2004**, *8*, 162-168.
- (5) Wu, A. J.; Penner-Hahn, J. E.; Pecoraro, V. L. *Chem. Rev.* **2004**, *104*, 903-938.
- (6) Hage, R.; Lienke, A. *Angew. Chem. Int. Ed.* **2006**, *45*, 206-222.
- (7) Hage, R.; Lienke, A. *J. Mol. Catal. A: Chem.* **2006**, *251*, 150-158.
- (8) Lane, B. S.; Burgess, K. *Chem. Rev.* **2003**, *103*, 2457-2473.
- (9) Sibbons, K.; Shastri, K.; Watkinson, M. *Dalton Trans.* **2006**, *2006*, 645-661.
- (10) Bull, C.; Niederhoffer, E. C.; Yoshida, T.; Fee, J. A. *J. Am. Chem. Soc.* **1991**, *113*, 4069-4076.
- (11) Hearn, A. S.; Tu, C. K.; Nick, H. S.; Silverman, D. N. *J. Biol. Chem.* **1999**, *274*, 24457-24460.
- (12) Yin, G.; Buchalova, M.; Danby, A. M.; Perkins, C. M.; Kitko, D.; Carter, J. D.; Scheper, W. M.; Busch, D. H. *Inorg. Chem.* **2006**, *45*, 3467-3474.
- (13) Groni, S.; Blain, G.; Guillot, R.; Policar, C.; Anxolabéhère-Mallart, E. *Inorg. Chem.* **2007**, *46*, 1951-1953.
- (14) Groni, S.; Dorlet, P.; Blain, G.; Bourcier, S.; Guillot, R.; Anxolabéhère-Mallart, E. *Inorg. Chem.* **2008**, *47*, 3166-3172.
- (15) Shook, R. L.; Gunderson, W. A.; Greaves, J.; Ziller, J. W.; Hendrich, M. P.; Borovik, A. S. *J. Am. Chem. Soc.* **2008**, *130*, 8888-8889.
- (16) Kitajima, N.; Komatsuzaki, H.; Hikichi, S.; Osawa, M.; Moro-oka, Y. *J. Am. Chem. Soc.* **1994**, *116*, 11596-11597.
- (17) Seo, M. S.; Kim, J. Y.; Annaraj, J.; Kim, Y.; Lee, Y.-M.; Kim, S.-J.; Kim, J.; Nam, W. *Angew. Chem. Int. Ed.* **2007**, *46*, 377-380.
- (18) Singh, U. P.; Sharma, A. K.; Hikichi, S.; Komatsuzaki, H.; Moro-oka, Y.; Akita, M. *Inorg. Chim. Acta* **2006**, *359*, 4407-4411.
- (19) VanAtta, R. B.; Strouse, C. E.; Hanson, L. K.; Valentine, J. S. *J. Am. Chem. Soc.* **1987**, *109*, 1425-1434.
- (20) Jackson, T. A.; Brunold, T. C. *Acc. Chem. Res.* **2004**, *37*, 461-470.

- (21) Annaraj, J.; Cho, J.; Lee, Y.-M.; Kim, S. Y.; Latifi, R.; de Visser, S. P.; Nam, W. *Angew. Chem. Int. Ed.* **2009**, *48*, 4150-4153.
- (22) Costas, M.; Mehn, M. P.; Jensen, M. P.; Que, L. J. *Chem. Rev.* **2004**, *104*, 939-986.
- (23) Sisemore, M. F.; Selke, M.; Burstyn, J. N.; Valentine, J. S. *Inorg. Chem.* **1997**, *36*, 979-984.
- (24) Armarego, W.; Chai, C. *Purifications of Laboratory Chemicals*; Fifth ed.; Elsevier: Burlington, MA, 2003.
- (25) Evans, D. F.; Jakubovic, D. A. *J. Chem. Soc., Dalton Trans.* **1988**, 2927-2933.
- (26) Mayilmurugan, R.; Stoeckli-Evans, H.; Palaniandavar, M. *Inorg. Chem* **2008**, *47*, 6645-6658.
- (27) *Data Collection: SMART Software Reference Manual*. Bruker-AXS. 5465 E. Cheryl Parkway, Madison, WI 53711-5373 USA, 1998.
- (28) Sheldrick, G. M.; Bruker-AXS, 5465 E. Cheryl Parkway, Madison, WI 53711-5373 USA: Bruker-AXS, 5465 E. Cheryl Parkway, Madison, WI 53711-5373 USA, 2000.
- (29) Neese, F.; Solomon, E. I. *Inorg. Chem.* **1999**, *38*, 1847-1865.
- (30) Jackson, T. A.; Karapetian, A.; Miller, A.-F.; Brunold, T. C. *Biochemistry* **2005**, *44*, 1504-1520.
- (31) Neese, F., *ORCA - an ab initio, Density Functional and Semiempirical Program Package, Version 2.7*, University of Bonn, 2009.
- (32) Becke, A. D. *J. Chem. Phys.* **1986**, *84*, 4524-4529.
- (33) Perdew, J. P. *Phys. Rev. B* **1986**, *33*, 8822-8824.
- (34) Schäfer, A.; Horn, H.; Ahlrichs, R. *J. Chem. Phys.* **1992**, *97*, 2571-2577.
- (35) Schäfer, G.; Huber, C.; Ahlrichs, R. *J. Chem. Phys.* **1994**, *100*, 5829-5835.
- (36) Neese, F. *J. Comput. Chem.* **2003**, *24*, 1740-1747.
- (37) Sinnecker, S.; Rajendran, A.; Klamt, A.; Diedenhofen, M.; Neese, F. *J. Phys. Chem. A* **2006**, *110*, 2235-2245.
- (38) Siegbahn, P. E. M. *J. Biol. Inorg. Chem.* **2006**, *11*, 695-701.
- (39) Bauernschmitt, R.; Ahlrichs, R. *Chem. Phys. Lett.* **1996**, *256*, 454-464.
- (40) Casida, E. M.; Jamorski, C.; Casida, K. C.; Salahub, D. R. *J. Chem. Phys.* **1998**, *108*, 4439-4449.
- (41) Stratman, R. E.; Scuseria, G. E.; Frisch, M. J. *J. Chem. Phys.* **1998**, *109*, 8218-8224.
- (42) Hirata, S.; Head-Gordon, M. *Chem. Phys. Lett.* **1999**, *302*, 375-382.
- (43) Hirata, S.; Head-Gordon, M. *Chem. Phys. Lett.* **1999**, *314*, 291-299.
- (44) Becke, A. D. *J. Chem. Phys.* **1993**, *98*, 1372-1377.
- (45) Becke, A. D. *J. Chem. Phys.* **1993**, *98*, 5648-5652.
- (46) Lee, C.; Yang, W.; Parr, R. G. *Phys. Rev. B* **1988**, *37*, 785-789.
- (47) Ghachtouli, S. E.; Mohamadou, A.; Barbier, J.-P. *Inorganica Chimica Acta* **2005**, *358*, 3873-3880.
- (48) Wang, S.; Westmoreland, D. *Inorg. Chem* **2008**, *48*, 719-727.
- (49) Darensbourg, D. J.; Frantz, E. B. *Inorg. Chem.* **2008**, *47*, 4977-4987.
- (50) Hureau, C.; Blondin, G.; Charlot, M.-F.; Philouze, C.; Nierlich, M.; Cesario, M.; Anxolabehere-Mallart, E. *Inorg. Chem.* **2005**, *44*, 3669-3683.
- (51) Murphy, A.; Dubois, G.; Stack, T. D. P. *J. Am. Chem. Soc.* **2003**, *125*, 5250-5251.
- (52) Murphy, A.; Stack, T. D. P. *J. Mol. Catal. A: Chem.* **2006**, *251*, 78-88.
- (53) Glerup, J.; Goodson, P. A.; Hazell, A.; Hazell, R.; Hodgson, D. J.; McKenzie, C. J.; Michelsen, K.; Rychlewska, U.; Toftlund, H. *Inorg. Chem.* **2002**, *33*, 4105-4111.

- (54) Goodson, P. A.; Glerup, J.; Hodgson, D. J.; Michelsen, K.; Pedersen, E. *Inorg. Chem.* **1990**, 29, 503-508.
- (55) Goodson, P. A.; Hodgson, D. J. *Inorg. Chem.* **1989**, 28, 3606-3608.
- (56) Goodson, P. A.; Glerup, J.; Hodgson, D. J.; Michelsen, K.; Weihe, H. *Inorg. Chem.* **1991**, 30, 4909-4914.
- (57) Goodson, P. A.; Oki, A. R.; Glerup, J.; Hodgson, D. J. *J. Am. Chem. Soc.* **1990**, 112, 6248-6254.
- (58) Collins, M. A.; Hodgson, D. J.; Michelsen, K.; Towle, D. K. *J. Chem. Soc., Chem. Commun.* **1987**, 1659-1660.
- (59) Halfen, J. A.; Moore, H. L.; Fox, D. C. *Inorg. Chem.* **2002**, 41.
- (60) Halfen, J. A.; Uhan, J. M.; Fox, D. C.; Mehn, M. P.; Lawrence Que, J. *Inorg. Chem.* **2000**, 29.
- (61) Chen, K.; Que, L. J. *Angew. Chem. Int. Ed.* **1999**, 38, 2227-2229.
- (62) Glerup, J.; Goodson, P. A.; Hazell, A.; Hazell, R.; Hodgson, D. J.; McKenzie, C. J.; Michelsen, K.; Rychlewska, U.; Toftlund, H. *Inorg. Chem.* **1994**, 33, 4105-4111.
- (63) Lever, A. B. P. *Inorganic Electronic Spectroscopy*; 2nd ed.; Elsevier: Amsterdam; New York, 1984.
- (64) Neese, F.; Solomon, E. I. *J. Am. Chem. Soc.* **1998**, 120, 12829-12848.
- (65) Oganessian, V. S.; George, S. J.; Cheesman, M. R.; Thomson, A. J. *J. Chem. Phys.* **1999**, 110, 762-777.
- (66) International Tables for Crystallography, Vol A, 4<sup>th</sup> ed., Kluwer: Boston (1996).
- (67) Data Collection: SMART Software Reference Manual (1998). Bruker-AXS, 5465 E. Cheryl Parkway, Madison, WI 53711-5373 USA.
- (68) Data Reduction: SAINT Software Reference Manual (1998). Bruker-AXS, 6300 Enterprise Dr., Madison, WI 53719-1173, USA.
- (69) G. M. Sheldrick (2000). SHELXTL Version 6.10 Reference Manual. Bruker-AXS, 5465 E. Cheryl Parkway, Madison, WI 53711-5373 USA.



### Chapter 3

#### **Nucleophilic Reactivity of a Series of Peroxomanganese(III) Complexes Supported by Tetradentate Aminopyridyl Ligands**

This work has been published under the following: Geiger R. A.; Chattopadhyay S.; Day V. W.; Jackson T. A.; Nucleophilic Reactivity of a Series of Peroxomanganese(III) Complexes Supported by Tetradentate Aminopyridyl Ligands; *Dalton Trans.* **2011**, 40, 1707-1715.

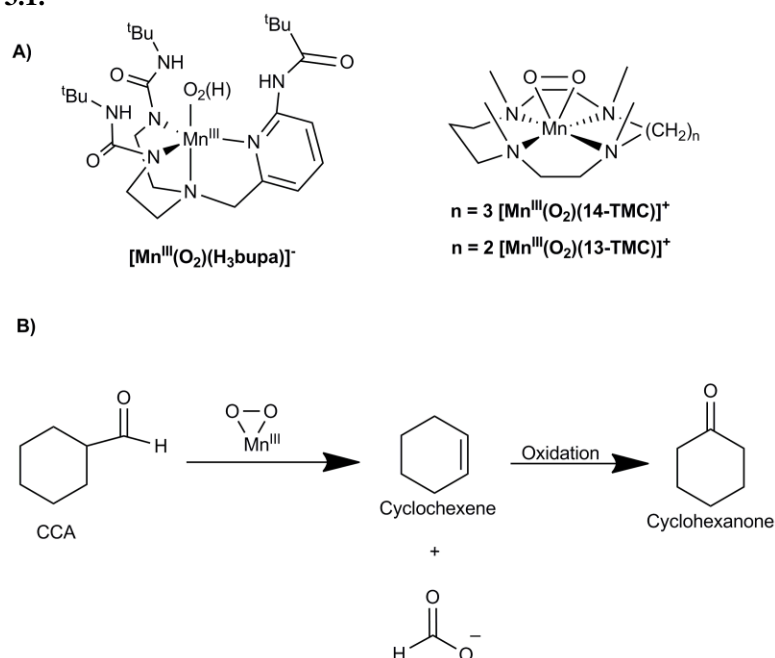
### 3. 1 Introduction.

Peroxoiron(III) and peroxomanganese(III) complexes play important roles in biological systems and in catalytic oxidation reactions. A ferric-peroxo species is implicated as a key intermediate in certain cytochrome P450-catalyzed reactions, including the aromatization of androgen to estrogen by cytochrome P450 aromatase<sup>1</sup> and oxidation of L-arginine to citrulline by the P450 mono-oxygenase nitric oxide synthase.<sup>2</sup> Peroxomanganese(III) complexes are potential intermediates in manganese containing enzymes, including manganese superoxide dismutase, manganese catalase, and manganese ribonucleotide reductase.<sup>3-7</sup> While the mechanisms of these systems remain the subject of much current work, the importance of peroxo-level intermediates has been outlined in several reports.<sup>8-11</sup> An example is the manganese superoxide dismutase enzyme that forms a product-inhibited complex proposed to contain a peroxomanganese(III) adduct.<sup>8,9,12</sup>

A variety of different ligands sets, ranging from neutral, tetraamine macrocyclic ligands to anionic, facially-coordinating tris(pyrazolyl)borate chelates, have been used to stabilize peroxomanganese(III) intermediates.<sup>13-21</sup> Of the structurally characterized complexes, all exhibit side-on ( $\eta^2$ ) peroxo ligands with Mn–O distances in the range of 1.85 to 1.88 Å,<sup>13,15,16,21,22</sup> although it has been proposed that this distance can be modulated by the inclusion of electron-donating groups *trans*<sup>16</sup> or *cis*<sup>20</sup> to the peroxo unit. A convenient way to compare the relative reactivities of these diverse complexes, and thus define different steric and electronic influences on reactivity, is by using a common reaction. Because aldehyde deformylation appears to be characteristic of both Mn<sup>III</sup>-peroxo<sup>15,16</sup> and Fe<sup>III</sup>-peroxo<sup>23,24</sup> complexes, it is ideal for this purpose. Indeed, peroxomanganese(III) adducts assembled using very different supporting ligands (Scheme 3.1) deformylate cyclohexanecarboxaldehyde (CCA).<sup>15-17</sup> For Mn<sup>III</sup>-O<sub>2</sub> adducts

supported by the 14-TMC and 13-TMC ligands (14-TMC = 1,4,8,11-tetramethyl-1,4,8,11-tetraazacyclotetradecane and 13-TMC = 1,4,7,10-tetramethyl-1,4,7,10-tetraazacyclotridecane), nearly identical second-order rate constants were reported ( $k_2 = 2.4$  and  $1.2 \text{ M}^{-1} \text{ min}^{-1}$  respectively at  $10^\circ \text{C}$ ). Cyclohexene, the expected product of CCA deformylation (Scheme 3.1), was observed in both cases in ~55% yield.<sup>15,16</sup> Using a peroxomanganese(III) complex supported by the anionic  $\text{H}_3\text{bupa}$  ligand ( $\text{H}_3\text{bupa}$  is the dianion of bis[ $(N'$ -*tert*-butylurealy)- $N$ -ethyl]-(6-pivalamido-2-pyridylmethyl)amine), Borovik *et al.* reported the oxidative deformylation of CCA to give cyclohexanone in 40% yield.<sup>17</sup>

**Scheme 3.1.**

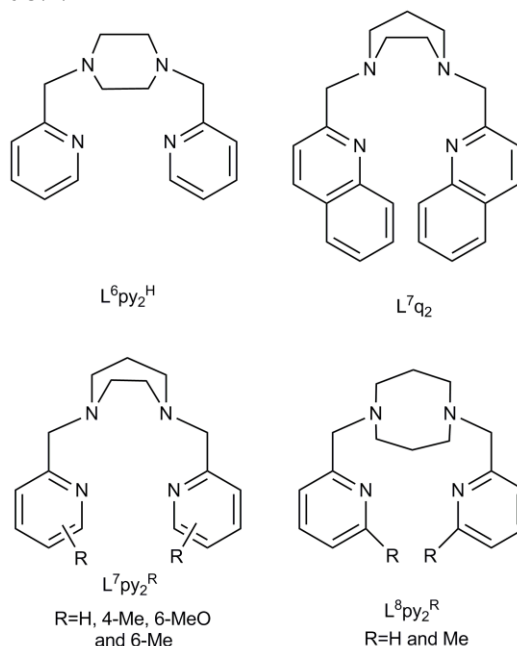


The identity of the ligand *trans* to the peroxo group has been shown to have a dramatic effect on the rate of CCA deformylation. The addition of anions to  $[\text{Mn}^{\text{III}}(\text{O}_2)(13\text{-TMC})]^+$  leads to the formation of neutral, seven-coordinate  $\text{Mn}^{\text{III}}\text{-O}_2$  adducts, formulated as  $[\text{Mn}^{\text{III}}(\text{O}_2)(13\text{-TMC})(\text{X})]$  (where  $\text{X}^- = \text{CN}^-$ ,  $\text{NCS}^-$ ,  $\text{CF}_3\text{CO}_2^-$ , and  $\text{N}_3^-$ ) that showed dramatically enhanced rates for CCA deformylation.<sup>16</sup> In particular  $[\text{Mn}^{\text{III}}(\text{O}_2)(13\text{-TMC})(\text{N}_3)]$  displayed a second-order rate

constant  $10^4$  larger than that of  $[\text{Mn}^{\text{III}}(\text{O}_2)(13\text{-TMC})]^+$ . This remarkably large rate enhancement was attributed to the strong electron donating properties of the axial azide ligand. It was postulated that the trans  $\text{N}_3^-$  ligand favors a peroxo binding mode intermediate between side-on and end-on, increasing the nucleophilicity of one oxygen atom of the peroxo ligand.

We have recently reported a series of  $\text{Mn}^{\text{III}}\text{-O}_2$  complexes supported by tetradentate dipyridyldiazacycloalkane ligands:  $\text{L}^7\text{py}_2^{\text{H}}$ ,  $\text{L}^7\text{py}_2^{5\text{-Br}}$ ,  $\text{L}^7\text{py}_2^{6\text{-Me}}$ , and  $\text{L}^7\text{py}_2^{6\text{-MeO}}$  ( $\text{L}^7\text{py}_2^{\text{H}}$  = 1,4-bis(2-pyridylmethyl)-1,4-diazepane; see Scheme 3.2).<sup>20</sup> By changing the substituent on the pyridine ring, the spectroscopic properties and stability of these peroxomanganese(III) complexes were perturbed. For  $[\text{Mn}^{\text{III}}(\text{O}_2)(\text{L}^7\text{py}_2^{\text{H}})]^+$  and  $[\text{Mn}^{\text{III}}(\text{O}_2)(\text{L}^7\text{py}_2^{6\text{-Me}})]^+$ , these spectroscopic changes were linked to the geometric and electronic structure of the  $\text{Mn}^{\text{III}}\text{-O}_2$  unit. Specifically we proposed that the inclusion of the electron donating methyl-substituents lead to an elongation in one of the Mn-O bonds, affording a more asymmetric, end-on binding mode. In accordance with the reactivity studies described above, this should render the peroxo in  $[\text{Mn}^{\text{III}}(\text{O}_2)(\text{L}^7\text{py}_2^{6\text{-Me}})]^+$  more nucleophilic than that of  $[\text{Mn}^{\text{III}}(\text{O}_2)(\text{L}^7\text{py}_2^{\text{H}})]^+$ . To evaluate this prediction and further explore steric and electronic influences on reactivity, we performed systematic ligand modifications by altering i) the nature and location of pyridine ring substituents, ii) the size of the diazacycloalkane backbone, and iii) the type of N-ligand from pyridine to quinoline (Scheme 3.2). The structures of the  $\text{Mn}^{\text{II}}$  precursors were solved by X-ray diffraction, and their geometries report the effects of these ligand perturbations. In cases where these new ligands supported stable peroxomanganese(III) adducts, these species were reacted with CCA to determine the effect of ligand modifications on the rate of CCA deformylation. Unlike previous observations, CCA deformylation by the  $\text{Mn}^{\text{III}}\text{-O}_2$  units in these complexes appears to be largely influence by the sterics of the supporting ligand.

Scheme 3.2.



### 3.2 Results and discussion.

To complement our previously reported peroxomanganese(III) complexes generated using the  $L^7py_2^H$ ,  $L^7py_2^{6-Me}$ , and  $L^7py_2^{6-MeO}$  ligands,<sup>20</sup> we assembled five new  $Mn^{II}$  complexes using the  $L^6py_2^H$ ,  $L^7py_2^{4-Me}$ ,  $L^7q_2$ ,  $L^8py_2^H$  and  $L^8py_2^{6-Me}$  ligands (Scheme 3.2). With these new ligands, our initial objective was to assess the effects of four variables on the stability and reactivity of the  $Mn^{III}-O_2$  unit. These variables are i) nature of the pyridine substituent ( $L^7py_2^H$  versus  $L^7py_2^{6-Me}$  and  $L^8py_2^H$  versus  $L^8py_2^{6-Me}$ ), ii) position of the pyridine substituent ( $L^7py_2^{6-Me}$  versus  $L^7py_2^{4-Me}$ ), iii) size of the diazacycloalkane backbone ( $L^6py_2$  versus  $L^7py_2$  and  $L^8py_2$ ), and iv) identity of the N-donor ligand ( $L^7py_2$  versus  $L^7q_2$ ).

**3.2.1 Structural properties of  $Mn^{II}$  complexes.** Figure 3.1 displays ORTEP diagrams for the five manganese(II) complexes  $[Mn^{II}(L^6py_2^H)(NCMe)_3](ClO_4)_2$ ,  $[Mn^{II}(L^7py_2^{4-Me})(OTf)_2]$ ,  $[Mn^{II}(L^7q_2)(ClO_4)_2]$ ,  $[Mn^{II}(L^8py_2^H)(ClO_4)_2]$ , and  $[Mn^{II}(L^8py_2^{6-Me})(OTf)_2]$ . Selected bond

distances are given in Table 3.1. For each of the five complexes, the linear, tetradentate ligand is bound in the *trans* conformation, creating two axial coordination sites occupied by solvent ( $L^6py_2^H$ ) or anionic ligands ( $ClO_4^-$  for  $L^7q_2$  and  $L^8py_2^H$ , and  $OTf^-$  for  $L^7py_2^{4-Me}$  and  $L^8py_2^{6-Me}$ ). In the case of  $[Mn^{II}(L^6py_2^H)(NCMe)_3](ClO_4)_2$ , a seventh ligand is bound in the equatorial plane, giving a near pentagonal bipyramidal geometry around the Mn(II) center. For all the complexes, the  $Mn^{II}$ –ligand bond lengths range from  $\sim 2.1$  to  $2.5 \text{ \AA}$ , indicative of high-spin  $Mn^{II}$  centers.

The differences in geometry of the  $Mn^{II}$  complexes supported by the  $L^6py_2^H$ ,  $L^7py_2^H$ , and  $L^8py_2^H$  ligands are directly related to the variation in diazacycloalkane ring size. The  $[Mn^{II}(L^8py_2^H)(ClO_4)_2]$  complex is six-coordinate, while the corresponding  $L^7py_2^H$  and  $L^6py_2^H$  complexes display seven-coordinate  $Mn^{II}$  centers. Although heptacoordinate  $Mn^{II}$  complexes are not unusual,<sup>25-28</sup> they are far less common than six-coordinate analogues. We attribute the structural differences among these ligands to the variation in N3–Mn–N4 bite angle as a function of the diazacycloalkane ring size (although the identity of the X ligand, NCMe or  $ClO_4^-$ , will also be important). When bound to the  $Mn^{II}$  center, the  $L^6py_2^H$  ligand creates a N3–Mn–N4 bite angle of  $62.8^\circ$ , which is smaller than those of the corresponding  $L^7py_2^H$  and  $L^8py_2^H$  complexes ( $67.4^\circ$  and  $78.1^\circ$ , respectively). Equatorial angles of  $72^\circ$  are expected for idealized pentagonal bipyramidal complexes, consistent with  $[Mn^{II}(L^6py_2^H)(NCMe)_3]^{2+}$  and  $[Mn^{II}(L^7py_2^H)(NCMe)_3]^{2+}$  being seven-coordinate. The bite angles also offer a rationale for the smaller meridional Mn–NCMe bond length for  $[Mn^{II}(L^6py_2^H)(NCMe)_3]^{2+}$  compared with  $[Mn^{II}(L^7py_2^H)(NCMe)_3]^{2+}$  ( $2.37$  versus  $2.48 \text{ \AA}$ , respectively; see Mn–X<sub>3</sub> in Table 3.1). Binding of a fifth equatorial ligand is also associated with significant canting of the pyridines, as assessed by the torsional angle resulting from the two planes of the pyridine rings (Table 3.1). This canting is nicely illustrated pictorially in the space-filling model of  $[Mn^{III}(L^6py_2^H)]^{2+}$  shown in Figure 3.1F.

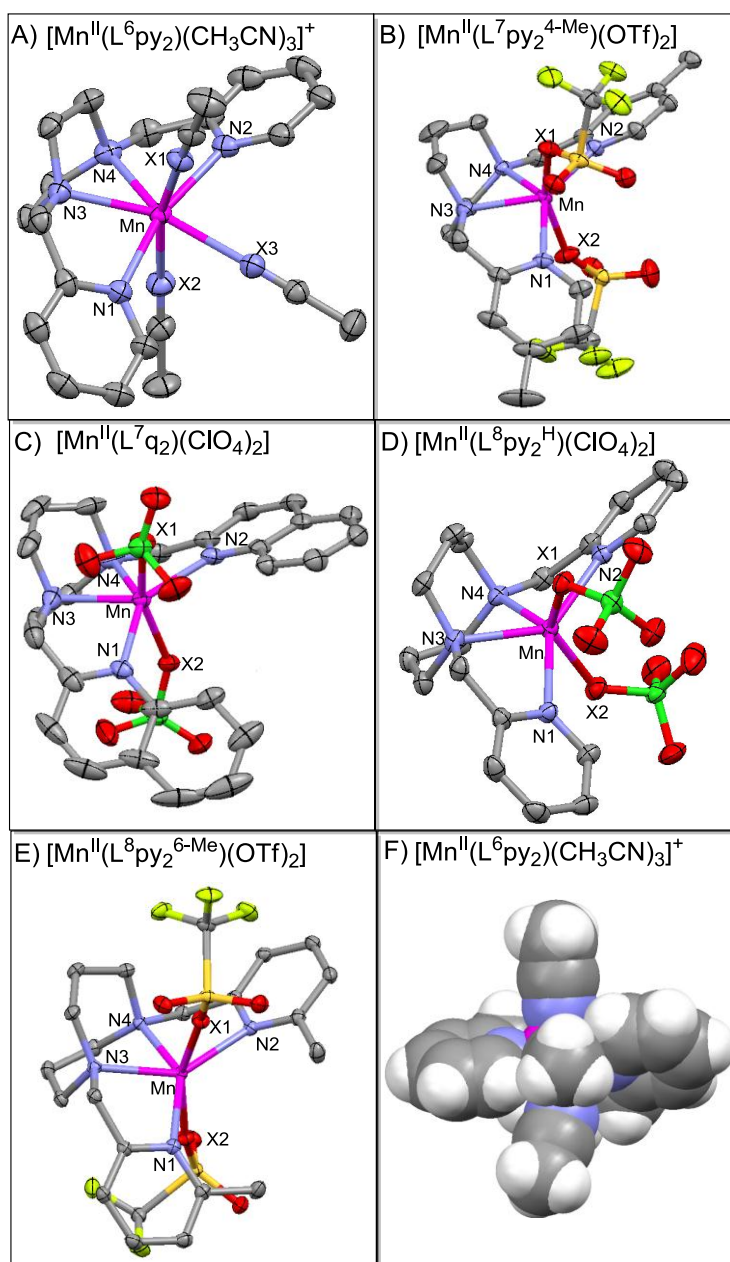


**Figure 3.1.** ORTEP diagrams of A)  $[\text{Mn}^{\text{II}}(\text{L}^6\text{py}_2^{\text{H}})(\text{NCMe})_3](\text{ClO}_4)_2$ , B)  $[\text{Mn}^{\text{II}}(\text{L}^7\text{py}_2^{4-\text{Me}})(\text{OTf})_2]$ , C)  $[\text{Mn}^{\text{II}}(\text{L}^7\text{q}_2)(\text{ClO}_4)_2]$ , D)  $[\text{Mn}^{\text{II}}(\text{L}^8\text{py}_2^{\text{H}})(\text{ClO}_4)_2]$ , and E)  $[\text{Mn}^{\text{II}}(\text{L}^8\text{py}_2^{6-\text{Me}})(\text{OTf})_2]$  showing 50% probability thermal ellipsoids. F) Space filling model for  $[\text{Mn}^{\text{II}}(\text{L}^6\text{py}_2^{\text{H}})(\text{NCMe})_3]$  viewed along the Mn-X<sub>3</sub> axis. For ORTEP structures, hydrogen atoms and noncoordinating counteranions have been removed for clarity. Significant interatomic distances and angles are listed in Table 3.1.

**Table 3.1.** Selected Bond Lengths (Å) and Angles (°) for Manganese(II) Complexes.

Complex	Mn-N(1)	Mn-N(2)	Mn-N(3)	Mn-N(4)	Mn-X(1)	Mn-X(2)	Mn-X(3) <sup>a</sup>	N3-Mn-N4	C1-N1-Mn-N2-C11
[Mn <sup>II</sup> (L <sup>6</sup> py <sub>2</sub> <sup>H</sup> )(NCMe) <sub>3</sub> ](ClO <sub>4</sub> ) <sub>2</sub>	2.313(2)	2.307(2)	2.339(2)	2.360(3)	2.286(3) <sup>a</sup>	2.314(2) <sup>a</sup>	2.370(3)	62.82(8)	-57.0(3)
[Mn <sup>II</sup> (L <sup>7</sup> py <sub>2</sub> <sup>H</sup> )(NCMe) <sub>3</sub> ](ClO <sub>4</sub> ) <sub>2</sub> <sup>b</sup>	2.306(9)	2.308(3)	2.369(3)	2.357(3)	2.268(2) <sup>a</sup>	2.311(2) <sup>a</sup>	2.478(2)	67.40(1)	-66.3(6)
[Mn <sup>II</sup> (L <sup>7</sup> py <sub>2</sub> <sup>6-Me</sup> )(ClO <sub>4</sub> ) <sub>2</sub> ] <sup>b</sup>	2.283(2)	2.284(2)	2.306(9)	2.285(2)	2.212(2) <sup>c</sup>	2.280(2) <sup>a</sup>	NA	69.50(7)	-48.1(2)
[Mn <sup>II</sup> (L <sup>7</sup> py <sub>2</sub> <sup>4-Me</sup> )(OTf) <sub>2</sub> ]	2.216(2)	2.213(2)	2.288(2)	2.277(2)	2.198(2) <sup>d</sup>	2.235(2) <sup>d</sup>	NA	71.13(6)	-44.5(2)
[Mn <sup>II</sup> (L <sup>7</sup> py <sub>2</sub> <sup>6-MeO</sup> )(ClO <sub>4</sub> ) <sub>2</sub> ] <sup>b</sup>	2.176(2)	2.176(2)	2.308(2)	2.308(2)	2.278(2) <sup>c</sup>	2.278(2) <sup>c</sup>	NA	70.36(9)	-43.2(2)
[Mn <sup>II</sup> (L <sup>7</sup> q <sub>2</sub> )(ClO <sub>4</sub> ) <sub>2</sub> ]	2.226(2)	2.254(2)	2.274(2)	2.263(2)	2.209(1) <sup>c</sup>	2.282(1) <sup>c</sup>	NA	70.77(6)	-42.1(2)
[Mn <sup>II</sup> (L <sup>8</sup> py <sub>2</sub> <sup>H</sup> )(ClO <sub>4</sub> ) <sub>2</sub> ]	2.246(1)	2.257(1)	2.292(1)	2.320(1)	2.244(1) <sup>c</sup>	2.266(1) <sup>c</sup>	NA	78.08(5)	-68.7(1)
[Mn <sup>II</sup> (L <sup>8</sup> py <sub>2</sub> <sup>6-Me</sup> )(OTf) <sub>2</sub> ]	2.273(1)	2.273(1)	2.290(1)	2.290(1)	2.205(1) <sup>d</sup>	2.205(1) <sup>d</sup>	NA	76.27(4)	-62.2(1)

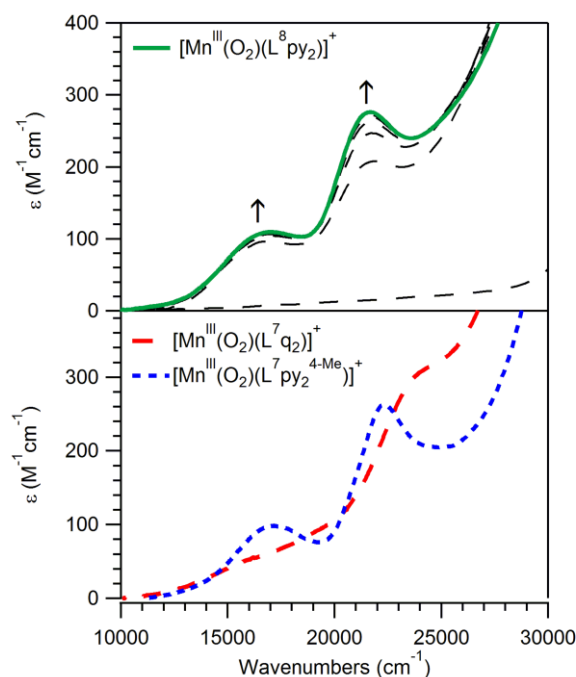
<sup>a</sup>X = N(CMe). <sup>b</sup>From reference 20. <sup>c</sup>X = O(ClO<sub>3</sub>)<sup>-</sup>. <sup>d</sup>X = O(Tf)<sup>-</sup>.

In all cases, the inclusion of pyridine substituents, or substitution of pyridines for quinolines, results in six-coordinate complexes. On the basis of their small N3–Mn–N4 bite angles of ~70° (Table 3.1), the Mn<sup>II</sup> complexes supported by the L<sup>7</sup>q<sub>2</sub> ligand and the substituted L<sup>7</sup>py<sub>2</sub><sup>R</sup> ligands (R = 6-Me, 6-MeO, and 4-Me) should be able to accommodate a fifth equatorial ligand. For the L<sup>7</sup>py<sub>2</sub><sup>6-Me</sup>, L<sup>7</sup>py<sub>2</sub><sup>6-MeO</sup>, and L<sup>7</sup>q<sub>2</sub> complexes, steric crowding of the equatorial plane hinders the binding of a seventh ligand. For the [Mn<sup>II</sup>(L<sup>7</sup>py<sub>2</sub><sup>4-Me</sup>)(OTf)<sub>2</sub>] complex, the lack of heptacoordination is tentatively attributed to the shorter Mn–N(pyridine) bonds relative to [Mn<sup>II</sup>(L<sup>7</sup>py<sub>2</sub><sup>H</sup>)(NCMe)<sub>3</sub>]<sup>2+</sup> (2.22 versus 2.31 Å, respectively; Table 3.1), which are due to the electron-donating 4-Me groups. These shorter distances for [Mn<sup>II</sup>(L<sup>7</sup>py<sub>2</sub><sup>4-Me</sup>)(OTf)<sub>2</sub>] further crowd the equatorial plane and lead to similar pyridine ring canting when compared with the L<sup>7</sup>py<sub>2</sub><sup>6-Me</sup> and L<sup>7</sup>py<sub>2</sub><sup>6-MeO</sup> analogues that must cant to avoid steric clashing between the 6-substituents. Space-filling models highlighting these effects are including in the appendix (Figure A3.1).

**3.2.2 Formation of peroxomanganese(III) complexes.** The absorption spectra of acetonitrile solutions of the five new manganese(II) complexes, [Mn<sup>II</sup>(L<sup>6</sup>py<sub>2</sub><sup>H</sup>)(NCMe)<sub>3</sub>]<sup>2+</sup>, [Mn<sup>II</sup>(L<sup>7</sup>py<sub>2</sub><sup>4-Me</sup>)(OTf)<sub>2</sub>], [Mn<sup>II</sup>(L<sup>7</sup>q<sub>2</sub>)(ClO<sub>4</sub>)<sub>2</sub>], [Mn<sup>II</sup>(L<sup>8</sup>py<sub>2</sub><sup>H</sup>)(ClO<sub>4</sub>)<sub>2</sub>], and [Mn<sup>II</sup>(L<sup>8</sup>py<sub>2</sub><sup>6-Me</sup>)(OTf)<sub>2</sub>], are



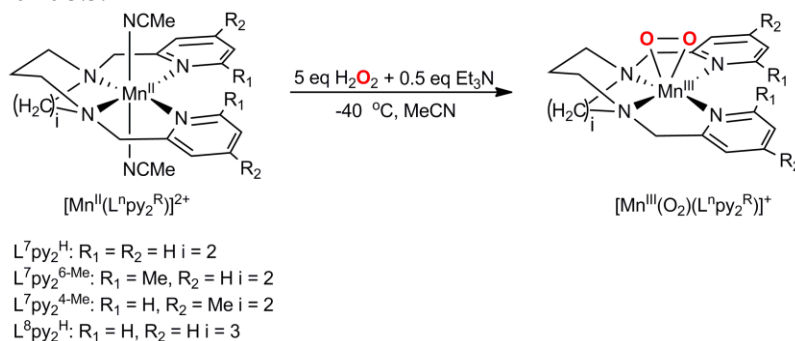
featureless at energies below  $33\,000\text{ cm}^{-1}$ , indicative of high spin  $\text{Mn}^{\text{II}}$  centers. Treatment of the  $[\text{Mn}^{\text{II}}(\text{L}^7\text{py}_2^{4\text{-Me}})]^{2+}$ ,  $[\text{Mn}^{\text{II}}(\text{L}^7\text{q}_2)]^{2+}$ , and  $[\text{Mn}^{\text{II}}(\text{L}^8\text{py}_2^{\text{H}})]^{2+}$  complexes with 5 equivalents  $\text{H}_2\text{O}_2$  and 0.5 equivalents triethylamine at  $-40\text{ }^\circ\text{C}$  results in the formation of new absorption features in the visible region (Figure 3.2 and Table 3.2). Mass spectrometry experiments on these colored solutions reveal major ion peaks consistent with  $[\text{Mn}^{\text{III}}(\text{O}_2)(\text{L}^7\text{py}_2^{4\text{-Me}})]^+$ ,  $[\text{Mn}^{\text{III}}(\text{O}_2)(\text{L}^7\text{q}_2)]^+$ , and  $[\text{Mn}^{\text{III}}(\text{O}_2)(\text{L}^8\text{py}_2^{\text{H}})]^+$ . Thus, these  $\text{Mn}^{\text{II}}$  centers form metastable  $\text{Mn}^{\text{III}}\text{-O}_2$  adducts when reacted with  $\text{H}_2\text{O}_2$  in the presence of base at low temperature (Scheme 3.3), consistent with a previous report on similar complexes.<sup>20</sup> While  $[\text{Mn}^{\text{II}}(\text{L}^8\text{py}_2^{6\text{-Me}})]^{2+}$  reacts with 5 equivalents  $\text{H}_2\text{O}_2$  and 0.5 equivalents triethylamine at  $-40\text{ }^\circ\text{C}$  to form a colored intermediate, the fleeting nature of this chromophore ( $t_{1/2} = \text{seconds}$  at  $-40\text{ }^\circ\text{C}$ ) prevented its further characterization. Notably,  $[\text{Mn}^{\text{II}}(\text{L}^6\text{py}_2^{\text{H}})]^{2+}$  showed no reaction under these conditions.



**Figure 3.2.** Top: Formation of  $[\text{Mn}^{\text{III}}(\text{O}_2)(\text{L}^8\text{py}_2^{\text{H}})]^+$  after the addition of 5 equivalents  $\text{H}_2\text{O}_2$  and 0.5 equivalents triethylamine of at  $-40\text{ }^\circ\text{C}$  in MeCN. Bottom: Electronic absorption spectra of  $[\text{Mn}^{\text{III}}(\text{O}_2)(\text{L}^7\text{q}_2)]^+$  and  $[\text{Mn}^{\text{III}}(\text{O}_2)(\text{L}^7\text{py}_2^{4\text{-Me}})]^+$  at  $-40\text{ }^\circ\text{C}$  in MeCN.

**Table 3.2.** Properties of Peroxomanganese(III) Complexes

complex	$\lambda_{\text{max}}$ ( $\text{cm}^{-1}$ ) ( $\epsilon(\text{M}^{-1} \text{cm}^{-1})$ )	$t_{1/2}$ at 0 $^{\circ}\text{C}$
$[\text{Mn}^{\text{III}}(\text{O}_2)(\text{L}^7\text{py}_2^{\text{H}})]^{+a}$	22 470 (280) 17 000 (120)	15 min
$[\text{Mn}^{\text{III}}(\text{O}_2)(\text{L}^7\text{py}_2^{6\text{-Me}})]^{+a}$	24 100 (280) ~16 130 (80)	6 min
$[\text{Mn}^{\text{III}}(\text{O}_2)(\text{L}^7\text{py}_2^{6\text{-MeO}})]^{+a}$	24 000 (250) 17 900 (80)	~ seconds
$[\text{Mn}^{\text{III}}(\text{O}_2)(\text{L}^7\text{py}_2^{4\text{-Me}})]^{+}$	22 470 (260) ~17 000 (100)	6 min
$[\text{M}^{\text{III}}(\text{O}_2)(\text{L}^7\text{q}_2)]^{+}$	24 050 (305) ~16 500 (70)	4 min
$[\text{Mn}^{\text{III}}(\text{O}_2)(\text{L}^8\text{py}_2^{\text{H}})]^{+}$	21 550 (280) 16 700 (120)	12 min

<sup>a</sup> From reference 20.**Scheme 3.3.**

The absorption maxima of  $[\text{Mn}^{\text{III}}(\text{O}_2)(\text{L}^7\text{py}_2^{4\text{-Me}})]^{+}$  and  $[\text{Mn}^{\text{III}}(\text{O}_2)(\text{L}^8\text{py}_2^{\text{H}})]^{+}$  are nearly identical to those of  $[\text{Mn}^{\text{III}}(\text{O}_2)(\text{L}^7\text{py}_2^{\text{H}})]^{+}$ , consisting of a weak feature at  $\sim 17\,000\text{ cm}^{-1}$  and a more intense band at  $\sim 22\,000\text{ cm}^{-1}$  (Table 3.2). In contrast, the absorption spectra of  $[\text{Mn}^{\text{III}}(\text{O}_2)(\text{L}^7\text{q}_2)]^{+}$  resembles that of  $[\text{Mn}^{\text{III}}(\text{O}_2)(\text{L}^7\text{py}_2^{6\text{-Me}})]^{+}$  and  $[\text{Mn}^{\text{III}}(\text{O}_2)(\text{L}^7\text{py}_2^{6\text{-MeO}})]^{+}$  ( $\lambda_{\text{max}} \approx 16\,000$  and  $24\,000\text{ cm}^{-1}$ ). Among this set of complexes, the common link between ligand structure and absorption maxima is steric bulk in the 6-position of the pyridine ring (assuming the quinoline as a “bulky” pyridine). With the aid of density functional theory (DFT) computations, we previously attributed differences in absorption and, especially, magnetic circular dichroism (MCD) spectra of  $[\text{Mn}^{\text{III}}(\text{O}_2)(\text{L}^7\text{py}_2^{\text{H}})]^{+}$  and  $[\text{Mn}^{\text{III}}(\text{O}_2)(\text{L}^7\text{py}_2^{6\text{-Me}})]^{+}$  to a

change from a side-on-bound peroxo ligand with identical Mn–O<sub>peroxo</sub> distances of 1.87 Å in the former complex to a more end-on peroxo with Mn–O<sub>peroxo</sub> distances of 1.87 and 1.91 Å in the latter species.<sup>20</sup> It was suggested that the increased Lewis acidity of the manganese center in [Mn<sup>III</sup>(O<sub>2</sub>)(L<sup>7</sup>py<sub>2</sub><sup>6-Me</sup>)]<sup>+</sup> led to the longer, asymmetric Mn–O<sub>peroxo</sub> bond lengths. The data presented in Table 3.2 suggests an alternative explanation. The inclusion of bulky groups in the 6-position is expected to cause significant canting of the pyridine rings, as evidence in the XRD structures of the Mn<sup>II</sup> complexes (Figure 3.1 and Table 3.1). This increased canting causes the 6-substituents to partially block the axial positions, sterically disfavoring the formation of a symmetric, side-on peroxo ligand in the L<sup>7</sup>py<sub>2</sub><sup>6-Me</sup>, L<sup>7</sup>py<sub>2</sub><sup>6-MeO</sup>, and L<sup>7</sup>q<sub>2</sub> complexes. Importantly, this model would also account for the similarities of the absorption maxima of the [Mn<sup>III</sup>(O<sub>2</sub>)(L<sup>7</sup>py<sub>2</sub><sup>H</sup>)]<sup>+</sup> and [Mn<sup>III</sup>(O<sub>2</sub>)(L<sup>7</sup>py<sub>2</sub><sup>4-Me</sup>)]<sup>+</sup> complexes.

**3.2.3 Reactivity of peroxomanganese(III) complexes.** The addition of excess CCA to the green acetonitrile solution of [Mn<sup>III</sup>(O<sub>2</sub>)(L<sup>7</sup>py<sub>2</sub><sup>H</sup>)]<sup>+</sup> at -40 °C, led to the disappearance of the characteristic visible bands at 22 300 and 17 050 cm<sup>-1</sup>, indicating the decay of the peroxomanganese(III) complex (Figure 3.3A). This decay followed pseudo-first order behavior when excess CCA was used. By plotting the range of pseudo-first order rate constants (*k*<sub>obs</sub>) as a function of CCA concentration, we determined a second-order-rate constant (*k*<sub>2</sub>) of 3.11 M<sup>-1</sup> min<sup>-1</sup> at -40 °C (Figure 3.3B). Reactions performed with either perchlorate or triflate as counteranion displayed identical rates. The organic product of this reaction was determined by GC-MS, and cyclohexanone was identified in ~50% yield based on the concentration of the peroxomanganese(III) complex. The formation of a ketone product in aldehyde deformylation has been previously observed for other peroxoiron(III)<sup>23,24</sup> and peroxomanganese(III)<sup>17</sup> complexes.

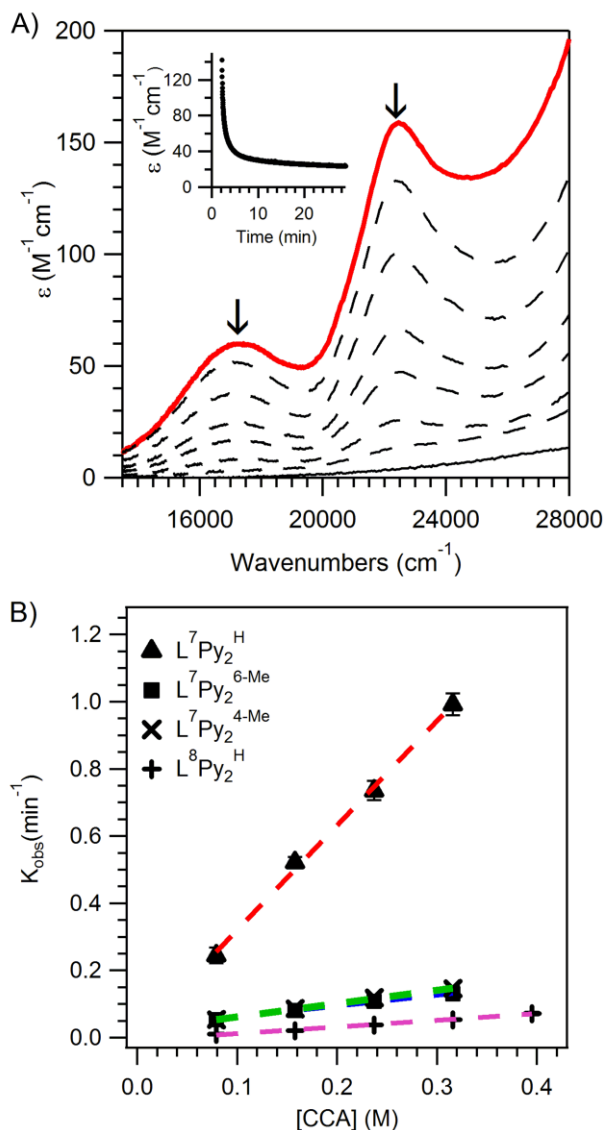


**Figure 3.3.** A) Electronic absorption spectral changes for  $[\text{Mn}^{\text{III}}(\text{O}_2)(\text{L}^7\text{py}_2^{\text{H}})]^+$  (2.5 mM) upon addition of cyclohexanecarboxaldehyde (60 equivalents, 150 mM) at  $-40^\circ\text{C}$  in MeCN. Insert shows the time course of the absorbance at  $23\,000\text{ cm}^{-1}$ . B)  $k_{\text{obs}}$  versus cyclohexanecarboxaldehyde concentration. Error bars represent two standard deviations determined from 3 or 4 replicate experiments.

To date the most reactive peroxomanganese(III) complex for CCA deformylation is  $[\text{Mn}^{\text{III}}(\text{O}_2)(13\text{-TMC})(\text{N}_3)]$ .<sup>16</sup> Using the  $\Delta H^\ddagger$  and  $\Delta S^\ddagger$  values reported for this reaction, we estimate a  $k_2$  value of  $\sim 220\text{ M}^{-1}\text{ min}^{-1}$  at  $-40^\circ\text{C}$ , which is 100-fold larger than that of  $[\text{Mn}^{\text{III}}(\text{O}_2)(\text{L}^7\text{py}_2^{\text{H}})]^+$ . On the basis of this comparison, as well as the other reactivity data reported by Nam *et al.* for the series of  $[\text{Mn}^{\text{III}}(\text{O}_2)(13\text{-TMC})(\text{X})]$  complexes,<sup>16</sup> this implies that the  $k_2$  value of

$[\text{Mn}^{\text{III}}(\text{O}_2)(\text{L}^7\text{py}_2^{\text{H}})]^+$  is comparable to that of  $[\text{Mn}^{\text{III}}(\text{O}_2)(13\text{-TMC})(\text{CN})]$  and  $10^2$ -fold greater than that of the parent complex,  $[\text{Mn}^{\text{III}}(\text{O}_2)(13\text{-TMC})]^+$ . Thus,  $[\text{Mn}^{\text{III}}(\text{O}_2)(\text{L}^7\text{py}_2^{\text{H}})]^+$  represents the fastest  $\text{Mn}^{\text{III}}\text{-O}_2$  CCA deformylation agent lacking an anionic ligand.

**Table 3.3.** Second-Order-Rate Constants for CCA Deformylation at  $-40^\circ\text{C}$ .

complex	$k_2 (\text{M}^{-1}\text{min}^{-1})$
$[\text{Mn}^{\text{III}}(\text{O}_2)(\text{L}^7\text{py}_2^{\text{H}})]^+$	3.1
$[\text{Mn}^{\text{III}}(\text{O}_2)(\text{L}^7\text{py}_2^{6\text{-Me}})]^+$	0.32
$[\text{Mn}^{\text{III}}(\text{O}_2)(\text{L}^7\text{py}_2^{4\text{-Me}})]^+$	0.40
$[\text{Mn}^{\text{III}}(\text{O}_2)(\text{L}^8\text{py}_2^{\text{H}})]^+$	0.19

The nucleophilic nature of the aldehyde deformylation reaction was confirmed by reacting  $[\text{Mn}^{\text{III}}(\text{O}_2)(\text{L}^7\text{py}_2^{\text{H}})]^+$  with *para*-substituted benzaldehydes (Cl, H, Me, and OMe). Because the deformylation reaction presumably involves nucleophilic attack of the peroxo on the carbonyl carbon on the aldehyde, electron withdrawing groups on the substrate should make the reaction more facile. The  $k_{\text{obs}}$  values for all four *para*-substituted benzaldehydes were determined under invariant conditions of temperature and concentration. The *para*-substituents were found to affect  $k_{\text{obs}}$  in the manner expected for a nucleophilic reaction (*i.e.*,  $k_{\text{obs}}$  increased with increasing electron-withdrawing properties:  $\text{Cl} > \text{H} > \text{Me} > \text{OMe}$ ). Indeed, the plot of  $\log k_{\text{obs}}$  versus Hammett constants ( $\sigma_{\text{p}}$ ) are linear with a  $\rho$  value of 1.25, as shown in Figure 3.4. Similar values for  $\rho$  have been observed for other nucleophilic aldehyde deformylation reactions.<sup>16</sup>

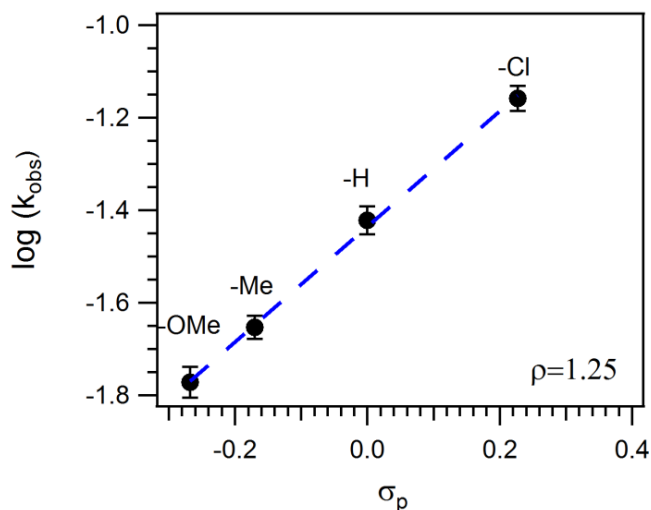


**Figure 3.4.** Hammett correlation of the reaction with para-substituted benzaldehydes with  $[\text{Mn}^{\text{III}}(\text{O}_2)(\text{L}^7\text{py}_2^{\text{H}})]^+$ . Error bars represent two standard deviations from three replicate experiments.

The other three  $\text{Mn}^{\text{III}}\text{-O}_2$  complexes  $[\text{Mn}^{\text{III}}(\text{O}_2)(\text{L}^7\text{py}_2^{6\text{-Me}})]^+$ ,  $[\text{Mn}^{\text{III}}(\text{O}_2)(\text{L}^7\text{py}_2^{4\text{-Me}})]^+$ , and  $[\text{Mn}^{\text{III}}(\text{O}_2)(\text{L}^8\text{py}_2^{\text{H}})]^+$  were reacted with CCA in a similar manner, and in each case cyclohexanone was observed as the organic product. The second-order-rate constants are less than that for  $[\text{Mn}^{\text{III}}(\text{O}_2)(\text{L}^7\text{py}_2^{\text{H}})]^+$  by an order of magnitude (Table 3.3). Because the rate of aldehyde deformylation is expected to increase as the nucleophilicity of the peroxo ligand increases,<sup>16,23</sup> it is initially surprising that the  $[\text{Mn}^{\text{III}}(\text{O}_2)(\text{L}^7\text{py}_2^{6\text{-Me}})]^+$  and  $[\text{Mn}^{\text{III}}(\text{O}_2)(\text{L}^7\text{py}_2^{4\text{-Me}})]^+$  complexes, which bear pyridine rings with electron-donating methyl groups, exhibit smaller second-order-rate constants than  $[\text{Mn}^{\text{III}}(\text{O}_2)(\text{L}^7\text{py}_2^{\text{H}})]^+$ . We attribute this to steric hindrance of CCA-peroxo interactions caused by canting of the pyridine rings ( $\text{L}^7\text{py}_2^{6\text{-Me}}$  and  $\text{L}^7\text{py}_2^{4\text{-Me}}$ ) or the presence of the bulkier 8-membered diazacycloalkane backbone ( $\text{L}^8\text{py}_2^{\text{H}}$ ). In support, Figure 3.5 shows space-filling models of  $[\text{Mn}^{\text{III}}(\text{O}_2)(\text{L}^7\text{py}_2^{\text{H}})]^+$ ,  $[\text{Mn}^{\text{III}}(\text{O}_2)(\text{L}^7\text{py}_2^{6\text{-Me}})]^+$  and  $[\text{Mn}^{\text{III}}(\text{O}_2)(\text{L}^7\text{py}_2^{4\text{-Me}})]^+$  complexes developed using density functional theory (DFT) geometry optimization. The peroxo ligand in the optimized model of  $[\text{Mn}^{\text{III}}(\text{O}_2)(\text{L}^7\text{py}_2^{\text{H}})]^+$  is the most

exposed, whereas the peroxo groups in the other complexes are buffeted by the canting of the pyridine rings.

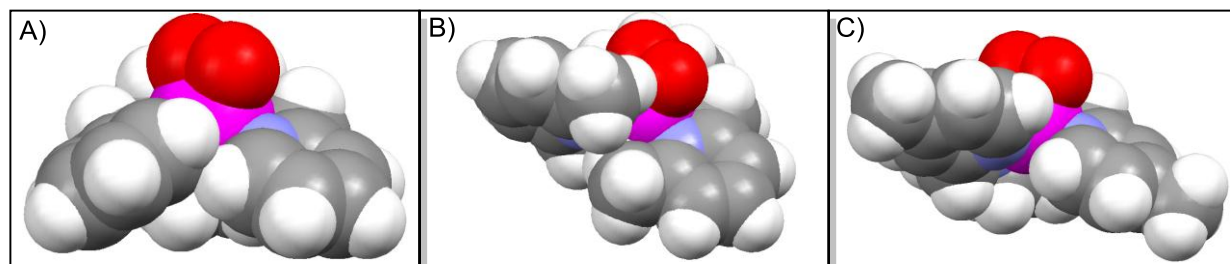


**Figure 3.5.** Space filling models for A)  $[\text{Mn}^{\text{III}}(\text{O}_2)(\text{L}^7\text{py}_2^{\text{H}})]^+$ , B)  $[\text{Mn}^{\text{III}}(\text{O}_2)(\text{L}^7\text{py}_2^{6\text{-Me}})]^+$ , and C)  $[\text{Mn}^{\text{III}}(\text{O}_2)(\text{L}^7\text{py}_2^{4\text{-Me}})]^+$  based on structures derived from DFT energy minimizations.

### 3.3 Summary.

Because peroxomanganese(III) intermediates play an important role in manganese-containing enzymes and small molecule oxidation catalysts, it is important to identify the factors affecting the nucleophilicity of the peroxo ligand. A characteristic reaction of synthetic peroxomanganese(III) complexes is aldehyde deformylation, which offers a convenient method for comparing relative reactivities of peroxomanganese(III) complexes supported by different ligands. Herein, we reported the X-ray structures of a series of  $\text{Mn}^{\text{II}}$  complexes with tetradentate dipyridyldiazacycloalkane ligands. Both the size of the diazacycloalkane backbone and the position and identity of the ring substituents have a large influence on the geometry of the  $\text{Mn}^{\text{II}}$  complex, with both seven- and six-coordinate complexes observed. Treatment of some of these  $\text{Mn}^{\text{II}}$  complexes with  $\text{H}_2\text{O}_2/\text{EtN}_3$  at  $-40\text{ }^\circ\text{C}$  resulted in the formation of peroxomanganese(III) adducts. The thermally stable complexes were treated with CCA to determine the effects of small ligand perturbations on the reactivity of the peroxo group.  $[\text{Mn}^{\text{III}}(\text{O}_2)(\text{L}^7\text{py}_2^{\text{H}})]^+$  was observed to have the largest second-order rate constant ( $k_2$ ), by an order of magnitude, compared to the other complexes. This result was initially surprising because the electron rich  $\text{L}^7\text{py}_2^{4\text{-Me}}$

and  $L^7py_2^{6-Me}$  ligands were expected to increase the nucleophilicity of the peroxo.  $[Mn^{III}(O_2)(L^8py_2^H)]^+$  was observed to have the slowest  $k_2$  value. The decrease in  $k_2$  values was attributed to the steric hindrance of nucleophilic attack of the peroxo ligand on the carbonyl carbon of the aldehyde. This is the first observation of steric hindrance in aldehyde deformylation reaction for a series of  $Mn^{III}-O_2$  complexes.

### 3.4 Material and Methods.

**3.4.1 Materials.** All chemicals were obtained from commercial vendors at ACS reagent-grade or better and were used without further purification except for CCA. Fractional distillation at 43 °C was performed under reduced pressure (10 torr) to remove acid impurities from CCA. All solvents were dried by routine techniques under an inert argon atmosphere.<sup>29</sup> Unless otherwise stated, manipulations of  $Mn^{II}$  complexes were carried out under argon using a glovebox or Schlenk techniques.

**3.4.2 Instrumentation.**  $^1H$  NMR spectra were obtained on a Bruker DRX 400 MHz NMR spectrometer. Electronic absorption spectra were recorded on a Cary 50 Bio spectrophotometer (Varian) or an Agilent 8453 spectrometer, each of which is interfaced with a Unisoku cryostat (USP-203-A). ESI-mass spectrometry experiments were performed using an LCT Primers MicroMass electrospray-ionization time-of-flight instrument. Elemental analysis was performed by Columbia Analytical Services, Tucson AZ. The gas chromatography-mass spectrometric data were collected on an Agilent 6890N Gas Chromatograph interfaced with quadrupole mass analyzer (Quattro Micro GC, Waters Corporation, Milford MA). A 5% phenyl, methyl silicone stationary phase (HP-5MS), 15 meter column with a 0.25" ID was used. The carrier gas was helium and constant flow mode was used to maintain 1.5 ml/min. Injections of 1.0  $\mu$ l were made



into the injector port heated to 240 °C and a split ratio of 20:1 was used. The GC thermal gradient was an initial 30 °C with a 1 minute hold after which the temperature was increased 15 °C/min to a final temperature of 300 °C and held for 2 minutes. Ionization was by electron impact at 70 eV and the mass analyzer scanned from 45 to 600 u in 0.5 seconds. The analyzers were tuned to 0.6 u FWHH and data collected in centroid mode.

**3.4.3 Ligand Synthesis.** 1,4-bis(2-pyridinylmethyl)piperazine ( $L^6\text{py}_2^H$ ), 1,4-bis(2-pyridylmethyl)-1,4-diazepane ( $L^7\text{py}_2^H$ ) and 1,4-bis(6-methyl-2-pyridylmethyl)-1,4-diazepane ( $L^7\text{py}_2^{6-\text{Me}}$ ) were prepared as previously described.<sup>30,31</sup> The ligands 1,4-bis(4-methyl-2-pyridylmethyl)-1,4-diazepane ( $L^7\text{py}_2^{4-\text{Me}}$ ) and 1,4-bis(2-quinolinylmethyl)-1,4-diazepane ( $L^7\text{q}_2$ ) were respectively prepared by reacting homopiperazine with 4-methylpicolinaldehyde or quinoline-2-carboxaldehyde (67% and 63% yield), using similar procedures. <sup>1</sup>H NMR data (400 MHz) for  $L^7\text{py}_2^{4-\text{Me}}$ , and  $L^7\text{q}_2$  are as follows:  $L^7\text{py}_2^{4-\text{Me}}$  ( $\text{CDCl}_3$ ;  $\delta$ ) 8.36 (d, 2H  $J_{\text{HH}} = 4.04$ ), 7.28 (s, 2H), 6.96 (br d, 2H,  $J_{\text{HH}} = 3.88$ ), 3.77 (s, 4H), 2.81 (t, 4H,  $J_{\text{HH}} = 4.84$ ), 2.77 (s, 4H), 2.34 (s, 6H) 1.85 (p, 2H,  $J_{\text{HH}} = 4.56$ );  $L^7\text{q}_2$  ( $\text{CDCl}_3$ ;  $\delta$ ) 8.12 - 8.05 (m, 4H), 7.79 - 7.65 (m, 6H), 7.51 - 7.49 (m, 2H), 3.99 (s, 4H), 2.85 (t, 4H,  $J_{\text{HH}} = 6.00$ ), 2.83 (s, 4H), 1.86 (p, 2H,  $J_{\text{HH}} = 6.44$ ). 1,5-bis(2-pyridylmethyl)-1,5-diazacyclooctane ( $L^8\text{py}_2^H$ ) was prepared by a previously reported substitution reaction, where 1,5-diazacyclooctane dihydrobromide is reacted with 2-picoly chloride hydrochloride.<sup>30</sup> 1,5-bis((6-methyl-2-pyridyl)methyl)-1,5-diazacyclooctane ( $L^8\text{py}_2^{6-\text{Me}}$ ) was prepared by the same procedure using 2-(bromomethyl)-6-methylpyridine (42% yield). <sup>1</sup>H NMR data (400 MHz)  $L^8\text{py}_2^{6-\text{Me}}$  are as follows: ( $\text{CDCl}_3$ ;  $\delta$ ) 7.55-7.51 (m, 2H), 7.34 (d, 2H,  $J_{\text{HH}} = 7.68$ ), 7.00 (d, 2H,  $J_{\text{HH}} = 7.48$ ), 3.79 (s, 4H), 2.79 (t, 8H,  $J_{\text{HH}} = 5.88$ ), 2.51 (s, 6H), 1.67 (p, 4H,  $J_{\text{HH}} = 5.84$ ).

**3.4.4 Preparation of Mn<sup>II</sup> Complexes.** *Caution! While no problems were encountered during this work, care should always be taken when handling perchlorate salts of metal complexes because of the possibility of explosion.* The [Mn<sup>II</sup>(L<sup>7</sup>py<sub>2</sub><sup>R</sup>)](ClO<sub>4</sub>)<sub>2</sub> (R = H and 6-Me) complexes were prepared by a previously reported metalation reaction.<sup>20</sup> The other metal complexes were synthesized with excellent yields (>85%) by reacting L<sup>6</sup>py<sub>2</sub><sup>H</sup>, L<sup>7</sup>py<sub>2</sub><sup>4-Me</sup>, L<sup>7</sup>q<sub>2</sub>, and L<sup>8</sup>py<sub>2</sub><sup>R</sup> (R = H and 6-Me) ligands with Mn(ClO<sub>4</sub>)<sub>2</sub> or Mn(OTf)<sub>2</sub> in MeCN solution in a 1:1 molar ratio. Mn(OTf)<sub>2</sub> was prepared by a previously reported procedure by reacting equimolar amounts of (CH<sub>3</sub>)<sub>3</sub>Si(OTf) and anhydrous MnCl<sub>2</sub>.<sup>15</sup> Details of a representative preparation for a metal complex are as followed. To a stirred solution of 277 mg (0.785 mmol) of Mn(OTf)<sub>2</sub> in 10 mL of MeCN was added L<sup>7</sup>q<sub>2</sub> (300 mg, 0.785 mmol) in 10 mL of MeCN. The yellow solution was stirred overnight and evaporated under reduced pressure. The solid thus obtained was dried in vacuo. Recrystallization of the crude solid from MeCN/diethyl ether afforded nearly colorless crystals of [Mn(L<sup>7</sup>q<sub>2</sub>)](OTf)<sub>2</sub>. (505 mg, 87%) [Found for [Mn(L<sup>7</sup>q<sub>2</sub>)](OTf)<sub>2</sub>: C<sub>27</sub>H<sub>26</sub>F<sub>6</sub>MnN<sub>4</sub>O<sub>6</sub>S<sub>2</sub>: C, 43.6; H, 3.5; N, 7.4% ; M<sup>+</sup> ([Mn(L<sup>7</sup>q<sub>2</sub>)](OTf))<sup>+</sup> 586.1. C<sub>27</sub>H<sub>26</sub>F<sub>6</sub>MnN<sub>4</sub>O<sub>6</sub>S<sub>2</sub> requires: C, 44.1; H, 3.6; N, 7.6% ; M<sup>+</sup>, 586.1], [Found for [Mn(L<sup>6</sup>py<sub>2</sub><sup>H</sup>)](OTf)<sub>2</sub>: C<sub>18</sub>H<sub>20</sub>F<sub>6</sub>MnN<sub>4</sub>O<sub>6</sub>S<sub>2</sub>: C, 34.4; H, 3.2; N, 8.8%; M<sup>+</sup> ([Mn(L<sup>6</sup>py<sub>2</sub><sup>H</sup>)](OTf))<sup>+</sup> 472.1. C<sub>18</sub>H<sub>20</sub>F<sub>6</sub>MnN<sub>4</sub>O<sub>6</sub>S<sub>2</sub> requires: C, 34.8; H, 3.2; N, 9.0% ; M<sup>+</sup>, 472.1], [Found for [Mn(L<sup>7</sup>py<sub>2</sub><sup>4-Me</sup>)](OTf)<sub>2</sub>: C<sub>21</sub>H<sub>26</sub>F<sub>6</sub>MnN<sub>4</sub>O<sub>6</sub>S<sub>2</sub>: C, 38.0; H, 3.8; N, 8.4% ; M<sup>+</sup> ([Mn(L<sup>7</sup>py<sub>2</sub><sup>4-Me</sup>)](OTf))<sup>+</sup> 514.1. C<sub>18</sub>H<sub>20</sub>F<sub>6</sub>MnN<sub>4</sub>O<sub>6</sub>S<sub>2</sub> requires: C, 38.0; H, 4.0; N, 8.4%; M<sup>+</sup>, 514.1], [Found for [Mn(L<sup>8</sup>py<sub>2</sub><sup>H</sup>)](OTf)<sub>2</sub>: C<sub>20</sub>H<sub>24</sub>F<sub>6</sub>MnN<sub>4</sub>O<sub>6</sub>S<sub>2</sub>: C, 37.1; H, 3.5; N, 8.5%; M<sup>+</sup> ([Mn(L<sup>8</sup>py<sub>2</sub><sup>H</sup>)](OTf))<sup>+</sup> 500.1. C<sub>20</sub>H<sub>24</sub>F<sub>6</sub>MnN<sub>4</sub>O<sub>6</sub>S<sub>2</sub> requires: C, 37.0; H, 3.7; N, 8.6% ; M<sup>+</sup>, 500.1], and [Found for [Mn(L<sup>8</sup>py<sub>2</sub><sup>6-Me</sup>)](OTf)<sub>2</sub>: C<sub>22</sub>H<sub>28</sub>F<sub>6</sub>MnN<sub>4</sub>O<sub>6</sub>S<sub>2</sub>: C, 39.0; H, 4.0; N, 8.2%;

$M^+$  ( $\{[Mn(L^7py_2^{4-Me})](OTf)]^+\}$ ) 514.1.  $C_{22}H_{28}F_6MnN_4O_6S_2$  requires: C, 39.0; H, 4.2; N, 8.3%;  $M^+$ , 514.1].

**3.4.5 X-ray Crystallography.** Single crystals of  $[Mn(L^6py_2^H)(CH_3CN)_3](ClO_4)_2$ ,  $[Mn(L^7py_2^{4-Me})(OTf)_2]$ ,  $[Mn(L^7q_2^H)(ClO_4)_2]$ ,  $[Mn(L^8py_2^H)(ClO_4)_2]$ , and  $[Mn(L^8py_2^{6-Me})(OTf)_2]$  were grown by vapor diffusion of ether into an MeCN solution of the complex at room temperature. Data collection and refinement parameters are summarized in the supporting information.

**3.4.6 In Situ Preparation of Peroxomanganese(III) Complexes.** The green peroxomanganese(III) intermediates were formed by treating a 2.5 mM MeCN solution of metal complex with 5 equivalents  $H_2O_2$  and 0.5 equivalents triethylamine at  $-40\text{ }^\circ\text{C}$ . The formation of the peroxomanganese(III) complexes was evident from the appearance of characteristic bands in the electronic absorption spectra and ESI-mass spectrometry. [Found  $M^+$   $\{[Mn^{III}(O_2)(L^7q_2)]^+\}$  : 469.1.  $\{[Mn^{III}(O_2)(L^7q_2)]^+\}$  requires:  $M^+$ , 469.1], [Found  $M^+$   $\{[Mn^{III}(O_2)(L^7py_2^{4-Me})]^+\}$  : 397.1.  $\{[Mn^{III}(O_2)(L^7py_2^{4-Me})]^+\}$  requires:  $M^+$ , 397.1], and [Found  $M^+$   $\{[Mn^{III}(O_2)(L^8py_2^H)]^+\}$  : 383.1.  $\{[Mn^{III}(O_2)(L^8py_2^H)]^+\}$  requires:  $M^+$ , 383.1]

**3.4.7 Kinetic and Reactivity Studies.** Kinetic analyses of aldehyde deformylation were carried out by adding excess CCA to 2.5 mM acetonitrile solutions of  $[Mn^{III}(O_2)(L^7py_2^R)]^+$  or  $[Mn^{III}(O_2)(L^8py_2^H)]^+$  and monitoring the time-dependent decay of the characteristic bands of the  $Mn^{III}-O_2$  intermediates at  $-40\text{ }^\circ\text{C}$  in MeCN. Kinetic measurements were made under pseudo-first-order conditions, which permitted the determination of  $k_{obs}$  values by fitting the decrease of absorption bands at  $\sim 23\ 000\text{ cm}^{-1}$ . Corresponding second-order-rate constants were obtained using  $k_{obs}$  values collected over a range of CCA concentrations. A 2.5 mM solution of  $[Mn^{III}(O_2)(L^7py_2^H)](OCIO_3)$  and  $[Mn^{III}(O_2)(L^7py_2^H)](OTf)$  was reacted with 120 equivalents of

CCA to compare if counter anion had any role on the pseudo first-order rate. The identity of the counteranion had no effect on the rate ( $k_{obs}$ ).

Product analysis was determined using GC-MS and percent yield was determined by comparing the ratio of the product to an internal standard and comparing the ratio to a standard curve for the product. A detailed procedure is as follows; a 10 mM solution of the metal complex solution was reacted with 120 equivalents of CCA at -40 °C. When the reaction was completed, it was allowed to warm to room temperature, and 1,2-dichlorobenzene was added as an internal standard.

The Hammett study was performed by reacting a 2.5 mM acetonitrile solution of  $[\text{Mn}^{\text{III}}(\text{O}_2)(\text{L}^7\text{py}_2^{\text{H}})]^+$  with benzaldehyde, 4-methylbenzaldehyde, 4-methoxybenzaldehyde, or 4-chlorobenzaldehyde under pseudo-first-order conditions, which permitted the determination of  $k_{obs}$  values by fitting the decrease absorption band at  $\sim 23\,000\text{ cm}^{-1}$ .

**3.4.8 Density Functional Theory Calculations.** The *ORCA* 2.7 software package was used for all DFT computations.<sup>32</sup> Initial models of  $[\text{Mn}^{\text{III}}(\text{O}_2)(\text{L}^7\text{py}_2^{\text{R}})]^+$  ( $\text{R} = \text{H}$ , 4-Me, and 6-Me) were built using the X-ray coordinates of the corresponding manganese(II) complexes, then adding side-on peroxo ligands, and then rotated the pyridines from a canted position to a planar position. Geometry optimizations for each model of the metal complexes were converged to the  $S = 2$  spin system. These calculations employed the Becke-Perdew (BP86) functional<sup>33,34</sup> and the SVP (Ahlich split valence polarized)<sup>35,36</sup> basis with the SV/C auxiliary basis for all atoms except for manganese, nitrogen, and oxygen, where the larger TZVP (Ahlich triple- $\zeta$  valence polarized)<sup>20</sup> basis in conjunction with the TZV/J auxiliary basis were used. The resolution of identity (RI) approximation, developed by Neese,<sup>37</sup> was used for all calculations. Solvation effects associated

with acetonitrile (dielectric constant  $\epsilon = 36.6$ ) were incorporated using COSMO, as implemented in *ORCA*.<sup>38</sup>

### 3.5 Supporting Information.

#### 3.5.1 Specific Details of XRD Data Collection and Analysis for

**[Mn(L<sup>6</sup>py<sub>2</sub>)(NCCH<sub>3</sub>)<sub>3</sub>][ClO<sub>4</sub>]<sub>2</sub>.** A colorless parallelepiped shaped crystal of [Mn(N<sub>4</sub>C<sub>16</sub>H<sub>20</sub>)(NCCH<sub>3</sub>)<sub>3</sub>][ClO<sub>4</sub>]<sub>2</sub> · CH<sub>3</sub>CN was cut from a larger single crystal. It was, at 173(2) K, triclinic, space group  $P\bar{1} - C_1^1$  (No. 2)<sup>39</sup> with  $a = 11.618(2)$  Å,  $b = 11.666(2)$  Å,  $c = 13.214(3)$  Å,  $\alpha = 88.508(2)^\circ$ ,  $\beta = 71.869(2)^\circ$ ,  $\gamma = 69.296(2)^\circ$ ,  $V = 1585.0(5)$  Å<sup>3</sup> and  $Z = 2$  molecules { $d_{\text{calcd}} = 1.438$  g/cm<sup>3</sup>;  $\mu_a(\text{MoK}\alpha) = 0.642$  mm<sup>-1</sup>}. A full hemisphere of diffracted intensities (1850 20-second frames with an  $\omega$  scan width of 0.30°) was measured for a single-domain specimen using graphite-monochromated MoK $\alpha$  radiation ( $\lambda = 0.71073$  Å) on a Bruker SMART APEX CCD Single Crystal Diffraction System<sup>40</sup>. X-rays were provided by a fine-focus sealed x-ray tube operated at 50kV and 30mA. Lattice constants were determined with the Bruker SAINT software package using peak centers for 3845 reflections. A total of 15336 integrated reflection intensities having  $2\theta(\text{MoK}\alpha) < 55.68^\circ$  were produced using the Bruker program SAINT<sup>41</sup>; 7423 of these were unique and gave  $R_{\text{int}} = 0.029$  with a coverage which was 98.3% complete. The data were corrected empirically for variable absorption effects using equivalent reflections; the relative transmission factors ranged from 0.872 to 1.000. The Bruker software package SHELXTL was used to solve the structure using “direct methods” techniques. All stages of weighted full-matrix least-squares refinement were conducted using  $F_o^2$  data with the SHELXTL Version 6.10 software package<sup>42</sup>.

The final structural model incorporated anisotropic thermal parameters for all

nonhydrogen atoms and isotropic thermal parameters for all hydrogen atoms. All methyl groups were incorporated into the structural model as rigid groups (using idealized  $sp^3$ -hybridized geometry and a C-H bond length of 0.98 Å) that were allowed to rotate about their C-C bonds during least squares refinement cycles. The remaining hydrogen atoms were included in the structural model as idealized atoms (assuming  $sp^2$ - or  $sp^3$ -hybridization of the carbon atoms and C-H bond lengths of 0.95 or 0.99 Å). The isotropic thermal parameters of all hydrogen atoms were fixed at values 1.2 (nonmethyl) or 1.5 (methyl) times the equivalent isotropic thermal parameter of the carbon atom to which they are covalently bonded. A total of 392 parameters were refined using no restraints, 7423 data and weights of  $w = 1 / [\sigma^2(F^2) + (0.0961 P)^2 + 0.6059 P]$  where  $P = [F_o^2 + 2F_c^2] / 3$ . Final agreement factors at convergence are:  $R_1$ (unweighted, based on  $F$ ) = 0.059 for 5916 independent absorption-corrected “observed” reflections having  $2\theta(\text{MoK}\alpha) < 55.68^\circ$  and  $I > 2\sigma(I)$ ;  $R_1$ (unweighted, based on  $F$ ) = 0.073 and  $wR_2$ (weighted, based on  $F^2$ ) = 0.170 for all 7423 independent absorption-corrected reflections having  $2\theta(\text{MoK}\alpha) < 55.68^\circ$ . The largest shift/s.u. was 0.000 in the final refinement cycle. The final difference map had maxima and minima of 0.84 and -0.71  $e/\text{\AA}^3$ , respectively.

**3.5.2 Specific Details of XRD Data Collection and Analysis for  $[\text{Mn}(\text{L}^7\text{py}_2^{4\text{-Me}})(\text{ClO}_4)_2]$ .** A colorless parallelepiped shaped crystal of  $[\text{Mn}(\text{C}_{19}\text{H}_{26}\text{N}_4)(\text{O}_3\text{SCF}_3)_2]$  was cut from a larger single crystal. It was, at 100(2) K, monoclinic, space group  $P2_1/c - C_{2h}^5$  (No. 14)<sup>39</sup> with  $a = 16.801(7)$  Å,  $b = 8.582(4)$  Å,  $c = 19.054(8)$  Å,  $\beta = 99.020(7)^\circ$ ,  $V = 2713(2)$  Å<sup>3</sup> and  $Z = 4$  molecules  $\{d_{\text{calcd}} = 1.624 \text{ g/cm}^3; \mu_a(\text{MoK}\alpha) = 0.726 \text{ mm}^{-1}\}$ . A full hemisphere of diffracted intensities (1850 10-second frames with an  $\omega$  scan width of  $0.30^\circ$ ) was measured for a single-domain specimen using graphite-monochromated MoK $\alpha$  radiation ( $\lambda = 0.71073$  Å) on a Bruker SMART APEX CCD

Single Crystal Diffraction System<sup>40</sup>. X-rays were provided by a fine-focus sealed x-ray tube operated at 50kV and 30mA. Lattice constants were determined with the Bruker SAINT software package using peak centers for 5226 reflections. A total of 24171 integrated reflection intensities having  $2\theta(\text{MoK}\alpha) < 58.31^\circ$  were produced using the Bruker program SAINT<sup>41</sup>; 6823 of these were unique and gave  $R_{\text{int}} = 0.041$  with a coverage which was 93.3% complete. The data were corrected empirically for variable absorption effects using equivalent reflections; the relative transmission factors ranged from 0.810 to 1.000. The Bruker software package SHELXTL was used to solve the structure using “direct methods” techniques. All stages of weighted full-matrix least-squares refinement were conducted using  $F_o^2$  data with the SHELXTL Version 6.10 software package<sup>42</sup>.

The final structural model incorporated anisotropic thermal parameters for all nonhydrogen atoms and isotropic thermal parameters for all hydrogen atoms. All methyl groups were incorporated into the structural model as rigid groups (using idealized  $sp^3$ -hybridized geometry and a C-H bond length of 0.98 Å) that were allowed to rotate about their C-C bonds during least squares refinement cycles. The remaining hydrogen atoms were included in the structural model as idealized atoms (assuming  $sp^2$ - or  $sp^3$ -hybridization of the carbon atoms and C-H bond lengths of 0.95 or 0.99 Å). The isotropic thermal parameters of all hydrogen atoms were fixed at values 1.2 (nonmethyl) or 1.5 (methyl) times the equivalent isotropic thermal parameter of the carbon atom to which they are covalently bonded. A total of 363 parameters were refined using no restraints, 6823 data and weights of  $w = 1 / [\sigma^2(F^2) + (0.0692 P)^2 + 0.3317 P]$  where  $P = [F_o^2 + 2F_c^2] / 3$ . Final agreement factors at convergence are:  $R_1$ (unweighted, based on  $F$ ) = 0.043 for 5777 independent absorption-corrected “observed” reflections having  $2\theta(\text{MoK}\alpha) < 58.31^\circ$  and  $I > 2\sigma(I)$ ;  $R_1$ (unweighted, based on  $F$ ) = 0.050 and  $wR_2$ (weighted, based

on  $F^2$ ) = 0.118 for all 6823 independent absorption-corrected reflections having  $2\theta(\text{MoK}\alpha) < 58.31^\circ$ . The largest shift/s.u. was 0.000 in the final refinement cycle. The final difference map had maxima and minima of 1.46 and  $-0.67 \text{ e}^-/\text{\AA}^3$ , respectively.

**3.5.3 Specific Details of XRD Data Collection and Analysis for  $[\text{Mn}(\text{L}^7\text{q}_2)(\text{ClO}_4)_2]$ .** A colorless near cube-shaped crystal of  $[\text{Mn}(\text{N}_4\text{C}_{25}\text{H}_{26})][\text{ClO}_4]_2$  was cut from a larger single crystal. It was, at 100(2) K, monoclinic, space group  $\text{P2}_1/\text{c} - \text{C}_{2\text{h}}^5$  (No. 14)<sup>39</sup> with  $\mathbf{a} = 9.012(2) \text{ \AA}$ ,  $\mathbf{b} = 8.305(2) \text{ \AA}$ ,  $\mathbf{c} = 34.494(6) \text{ \AA}$ ,  $\beta = 92.618(3)^\circ$ ,  $V = 2578.9(8) \text{ \AA}^3$  and  $Z = 4$  molecules  $\{\text{d}_{\text{calcd}} = 1.639 \text{ g/cm}^3$ ;  $\mu_{\text{a}}(\text{MoK}\alpha) = 0.778 \text{ mm}^{-1}\}$ . A full hemisphere of diffracted intensities (1850 10-second frames with a  $\omega$  scan width of  $0.30^\circ$ ) was measured for a single-domain specimen using graphite-monochromated  $\text{MoK}\alpha$  radiation ( $\lambda = 0.71073 \text{ \AA}$ ) on a Bruker SMART APEX CCD Single Crystal Diffraction System<sup>40</sup>. X-rays were provided by a fine-focus sealed x-ray tube operated at 50kV and 30mA. Lattice constants were determined with the Bruker SAINT software package using peak centers for 8878 reflections. A total of 23188 integrated reflection intensities having  $2\theta((\text{MoK}\alpha) < 58.35^\circ$  were produced using the Bruker program SAINT<sup>41</sup>; 6423 of these were unique and gave  $R_{\text{int}} = 0.048$  with a coverage which was 92.0% complete. The data were corrected empirically for variable absorption effects using equivalent reflections; the relative transmission factors ranged from 0.900 to 1.000. The Bruker software package SHELXTL was used to solve the structure using “direct methods” techniques. All stages of weighted full-matrix least-squares refinement were conducted using  $F_o^2$  data with the SHELXTL Version 6.10 software package<sup>42</sup>.

The final structural model incorporated anisotropic thermal parameters for all nonhydrogen atoms and isotropic thermal parameters for all hydrogen atoms. The first



perchlorate anion is disordered with two preferred orientations about the Cl(1)-O(11) bond. Atomic positions for oxygen atoms O(12), O(13) and O(14) correspond to the major orientation and are occupied 53% of the time; atomic positions for oxygen atoms O(12'), O(13') and O(14') correspond to the minor orientation and are occupied 47% of the time. All hydrogen atoms were located in a difference Fourier and included in the structural model as independent isotropic atoms whose parameters were allowed to vary in least-squares refinement cycles. A total of 493 parameters were refined using no restraints, 6423 data and weights of  $w = 1 / [\sigma^2(F^2) + (0.0652 P)^2 + 0.3766 P]$ , where  $P = [Fo^2 + 2Fc^2] / 3$ . Final agreement factors at convergence are:  $R_1$ (unweighted, based on  $F$ ) = 0.044 for 5411 independent absorption-corrected “observed” reflections having  $2\theta(\text{MoK}\alpha) < 58.35^\circ$  and  $I > 2\sigma(I)$ ;  $R_1$ (unweighted, based on  $F$ ) = 0.053 and  $wR_2$ (weighted, based on  $F^2$ ) = 0.113 for all 6423 independent absorption-corrected reflections having  $2\theta(\text{MoK}\alpha) < 58.35^\circ$ . The largest shift/s.u. was 0.000 in the final refinement cycle. The final difference map had maxima and minima of 0.56 and -0.47  $e^-/\text{\AA}^3$ , respectively.

### 3.5.4 Specific Details of XRD Data Collection and Analysis for $[\text{Mn}(\text{L}^8\text{py}_2^{\text{H}})(\text{ClO}_4)_2]$ .

Colorless crystals of  $[\text{Mn}(\text{N}_4\text{C}_{18}\text{H}_{24})][\text{ClO}_4]_2$  are, at 173(2) K, monoclinic, space group  $P2_1/c - C_{2h}^5$  (No. 14)<sup>39</sup> with  $a = 14.731(2) \text{ \AA}$ ,  $b = 17.692(2) \text{ \AA}$ ,  $c = 8.752(1) \text{ \AA}$ ,  $\beta = 95.547(1)^\circ$ ,  $V = 2270.1(5) \text{ \AA}^3$  and  $Z = 4$  molecules  $\{d_{\text{calcd}} = 1.610 \text{ g/cm}^3; \mu_a(\text{MoK}\alpha) = 0.870 \text{ mm}^{-1}\}$ . A full hemisphere of diffracted intensities (1850 10-second frames with a  $\omega$  scan width of  $0.30^\circ$ ) was measured for a specimen using graphite-monochromated MoK $\alpha$  radiation ( $\lambda = 0.71073 \text{ \AA}$ ) on a Bruker SMART APEX CCD Single Crystal Diffraction System<sup>40</sup>. X-rays were provided by a fine-focus sealed x-ray tube operated at 50kV and 30mA. Lattice constants were determined with the Bruker SAINT software package using peak centers for 6611 reflections. A total of 18486 integrated reflection intensities having  $2\theta(\text{MoK}\alpha) < 59.14^\circ$  were produced using the

Bruker program SAINT<sup>41</sup>; 6352 of these were unique and gave  $R_{\text{int}} = 0.036$  with a coverage which was 99.7% complete. The data were corrected empirically for variable absorption effects using equivalent reflections; the relative transmission factors ranged from 0.961 to 1.000. The Bruker software package SHELXTL was used to solve the structure using “direct methods” techniques. All stages of weighted full-matrix least-squares refinement were conducted using  $F_o^2$  data with the SHELXTL Version 6.10 software package<sup>42</sup>.

The final structural model incorporated anisotropic thermal parameters for all nonhydrogen atoms and isotropic thermal parameters for all hydrogen atoms. All hydrogen atoms were included in the structural model as idealized atoms (assuming  $sp^2$ - or  $sp^3$ -hybridization of the carbon atoms and C-H bond lengths of 0.95 or 0.99 Å). The isotropic thermal parameters of all hydrogen atoms were fixed at values 1.2 times the equivalent isotropic thermal parameter of the carbon atom to which they are covalently bonded. A total of 298 parameters were refined using no restraints, 6352 data and weights of  $w = 1 / [\sigma^2(F^2) + (0.0498 P)^2 + 0.9315 P]$ , where  $P = [F_o^2 + 2F_c^2] / 3$ . Final agreement factors at convergence are:  $R_1$ (unweighted, based on  $F$ ) = 0.037 for 5524 independent absorption-corrected “observed” reflections having  $2\theta(\text{MoK}\alpha) < 59.14^\circ$  and  $I > 2\sigma(I)$ ;  $R_1$ (unweighted, based on  $F$ ) = 0.043 and  $wR_2$ (weighted, based on  $F^2$ ) = 0.095 for all 6352 independent absorption-corrected reflections having  $2\theta(\text{MoK}\alpha) < 59.14^\circ$ . The largest shift/s.u. was 0.001 in the final refinement cycle. The final difference map had maxima and minima of 0.45 and -0.36  $e^-/\text{\AA}^3$ , respectively.

### 3.5.5 Specific Details of XRD Data Collection and Analysis for $[\text{Mn}(\text{L}^{\text{py}})_2^{\text{6-Me}}](\text{OTf})_2$ .

Colorless crystals of  $\text{Mn}(\text{C}_{20}\text{H}_{28}\text{N}_4)(\text{O}_3\text{SCF}_3)_2$  are, at 100(2) K, monoclinic, space group  $C2/c - C_{2h}^6$  (No. 15)<sup>39</sup> with  $a = 13.546(3)$  Å,  $b = 10.324(2)$  Å,  $c = 19.340(4)$  Å,  $\beta = 99.912(3)^\circ$ ,  $V =$

2664.4(8) Å<sup>3</sup> and  $Z = 4$  molecules { $d_{\text{calcd}} = 1.689 \text{ g/cm}^3$ ;  $\mu_a(\text{MoK}\alpha) = 0.741 \text{ mm}^{-1}$ }. A full hemisphere of diffracted intensities (1850 10-second frames with an  $\omega$  scan width of 0.30°) was measured for a single-domain specimen using graphite-monochromated MoK $\alpha$  radiation ( $\lambda = 0.71073 \text{ Å}$ ) on a Bruker SMART APEX CCD Single Crystal Diffraction System<sup>40</sup>. X-rays were provided by a fine-focus sealed x-ray tube operated at 50kV and 30mA. Lattice constants were determined with the Bruker SAINT software package using peak centers for 9403 reflections. A total of 11982 integrated reflection intensities having  $2\theta(\text{MoK}\alpha) < 58.21^\circ$  were produced using the Bruker program SAINT<sup>41</sup>; 3356 of these were unique and gave  $R_{\text{int}} = 0.052$  with a coverage which was 93.7% complete. The data were corrected empirically for variable absorption effects using equivalent reflections; the relative transmission factors ranged from 0.815 to 1.000. The Bruker software package SHELXTL was used to solve the structure using “direct methods” techniques. All stages of weighted full-matrix least-squares refinement were conducted using  $F_o^2$  data with the SHELXTL Version 6.10 software package<sup>42</sup>.

The final structural model incorporated anisotropic thermal parameters for all nonhydrogen atoms and isotropic thermal parameters for all hydrogen atoms. All hydrogen atoms were located from a difference Fourier and included in the structural model as independent isotropic atoms whose parameters were allowed to vary in least-squares refinement cycles. A total of 242 parameters were refined using no restraints, 3356 data and weights of  $w = 1 / [\sigma^2(F^2) + (0.0504 P)^2 + 2.1167 P]$  where  $P = [F_o^2 + 2F_c^2] / 3$ . Final agreement factors at convergence are:  $R_1(\text{unweighted, based on } F) = 0.030$  or 3223 independent absorption-corrected “observed” reflections having  $2\theta(\text{MoK}\alpha) < 58.21^\circ$  and  $I > 2\sigma(I)$ ;  $R_1(\text{unweighted, based on } F) = 0.031$  and  $wR_2(\text{weighted, based on } F^2) = 0.085$  for all 3356 independent absorption-corrected reflections having  $2\theta(\text{MoK}\alpha) < 58.21^\circ$ . The largest shift/s.u. was 0.001 in the final refinement cycle. The

final difference map had maxima and minima of 0.50 and -0.33 e<sup>-</sup>/Å<sup>3</sup>, respectively.

### 3.6 References.

- (1) Momenteau, M.; Reed, C. A. *Chem. Rev.* **1994**, *94*, 659.
- (2) Woodward, J. J.; Chang, M. M.; Martin, N. I.; Marletta, M. A. *J. Am. Chem. Soc.* **2008**, *131*, 297.
- (3) Wu, A. J.; Penner-Hahn, J. E.; Pecoraro, V. L. *Chem. Rev.* **2004**, *104*, 903.
- (4) Miller, A.-F. *Curr. Opin. Chem. Biol.* **2004**, *8*, 162.
- (5) Grove, L. E.; Brunold, T. C. *Comments Inorg. Chem.* **2008**, *29*, 134.
- (6) Cotruvo, J. A.; Stubbe, J. *Biochemistry* **2010**, *49*, 1297.
- (7) Willing, A.; Follmann, H.; Auling, G. *Eur. J. Biochem.* **1988**, *170*, 603.
- (8) Bull, C.; Niederhoffer, E. C.; Yoshida, T.; Fee, J. A. *J. Am. Chem. Soc.* **1991**, *113*, 4069.
- (9) Hearn, A. S.; Tu, C. K.; Nick, H. S.; Silverman, D. N. *J. Biol. Chem.* **1999**, *274*, 24457.
- (10) Hayden, J.; Hendrich, M. *J. Biol. Inorg. Chem.* **2010**, *15*, 729.
- (11) Cox, N.; Ogata, H.; Stolle, P.; Reijerse, E.; Auling, G.; Lubitz, W. *J. Am. Chem. Soc.* **2010**, *132*, 11197.
- (12) Jackson, T. A.; Karapetian, A.; Miller, A.-F.; Brunold, T. C. *Biochemistry* **2005**, *44*, 1504.
- (13) VanAtta, R. B.; Strouse, C. E.; Hanson, L. K.; Valentine, J. S. *J. Am. Chem. Soc.* **1987**, *109*, 1425.
- (14) Kitajima, N.; Komatsuzaki, H.; Hikichi, S.; Osawa, M.; Moro-oka, Y. *J. Am. Chem. Soc.* **1994**, *116*, 11596.
- (15) Seo, M. S.; Kim, J. Y.; Annaraj, J.; Kim, Y.; Lee, Y.-M.; Kim, S.-J.; Kim, J.; Nam, W. *Angew. Chem. Int. Ed.* **2007**, *46*, 377.
- (16) Annaraj, J.; Cho, J.; Lee, Y.-M.; Kim, S. Y.; Latifi, R.; de Visser, S. P.; Nam, W. *Angew. Chem. Int. Ed.* **2009**, *48*, 4150.
- (17) Shook, R. L.; Gunderson, W. A.; Greaves, J.; Ziller, J. W.; Hendrich, M. P.; Borovik, A. S. *J. Am. Chem. Soc.* **2008**, *130*, 8888.
- (18) Groni, S.; Blain, G.; Guillot, R.; Policar, C.; Anxolabéhère-Mallart, E. *Inorg. Chem.* **2007**, *46*, 1951.
- (19) Groni, S.; Dorlet, P.; Blain, G.; Bourcier, S.; Guillot, R.; Anxolabéhère-Mallart, E. *Inorg. Chem.* **2008**, *47*, 3166.
- (20) Geiger, R. A.; Chattopadhyay, S.; Day, V. W.; Jackson, T. A. *J. Am. Chem. Soc.* **2010**, *132*, 2821.
- (21) Singh, U. P.; Sharma, A. K.; Hikichi, S.; Komatsuzaki, H.; Moro-oka, Y.; Akita, M. *Inorg. Chim. Acta* **2006**, *359*, 4407.
- (22) Kitajima, N.; Fukui, H.; Moro-oka, Y. *J. Am. Chem. Soc.* **1990**, *112*, 6402.
- (23) Annaraj, J.; Suh, Y.; Seo, M. S.; Kim, S. O.; Nam, W. *Chem. Commun.* **2005**, 4529.
- (24) Goto, Y.; Wada, S.; Morishima, I.; Watanabe, Y. *J. Inorg. Biochem.* **1998**, *69*, 241.
- (25) Ghachtouli, S. E.; Mohamadou, A.; Barbier, J.-P. *Inorg. Chim. Acta* **2005**, *358*, 3873.
- (26) Paris, S. I. M.; Laskay, Ü. A.; Liang, S.; Pavlyuk, O.; Tschirschwitz, S.; Lönnecke, P.; McMills, M. C.; Jackson, G. P.; Petersen, J. L.; Hey-Hawkins, E.; Jensen, M. P. *Inorg. Chim. Acta* **2010**, *363*, 3390.
- (27) Wang, S.; Westmoreland, T. D. *Inorg. Chem.* **2008**, *48*, 719.
- (28) Dabrowiak, J. C.; Nafie, L. A.; Bryan, P. S.; Torkelson, A. T. *Inorg. Chem.* **1977**, *16*, 540.

- (29) Armarego, W. L. F.; Perrin, D. D. *Purification of Laboratory Chemicals*; Butterworth-Heinemann: Oxford, U.K., 1997.
- (30) Halfen, J. A.; Uhan, J. M.; Fox, D. C.; Mehn, M. P.; Que, L., Jr. *Inorg. Chem.* **2000**, *39*, 4913.
- (31) Mayilmurugan, R.; Stoeckli-Evans, H.; Palaniandavar, M. *Inorg. Chem.* **2008**, *47*, 6645.
- (32) Neese, F., *ORCA - an ab initio, Density Functional and Semiempirical Program Package, Version 2.7*, University of Bonn, 2009.
- (33) Becke, A. D. *J. Chem. Phys.* **1986**, *84*, 4524.
- (34) Perdew, J. P. *Physical Review B* **1986**, *33*, 8822.
- (35) Schäfer, A.; Horn, H.; Ahlrichs, R. *J. Chem. Phys.* **1992**, *97*, 2571.
- (36) Schäfer, G.; Huber, C.; Ahlrichs, R. *J. Chem. Phys.* **1994**, *100*, 5829.
- (37) Neese, F. *J. Comput. Chem.* **2003**, *24*, 1740.
- (38) Sinnecker, S.; Rajendran, A.; Klamt, A.; Diedenhofen, M.; Neese, F. *J. Phys. Chem. A* **2006**, *110*, 2235.
- (39) International Tables for Crystallography, Vol A, 4<sup>th</sup> ed., Kluwer: Boston (1996).  
Data Collection: SMART Software Reference Manual (1998). Bruker-AXS, 5465 E. Cheryl Parkway, Madison, WI 53711-5373 USA.
- (40) Parkway, Madison, WI 53711-5373 USA.
- (41) Data Reduction: SAINT Software Reference Manual (1998). Bruker-AXS, 6300 Enterprise Dr., Madison, WI 53719-1173, USA.
- (42) G. M. Sheldrick (2000). SHELXTL Version 6.10 Reference Manual. Bruker-AXS, 5465 E. Cheryl Parkway, Madison, WI 53711-5373 USA.

## **Chapter 4**

### **Steric and Electronic Influences on the Structures of Peroxomanganese(III) Complexes Supported by Tetradentate Ligands**

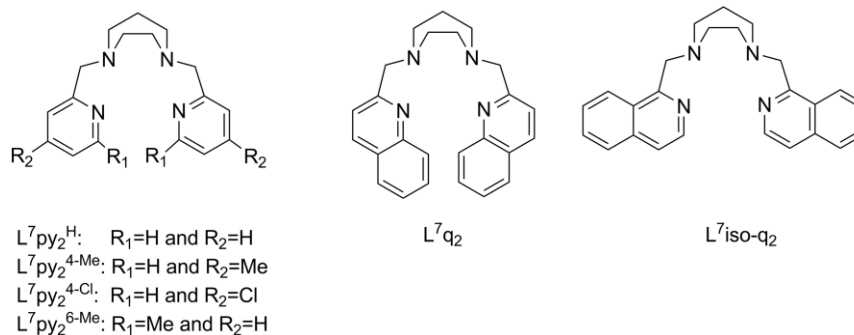
## 4. 1 Introduction.

Manganese centers that react with dioxygen and its reduced derivatives play important roles in biological systems and synthetic applications. Peroxomanganese(III) adducts are proposed as important intermediates in manganese containing enzymes, including manganese superoxide dismutase, manganese catalase, and manganese ribonucleotide reductase.<sup>1-5</sup> Peroxomanganese(III) adducts have also been proposed as an important catalytic intermediate in synthetically useful oxygenation reactions, including olefin epoxidation, C-H bond hydroxylation, and alcohol oxidation.<sup>6-9</sup> While the mechanisms of these systems remain the subject of much current work, the importance of peroxomanganese(III) intermediates has been outlined in several reports.<sup>10-13</sup>

Previously we reported that  $\text{Mn}^{\text{III}}\text{-O}_2$  adduct supported by  $\text{L}^7\text{py}_2^{\text{H}}$  and  $\text{L}^7\text{py}_2^{6\text{-Me}}$  ligands have different MCD profiles that correlate to the differences in Mn-O<sub>2</sub> bonding (Chapter 2).<sup>14</sup> Electronic absorption data for  $[\text{Mn}^{\text{III}}(\text{O}_2)(\text{L}^7\text{py}_2^{4\text{-Me}})]^+$  and  $[\text{Mn}^{\text{III}}(\text{O}_2)(\text{L}^7\text{q}_2)]^+$  (Chapter 3) suggested that differences in  $[\text{Mn}^{\text{III}}(\text{O}_2)(\text{L}^7\text{py}_2^{\text{H}})]^+$  and  $[\text{Mn}^{\text{III}}(\text{O}_2)(\text{L}^7\text{py}_2^{6\text{-Me}})]^+$  are due to steric and not electronic factors.<sup>15</sup> To further validate this conclusion, as well as additionally explore steric and electronic influences on  $\text{Mn}^{\text{III}}\text{-O}_2$  bonding, we report herein MCD data collected for  $\text{Mn}^{\text{III}}\text{-O}_2$  adducts supported by the previously reported<sup>15</sup>  $\text{L}^7\text{py}_2^{4\text{-Me}}$  and  $\text{L}^7\text{q}_2$  ligands as well as the new  $\text{L}^7\text{py}_2^{4\text{-Cl}}$  and  $\text{L}^7\text{isoq}_2$  ligands that contain 4-chloropyridine and isoquinoline pendant arms, respectively (Scheme 4.1). The ligand series  $\text{L}^7\text{py}_2^{4\text{-Me}}$ ,  $\text{L}^7\text{py}_2^{\text{H}}$ , and  $\text{L}^7\text{py}_2^{4\text{-Cl}}$  permits comparison of electronic effects, as these ligands differ only in the nature of the pyridine substituent in the four-position remove from the peroxo binding pocket. The  $\text{L}^7\text{isoq}_2$  ligand offers an electronic complement to  $\text{L}^7\text{q}_2$  that should lack the steric effects present when the latter ligand coordinates a metal. Specifically, these data suggest that substituents located at six-

position of the pyridine rings support more asymmetric end-on peroxo ligands due to steric clashing between the peroxo ligand and the six-substituent. A small electronic effect was observed when the electronic properties of the ligand are perturbed.

**Scheme 4.1**



## 4.2 Results and Discussion.

**4.2.1 Structural properties of  $Mn^{II}$  complexes.** Figure 4.1 displays ORTEP diagrams and space fillings models for  $[Mn^{II}(L^7isoq_2)(OTf)_2]$  and  $[Mn^{II}(L^7py_2^{4-Cl})(OTf)_2]$ . Selected bond distances are given in Table 4.1. For these complexes, the linear, tetradentate ligand is bound in the *trans* conformation, creating two axial coordination sites occupied by the anionic ligand triflate (OTf). The  $Mn^{II}$ –ligand bond lengths range from  $\sim 2.2$  to  $2.3 \text{ \AA}$ , indicative of high-spin  $Mn^{II}$  centers. The small N3–Mn–N4 bite angles of  $\sim 70^\circ$  (Table 4.1) of the  $Mn^{II}$  complex supported by the  $L^7isoq_2$  and  $L^7py_2^{4-Cl}$  ligands should allow for binding of a fifth equatorial ligand. The lack of heptacoordination for  $[Mn^{II}(L^7isoq_2)(OTf)_2]$  is tentatively attributed to the shorter Mn–N(quinoline) bonds relative to  $[Mn^{II}(L^7py_2^H)(NCMe)_3]^{2+}$  ( $2.22$  versus  $2.33 \text{ \AA}$ , respectively; Table 4.1), which is due to the electron-donating properties of the quinolone versus pyridine ligands. For  $[Mn^{II}(L^7py_2^{4-Cl})(OTf)_2]$ , which has similar bond distances as  $[Mn^{II}(L^7py_2^H)(NCMe)_3]^{2+}$  ( $2.30$  versus  $2.33 \text{ \AA}$ , respectively; Table 4.1), the lack of



hetpacoordination can be attributed to the shorter X1-Mn-X2 angle ( $117.1^\circ$  versus  $160.0^\circ$ , respectively); *i.e.*, the triflate ligands are significantly distorted from idealized axial positions.

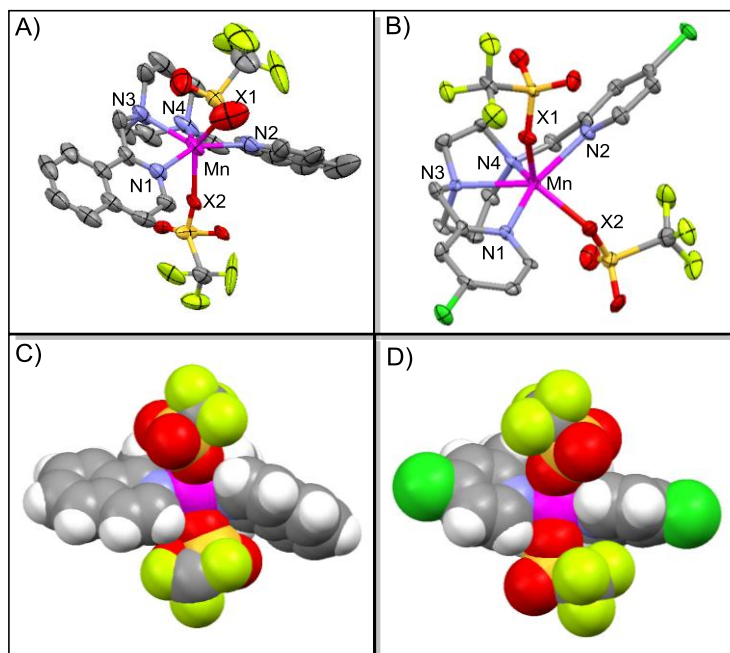


**Figure 4.1.** ORTEP diagrams of A)  $[\text{Mn}^{\text{II}}(\text{L}^7\text{isoq}_2)(\text{OTf})_2]$  and B)  $[\text{Mn}^{\text{II}}(\text{L}^7\text{py}_2^{4-\text{Cl}})(\text{OTf})_2]$ . F) Space filling models for C)  $[\text{Mn}^{\text{II}}(\text{L}^7\text{isoq}_2)(\text{OTf})_2]$  and B)  $[\text{Mn}^{\text{II}}(\text{L}^7\text{py}_2^{4-\text{Cl}})(\text{OTf})_2]$  viewed along the equatorial plane. For ORTEP diagrams hydrogen atoms have been removed for clarity. Significant interatomic distances and angles are listed in Table 4.1.

**Table 4.1.** Selected Bond Lengths ( $\text{\AA}$ ) and Angles ( $^\circ$ ) for  $\text{Mn}^{\text{II}}$  Complexes.

Complex	Mn-N(1)	Mn-N(2)	Mn-N(3)	Mn-N(4)	Mn-X(1)	Mn-X(2)	Mn-X(3) <sup>b</sup>	N3-Mn-N4	X1-Mn-X2
$[\text{Mn}^{\text{II}}(\text{L}^7\text{py}_2^{\text{H}})(\text{NCMe})_3](\text{ClO}_4)_2$ <sup>a</sup>	2.306(9)	2.308(3)	2.369(3)	2.357(3)	2.268(2) <sup>b</sup>	2.311(2) <sup>b</sup>	2.478(2)	67.40(1)	160.0(1)
$[\text{Mn}^{\text{II}}(\text{L}^7\text{isoq}_2)(\text{OTf})_2]$	2.225(3)	2.249(7)	2.312(4)	2.257(5)	2.149(4) <sup>c</sup>	2.233(1) <sup>c</sup>	NA	70.64(1)	137.7(6)
$[\text{Mn}^{\text{II}}(\text{L}^7\text{py}_2^{4-\text{Cl}})(\text{OTf})_2]$	2.272(8)	2.290(9)	2.305(7)	2.311(7)	2.109(9) <sup>c</sup>	2.203(4) <sup>c</sup>	NA	69.97(1)	117.1(1)

<sup>a</sup>From reference 14. <sup>b</sup>X = N(CMe). <sup>c</sup>X = OTf.

**4.2.2 Formation of peroxomanganese(III) complexes.** The absorption spectra of acetonitrile solutions of  $[\text{Mn}^{\text{II}}(\text{L}^7\text{isoq}_2)(\text{OTf})_2]$  and  $[\text{Mn}^{\text{II}}(\text{L}^7\text{py}_2^{4-\text{Cl}})(\text{OTf})_2]$  are featureless at energies below  $33\,000\text{ cm}^{-1}$ , indicative of high spin  $\text{Mn}^{\text{II}}$  centers. Treatment of  $[\text{Mn}^{\text{II}}(\text{L}^7\text{isoq}_2)(\text{OTf})_2]$  and  $[\text{Mn}^{\text{II}}(\text{L}^7\text{py}_2^{4-\text{Cl}})(\text{OTf})_2]$  with 5 equivalents  $\text{H}_2\text{O}_2$  and 0.5 equivalents triethylamine at  $-40^\circ\text{C}$  resulted in the formation of new absorption features in the visible region (Figure 4.2 and Table

4.2). Mass spectrometry experiments on these colored solutions revealed major ion peaks consistent with  $[\text{Mn}^{\text{III}}(\text{O}_2)(\text{L}^7\text{isoq}_2)]^+$  and  $[\text{Mn}^{\text{III}}(\text{O}_2)(\text{L}^7\text{py}_2^{4\text{-Cl}})]^+$ .

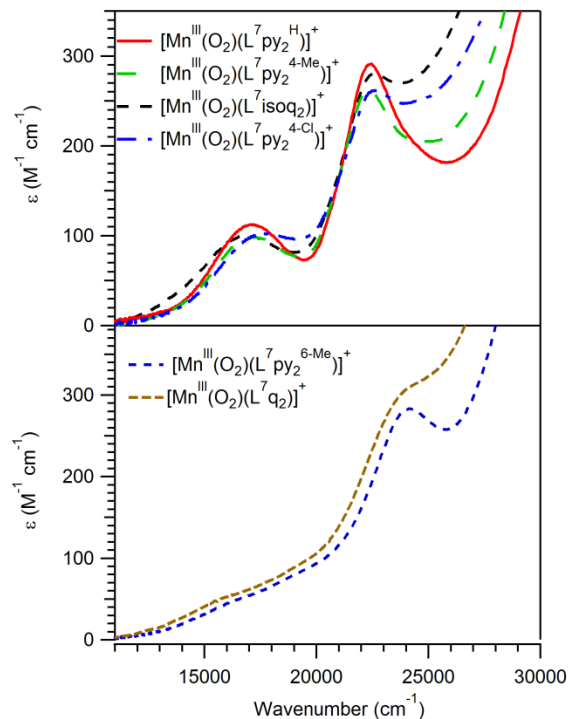


**Figure 4.2.** Top: Electronic absorption spectra of  $[\text{Mn}^{\text{III}}(\text{O}_2)(\text{L}^7\text{py}_2^{\text{H}})]^+$ ,  $[\text{Mn}^{\text{III}}(\text{O}_2)(\text{L}^7\text{py}_2^{4\text{-Me}})]^+$ ,  $[\text{Mn}^{\text{III}}(\text{O}_2)(\text{L}^7\text{isoq}_2)]^+$  at  $-40^\circ\text{C}$  in MeCN. Bottom: Electronic absorption spectra of  $[\text{Mn}^{\text{III}}(\text{O}_2)(\text{L}^7\text{q}_2)]^+$  and  $[\text{Mn}^{\text{III}}(\text{O}_2)(\text{L}^7\text{py}_2^{6\text{-Me}})]^+$  at  $-40^\circ\text{C}$  in MeCN.

**Table 4.2.** Properties of Peroxomanganese(III) Complexes

complex	$\lambda_{\text{max}}$ ( $\text{cm}^{-1}$ ) ( $\epsilon(\text{M}^{-1}\text{cm}^{-1})$ )	$t_{1/2}$ at $0^\circ\text{C}$
$[\text{Mn}^{\text{III}}(\text{O}_2)(\text{L}^7\text{py}_2^{\text{H}})]^+{}^a$	22 470 (280) 17 000 (120)	15 min
$[\text{Mn}^{\text{III}}(\text{O}_2)(\text{L}^7\text{py}_2^{6\text{-Me}})]^+{}^a$	24 100 (280) ~16 130 (80)	6 min
$[\text{Mn}^{\text{III}}(\text{O}_2)(\text{L}^7\text{py}_2^{4\text{-Me}})]^+{}^b$	22 470 (260) ~17 000 (100)	6 min
$[\text{M}^{\text{III}}(\text{O}_2)(\text{L}^7\text{q}_2)]^+{}^b$	24 050 (305) ~16 500 (70)	4 min
$[\text{Mn}^{\text{III}}(\text{O}_2)(\text{L}^7\text{isoq}_2)]^+{}^c$	22 421 (291) 17 038 (112)	30 min
$[\text{Mn}^{\text{III}}(\text{O}_2)(\text{L}^7\text{py}_2^{4\text{-Cl}})]^+$	22 623 (262) 17 607 (102)	10 min

<sup>a</sup> From reference <sup>14</sup> and <sup>b</sup> from reference <sup>15</sup> <sup>c</sup> decays to a different decay product.

The absorption spectra of  $[\text{Mn}^{\text{III}}(\text{O}_2)(\text{L}^7\text{isoq}_2)]^+$  and  $[\text{Mn}^{\text{III}}(\text{O}_2)(\text{L}^7\text{py}_2^{4\text{-Cl}})]^+$  are nearly identical to those of  $[\text{Mn}^{\text{III}}(\text{O}_2)(\text{L}^7\text{py}_2^{\text{H}})]^+$  and  $[\text{Mn}^{\text{III}}(\text{O}_2)(\text{L}^7\text{py}_2^{4\text{-Me}})]^+$ , consisting of a weak feature at  $\sim 17\,000\text{ cm}^{-1}$  and a more intense band at  $\sim 22\,000\text{ cm}^{-1}$  (Figure 4.2 and Table 4.2). Thus, these spectra are distinct from those of  $[\text{Mn}^{\text{III}}(\text{O}_2)(\text{L}^7\text{q}_2)]^+$  and  $[\text{Mn}^{\text{III}}(\text{O}_2)(\text{L}^7\text{py}_2^{6\text{-Me}})]^+$  and ( $\lambda_{\text{max}} \approx 16\,000$  and  $24\,000\text{ cm}^{-1}$ ).<sup>15</sup> Among this set of complexes, the common link between ligand structure and absorption maxima is steric bulk in the 6-position of the pyridine ring (assuming the quinoline as a “bulky” pyridine). With the aid of DFT computations, we previously attributed differences in absorption and MCD spectra of  $[\text{Mn}^{\text{III}}(\text{O}_2)(\text{L}^7\text{py}_2^{\text{H}})]^+$  and  $[\text{Mn}^{\text{III}}(\text{O}_2)(\text{L}^7\text{py}_2^{6\text{-Me}})]^+$  to a change from a side-on-bound peroxo ligand with symmetric Mn-O<sub>peroxo</sub> distances of 1.87 Å to more of an end-on peroxo with Mn-O<sub>peroxo</sub> distances of 1.87 and 1.91 Å.<sup>14</sup> We first speculated that the increased Lewis acidity of the Mn center in  $[\text{Mn}^{\text{III}}(\text{O}_2)(\text{L}^7\text{py}_2^{6\text{-Me}})]^+$  leads to longer and asymmetric Mn-O<sub>peroxo</sub> bond lengths. However, the data presented in Table 4.2 suggest an alternative explanation for the peroxo bonding modulations. The inclusion of bulky groups at the six-position is expected to cause significant canting of the pyridine rings. This increased canting, as evidence in the XRD structure of the  $\text{Mn}^{\text{II}}$  complexes (Table 4.1), causes the six-substituents to partially block the axial position and sterically disfavor the formation of symmetric side-on peroxo ligand in the  $\text{L}^7\text{py}_2^{6\text{-Me}}$  and  $\text{L}^7\text{q}_2$  complexes. This model would account for the similarities in the absorption maxima of  $[\text{Mn}^{\text{III}}(\text{O}_2)(\text{L}^7\text{py}_2^{\text{H}})]^+$ ,  $[\text{Mn}^{\text{III}}(\text{O}_2)(\text{L}^7\text{py}_2^{4\text{-Me}})]^+$ ,  $[\text{Mn}^{\text{III}}(\text{O}_2)(\text{L}^7\text{py}_2^{4\text{-Cl}})]^+$ , and  $[\text{Mn}^{\text{III}}(\text{O}_2)(\text{L}^7\text{isoq}_2)]^+$  complexes. To evaluate these Mn-O<sub>peroxo</sub> bond length perturbations in more detail, MCD spectroscopy and DFT computations were used to correlate spectroscopic properties with geometric structure.

**4.2.3 MCD Spectroscopy.** Figure 4.3 shows the 2 K, 7 T MCD spectra of  $[\text{Mn}^{\text{III}}(\text{O}_2)(\text{L}^7\text{py}_2^{\text{H}})]^+$ ,  $[\text{Mn}^{\text{III}}(\text{O}_2)(\text{L}^7\text{py}_2^{6\text{-Me}})]^+$ , and  $[\text{Mn}^{\text{III}}(\text{O}_2)(\text{L}^7\text{py}_2^{4\text{-Me}})]^+$ . The MCD spectra of  $[\text{Mn}^{\text{III}}(\text{O}_2)(\text{L}^7\text{py}_2^{\text{H}})]^+$  and  $[\text{Mn}^{\text{III}}(\text{O}_2)(\text{L}^7\text{py}_2^{4\text{-Me}})]^+$  are nearly identical. In each case the lowest energy d-d transition (band 1, see Figure 4.3) is observed at  $\sim 16\,300\text{ cm}^{-1}$ .<sup>a</sup> In contrast, this band is observed for  $[\text{Mn}^{\text{III}}(\text{O}_2)(\text{L}^7\text{py}_2^{6\text{-Me}})]^+$  at  $13\,600\text{ cm}^{-1}$ . Thus, these data confirm our prior conclusions, based solely on electronic absorption data, that it is the position, and not the identity, or the pyridine ring substituent that influences the energy of the lowest d-d band and the  $\text{Mn}^{\text{III}}\text{-O}_{\text{peroxo}}$  bond strength.

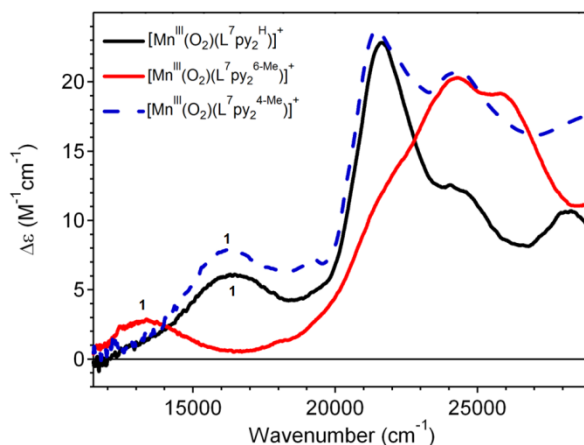


**Figure 4.3.** 2 K, 7 T MCD spectra of  $[\text{Mn}^{\text{III}}(\text{O}_2)(\text{L}^7\text{py}_2^{\text{H}})]^+$  (solid black),  $[\text{Mn}^{\text{III}}(\text{O}_2)(\text{L}^7\text{py}_2^{6\text{-Me}})]^+$  (solid red), and  $[\text{Mn}^{\text{III}}(\text{O}_2)(\text{L}^7\text{py}_2^{4\text{-Me}})]^+$  (blue dashed). Conditions: MCD data were collected for 15 mM frozen glass sample, in butyronitrile.

To further assess this steric effect caused by substituent location, low-temperature MCD data were also collected for  $[\text{Mn}^{\text{III}}(\text{O}_2)(\text{L}^7\text{q}_2)]^+$  and  $[\text{Mn}^{\text{III}}(\text{O}_2)(\text{L}^7\text{isoq}_2)]^+$  (Figure 4.4). While there are several differences in the MCD spectra of these complexes, there is a  $\sim 1\,100\text{ cm}^{-1}$  red-shift in band 1 for  $[\text{Mn}^{\text{III}}(\text{O}_2)(\text{L}^7\text{isoq}_2)]^+$  relative to  $[\text{Mn}^{\text{III}}(\text{O}_2)(\text{L}^7\text{q}_2)]^+$  (Table 4.3). This red shift

<sup>a</sup> Figures A.4.1 to A.4.4 show the iterative Gaussian deconvolution of absorption and MCD Spectra for  $[\text{Mn}^{\text{III}}(\text{O}_2)(\text{L}^7\text{py}_2^{\text{R}})]^+$  (R = 4-Cl and 4-Me),  $[\text{Mn}^{\text{III}}(\text{O}_2)(\text{L}^7\text{q}_2)]^+$ , and  $[\text{Mn}^{\text{III}}(\text{O}_2)(\text{L}^7\text{isoq}_2)]^+$ . The energy of band 1 was derived from the iterative Gaussian deconvolution.

is attributed to different topologies of the  $L^7q_2$  and  $L^7isoq_2$  ligands. When bound to a metal complex, the quinoline arms in  $L^7q_2$  must cant to minimize steric repulsion, which causes crowding of the axial peroxo binding site. This is similar to that observed for the  $L^7py_2^{6-Me}$  system. In contrast, the iso-quinoline arms in  $L^7isoq_2$  have minimal steric interactions, and the axial binding site is not crowded. The smaller red shift for  $[Mn^{III}(O_2)(L^7q_2)]^+$  and  $[Mn^{III}(O_2)(L^7isoq_2)]^+$  versus  $[Mn^{III}(O_2)(L^7py_2^{6-Me})]^+$  and  $[Mn^{III}(O_2)(L^7py_2^{4-Me})]^+$  is attributed to a smaller steric clash between the quinoline arms than the 6-methylpyridine groups.

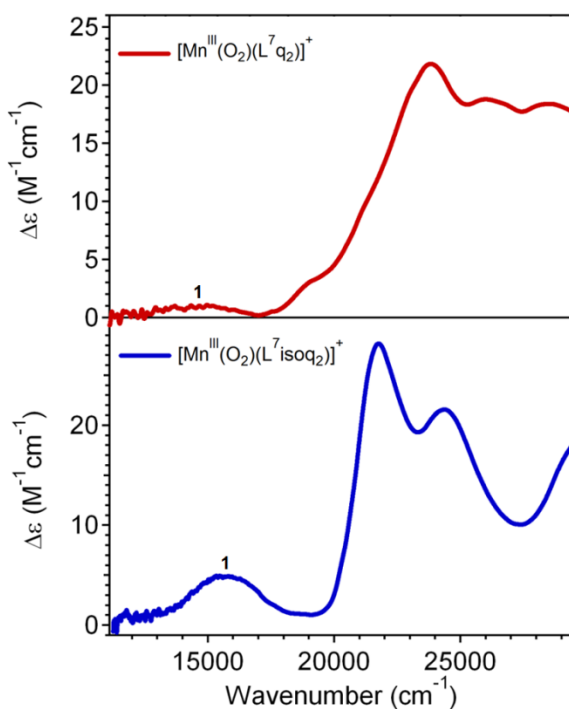


**Figure 4.4.** 2 K, 7 T MCD spectra of  $[Mn^{III}(O_2)(L^7q_2)]^+$  (top) and  $[Mn^{III}(O_2)(L^7isoq_2)]^+$  (Bottom). Conditions: MCD data were collected for a 15 mM frozen glass sample in butyronitrile.

To determine if there is any electronic effect on  $Mn^{III}-O_2$  bonding, low-temperature MCD spectra were collected for  $[Mn^{III}(O_2)(L^7py_2^{4-Cl})]^+$  (Figure A.4.4) to compare data sets collected for  $[Mn^{III}(O_2)(L^7py_2^H)]^+$  and  $[Mn^{III}(O_2)(L^7py_2^{4-Me})]^+$ . There is a slight blue shift for band 1 as the supporting ligand changes from electron donating to electron withdrawing in the

series,  $[\text{Mn}^{\text{III}}(\text{O}_2)(\text{L}^7\text{py}_2^{4-\text{Me}})]^+$ ,  $[\text{Mn}^{\text{III}}(\text{O}_2)(\text{L}^7\text{py}_2^{\text{H}})]^+$ , and  $[\text{Mn}^{\text{III}}(\text{O}_2)(\text{L}^7\text{py}_2^{4-\text{Cl}})]^+$  (Figure 4.5). Shifts in electronic transition energies indicate that the electronic structure of the  $\text{Mn}^{\text{III}}\text{-O}_2$  unit is only modestly influenced by the substituents on the pyridine ring. In order to correlate these spectral shifts with changes in the geometric and electronic structure of the  $\text{Mn}^{\text{III}}\text{-O}_2$  unit caused by ligand perturbations, DFT calculations were performed on models of these peroxomanganese(III) complexes.

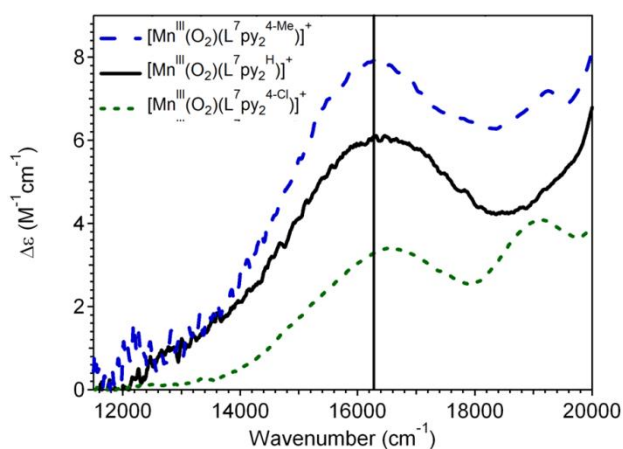


**Figure 4.5.** 2 K, 7 T MCD spectra of  $[\text{Mn}^{\text{III}}(\text{O}_2)(\text{L}^7\text{py}_2^{\text{H}})]^+$  (Solid Black),  $[\text{Mn}^{\text{III}}(\text{O}_2)(\text{L}^7\text{py}_2^{4-\text{Me}})]^+$  (Blue Dashed), and  $[\text{Mn}^{\text{III}}(\text{O}_2)(\text{L}^7\text{py}_2^{4-\text{Cl}})]^+$  (Green Dashed). Conditions: MCD data were collected for a 15 mM frozen glass sample in butyronitrile.

**Table 4.3.** Energy of MCD Band 1 for Peroxomanganese(III) Complexes and  $\text{Mn-O}_{\text{peroxo}}$  Bond Length Determined from DFT Computations

Complex	Band 1 Energy ( $\text{cm}^{-1}$ )	Mn-O Average ( $\text{\AA}$ )	Mn-O Long ( $\text{\AA}$ )	Mn-O Short ( $\text{\AA}$ )
$[\text{Mn}^{\text{III}}(\text{O}_2)(\text{L}^7\text{py}_2^{6-\text{Me}})]^+$	13 650	1.890	1.907	1.866
$[\text{Mn}^{\text{III}}(\text{O}_2)(\text{L}^7\text{q}_2)]^+$	14 600	1.880	1.886	1.866
$[\text{Mn}^{\text{III}}(\text{O}_2)(\text{L}^7\text{isoq}_2)]^+$	15 670	1.867	1.869	1.865
$[\text{Mn}^{\text{III}}(\text{O}_2)(\text{L}^7\text{py}_2^{4-\text{Me}})]^+$	16 260	1.871	1.873	1.869
$[\text{Mn}^{\text{III}}(\text{O}_2)(\text{L}^7\text{py}_2^{\text{H}})]^+$	16 350	1.870	1.872	1.868
$[\text{Mn}^{\text{III}}(\text{O}_2)(\text{L}^7\text{py}_2^{4-\text{Cl}})]^+$	16 530	1.868	1.869	1.866

**4.2.4 DFT Optimized Geometry.** Important metric parameters of our DFT-optimized models of these peroxomanganese(III) are collected in Table 4.3. In all cases, the optimized structures display six-coordinate  $\text{Mn}^{\text{III}}$  centers with side-on peroxo ligands. The nitrogen atoms of the

supporting ligand form the base of a square plane that sits below the  $\text{Mn}^{\text{III}}\text{-O}_2$  unit. Shown in Figure 4.6 and Table 4.3, large elongation of the  $\text{Mn-O}_{\text{peroxo}}$  bond lengths are predicted for  $[\text{Mn}^{\text{III}}(\text{O}_2)(\text{L}^7\text{py}_2^{6\text{-Me}})]^+$  and  $[\text{Mn}^{\text{III}}(\text{O}_2)(\text{L}^7\text{q}_2)]^+$  and these correlate well with the trend in MCD transition energy. Small modulations of the  $\text{Mn-O}_{\text{peroxo}}$  bond lengths can be observed for  $[\text{Mn}^{\text{III}}(\text{O}_2)(\text{L}^7\text{py}_2^{\text{R}})]^+$  ( $\text{R} = \text{H}, 4\text{-Me}, \text{and } 4\text{-Cl}$ ). The fact that a perfectly linear relationship is not observed between average Mn-O distance and the energy of band 1 is not surprising. While the energy of the acceptor orbital is tuned by  $\text{Mn-O}_{\text{peroxo}}$  interactions, the donor orbital for this transition is  $\text{Mn-L}^7\text{py}_2^{\text{R}}$   $\sigma$ -antibonding. Thus, changes in the electronic structure of the supporting ligand should modulate the transition energy. It is the greater covalency of the  $\text{Mn-O}_{\text{peroxo}}$  compared to  $\text{Mn-L}^7\text{py}_2^{\text{R}}$  that accounts for the for peroxo perturbations having the greatest influences on the transition energy.

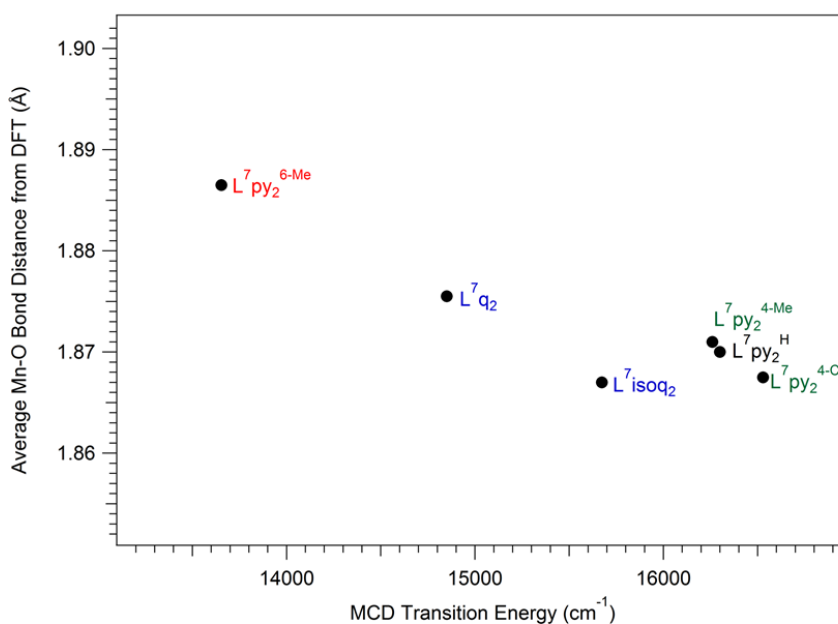


**Figure 4.6.** Plot of band 1 transition energy versus average  $\text{Mn-O}_{\text{peroxo}}$  computed bond distance.

### 4.3 Summary.

This chapter describes the generation and characterization of a set of peroxomanganese(III) complexes supported by tetradentate  $L^7py_2^R$  ( $R = H, 4-Me, 4-Cl, \text{ and } 6-Me$ ),  $L^7q_2$ , and  $L^7isoq_2$  ligands. This work provides further evidence that the lowest-energy  $d-d$  band can be used as a marker for the strength of the  $Mn-O_{\text{peroxo}}$   $\sigma$ -interaction. This correlation is possible because the acceptor orbital for this electronic transition is the  $Mn-O_2$   $\sigma$ -antibonding MO. These results show that when the supporting ligand has bulky pendant arms that clash with one another, the peroxo binding mode becomes more asymmetric with elongated  $Mn-O_{\text{peroxo}}$  bond lengths. Surprisingly, only a very minor perturbation was observed when the electronic properties of the supporting ligand were altered. These results suggest that the reactivities of peroxomanganese(III) intermediates, whether formed in manganese enzymes or synthetic catalysts, are tuned through steric, and not electronic, perturbations of the local coordination environment.

### 4.4 Material and Methods.

**4.4.1 Materials.** All chemicals were obtained from commercial vendors at ACS reagent-grade or better and were used without further purification. All solvents were dried by routine techniques under an inert argon atmosphere.<sup>16</sup> Manipulations of  $Mn^{II}$  complexes were carried out under argon using a glovebox or Schlenk techniques.

**4.4.2 Instrumentation.**  $^1H$  NMR spectra were obtained on a Bruker DRX 400 MHz NMR spectrometer. Electronic absorption spectra were recorded on a Cary 50 Bio spectrophotometer (Varian) interfaced with a Unisoku cryostat (USP-203-A). ESI-mass spectrometry experiments were performed using an LCT Primers MicroMass electrospray-ionization time-of-flight



instrument. Magnetic circular dichroism (MCD) spectra were collected on a spectropolarimeter (Jasco J-815) interfaced with a magnetocryostat (Oxford Instruments SM-4000-8) capable of horizontal fields up to 8 T.

**4.4.3 Ligand Synthesis.** 1,4-bis(2-pyridylmethyl)-1,4-diazepane ( $L^7py_2^H$ ), 1,4-bis(6-methyl-2-pyridylmethyl)-1,4-diazepane ( $L^7py_2^{6-Me}$ ), 1,4-bis(4-methyl-2-pyridylmethyl)-1,4-diazepane ( $L^7py_2^{4-Me}$ ), and 1,4-bis(2-quinolinylmethyl)-1,4-diazepane ( $L^7q_2$ ) were prepared as previously described.<sup>14-15,17</sup> Using similar procedures 4-bis(4-chloro-2-pyridylmethyl)-1,4-diazepane ( $L^7py_2^{4-Cl}$ ) was prepared by reacting homopiperazine with 4-chloropicolinaldehyde (70% yield). 1,4-bis(2-isoquinolinylmethyl)-1,4-diazepane ( $L^7isoq_2$ ) was prepared by reacting homopiperazine with 1-(bromomethyl)isoquinoline hydrobromide (65% yield).<sup>14-15,17</sup>  $^1H$  NMR data (400 MHz) for  $L^7py_2^{4-Cl}$  and  $L^7isoq_2$  are as follows:  $L^7py_2^{4-Cl}$  (CDCl<sub>3</sub>;  $\delta$ ) 8.43 (d, 2H,  $J_{HH}=4.28$ ), 7.54 (d, 2H,  $J_{HH}=1.52$ ), 7.17 (dd, 2H,  $J_{HH}=2.64$ ), 3.82 (s, 4H), 2.82 (t, 4H,  $J_{HH} = 3.44$ ), 2.78 (s, 4H), 1.86 (p, 2H,  $J_{HH} = 4.8$ ) and  $L^7isoq_2$  (CDCl<sub>3</sub>;  $\delta$ ) 8.56 (d, 2H,  $J_{HH}=8.4$ ), 8.41 (d, 2H,  $J_{HH}=5.72$ ), 7.81 – 7.55 (m, 8H), 4.19 (s, 4H), 2.85 (t, 4H,  $J_{HH} = 5.92$ ), 2.74 (s, 4H), 1.81 (p, 2H,  $J_{HH} = 5.96$ ).

**4.4.4 Preparation of Mn<sup>II</sup> Complexes.** The  $[Mn^{II}(L^7py_2^R)](OTf)_2$  ( $R = H, 4-Me, 6-Me$ ) and  $[Mn^{II}(L^7q_2^R)](OTf)_2$  complexes were prepared by a previously reported metalation reaction.<sup>15,18</sup> The other metal complexes were synthesized with excellent yields (>85%) by reacting  $L^7py_2^{4-Cl}$  or  $L^7isoq_2$  ligand with  $Mn(OTf)_2$  in MeCN solution in a 1:1 molar ratio.  $Mn(OTf)_2$  was prepared by a previously reported procedure by reacting equimolar amounts of  $(CH_3)_3Si(OTf)$  and anhydrous  $MnCl_2$ .<sup>19</sup> Details of a representative preparation for a metal complex are as followed. To a stirred solution of 757.45 mg (2.145 mmol) of  $Mn(OTf)_2$  in 10 mL of MeCN was added  $L^7isoq_2$  (821 mg, 2.145 mmol) in 10 mL of MeCN. The yellow solution was stirred overnight

and evaporated under reduced pressure. The solid thus obtained was dried in vacuum. Recrystallization of the crude solid from MeCN/diethyl ether afforded nearly colorless crystals of  $[\text{Mn}(\text{L}^7\text{isoq}_2)](\text{OTf})_2$ . (1.42 g, 90%)  $\text{M}^+ [(\{\text{Mn}(\text{L}^7\text{isoq}_2)](\text{Cl})\}^+)$  472.1 requires  $\text{M}^+$ , 472.1] and  $\text{M}^+ [(\{\text{Mn}(\text{L}^7\text{py}_2^{4-\text{Cl}})](\text{Cl})\}^+)$  440.0 requires  $\text{M}^+$ , 440.0]

**4.4.5 X-ray Crystallography.** Single crystals of  $[\text{Mn}(\text{L}^7\text{isoq}_2)(\text{OTf})_2]$  and  $[\text{Mn}(\text{L}^7\text{py}_2^{4-\text{Cl}})(\text{OTf})_2]$  were grown by vapor diffusion of ether into an MeCN solution of the complex at room temperature. Data collection and refinement parameters are summarized in the supporting information and in Tables A.4.1 – A.4.2.

**4.4.6 In Situ Preparation of Peroxomanganese(III) Complexes.** The green peroxomanganese(III) intermediates were formed by treating a 2.5 mM MeCN solution of metal complex with 5 equivalents  $\text{H}_2\text{O}_2$  and 0.5 equivalents triethylamine at  $-40^\circ\text{C}$ . The formation of the peroxomanganese(III) complexes was evident from the appearance of characteristic bands in the electronic absorption spectra and ESI-mass spectrometry. [Found  $\text{M}^+ \{[\text{Mn}^{\text{III}}(\text{O}_2)(\text{L}^7\text{py}_2^{4-\text{Cl}})]\}^+$  : 437.0  $\{[\text{Mn}^{\text{III}}(\text{O}_2)(\text{L}^7\text{py}_2^{4-\text{Cl}})]\}^+$  requires:  $\text{M}^+$ , 437.0]; [Found  $\text{M}^+ \{[\text{Mn}^{\text{III}}(\text{O}_2)(\text{L}^7\text{isoq}_2)]\}^+$  : 469.1.  $\{[\text{Mn}^{\text{III}}(\text{O}_2)(\text{L}^7\text{isoq}_2)]\}^+$  requires:  $\text{M}^+$ , 469.1]

**4.4.7 Magnetic Circular Dichroism Experiments.** 15 mM frozen glass samples of  $[\text{Mn}^{\text{III}}(\text{O}_2)(\text{L}^7\text{py}_2^{4-\text{Me}})]^+$ ,  $[\text{Mn}^{\text{III}}(\text{O}_2)(\text{L}^7\text{py}_2^{4-\text{Cl}})]^+$ ,  $[\text{Mn}^{\text{III}}(\text{O}_2)(\text{L}^7\text{isoq}_2)]^+$  and  $[\text{Mn}^{\text{III}}(\text{O}_2)(\text{L}^7\text{q}_2)]^+$  were prepared in butyronitrile at  $-40^\circ\text{C}$ . Butyronitrile was used instead of MeCN, as the former produces an optical-quality glass upon freezing. Once formation of the peroxomanganese(III) species was complete (as monitored by UV-visible spectroscopy), the samples were cooled to  $-80^\circ\text{C}$ , transferred to pre-cooled MCD cells, and flash-frozen in liquid  $\text{N}_2$ . The obtained MCD spectra were measured in mdeg ( $\theta$ ) and converted to  $\Delta\epsilon$  ( $\text{M}^{-1}\text{cm}^{-1}$ ) using the standard conversion

factor  $\Delta\epsilon = \theta/(32980 \cdot c \cdot d)$ , where  $c$  is the concentration of the sample and  $d$  is the path length. MCD spectra were collected at 2, 4, 8, and 15 K for positive and negative field strengths of 1 to 7 T in 1 T increments.

**4.4.8 Density Functional Theory Calculations.** The *ORCA* 2.7 software package was used for all DFT computations.<sup>20</sup> Initial models of  $[\text{Mn}^{\text{III}}(\text{O}_2)(\text{L}^7\text{py}_2^{\text{R}})]^+$  ( $\text{R} = \text{H}, 4\text{-Me}, 4\text{-Cl}, \text{and } 6\text{-Me}$ ),  $[\text{Mn}^{\text{III}}(\text{O}_2)(\text{L}^7\text{q}_2)]^+$ , and  $[\text{Mn}^{\text{III}}(\text{O}_2)(\text{L}^7\text{isoq}_2)]^+$  were built using the X-ray coordinates of the corresponding  $\text{Mn}^{\text{II}}$  complexes, then adding side-on peroxo ligands. The pyridyl and quinolinyl rings were rotated from a canted position to a planar position. Geometry optimizations of each model of the metal complexes were converged to the  $S = 2$  spin state. These calculations employed the Becke-Perdew (BP86) functional<sup>21-22</sup> and the SVP (Ahlichs split valence polarized)<sup>23-24</sup> basis set with the SV/C auxiliary basis set for all atoms except for manganese, nitrogen, and oxygen, where the larger TZVP (Ahlichs triple- $\zeta$  valence polarized)<sup>20</sup> basis set in conjunction with the TZV/J auxiliary basis set were used. The resolution of identity (RI) approximation, developed by Neese,<sup>25</sup> was used for all calculations. Solvation effects associated with acetonitrile (dielectric constant  $\epsilon = 36.6$ ) were incorporated using COSMO, as implemented in *ORCA*.<sup>26</sup>

## 4.6 References.

- (1) Wu, A. J.; Penner-Hahn, J. E.; Pecoraro, V. L. *Chem. Rev.* **2004**, *104*, 903-938.
- (2) Miller, A.-F. *Curr. Opin. Chem. Biol.* **2004**, *8*, 162-168.
- (3) Grove, L. E.; Brunold, T. C. *Comments Inorg. Chem.* **2008**, *29*, 134-168.
- (4) Cotruvo, J. A.; Stubbe, J. *Biochemistry* **2010**, *49*, 1297-1309.
- (5) Willing, A.; Follmann, H.; Auling, G. *Eur. J. Biochem.* **1988**, *170*, 603.
- (6) Hage, R.; Lienke, A. *Angew. Chem. Int. Ed.* **2006**, *45*, 206-222.
- (7) Hage, R.; Lienke, A. *J. Mol. Catal. A: Chem.* **2006**, *251*, 150-158.
- (8) Lane, B. S.; Burgess, K. *Chem. Rev.* **2003**, *103*, 2457-2473.
- (9) Sibbons, K.; Shastri, K.; Watkinson, M. *Dalton Transactions* **2006**, *2006*, 645-661.

- (10) Bull, C.; Niederhoffer, E. C.; Yoshida, T.; Fee, J. A. *J. Am. Chem. Soc.* **1991**, *113*, 4069-4076.
- (11) Hearn, A. S.; Tu, C. K.; Nick, H. S.; Silverman, D. N. *J. Biol. Chem.* **1999**, *274*, 24457-24460.
- (12) Hayden, J.; Hendrich, M. *J. Biol. Inorg. Chem.* **2010**, *15*, 729-736.
- (13) Cox, N.; Ogata, H.; Stolle, P.; Reijerse, E.; Auling, G.; Lubitz, W. *J. Am. Chem. Soc.* **2010**, *132*, 11197-11213.
- (14) Geiger, R. A.; Chattopadhyay, S.; Day, V. W.; Jackson, T. A. *J. Am. Chem. Soc.* **2010**, *132*, 2821-2831.
- (15) Geiger, R. A.; Chattopadhyay, S.; Day, V. W.; Jackson, T. A. *Dalton Trans.* **2011**, *40*, 1707-1715.
- (16) Armarego, W. L. F.; Perrin, D. D. *Purification of Laboratory Chemicals*; Butterworth-Heinemann: Oxford, U.K., 1997.
- (17) Mayilmurugan, R.; Stoeckli-Evans, H.; Palaniandavar, M. *Inorg. Chem* **2008**, *47*, 6645-6658.
- (18) Geiger, R. A.; Chattopadhyay, S.; Day, V. W.; Jackson, T. A. *J. Am. Chem. Soc.* **2010**, *132*, 2821-2831.
- (19) Seo, M. S.; Kim, J. Y.; Annaraj, J.; Kim, Y.; Lee, Y.-M.; Kim, S.-J.; Kim, J.; Nam, W. *Angew. Chem. Int. Ed.* **2007**, *46*, 377-380.
- (20) Neese, F., *ORCA - an ab initio, Density Functional and Semiempirical Program Package, Version 2.8*, University of Bonn, 2009.
- (21) Becke, A. D. *J. Chem. Phys.* **1986**, *84*, 4524-4529.
- (22) Perdew, J. P. *Physical Review B* **1986**, *33*, 8822-8824.
- (23) Schäfer, A.; Horn, H.; Ahlrichs, R. *J. Chem. Phys.* **1992**, *97*, 2571-2577.
- (24) Schäfer, G.; Huber, C.; Ahlrichs, R. *J. Chem. Phys.* **1994**, *100*, 5829-5835.
- (25) Neese, F. *J. Comput. Chem.* **2003**, *24*, 1740-1747.
- (26) Sinnecker, S.; Rajendran, A.; Klamt, A.; Diedenhofen, M.; Neese, F. *J. Phys. Chem. A* **2006**, *110*, 2235-2245.

## **Chapter 5**

### **Geometric and Electronic Structures of Peroxomanganese(III) Complexes Supported by Pentadentate Amino-pyridine and -imidazole Ligands**

## 5.1 Introduction.

Mononuclear superoxo- and peroxomanganese(III) species have been proposed to form in a number of redox-active, manganese enzymes, including manganese superoxide dismutase (MnSOD),<sup>1-6</sup> manganese-dependent homoprotocatechuate 2,3-dioxygenase (MndD),<sup>7,8</sup> and the oxalate-degrading enzymes oxalate oxidase<sup>9,10</sup> and oxalate decarboxylase.<sup>11-13</sup> In addition, manganese-peroxide interactions are relevant to the dinuclear enzymes manganese catalase<sup>14</sup> and manganese ribonucleotide reductase.<sup>15</sup> Experimental evidence for a peroxomanganese(III) adduct has been obtained for MnSOD. Under high superoxide concentrations, a product-inhibited complex is formed, and this species displays absorption features consistent with a peroxomanganese(III) adduct.<sup>4,6</sup> Notably, the kinetics associated with formation and decay of this intermediate are affected by substitution of outer-sphere amino acid residues.<sup>6,16-19</sup> Rapid freeze-quench EPR experiments on MndD under single-turnover conditions identified an  $S = 5/2$  intermediate with an axial zero-field splitting parameter too large for a  $\text{Mn}^{\text{II}}$  species ( $D = 2.5 \text{ cm}^{-1}$ ).<sup>7</sup> This intermediate was formulated as a superoxomanganese(III) adduct, although a peroxomanganese(III)-(homoprotocatechuate radical) is an alternative possibility.<sup>7</sup> Because these biological peroxo- and superoxomanganese(III) species are highly unstable, relatively little is known concerning their structural, electronic, and reactivity properties.

In contrast, a variety of mononuclear peroxomanganese(III) model complexes have been described (Figure 5.1),<sup>20-29</sup> and some of these have been structurally characterized using X-ray diffraction (XRD). The crystallographically-characterized complexes are supported by the dianionic TPP ligand (TPP = *meso*-tetraphenylporphyrin),<sup>20</sup> the monoanionic, facially-coordinating  $\text{Tp}^{i\text{Pr}2}$  ligand ( $\text{Tp}^{i\text{Pr}2}$  = hydrotris(3,5-diisopropylpyrazol-1-yl)borate),<sup>21,22</sup> and the neutral TMC and 13-TMC ligands (TMC = 1,4,8,11-tetramethyl-1,4,8,11-

tetraazacyclotetradecane and 13-TMC = 1,4,7,10-tetramethyl-1,4,7,10-tetraazacyclotridecane).<sup>23,24</sup> Although the properties of these supporting ligands are rather diverse, in all cases the peroxide is bound to the Mn<sup>III</sup> ions in a side-on ( $\eta^2$ ) fashion, and the coordination sphere is completed by four other donors, leading to six-coordinate Mn<sup>III</sup> centers (Figure 5.1). Nam and co-workers have reported that the Mn<sup>III</sup> center of the [Mn<sup>III</sup>(O<sub>2</sub>)(13-TMC)]<sup>+</sup> complex can be bound by exogenous anions X<sup>-</sup> (X<sup>-</sup> = N<sub>3</sub><sup>-</sup>, NCS<sup>-</sup>, CN<sup>-</sup>, and CF<sub>3</sub>CO<sub>2</sub><sup>-</sup>).<sup>23</sup> On the basis of the greater nucleophilicity of the resulting [Mn<sup>III</sup>(O<sub>2</sub>)(13-TMC)(X)] complexes, they have suggested that anion binding may convert the peroxo from side-on to end-on, thereby retaining a six-coordinate Mn<sup>III</sup> center.<sup>23</sup> While no structural or vibrational data are available to support this proposal, density functional theory (DFT) computations predict the end-on peroxo ligand to bear significantly more negative charge, in keeping with the increase in nucleophilicity observed experimentally.<sup>23</sup> While the above species were generated using H<sub>2</sub>O<sub>2</sub> or KO<sub>2</sub>, a peroxomanganese(III) adduct was generated from a Mn<sup>II</sup> center supported by a dianionic carboxyamidopyridyl-based ligand, [Mn<sup>II</sup>(H<sub>3</sub>bupa)] (H<sub>3</sub>bupa = bis[(*N'*-*tert*-butylureayl)-*N*-ethyl]-(6-pivalamido-2-pyridylmethyl)-amine), using O<sub>2</sub> and a sacrificial reductant.<sup>28,30</sup> We have recently reported spectroscopic and theoretical studies of a series of peroxomanganese(III) adducts supported by derivatives of the diazacycloalkane ligand L<sup>7</sup>py<sub>2</sub><sup>H</sup> (L<sup>7</sup>py<sub>2</sub><sup>H</sup> = 1,4-bis(2-pyridylmethyl)-1,4-diazepane).<sup>29,31</sup> A major conclusion of one of these studies was that the L<sup>7</sup>py<sub>2</sub><sup>6-Me</sup> ligand (L<sup>7</sup>py<sub>2</sub><sup>6-Me</sup> = 1,4-bis(6-methyl-2-pyridylmethyl)-1,4-diazepane), which features pyridines with electron-donating 6-methyl substituents, leads to a more end-on bound peroxo ligand when compared to an analogous compound with the L<sup>7</sup>py<sub>2</sub><sup>H</sup> ligand.<sup>29</sup> While this spectroscopic and theoretical evidence supports the proposal that the inclusion of electron-rich

substituents can lead to peroxo ligands bound in a more end-on fashion, structural information is only available for six-coordinate peroxomanganese(III) adducts with side-on peroxo ligands.

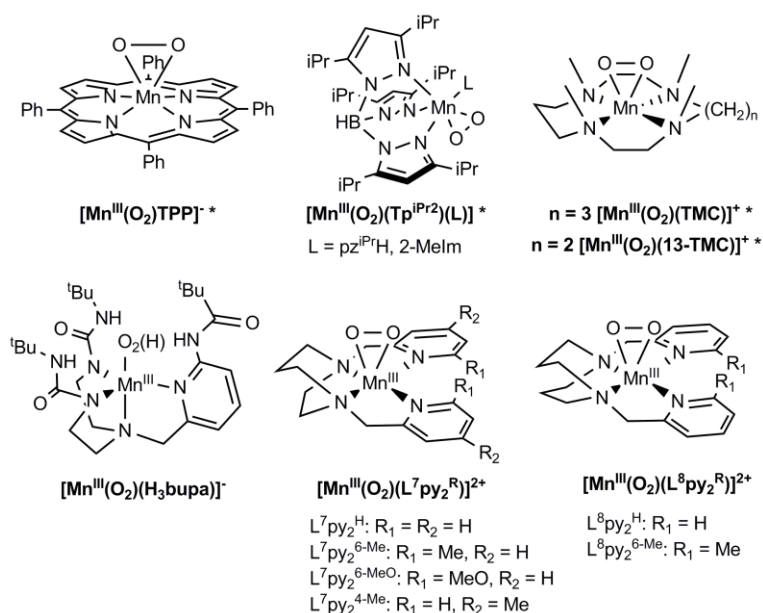


**Figure 5.1.** Mononuclear peroxomanganese(III) adducts. Complexes marked with an asterisk have been structurally characterized by X-ray diffraction.

Peroxomanganese(III) adducts with seven-coordination geometries, or with end-on peroxo ligands, could bear greater relevance to analogous enzymatic intermediates. For example, the product-inhibited form of MnSOD is generated by reaction of a five-coordinate Mn<sup>II</sup> center with superoxide (Figure 5.2, left). Thus, formation of a side-on peroxomanganese(III) adduct would result in a seven-coordinate Mn<sup>III</sup> complex, assuming none of the native ligands dissociate. Alternatively, an end-on peroxo ligand would result in a six-coordinate center. A model of the product-inhibited complex of MnSOD developed using DFT computations shows a Mn<sup>III</sup>-O<sub>2</sub> unit with a more end-on structure, with Mn-O<sub>peroxo</sub> distances of 1.80 and 2.22 Å.<sup>3</sup> The active-site Mn<sup>II</sup> ion of MndD is bound by three exogenous ligands and reacts with dioxygen in the presence of homoprotocatechuate (HPCA) substrate.<sup>7,8,32</sup> With substrate bound in the



expected bidentate fashion and assuming that none of the three proteinaceous ligands dissociate, only one coordinate site is available for interaction with oxygen. This site is occupied by water in an X-ray crystal structure (Figure 5.2, right).<sup>8</sup> Thus, the putative superoxomanganese(III) adduct observed experimentally is likely either an end-on bound six-coordinate species or a side-on bound seven-coordinate species.

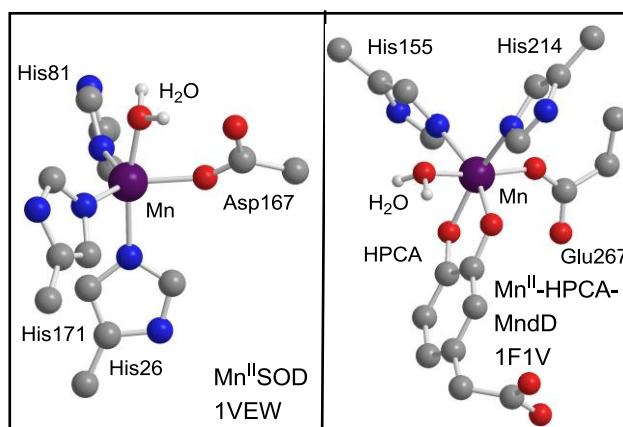
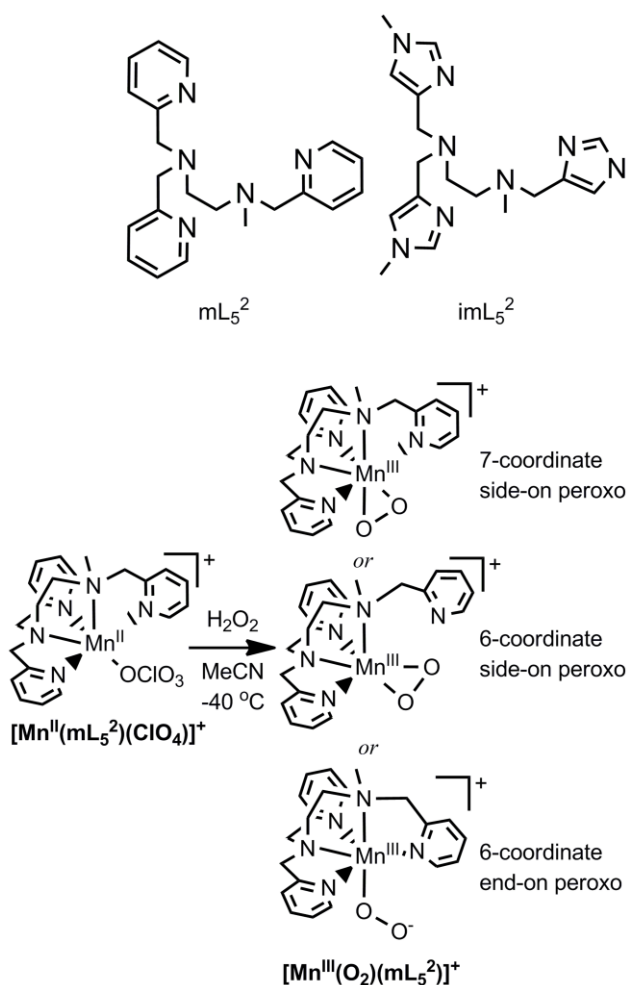


**Figure 5.2.** Active sites of  $\text{Mn}^{\text{II}}$ SOD (left) and the HPCA adduct of  $\text{Mn}^{\text{II}}$ MndD (right) derived from PDB files 1VEW and 1F1V, respectively. For clarity, only H-atoms on coordinated solvent ligands are shown.

In this chapter, we have examined the geometric and electronic structures of peroxomanganese(III) adducts supported by two pentadentate ligands (Scheme 5.1):  $\text{mL}_5^2$  (*N*-methyl-*N,N,N'*-tris(pyridin-2-ylmethyl)ethane-1,2-diamine) and  $\text{imL}_5^2$  (*N*-methyl-*N,N,N'*-tris((1-methyl-1H-imidazol-4-yl)methyl)ethane-1,2-diamine). Previous spectroscopic and reactivity studies of  $[\text{Mn}^{\text{III}}(\text{O}_2)(\text{mL}_5^2)]^+$  have clearly established the formulation of this species,<sup>26,27</sup> and results reported herein support the formulation of the new  $[\text{Mn}^{\text{III}}(\text{O}_2)(\text{imL}_5^2)]^+$  complex. This current study seeks to answer two important questions: Are the peroxomanganese(III) complexes supported by these pentadentate ligands six- or seven-coordinate? If the complexes are six-coordinate, which donor group is dissociating? On the basis of electronic absorption (Abs), MCD, VTVH MCD spectroscopies, as well as DFT and multireference *ab initio* computations,

we conclude that these complexes contain a six-coordinate  $\text{Mn}^{\text{III}}$  center with a side-on peroxo ligand and a dissociated pyridine (or imidazole). Thus, there is a strong preference for six-coordinate geometry for peroxomanganese(III) species, and end-on peroxomanganese(III) units are predicted to be unstable and, potentially, highly reactive. The relevance of these findings with respect to biological manganese centers is discussed.

Scheme 5.1



## 5.2 Results and Analysis.

**5.2.1 Comparison of Abs Spectra.** Figure 5.3 shows an overlay plot of the Abs spectra of the peroxomanganese(III) complexes,  $[\text{Mn}^{\text{III}}(\text{O}_2)(\text{mL}_5^2)]^+$  and  $[\text{Mn}^{\text{III}}(\text{O}_2)(\text{imL}_5^2)]^+$  at  $-20\text{ }^\circ\text{C}$ . As previously described,<sup>26,27</sup> the Abs spectrum of  $[\text{Mn}^{\text{III}}(\text{O}_2)(\text{mL}_5^2)]^+$  displays a prominent band at  $\sim 17\,200\text{ cm}^{-1}$  and a shoulder at  $\sim 23\,500\text{ cm}^{-1}$  ( $\epsilon = 89$  and  $90\text{ M}^{-1}\text{cm}^{-1}$ , respectively). For these compounds, no other Abs features are observed down to  $9\,100\text{ cm}^{-1}$ .

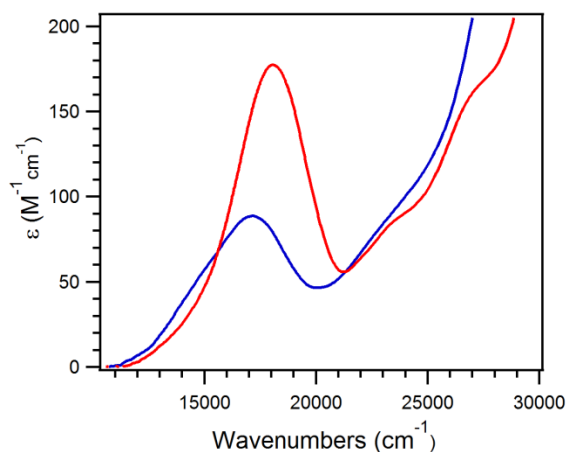


**Figure 5.3.** Electronic Abs spectra of  $[\text{Mn}^{\text{III}}(\text{O}_2)(\text{mL}_5^2)]^+$  (blue) and  $[\text{Mn}^{\text{III}}(\text{O}_2)(\text{imL}_5^2)]^+$  (red) at  $-20\text{ }^\circ\text{C}$ .

The lowest-energy Abs feature observed for  $[\text{Mn}^{\text{III}}(\text{O}_2)(\text{imL}_5^2)]^+$  is at  $\sim 18\,000\text{ cm}^{-1}$ , and the intensity of this band is roughly twice that of the low-energy bands of  $[\text{Mn}^{\text{III}}(\text{O}_2)(\text{mL}_5^2)]^+$  (Figure 5.3). Two well-resolved shoulders are observed for  $[\text{Mn}^{\text{III}}(\text{O}_2)(\text{imL}_5^2)]^+$  at  $\sim 23\,200$  and  $27\,000\text{ cm}^{-1}$ . Notably  $[\text{Mn}^{\text{III}}(\text{O}_2)(\text{mL}_5^2)]^+$  show a single shoulder at  $23\,000\text{ cm}^{-1}$  and the onset of more intense features at  $>25\,000\text{ cm}^{-1}$ . We attribute this difference to the presence of pyridines in the  $\text{mL}_5^2$  ligand, which likely give rise to charge-transfer transitions to low-lying  $\pi^*$  pyridine orbitals and intra-ligand transitions in the near-UV and UV regions that will obscure weaker Abs bands.

**5.2.2 Variable-Temperature Abs Data for  $[\text{Mn}^{\text{III}}(\text{O}_2)(\text{imL}_5^2)]^+$ .** As the temperature is decreased from 280 to 150 K, the Abs features of  $[\text{Mn}^{\text{III}}(\text{O}_2)(\text{imL}_5^2)]^+$  at  $\sim 27\,000$  and  $18\,000\text{ cm}^{-1}$  gain intensity (Figure 5.4), and the lower-energy band red-shifts by  $\sim 1\,500\text{ cm}^{-1}$ . The shoulder at  $\sim 23\,200\text{ cm}^{-1}$  changes neither energy nor intensity from 280 to 150 K. No isosbestic points are observed. Such behavior is reminiscent of that reported for  $[\text{Mn}^{\text{III}}(\text{O}_2)(\text{Tp}^{\text{iPr}})(\text{pz}^{\text{iPrH}})]^+$  ( $\text{pz}^{\text{iPrH}} = 3,5\text{-diisopropylpyrazole}$ ), where blue ( $\lambda_{\text{max}} = 17\,150\text{ cm}^{-1}$ ) and brown ( $\lambda_{\text{max}} = 17\,800\text{ cm}^{-1}$ ) isomers are formed at 195 and 253 K, respectively.<sup>21</sup> X-ray crystal structures of these isomers revealed a hydrogen-bond to the peroxo ligand in the blue form that gives rise to asymmetric Mn–O distances of 1.841 and 1.878 Å. In contrast, the brown isomer lacks this hydrogen-bond and displays symmetric Mn–O distances of 1.850 and 1.851 Å.<sup>21</sup> We propose that similar structural changes, though perhaps not involving intramolecular hydrogen-bonding, can account for the temperature dependence of the Abs spectrum of  $[\text{Mn}^{\text{III}}(\text{O}_2)(\text{imL}_5^2)]^+$ . In support, the absorption bands of  $[\text{Mn}^{\text{III}}(\text{O}_2)(\text{imL}_5^2)]^+$  display a near-linear increase in intensity as the temperature is lowered (Figure A.5.1). We attribute such behavior to thermal changes in covalency parameters, associated with a decrease in average metal-ligand bond lengths as temperature is lowered.<sup>33</sup> For metal centered *d-d* transitions that steal intensity from ligand-to-metal charge transfer transitions, shorter, more covalent metal-ligand bonds promote this intensity-gaining mechanism, leading to an increase in intensity of ligand-field transitions at lower temperatures.

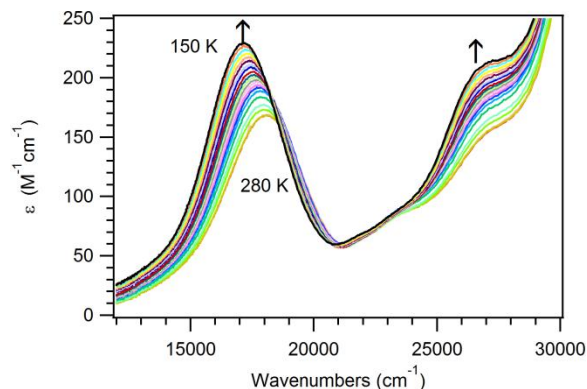


**Figure 5.4.** Abs spectra of  $[\text{Mn}^{\text{III}}(\text{O}_2)(\text{imL}_5^2)]^+$  from 280 K – 150 K collected in 5 K increments.

**5.2.3 MCD Spectroscopy.** To compare the  $[\text{Mn}^{\text{III}}(\text{O}_2)(\text{mL}_5^2)]^+$  and  $[\text{Mn}^{\text{III}}(\text{O}_2)(\text{imL}_5^2)]^+$  complexes in more detail, low-temperature MCD data were collected (Figure 5.5). For all complexes, the intensities of the MCD features between 11 000 and 34 000  $\text{cm}^{-1}$  show inverse temperature dependence (C-term behavior), consistent with the paramagnetic ground states of these compounds. The MCD spectrum of  $[\text{Mn}^{\text{III}}(\text{O}_2)(\text{imL}_5^2)]^+$  is considerably simpler than that of  $[\text{Mn}^{\text{III}}(\text{O}_2)(\text{mL}_5^2)]^+$  showing only three maxima (Figure 5.5). We attribute this to the lack of pyridines in the  $\text{imL}_5^2$  ligand, which results in fewer excited states with energies in the visible to near-UV region.

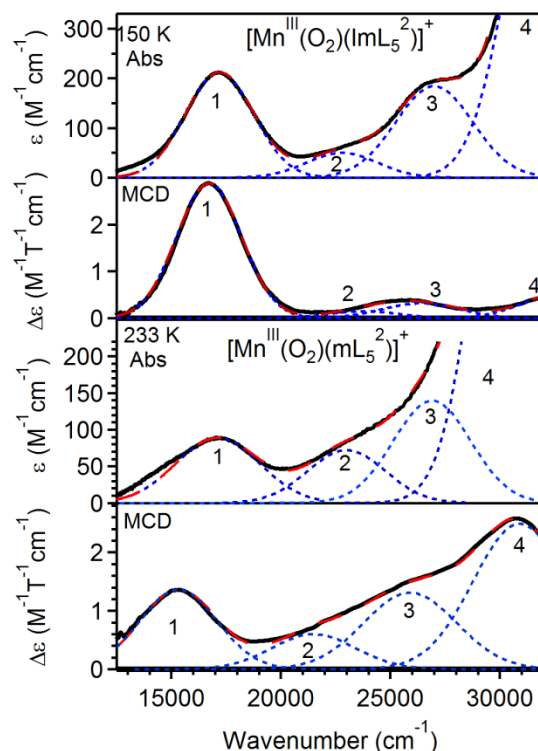


**Figure 5.5.** Abs and 4.5 K, 7 T MCD spectra of  $[\text{Mn}^{\text{III}}(\text{O}_2)(\text{imL}_5^2)]^+$  (top two panels) and  $[\text{Mn}^{\text{III}}(\text{O}_2)(\text{mL}_5^2)]^+$  (middle two panels). Abs data for  $[\text{Mn}^{\text{III}}(\text{O}_2)(\text{mL}_5^2)]^+$  were collected at 253 K in MeCN solution, whereas corresponding data for  $[\text{Mn}^{\text{III}}(\text{O}_2)(\text{imL}_5^2)]^+$  was collected for a frozen solution in butyronitrile at 150 K. MCD data for  $[\text{Mn}^{\text{III}}(\text{O}_2)(\text{imL}_5^2)]^+$  were collected from frozen butyronitrile solutions; MCD data for  $[\text{Mn}^{\text{III}}(\text{O}_2)(\text{mL}_5^2)]^+$  was of a 50:50 vol:vol ethanol:butyronitrile mixture. Individual transitions (blue dotted lines) and their sums (red dashed lines) obtained from an iterative Gaussian fit of the data sets, are displayed on their respective spectra. Complete fit parameters are included in Supporting Information.

Iterative Gaussian deconvolutions of the Abs and MCD data shown in Figure 5.5 were performed to determine the minimum number of electronic transitions responsible for the spectral features of  $[\text{Mn}^{\text{III}}(\text{O}_2)(\text{mL}_5^2)]^+$  and  $[\text{Mn}^{\text{III}}(\text{O}_2)(\text{imL}_5^2)]^+$ . Because the Abs and MCD data were collected at different temperatures, the positions of the Gaussian bands were allowed to shift by up to  $1\,000\text{ cm}^{-1}$ , but in most cases shifts were significantly smaller. The energies obtained from deconvolution of these data sets are collected in Table 5.1, along with oscillator strengths for the Abs bands. Complete information regarding Abs and MCD deconvolutions are

in the appendix (Table A.5.11). Because of the apparent simplicity of the Abs and MCD data for  $[\text{Mn}^{\text{III}}(\text{O}_2)(\text{imL}_5^2)]^+$ , the spectral analysis of this complex will be discussed first.

**Table 5.1.** Energies ( $\text{cm}^{-1}$ ) and oscillator strengths ( $f_{\text{exp}} \times 10^3$ ) of electronic transitions for  $[\text{Mn}^{\text{III}}(\text{O}_2)(\text{imL}_5^2)]^+$  and  $[\text{Mn}^{\text{III}}(\text{O}_2)(\text{mL}_5^2)]^+$ . Obtained from Gaussian deconvolutions of experimental Abs and MCD spectra

$[\text{Mn}^{\text{III}}(\text{O}_2)(\text{imL}_5^2)]^+$			$[\text{Mn}^{\text{III}}(\text{O}_2)(\text{mL}_5^2)]^+$		
band	energy	$f_{\text{exp}} \times 10^3$	band	energy	$f_{\text{exp}} \times 10^3$
1	Abs: 17 200 MCD: 16 720	3.58	1	Abs: 17 120 MCD: 15 325	1.84
2	Abs: 22 800 MCD: 23 800	0.883	2	Abs: 23 000 MCD: 21 500	1.38
3	Abs: 27 000 MCD: 26 400	3.53	3	Abs: 26 900 MCD: 25 900	2.68
4	Abs: 32 200 MCD: 32 800	13.8	4	Abs: 31 000 MCD: 30 900	14.39

**5.2.4 Spectral Deconvolutions of  $[\text{Mn}^{\text{III}}(\text{O}_2)(\text{imL}_5^2)]^+$ .** Spectral deconvolution for  $[\text{Mn}^{\text{III}}(\text{O}_2)(\text{imL}_5^2)]^+$  reveals at least four bands from 13 000 to 33 000  $\text{cm}^{-1}$ . Band 1 gives rise to the prominent Abs and MCD feature at  $\sim 16\,700\text{ cm}^{-1}$ , that shows a strong blue-shift as temperature is increased (Figure 5.4). Bands 2 and 3 are responsible for the other two Abs maxima at  $\sim 23\,200$  and  $27\,000\text{ cm}^{-1}$ , and contribute to a weak MCD feature centered at  $\sim 26\,000\text{ cm}^{-1}$ . Band 4 accounts in part for the rising Abs intensity at  $\sim 30\,000\text{ cm}^{-1}$ , but is responsible for a weak MCD feature. Because of the expected low symmetry of the  $\text{Mn}^{\text{III}}$  center in  $[\text{Mn}^{\text{III}}(\text{O}_2)(\text{imL}_5^2)]^+$ , four  $d-d$  transitions are anticipated for this  $d^4$  metal. Band 1 is the lowest energy feature observed for  $[\text{Mn}^{\text{III}}(\text{O}_2)(\text{imL}_5^2)]^+$ , and, considering its relatively large MCD intensity as well as its temperature-dependent Abs intensity, this band is assigned as the lowest energy  $d-d$  transition, which, using symmetry labels of the parent octahedral point group, involves a one-electron excitation within the  $e_g$ -derived orbitals. For peroxomanganese(III) complexes, the splitting of these orbitals arises because of the stronger  $\sigma$ -interactions with the peroxo ligands relative to the N-donor ligands.<sup>29</sup> The low oscillator strengths of bands 2 and 3 (Table 5.1) lead us to tentatively attributed these bands to  $\text{Mn}^{\text{III}}$   $d-d$  transitions as well, although

these transitions, especially band 2 which carries almost negligible MCD intensity, could also be weak peroxo-to-manganese(III) charge-transfer (CT) bands.<sup>29</sup> Given its considerably larger Abs intensity, band 4 is assigned as a peroxo-to-manganese(III) CT transition.

**5.2.5 Spectral Deconvolutions of  $[\text{Mn}^{\text{III}}(\text{O}_2)(\text{mL}_5^2)]^+$ .** The Abs and MCD spectra of  $[\text{Mn}^{\text{III}}(\text{O}_2)(\text{mL}_5^2)]^+$  are both well fit with a minimum of four Gaussian bands between 12 000 and 32 000  $\text{cm}^{-1}$  (Figure 5.5). The energies of these bands are very similar to those of  $[\text{Mn}^{\text{III}}(\text{O}_2)(\text{imL}_5^2)]^+$  (Table 5.1), as anticipated on the basis of the qualitative similarities in the absorption spectra of these complexes. Thus, the tentative band assignments discussed above for  $[\text{Mn}^{\text{III}}(\text{O}_2)(\text{imL}_5^2)]^+$  are expected to transfer to the  $[\text{Mn}^{\text{III}}(\text{O}_2)(\text{mL}_5^2)]^+$  complex as well. Overall, the Gaussian analyses of Abs and MCD data collected for these peroxomanganese(III) adducts lends further credence to our conclusion that the  $\text{Mn}^{\text{III}}$  centers in these complexes share a common geometry.

**5.2.6 VTVH MCD Spectroscopy.** Variable-temperature, variable-field (VTVH) MCD spectroscopy was used to determine ground-state zero-field splitting (ZFS) parameters and transition polarizations for these peroxomanganese(III) complexes. In these experiments, the intensity of an MCD signal at a given wavelength is monitored as a function of magnetic field at various fixed temperatures. For  $S > 1/2$  systems, the saturation behavior of these curves reflect the ground-state  $g$ -values and axial ( $D$ ) and rhombic ( $E/D$ ) zero-field splitting (ZFS) parameters as well as transition polarization.<sup>34,35</sup> VTVH MCD curves collected at several wavelengths for the same sample are thus useful for evaluating the polarizations of different transitions. For example, VTVH MCD data collected for bands 1 and 4 of  $[\text{Mn}^{\text{III}}(\text{O}_2)(\text{mL}_5^2)]^+$  (16 700 and 30 800  $\text{cm}^{-1}$ ) show distinct saturation behavior (Figure 5.6, A and B), with the MCD signal saturating more rapidly for band 1. Fits of these data sets using ZFS parameters and  $g$ -values obtained by EPR



experiments ( $g_{\text{iso}} = 2.0$ ,  $D = -2.9 \text{ cm}^{-1}$  and  $E/D = 0.075$ )<sup>27</sup> reveal that band 1 is predominantly  $y$ -polarized with a minor  $x$ -component (15%  $x$ -, 81%  $y$ -, and 5%  $z$ -polarization), whereas band 4 is nearly 100%  $z$ -polarized (<1%  $x$ , <1%  $y$ -, and 99%  $z$ -polarization). VTVH MCD data collected for band 3 ( $26\,700 \text{ cm}^{-1}$ ) appear almost identical to those of band 4, indicating that this band is also  $z$ -polarized (Table A.5.12).

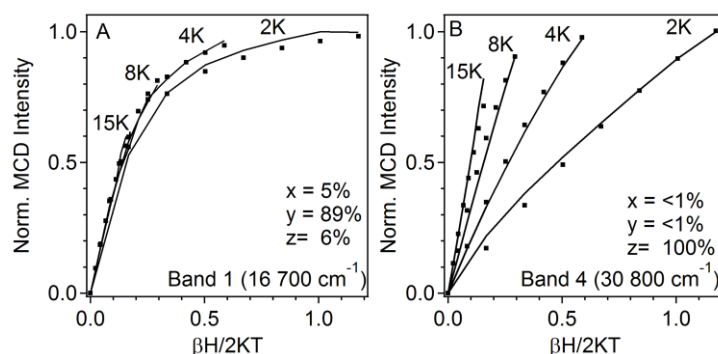


**Figure 5.6.** VTVH MCD data collected for  $[\text{Mn}^{\text{III}}(\text{O}_2)(\text{mL}_5^2)]^+$  (dots) and fits (solid lines) at  $16\,700$  (left) and  $30\,800 \text{ cm}^{-1}$  (right) using  $D = -2.9 \text{ cm}^{-1}$ ,  $E/D = 0.075$ ,  $g_{\text{iso}} = 2.0$ , and polarizations listed in the insets.

Because ZFS parameters have not been previously determined for  $[\text{Mn}^{\text{III}}(\text{O}_2)(\text{imL}_5^2)]^+$  VTVH MCD data for this complex was systematically fit to extract both ZFS parameters and transition polarizations. In this protocol,  $D$  and  $E/D$  were respectively varied from  $-3$  to  $3 \text{ cm}^{-1}$  and  $0$  to  $0.3$  in increments of  $0.5$  and  $0.05 \text{ cm}^{-1}$ .<sup>3</sup> Transition-moment products were optimized to fit the experimental data for a given set of  $D$  and  $E/D$  values. The goodness of fit was assessed by the  $\chi^2$  value, which is the sum of the squares of the differences between experimental and fit data sets. All data sets were best fit assuming an  $S = 2$  ground state. To evaluate the accuracy of this protocol in determining ZFS parameters for peroxomanganese(III) complexes, it was first applied to  $[\text{Mn}^{\text{III}}(\text{O}_2)(\text{mL}_5^2)]^+$ . Figure A.5.3 shows contours plots of  $\chi^2$  as a function of  $D$  and  $E/D$  for VTVH MCD data collected at bands 3 and 4 ( $26\,700$  and  $30\,800 \text{ cm}^{-1}$ , respectively). Excellent fits are obtained for  $|D| = 2.5 - 3 \text{ cm}^{-1}$  and  $E/D = 0.05 - 0.30$ . Thus, for this system,

the goodness of fit is strongly dependent on the magnitude of  $D$ , but quite insensitive to the sign of  $D$  and fairly insensitive to the rhombicity. Nonetheless, the ZFS parameters determined by EPR spectroscopy ( $D = -2.9 \text{ cm}^{-1}$  and  $E/D = 0.075$ ) fall within this range.<sup>26,27</sup> We thus conclude that this protocol will yield accurate values for the magnitude of  $D$  for  $[\text{Mn}^{\text{III}}(\text{O}_2)(\text{imL}_5^2)]^+$ .

VTVH MCD data collected for  $[\text{Mn}^{\text{III}}(\text{O}_2)(\text{imL}_5^2)]^+$  at  $16\,700 \text{ cm}^{-1}$  were well fit ( $\chi^2 < 0.15$ ) within the two ranges  $D = -1.5 - -2 \text{ cm}^{-1}$ ,  $E/D = 0.1 - 0.3$  and  $D = +2$ ,  $E/D = 0.1 - 0.25$  (Figure A.5.4, left). However, the acceptable range for  $D < 0 \text{ cm}^{-1}$  can be narrowed to  $D = -2 \text{ cm}^{-1}$ ,  $E/D = 0.25 - 0.30$  when data collected at  $25\,600 \text{ cm}^{-1}$  are also considered (Figure A.5.4, right). The magnitude of  $D$  is reduced relative to that of  $[\text{Mn}^{\text{III}}(\text{O}_2)(\text{mL}_5^2)]^+$ , but the sign of  $D$  cannot be unambiguously assigned. Given the strong similarities between the Abs and MCD data of these complexes, as well as the fact that all ZFS parameters determined for peroxomanganese(III) adducts to date show  $D < 0$ ,<sup>26-29</sup> we conclude that  $[\text{Mn}^{\text{III}}(\text{O}_2)(\text{imL}_5^2)]^+$  likewise has negative  $D$  values (Table 5.2). Under this assumption, and using ZFS parameters giving optimal  $\chi^2$  values, transition polarizations were determined for the different MCD features of  $[\text{Mn}^{\text{III}}(\text{O}_2)(\text{imL}_5^2)]^+$  (Table A.512).

**Table 5.2.** Axial ( $D$ ) and Rhombic ( $E/D$ ) Zero-Field Splitting Parameters for Peroxomanganese(III) Complexes

	$D \text{ (cm}^{-1}\text{)}$	$E/D$	reference
$[\text{Mn}^{\text{III}}(\text{O}_2)(\text{mL}_5^2)]^+$	-2.9	0.075	26,27
$[\text{Mn}^{\text{III}}(\text{O}_2)(\text{imL}_5^2)]^+$	-2.0	0.25 – 0.30	<sup>a</sup>
$[\text{Mn}^{\text{III}}(\text{O}_2)(\text{L}^7\text{py}_2^{\text{H}})]^{+b}$	-2	0.13	29
$[\text{Mn}^{\text{III}}(\text{O}_2)(\text{L}^7\text{py}_2^{6\text{-Me}})]^{+c}$	-3	0.05	29
$[\text{Mn}^{\text{III}}(\text{O}_2)(\text{H}_3\text{bupa})]^{-d}$	-2.0	0.13	28

<sup>a</sup>This work.

Taken together, the results of the MCD and VTVH MCD experiments reveal that the ground- and excited-state properties of these complexes are quite similar, suggesting only minor

differences in coordination geometry. Importantly, these spectroscopic data can provide a basis for evaluating a variety of hypothetical models developed using DFT computations through comparison of computed and experimental spectroscopic parameters.

### 5.2.7 Density Functional Theory Computations. Hypothetical Structures for

$[\text{Mn}^{\text{III}}(\text{O}_2)(\text{mL}_5^2)]^+$ . Several structures were considered as hypothetical models of  $[\text{Mn}^{\text{III}}(\text{O}_2)(\text{mL}_5^2)]^+$ : i) a seven-coordinate  $\text{Mn}^{\text{III}}$  center with a side-on peroxo ligand and  $\text{mL}_5^2$  bound in a pentadentate fashion, ii) a six-coordinate complex with an end-on peroxo ligand and  $\text{mL}_5^2$  bound in a pentadentate fashion, and iii) a six-coordinate complex with a side-on peroxo ligand and  $\text{mL}_5^2$  bound in a tetradentate fashion (*i.e.*, with a dissociated amine or pyridine group). Notably, dissociation of a pyridine arm for  $\text{mL}_5^2$  was previously observed in the X-ray crystal structure of  $[\text{Fe}_2(\mu\text{-O})(\text{Cl})_2(\text{mL}_5^2)_2](\text{NEt}_4)_2$ .<sup>36</sup> We first examined the possibility of side-on versus end-on peroxo coordination with the  $\text{mL}_5^2$  ligand bound in its commonly observed pentadentate binding mode. Starting geometries were obtained by modifying the crystal structure coordinates of  $[\text{Mn}^{\text{II}}(\text{ClO}_4)(\text{mL}_5^2)]^+$  by replacing perchlorate with a peroxo ligand in either a side-on or end-on geometry. In both cases, these starting geometries yielded the same structure upon convergence (referred to as  $[\text{Mn}^{\text{III}}(\text{O}_2)(\text{mL}_5^2)\text{-N(1)}]^+$ ; see Figure 5.7): a side-on  $\text{Mn}^{\text{III}}\text{-O}_2$  adduct with Mn–O distances of 1.873 and 1.880 Å (Table 5.3). In this structure, the amine nitrogen *trans* to the peroxo unit, N(1), displays a long Mn–N(1) distance of 2.62 Å. To evaluate the energetic and structural consequences associated with conversion from the  $[\text{Mn}^{\text{III}}(\text{O}_2)(\text{mL}_5^2)\text{-N(1)}]^+$  geometry to a  $\text{Mn}^{\text{III}}\text{-O}_2$  complex with an end-on peroxo, we performed a relaxed surface scan where one Mn–O distance was elongated from 1.85 to 2.60 Å in 0.1 Å increments. As shown in Figure A.5.6 (top), elongation of the Mn–O distance leads to a substantial increase in energy, indicating that the side-on peroxo binding mode is strongly favored. The O–O bond

length decreases from 1.413 to 1.363 Å as one Mn–O distance is elongated (Figure A.5.5, center). The shortest O–O distance is midway between common ranges observed for peroxo and superoxo ligands (1.50 – 1.40 and 1.30 – 1.20 Å, respectively). Notably the elongation in one Mn–O distance is associated with a shortening of the Mn–N(1) bond length by 0.3 Å over the course of the surface scan (Figure A.5.6, bottom). A complementary surface scan of Mn–N(1) distance showed a similar inverse correlation between the Mn–N(1) distance and one Mn–O bond length (Figure A.5.7, which is taken to indicate the preference for hexacoordination for the Mn<sup>III</sup> center. In either case, elongation of one Mn–O bond by more than ~0.2 Å results in models with significantly higher energies relative to [Mn<sup>III</sup>(O<sub>2</sub>)(mL<sub>5</sub><sup>2</sup>)-N(1)]<sup>+</sup>.

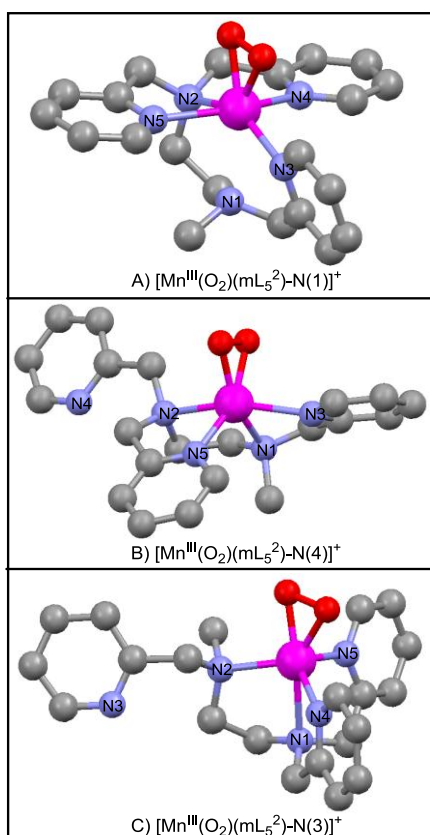


**Figure 5.7.** Hypothetical structures of [Mn<sup>III</sup>(O<sub>2</sub>)(mL<sub>5</sub><sup>2</sup>)]<sup>+</sup> complexes developed using DFT computations.

**Table 5.3.** Relative Energies (kcal/mol) and Mn-Ligand Bond Lengths (Å) for Four Hypothetical Models of  $[\text{Mn}^{\text{III}}(\text{O}_2)(\text{mL}_5^2)]^+$  Developed using DFT Computations.

	Relative Energy	Mn-O	O-O	Mn-N(1)	Mn-N(2)	Mn-N(3)	Mn-N(4)	Mn-N(5)
$[\text{Mn}^{\text{III}}(\text{O}_2)(\text{mL}_5^2)\text{-N}(1)]^+$	17.9	1.899	1.427	2.610	2.349	2.187	2.275	2.272
	19.3 <sup>a</sup>	1.894						
$[\text{Mn}^{\text{III}}(\text{O}_2)(\text{mL}_5^2)\text{-N}(4)]^+$	0	1.850	1.433	2.204	2.368	2.285	5.209	2.095
	0 <sup>a</sup>	1.848						
$[\text{Mn}^{\text{III}}(\text{O}_2)(\text{mL}_5^2)\text{-N}(3)]^+$	6.5	1.873	1.422	2.444	2.226	5.137	2.167	2.244
	7.6 <sup>a</sup>	1.864						
$[\text{Mn}^{\text{III}}(\text{O}_2)(\text{imL}_5^2)\text{-N}(1)]^+$	25.1	1.875	1.419	2.809	2.460	2.118	2.268	2.268
	25.3 <sup>a</sup>	1.869						
$[\text{Mn}^{\text{III}}(\text{O}_2)(\text{imL}_5^2)\text{-N}(4)]^+$	7.2	1.855	1.431	2.236	2.404	2.281	5.489	2.084
	5.3 <sup>a</sup>	1.847						
$[\text{Mn}^{\text{III}}(\text{O}_2)(\text{imL}_5^2)\text{-N}(3)]^+$	0	1.863	1.429	2.671	2.339	5.395	2.099	2.097
	0 <sup>a</sup>	1.860						

<sup>a</sup> Calculation of total energy included solvation effects incorporated using the COSMO method.

Given the clear preference for both side-on peroxo binding and a six-coordinate  $\text{Mn}^{\text{III}}$  center, we next evaluated the possibility of dissociation of one of the pyridine rings of  $\text{mL}_5^2$  through two relaxed surface scans. In these calculations the Mn–N(4) and Mn–N(3) distances (see Figure 5.7 for atom labeling) were elongated through rotation of the appropriate pyridine rings. In both scans, local minima were found that correspond to six-coordinate complexes with side-on peroxo ligands and dissociated pyridines. These structures are referred to as  $[\text{Mn}^{\text{III}}(\text{O}_2)(\text{mL}_5^2)\text{-N}(4)]^+$  and  $[\text{Mn}^{\text{III}}(\text{O}_2)(\text{mL}_5^2)\text{-N}(3)]^+$  for dissociated N(3) and N(4) atoms, respectively. These structures were subjected to full geometry optimization, with no structural parameters fixed, to provide an even comparison with  $[\text{Mn}^{\text{III}}(\text{O}_2)(\text{mL}_5^2)\text{-N}(1)]^+$ . The fully optimized models of  $[\text{Mn}^{\text{III}}(\text{O}_2)(\text{mL}_5^2)\text{-N}(4)]^+$  and  $[\text{Mn}^{\text{III}}(\text{O}_2)(\text{mL}_5^2)\text{-N}(3)]^+$  are lower in energy than  $[\text{Mn}^{\text{III}}(\text{O}_2)(\text{mL}_5^2)\text{-N}(1)]^+$  by ~20 and 14 kcal/mol, clearly showing that pyridine dissociation is favored for this species. The relative energies show a very small dependence on solvation effects, which were incorporated using the COSMO method (Table 5.3). Given the expected accuracy of total energies obtained by B3LYP DFT calculations for transition metal systems (~5

kcal/mol),<sup>37</sup> both  $[\text{Mn}^{\text{III}}(\text{O}_2)(\text{mL}_5^2)\text{-N}(4)]^+$  and  $[\text{Mn}^{\text{III}}(\text{O}_2)(\text{mL}_5^2)\text{-N}(3)]^+$  appear to be reasonable models.

The optimized structures of  $[\text{Mn}^{\text{III}}(\text{O}_2)(\text{mL}_5^2)\text{-N}(4)]^+$  and  $[\text{Mn}^{\text{III}}(\text{O}_2)(\text{mL}_5^2)\text{-N}(3)]^+$  reveal the coordinative flexibility of the  $\text{mL}_5^2$  ligand (Figure 5.7 and Table 5.3). The  $\text{Mn}^{\text{III}}$  center of  $[\text{Mn}^{\text{III}}(\text{O}_2)(\text{mL}_5^2)\text{-N}(4)]^+$  is in a distorted octahedral geometry, with  $\text{N}(2)\text{-Mn-N}(3)$  and  $\text{N}(1)\text{-Mn-N}(5)$  angles of  $156^\circ$  and  $101^\circ$ . With regards to the  $\text{Mn}^{\text{III}}$  coordination geometry,  $[\text{Mn}^{\text{III}}(\text{O}_2)(\text{mL}_5^2)\text{-N}(4)]^+$  is very similar to the XRD structures of  $[\text{Mn}^{\text{III}}(\text{O}_2)(12\text{-TMC})]^+$  and  $[\text{Mn}^{\text{III}}(\text{O}_2)(14\text{-TCM})]^+$ ,<sup>23,24</sup> as well as the DFT-computed structures of  $[\text{Mn}^{\text{III}}(\text{O}_2)(\text{L}^7\text{py}_2^{\text{R}})]^+$  complexes (Figure 5.1).<sup>29,31</sup> In contrast, the N ligands in  $[\text{Mn}^{\text{III}}(\text{O}_2)(\text{mL}_5^2)\text{-N}(3)]^+$  are bound in a tripodal fashion, with  $\text{N}(1)$  occupying the basal position and  $\text{N}(2)$ ,  $\text{N}(4)$ , and  $\text{N}(5)$  defining an equatorial plane. The complete coordination geometry around the  $\text{Mn}^{\text{III}}$  center is thus rather similar to that proposed for  $[\text{Mn}^{\text{III}}(\text{O}_2)(\text{H}_2\text{bupa})]^-$ , although the latter complex contains a dianionic ligand and likely possesses second-sphere H-bonding interactions with the peroxo moiety (Figure 1).<sup>28,30</sup>

**5.2.8 Spectroscopic Properties of  $[\text{Mn}^{\text{III}}(\text{O}_2)(\text{mL}_5^2)\text{-N}(4)]^+$  and  $[\text{Mn}^{\text{III}}(\text{O}_2)(\text{mL}_5^2)\text{-N}(3)]^+$ .** To evaluate the validity of the  $[\text{Mn}^{\text{III}}(\text{O}_2)(\text{mL}_5^2)\text{-N}(4)]^+$  and  $[\text{Mn}^{\text{III}}(\text{O}_2)(\text{mL}_5^2)\text{-N}(3)]^+$  models, the TD-DFT method was used to determine electronic transition energies and oscillator strengths. The Abs spectra obtained from these computations are shown in Figure 5.8, and the experimental spectrum is included for comparison. The TD-DFT-computed Abs spectra of  $[\text{Mn}^{\text{III}}(\text{O}_2)(\text{mL}_5^2)\text{-N}(4)]^+$  and  $[\text{Mn}^{\text{III}}(\text{O}_2)(\text{mL}_5^2)\text{-N}(3)]^+$  both contain sets of bands at  $\sim 18\,000$  and  $23\,500\text{ cm}^{-1}$  (bands *i* and *ii*) that are in good agreement with the experimental Abs spectrum of  $[\text{Mn}^{\text{III}}(\text{O}_2)(\text{mL}_5^2)]^+$ , which shows a band at  $\sim 17\,300\text{ cm}^{-1}$ , a shoulder at  $\sim 23\,500\text{ cm}^{-1}$ , and more intense features at higher energy. However, the intensity ratios of bands *i* and *ii* are dramatically

different for  $[\text{Mn}^{\text{III}}(\text{O}_2)(\text{mL}_5^2)\text{-N(4)}]^+$  and  $[\text{Mn}^{\text{III}}(\text{O}_2)(\text{mL}_5^2)\text{-N(3)}]^+$  (0.06:1 and 0.80:1, respectively). Only the latter is in reasonable agreement with the  $\sim 1:1$  experimental ratio. Band *i* of  $[\text{Mn}^{\text{III}}(\text{O}_2)(\text{mL}_5^2)\text{-N(3)}]^+$  is predominantly *y*-polarized with a slight *x*-component (14% *x*-, 85% *y*-, and <1% *z*-polarization), in excellent agreement with analysis of VTVH MCD data collected for band 1 (15% *x*-, 81% *y*-, and 5% *z*-polarization; see Figure 5.6). In contrast, band *i* of  $[\text{Mn}^{\text{III}}(\text{O}_2)(\text{mL}_5^2)\text{-N(4)}]^+$  is *yz*-polarized (4% *x*-, 67% *y*-, and 29% *z*-polarization), inconsistent with experimental data. On the basis of the agreement between experimental and TD-DFT-computed electronic transition energies, oscillator strengths, and polarizations  $[\text{Mn}^{\text{III}}(\text{O}_2)(\text{mL}_5^2)\text{-N(3)}]^+$  is a better model for  $[\text{Mn}^{\text{III}}(\text{O}_2)(\text{mL}_5^2)]^+$ .

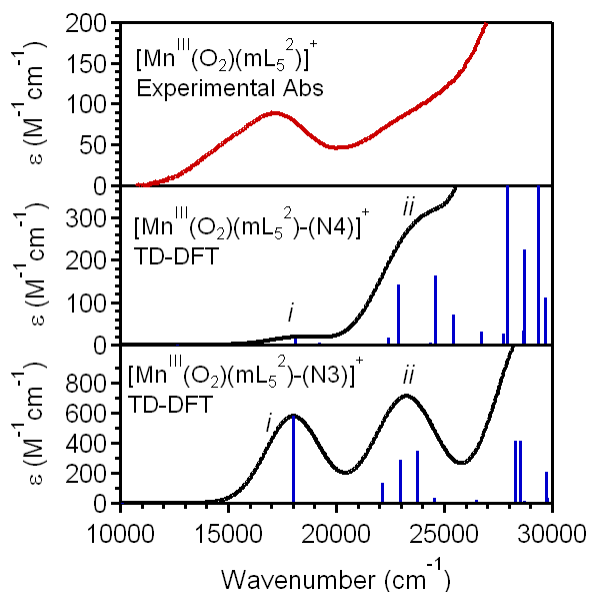


**Figure 5.8.** Experimental electronic Abs spectrum of  $[\text{Mn}^{\text{III}}(\text{O}_2)(\text{mL}_5^2)]^+$  (top) and TD-DFT-computed Abs spectra for  $[\text{Mn}^{\text{III}}(\text{O}_2)(\text{mL}_5^2)\text{-N(4)}]^+$  (center) and  $[\text{Mn}^{\text{III}}(\text{O}_2)(\text{mL}_5^2)\text{-N(3)}]^+$  (bottom).

To ensure that our selection of  $[\text{Mn}^{\text{III}}(\text{O}_2)(\text{mL}_5^2)\text{-N(3)}]^+$  over  $[\text{Mn}^{\text{III}}(\text{O}_2)(\text{mL}_5^2)\text{-N(4)}]^+$  is not based solely on TD-DFT computations, which can suffer from well-documented defects including calculated transition energies in error by  $\sim 5\,000\text{ cm}^{-1}$  and CT transitions at

unrealistically low energies,<sup>37</sup> these models were further compared on the basis of electronic transition energies using the multireference SORCI method.<sup>38</sup> Because of the computational demands of this method, SORCI calculations were performed on truncated species, where the  $mL_5^2$  ligand was modeled by  $NH_3$  groups. These models are referred to as  $[Mn^{III}(O_2)(NH_3)_4-N(4)]^+$  and  $[Mn^{III}(O_2)(NH_3)_4-N(3)]^+$ . The consequences of this truncation were evaluated by comparing TD-DFT-computed Abs spectra of truncated models with those of authentic systems. As shown in Figure A.5.7, this truncation procedure results in i) a drop in absorption intensity, especially in the near-UV region, and ii) a blue-shift of the electronic transition energies. Thus, in using SORCI computations to evaluate these models, we will only compare the computed electronic transition energies. The Abs spectra afforded from these calculations (Figure 5.9) provide further validation for the  $[Mn^{III}(O_2)(mL_5^2)-N(3)]^+$  model as an accurate representation of  $[Mn^{III}(O_2)(mL_5^2)]^+$ . Indeed, considering the expected blue-shift and loss of absorption intensity for higher-energy transitions, the SORCI-computed Abs spectrum is in remarkable agreement with experimental data. For example, the lowest-energy d-d transition of  $[Mn^{III}(O_2)(NH_3)_4-N(3)]^+$  (band *iii*) is predicted at  $18\,172\text{ cm}^{-1}$  (xy-polarized), in good agreement with the position and polarization of band 1 (Figure 5.9). In addition, the SORCI computations predict a set of two d-d and three peroxo-to- $Mn^{III}$  CT transitions from  $23\,300 - 27\,000\text{ cm}^{-1}$  (band *iv*), in excellent agreement with the Gaussian deconvolutions of the Abs and MCD data sets, which show a set of at least three bands in this spectral window (Figure 5.5). In contrast, the lowest-energy band for  $[Mn^{III}(O_2)(NH_3)_4-N(4)]^+$  is centered at  $\sim 22\,000\text{ cm}^{-1}$  (band *i*) and contains contributions from two transitions, a peroxo-to-manganese(III) CT transition at  $21\,589\text{ cm}^{-1}$  and a d-d transition at  $22\,225\text{ cm}^{-1}$ , in poor agreement with the experimental data that show one band at  $\sim 17\,000\text{ cm}^{-1}$ .



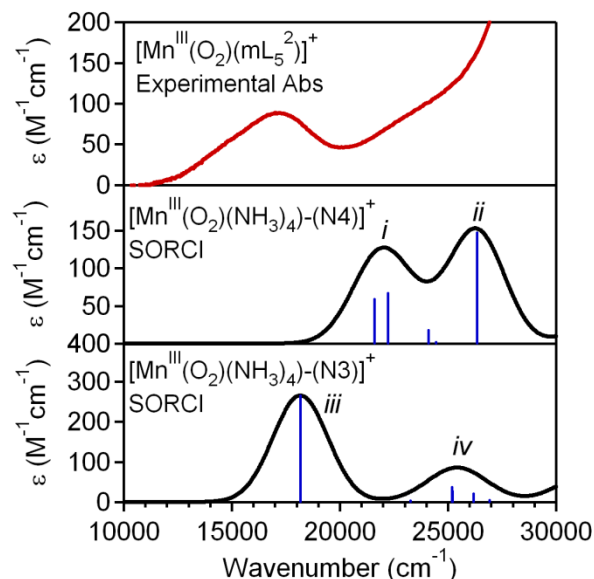


**Figure 5.9.** Experimental electronic Abs spectrum of  $[\text{Mn}^{\text{III}}(\text{O}_2)(\text{mL}_5^2)]^+$  (top) and SORCI-computed Abs spectra for  $[\text{Mn}^{\text{III}}(\text{O}_2)(\text{NH}_3)_4\text{-N}(4)]^+$  (center) and  $[\text{Mn}^{\text{III}}(\text{O}_2)(\text{NH}_3)_4\text{-N}(3)]^+$  (bottom).

Given the success of the TD-DFT and SORCI computations for  $[\text{Mn}^{\text{III}}(\text{O}_2)(\text{mL}_5^2)\text{-N}(3)]^+$  in reproducing the major spectral features of  $[\text{Mn}^{\text{III}}(\text{O}_2)(\text{mL}_5^2)]^+$ , it is warranted to make assignments on the basis of these calculations, as well as discuss similarities and differences in the bonding descriptions afforded by these methods. The  $\text{Mn}^{\text{III}}$  3d splitting pattern afforded by the DFT computations is shown in Figure 5.10. The compositions of the spin-up Mn 3d-based Kohn-Sham MOs are in Table 5.4, and more complete information is provided in the appendix (Table A.5.13). Because of the trigonal arrangement of the equatorial nitrogen donors, the Mn 3d-based MOs are mixtures of the canonical 3d orbitals, which we have labeled according to the dominant contributor.<sup>a</sup> The lowest-energy Mn d-based MOs ( $xz$  and  $yz$ ), which are both singly-occupied, are involved in  $\pi$ -antibonding interactions with the peroxo ligand, as evidenced by the ~17% peroxo character in the spin-up MOs (MOs 105 and 109 in Table 5.4). The higher-energy

<sup>a</sup> For example, MO 120 is labeled as  $x^2-y^2$ , but this orbital contains significant contributions from  $x^2-y^2$  (33%),  $xy$  (19%),  $z^2$  (10%) and  $xz$  (10%). Because of this mixing, the surface contour plot of this MO only slightly resembles a canonical  $x^2-y^2$  orbital (Figure 5.10).

$yz$  MO carries some contributions from the  $mL_5^2$  ligand, which cause its destabilization relative to  $xz$ . The singly-occupied  $z^2$  and  $x^2-y^2$  MOs are predominantly involved in  $\sigma$ -antibonding interactions with the  $mL_5^2$  ligand, with the  $x^2-y^2$  MO carrying more peroxo character than  $z^2$  (11 versus 5%, respectively). The highest-energy Mn d-based MO ( $xy$ ) is unoccupied and is the dominant Mn-O<sub>2</sub>  $\sigma$ -antibonding MO, containing nearly equal contributions from Mn 3d and peroxo in-plane  $\pi^*$  MOs ( $\pi_{ip}^*$ ).<sup>b</sup> This electronic structure description, consisting of a high-spin ( $S = 2$ ) Mn<sup>III</sup> center and a peroxo (O<sub>2</sub><sup>2-</sup>) ligand, is largely consistent with that afforded by the SORCI computations, where the leading (70%) configuration in the ground-state is  $(\pi_{ip}^*)^2(\pi_{op}^*)^2(xz)^1(yz)^1(z^2)^1(x^2-y^2)^1(xy)^0$ . However, this state contains an appreciable (10%) contribution from a  $(\pi_{ip}^*)^1(\pi_{op}^*)^2(xz)^1(yz)^1(z^2)^1(x^2-y^2)^1(xy)^1$  configuration, which would formally be described as a high-spin ( $S = 5/2$ ) Mn<sup>II</sup> antiferromagnetically coupled to a superoxo ligand ( $S = 1/2$ ) to give  $S_{tot} = 2$ . Though, while this system is best described as a peroxomanganese(III), there is small superoxomanganese(II) character in the ground-state wavefunction.

**Table 5.4.** Energies (eV) and Compositions of the Mn 3d-based MOs from B3LYP Spin-Unrestricted DFT Computations for  $[Mn^{III}(O_2)(mL_5^2)]^+$

	$xz$ (105a)	$yz$ (109a)	$z^2$ (110a)	$x^2-y^2$ (113a)	$xy$ (115a)
Energy	-10.855	-10.221	-9.836	-9.014	-4.842
Mn 3d	57.3	33.0	24.9	39.2	30.7
$z^2$	5.9	1.1	13.3	12	0.3
$x^2-y^2$	39.5	1.1	8.6	1.9	0.1
$xy$	0.4	25.8	0.5	0.3	1.7
$xz$	9.9	2.2	1.1	14.5	9.8
<b><math>yz</math></b>	<b>1.6</b>	<b>2.8</b>	<b>1.4</b>	<b>10.5</b>	<b>18.8</b>
O <sub>2</sub> 2p	16.5	17.3	5.1	11.3	48.3
$mL_5^2$ (N 2p)	7.3	24.5	38.9	32.8	5.9

<sup>b</sup> The peroxo frontier orbitals, which are O-O  $\pi$ -antibonding, are conventionally classified as in-plane ( $\pi_{ip}^*$ ) or out-of-plane ( $\pi_{op}^*$ ) depending on their orientation with respect to the metal-peroxo bond vectors.

According to the TD-DFT calculations, the lowest-energy  $d-d$  transitions involves excitation from  $x^2-y^2$  to  $z^2$ , which is predicted at  $18\,015\text{ cm}^{-1}$  (band *i* in Figure 5.8, bottom), in good agreement with the energy of band 1 (Table 5.1). In agreement, the lowest-energy SORCI-computed transition at  $18\,172\text{ cm}^{-1}$  (band *iii* in Figure 5.9, bottom) is due to an  $x^2-y^2 \rightarrow z^2$  one-electron excitation. At higher-energy, both the TD-DFT and SORCI methods predict an absorption band centered at  $\sim 23\,000 - 25\,000\text{ cm}^{-1}$  that contains contributions from a cluster of transitions, including peroxo-to-manganese(III) CT bands, of which the  $\text{O}_2\ \pi_{\text{op}}^* \rightarrow yz$  is predicted as the most intense by both methods, and two  $d-d$  transitions ( $z^2 \rightarrow xy$  and  $yz \rightarrow xy$ ). Thus, these two computational methods are both in good agreement with our Gaussian analysis of Abs and MCD data collected for  $[\text{Mn}^{\text{III}}(\text{O}_2)(\text{mL}_5^2)\text{-N}(3)]^+$ .

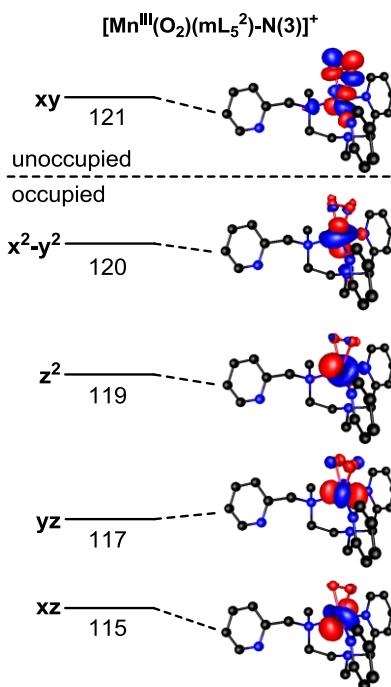


**Figure 5.10.** Schematic molecular orbital splitting diagram for  $[\text{Mn}^{\text{III}}(\text{O}_2)(\text{mL}_5^2)\text{-N}(3)]^+$  and surface contour plots of quasi-restricted orbitals based on DFT computations. For comparison, orbital energies are relative to the lowest-energy spin-up d-based MO of each complex.

**5.2.9 Hypothetical Structures for  $[\text{Mn}^{\text{III}}(\text{O}_2)(\text{imL}_5^2)]^+$ .** The spectroscopic similarities of  $[\text{Mn}^{\text{III}}(\text{O}_2)(\text{mL}_5^2)]^+$  with  $[\text{Mn}^{\text{III}}(\text{O}_2)(\text{imL}_5^2)]^+$  require that these three complexes have similar geometries. DFT geometry optimizations of hypothetical models of  $[\text{Mn}^{\text{III}}(\text{O}_2)(\text{imL}_5^2)]^+$  and provide compelling evidence that ligand dissociation, resulting in the formation of six-coordinate  $\text{Mn}^{\text{III}}$  centers with side-on peroxo ligands, is energetically feasible for these systems as well (Table 5.3 and Figure 5.11). For  $[\text{Mn}^{\text{III}}(\text{O}_2)(\text{imL}_5^2)]^+$ , dissociation of imidazole groups in models  $[\text{Mn}^{\text{III}}(\text{O}_2)(\text{imL}_5^2)\text{-N}(4)]^+$  and  $[\text{Mn}^{\text{III}}(\text{O}_2)(\text{imL}_5^2)\text{-N}(3)]^+$  leads to significantly lower energies ( $\sim 20 - 25$  kcal/mol) relative to a model with a dissociated amine nitrogen *trans* to the peroxo group ( $[\text{Mn}^{\text{III}}(\text{O}_2)(\text{imL}_5^2)\text{-N}(1)]^+$ ). The structure of  $[\text{Mn}^{\text{III}}(\text{O}_2)(\text{imL}_5^2)\text{-N}(3)]^+$  is virtually identical to that of  $[\text{Mn}^{\text{III}}(\text{O}_2)(\text{mL}_5^2)\text{-N}(3)]^+$ , consisting of an amine nitrogen *trans* to the peroxo unit and three equatorial nitrogen donors (cf. Figure 5.11, top and Figure 5.7, bottom). While the Mn-N(1) distance is quite long in  $[\text{Mn}^{\text{III}}(\text{O}_2)(\text{imL}_5^2)\text{-N}(3)]^+$  (2.67 Å; see Table 5.3), shortening this bond to 2.40 Å is associated with an increase in energy of only 2 kcal/mol (Table A.5.14 and Figure A.5.9, top); thus this distance might be exaggerated in the energy-minimized structure. In the TD-DFT-computed Abs spectra, shortening the Mn-N(1) distance leads to a red-shift of the lowest-energy Abs band (Figure A.5.9, bottom), lending credence to our proposal that the temperature-dependence of the experimental Abs spectrum of  $[\text{Mn}^{\text{III}}(\text{O}_2)(\text{imL}_5^2)]^+$  (Figure 5.4) is due to small, temperature-dependent changes in metal-ligand distances.

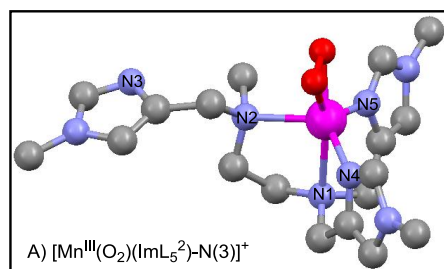


**Figure 5.11.** Molecular structures of  $[\text{Mn}^{\text{III}}(\text{O}_2)(\text{imL}_5^2)\text{-N}(3)]^+$  developed using DFT computations.

### 5.3 Discussion.

While pentadentate ligands are often used to support peroxometal intermediates, including manganese<sup>26,27</sup> and iron<sup>39-42</sup> species, the molecular structures of these species have remained elusive. For example, while there are several crystallographically characterized peroxomanganese(III) adducts supported by tetradentate<sup>20,23,24</sup> and tridentate<sup>21,22</sup> ligands, corresponding adducts featuring pentadentate ligands are comparatively scarce and structural data is lacking for these species.<sup>26,27</sup> This is despite the fact that such pentadentate frameworks may provide higher fidelity to the first coordination spheres of manganese enzymes that react with oxygen and its reduced derivatives, as these often consist of five, tightly bound ligands (see Figure 5.1).<sup>2,8,43</sup> In this study, we have used a variety spectroscopic and computational methods to demonstrate that the peroxomanganese(III) adducts supported by the pentadentate  $\text{mL}_5^2$  and  $\text{imL}_5^2$  ligands feature six-coordinate  $\text{Mn}^{\text{III}}$  centers with side-on peroxo ligands, which requires the ligands convert from a pentadentate binding mode in the  $\text{Mn}^{\text{II}}$  complexes to a tetradentate mode for the  $\text{Mn}^{\text{III}}\text{-O}_2$  species. Specifically, on the basis of relative, DFT-computed energies and the agreement between experimental and calculated spectroscopic data, we conclude that these six-coordinate, side-on peroxomanganese(III) complexes feature dissociation of pyridine (or imidazole) arms from the supporting ligand. The implications of these studies for biological Mn

enzymes, related peroxometal adducts, and peroxomanganese(III) decay pathways are discussed below.

**5.3.1 Relevance to Catalytic Mn centers in Biological and Synthetic Systems.** Dissociation of a pyridine or imidazole arm for the  $\text{mL}_5^2$  and  $\text{imL}_5^2$  ligands is possible in the corresponding peroxomanganese(III) complexes because these ligands can adopt a variety of metal-binding modes, often of comparable energy, which is illustrated in the three hypothetical structures developed for  $[\text{Mn}^{\text{III}}(\text{O}_2)(\text{mL}_5^2)]^+$  (Figure 5.7). In contrast to these apparently flexible pentadentate ligands, metalloenzyme active sites, such as those of MnSOD and MndD (Figure 5.1), typically feature amino acid ligands whose positions are greatly constrained by the protein matrix, where ligand dissociation would presumably be disfavored energetically. By limiting the coordination sites available for peroxo (or superoxo) binding, these sites may disfavor the formation of more thermodynamically stable side-on peroxomanganese(III) centers. Surface scans evaluating the conversion from side-on to end-on peroxo binding mode for  $[\text{Mn}^{\text{III}}(\text{O}_2)(\text{mL}_5^2)]^+$  revealed an inverse correlation between one  $\text{Mn}-\text{O}_{\text{peroxo}}$  distance and the  $\text{Mn}-\text{N}(1)$  distance, where the  $\text{N}(1)$  ligand is *trans* to the peroxo unit. On the basis of this correlation, a strong, short  $\text{Mn}-\text{L}$  bond *trans* to the peroxo unit would favor end-on peroxo binding. In the case of  $[\text{Mn}^{\text{III}}(\text{O}_2)(\text{mL}_5^2)]^+$ , shorter  $\text{Mn}-\text{N}(1)$  and longer  $\text{Mn}-\text{O}_{\text{peroxo}}$  distances led to a thermodynamic destabilization, because strengthening the  $\text{Mn}-\text{N}(1)$  bond could not compensate for weakening the  $\text{Mn}-\text{O}_{\text{peroxo}}$  bond. However, it is speculated that stronger *trans* ligands, such as a carboxylate, could make side-on and end-on peroxo binding modes comparable in energy. This model is consistent with the proposal by Nam and co-workers that anionic *trans* ligands in  $[\text{Mn}^{\text{III}}(\text{O}_2)(13\text{-TMC})(\text{X})]$  could elongate one  $\text{Mn}-\text{O}_{\text{peroxo}}$  bond, thus leading to the observed increase in reactivity upon  $\text{X}^-$  binding.<sup>23</sup> In addition, according to this model, the presence of a

carboxylate ligand *trans* to the expected peroxide and dioxygen binding sites in MnSOD and MndD, respectively, would further disfavor side-on binding in these active sites. We speculate that a combination of this *trans* carboxylate, H-bonding interactions with a tyrosine residue and the preference for hexacoordination by the Mn<sup>III</sup> center all contribute to the asymmetric binding predicted computationally for the putative peroxomanganese(III) adduct of MnSOD.<sup>3</sup>

The proposal that pyridine and imidazole dissociation is possible for the mL<sub>5</sub><sup>2</sup> and imL<sub>5</sub><sup>2</sup>, ligands also has relevance for metal-catalyzed transformations that utilize these types of pentadentate ligands. Such ligands are employed in catalytic reactions including textile and wood pulp bleaching, a variety of substrate oxygenation reactions, and atom transfer radical polymerizations.<sup>44-49</sup> On the basis of our results, it may not be well-founded to assume that such ligands remain bound in a pentadentate mode during catalysis.

**5.3.2 Comparison to Peroxoiron(III) Adducts.** The mL<sub>5</sub><sup>2</sup> ligand has been previously used to support high-spin peroxoiron(III) complexes.<sup>42,50,51</sup> While there is consensus that this species contains a side-on peroxide ligand, it is unclear as to whether the mL<sub>5</sub><sup>2</sup> ligand is bound in a pentadentate or tetradentate fashion, which would respectively give rise to seven- and six-coordinate ferric centers.<sup>41,42,50-52</sup> While our data supports tetradentate ligand binding for the peroxomanganese(III) complex of the mL<sub>5</sub><sup>2</sup> ligand, one should take caution in transferring this conclusion to the corresponding peroxoiron(III) systems. One contrast between these systems are the significantly longer Fe-O<sub>peroxo</sub> distances, which, on the basis of analysis of iron K-edge extended X-ray Abs fine structure (EXAFS) data and DFT computations, range from 1.91 to 1.99 Å.<sup>41,42,53</sup> These distances are roughly 0.05 – 0.1 Å longer than Mn-O<sub>peroxo</sub> bond lengths observed by X-ray crystallography.<sup>20-24</sup> This relatively large difference in bond length can be attributed to the different electronic configurations of Fe<sup>III</sup>-O<sub>2</sub> and Mn<sup>III</sup>-O<sub>2</sub> species. For the

high-spin  $d^5$   $\text{Fe}^{\text{III}}\text{-O}_2$  species, the  $\text{Fe-O}_2$   $\sigma^*$ -based MO, which consists of interactions between a metal  $d_\sigma$  orbitals (typically  $d_{xy}$ ) and the in-plane peroxo  $\pi$ -antibonding orbitals ( $\text{O}_2$   $\pi_{ip}^*$ ) is singly-occupied.<sup>54,55</sup> For the corresponding high-spin,  $d^4$   $\text{Mn}^{\text{III}}\text{-O}_2$  system, this orbital is unoccupied,<sup>29</sup> which leads to a strengthening and shortening of the metal-peroxo bond. This difference in  $\text{M-O}_2$   $\sigma^*$ -orbital occupancy is also partly responsible for the higher O-O stretching frequencies ( $\nu_{\text{O-O}}$ ) observed for the  $\text{Mn}^{\text{III}}\text{-O}_2$  adducts, which are blue-shifted by  $\sim 70\text{ cm}^{-1}$  compared to those of high-spin  $\text{Fe}^{\text{III}}\text{-O}_2$  complexes. Because the  $\text{Mn-O}_2$   $\sigma^*$ -based MO is unoccupied, the O-O bond is strengthened by the admixture of more  $\text{O}_2$   $\pi_{ip}^*$  character in this MO.

**5.3.3 Acid-assisted Decay pathway of  $[\text{Mn}^{\text{III}}(\text{O}_2)(\text{mL}_5^2)]^+$ .** In the presence of acid, the decay pathway of  $[\text{Mn}^{\text{III}}(\text{O}_2)(\text{mL}_5^2)]^+$  involves ligand oxidation, where 2-pyridinecarboxylate is generated by oxidative cleavage of a pyridine arm from the  $\text{mL}_5^2$  ligand.<sup>27</sup> This observed decay product is suggestive of acid-assisted O-O bond activation to create an oxomanganese species (either  $\text{Mn}^{\text{IV}}$  or  $\text{Mn}^{\text{V}}$ , depending on whether O-O cleavage occurs by a hemolytic or heterolytic pathway). Alternatively, there is growing evidence that, under certain circumstances, hydroperoxometal species are capable of acting as H-atom abstraction agents, initiating oxidation reactions. Regardless of the nature of the active oxidation in this process, there is currently no experimental data to offer insight into whether this decay pathway involves inter- or intramolecular ligand oxidation. However, the geometric structure of  $[\text{Mn}^{\text{III}}(\text{O}_2)(\text{mL}_5^2)\text{-N(3)}]^+$  (Figure 5.7, bottom) lends credence to an intramolecular pathway, because the orientation of the methyl linker in the dissociated pyridine appears well positioned for intramolecular attack by a  $\text{Mn=O}$  (or  $\text{Mn-OOH}$ ) species ( $\text{H-O}_{\text{peroxo}}$  distance of  $2.6\text{ \AA}$  in  $[\text{Mn}^{\text{III}}(\text{O}_2)(\text{mL}_5^2)\text{-N(3)}]^+$ ). Alternatively, hydroxyl radicals formed by acid-assisted O-O hemolysis could be responsible for



ligand oxidation. Determining the nature of the active oxidant as well as the details of this ligand degradation pathway, would not only aid in understanding of O-O bond activation in Mn systems, but also could provide insights into the design of more robust ligands for use in catalytic oxidation reactions.

## 5.4 Material and Methods.

**5.4.1 Chemicals and Instrumentation.** All chemicals and solvents were obtained from commercial vendors and were ACS grade or better and used as received. Electronic Abs spectra were obtained on a Varian Cary 50 Bio spectrophotometer that was interfaced with a Unisoku cryostat (USP-203-A) capable of maintaining temperatures between 83 and 373 K. MCD spectra were collected on a Jasco spectropolarimeter (J-815) interfaced with an Oxford Instruments magnetocryostat (SM-4000-8) capable of horizontal fields up to 8 T and a temperature range of 1.5 to 300 K.

**5.4.2 Preparation of Peroxomanganese(III) Complexes for MCD Experiments.**  $\text{Mn}^{\text{II}}$  complexes were supplied by Professor Elodie Anxolabéhère-Mallart. Samples of peroxomanganese(III) complexes supported by the  $\text{mL}_5^2$  and  $\text{imL}_5^2$ , were prepared to investigate the geometric and electronic structures of these complexes. Unlike the  $[\text{Mn}^{\text{II}}(\text{mL}_5^2)](\text{CF}_3\text{SO}_2)_2$  salt,  $[\text{Mn}^{\text{II}}(\text{mL}_5^2)](\text{BPh}_4)_2$  is not soluble in ethanol. Accordingly,  $[\text{Mn}^{\text{III}}(\text{O}_2)(\text{mL}_5^2)]^+$  was prepared by a modification of the reported procedure.<sup>27</sup> A 5 mM frozen solution of  $[\text{Mn}^{\text{III}}(\text{O}_2)(\text{mL}_5^2)]^+$  was generated by dissolving solid  $[\text{Mn}^{\text{II}}(\text{mL}_5^2)](\text{BPh}_4)_2$  in a minimal amount of butyronitrile and cooling the resulting solution to -20 °C. Two hundred equivalents of urea- $\text{H}_2\text{O}_2$  and a few  $\mu\text{l}$   $\text{H}_2\text{O}$  in methanol were added to the butyronitrile solution. Once formation of  $[\text{Mn}^{\text{III}}(\text{O}_2)(\text{mL}_5^2)]^+$  was complete on the basis of electronic Abs data, the solution was passed

through a pre-cooled syringe filter to remove undissolved urea. The filtered solution was transferred to an MCD cell and flash-frozen in liquid N<sub>2</sub>. A 5 mM frozen solution of [Mn<sup>III</sup>(O<sub>2</sub>)(imL<sub>5</sub><sup>2</sup>)]<sup>+</sup> was prepared at -40 °C by adding 10 equivalents H<sub>2</sub>O<sub>2</sub> and 0.5 equivalents triethylamine in ethanol to a butyronitrile solution of [Mn<sup>II</sup>(imL<sub>5</sub><sup>2</sup>)](ClO<sub>4</sub>)<sub>2</sub>. Once formation was judged complete by Abs spectroscopy, the sample was further cooled to -80 °C, transferred to a pre-cooled MCD sample cell at -80 °C, and flash-frozen in liquid N<sub>2</sub>. Because of a temperature-dependent shift of the dominant absorption band at ~18 000 cm<sup>-1</sup> (*vide infra*), the [Mn<sup>III</sup>(O<sub>2</sub>)(imL<sub>5</sub><sup>2</sup>)]<sup>+</sup> sample changes color from purple to blue upon freezing.

**5.4.3 Computations.** All calculations utilized the *ORCA* 2.8.0 software package developed by F. Neese (University of Bonn, Germany).<sup>56</sup> Crystal structure coordinates of the [Mn<sup>II</sup>(mL<sub>5</sub><sup>2</sup>)(ClO<sub>4</sub>)<sub>2</sub>] and [Mn<sup>II</sup>(imL<sub>5</sub><sup>2</sup>)(ClO<sub>4</sub>)<sub>2</sub>] complexes were modified to include peroxo ligands and served as the starting points for geometry optimizations. Geometry optimizations and surface scans were performed at the spin-unrestricted level using the Becke-Perdew (BP) functional<sup>57,58</sup> and TZVP (for Mn, O, and N) and the SVP (for C and H) basis sets.<sup>59,60</sup> These calculations employed the resolution of the identity (RI) approximation<sup>61</sup> that employed the TZV/J and SV/J auxiliary basis sets.<sup>61</sup> Frequency calculations verified that all energy-minimized models showed no imaginary frequencies. Single-point calculations to obtain energies for the optimized structures employed the B3LYP functional<sup>62-64</sup> and TZVPP basis sets for all atoms.<sup>59,60,65</sup> The effects of solvation on the total energies of these systems were evaluated using the COSMO method as implemented in *ORCA*. *D*-tensor orientations for models of [Mn<sup>III</sup>(O<sub>2</sub>)(mL<sub>5</sub><sup>2</sup>)]<sup>+</sup> were computed using a so-called coupled-perturbed spin-orbit coupling approach,<sup>66</sup> which utilized the B3LYP functional and TZVP basis set for all atoms. Isosurface

plots of quasi-restricted molecular orbitals (MOs) were generated using the gOpenMol program and the isodensity values of 0.05 au.<sup>67,68</sup>

Electronic transition energies and intensities were computed for select models using the time-dependent DFT (TD-DFT)<sup>69-72</sup> and spectroscopy oriented configuration interaction (SORCI)<sup>73,74</sup> procedures. TD-DFT calculations were performed within the Tamm-Dancoff approximation and utilized the TZVP (for Mn, N, and O) and SVP (for C and H) basis sets. For each calculation, 40 excited states were calculated by including all one-electron excitations within a  $\pm 3$  hartree energy window with respect to the highest occupied and lowest unoccupied MOs. The SORCI calculations used an active space consisting of quasi-restricted Mn 3d-based and peroxo  $\pi^*_{ip}$ - and  $\pi^*_{op}$ -based orbitals (CAS 8,7) obtained from an initial DFT calculation using the level of theory described above. The CI thresholds  $T_{sel}$ ,  $T_{pre}$ , and  $T_{nat}$  were set to  $10^{-6}$  hartrees,  $10^{-4}$ , and  $10^{-5}$ , respectively.

## 5.5 References.

- (1) Grove, L. E.; Brunold, T. C. *Comments Inorg. Chem.* **2008**, *29*, 134.
- (2) Miller, A.-F. *Curr. Opin. Chem. Biol.* **2004**, *8*, 162.
- (3) Jackson, T. A.; Karapetian, A.; Miller, A.-F.; Brunold, T. C. *Biochemistry* **2005**, *44*, 1504.
- (4) Bull, C.; Niederhoffer, E. C.; Yoshida, T.; Fee, J. A. *J. Am. Chem. Soc.* **1991**, *113*, 4069.
- (5) Hearn, A. S.; Stroupe, M. E.; Cabelli, D. E.; Lepock, J. R.; Tainer, J. A.; Nick, H. S.; Silverman, D. N. *Biochemistry* **2001**, *40*, 12051.
- (6) Hearn, A. S.; Tu, C. K.; Nick, H. S.; Silverman, D. N. *J. Biol. Chem.* **1999**, *274*, 24457.
- (7) Gunderson, W. A.; Zatsman, A. I.; Emerson, J. P.; Farquhar, E. R.; Que, L.; Lipscomb, J. D.; Hendrich, M. P. *J. Am. Chem. Soc.* **2008**, *130*, 14465.
- (8) Vetting, M. W.; Wackett, L. P.; Que, L., Jr.; Lipscomb, J. D.; Ohlendorf, D. H. *J. Bacteriol.* **2004**, *186*, 1945.
- (9) Opaleye, O.; Rose, R.-S.; Whittaker, M. M.; Woo, E.-J.; Whittaker, J. W.; Pickersgill, R. W. *J. Biol. Chem.* **2006**, *281*, 6428.
- (10) Borowski, T.; Bassan, A.; Richards, N. G. J.; Siegbahn, P. E. M. *Journal of Chemical Theory and Computation* **2005**, *1*, 686.
- (11) Reinhardt, L. A.; Svedruzic, D.; Chang, C. H.; Cleland, W. W.; Richards, N. G. J. *J. Am. Chem. Soc.* **2003**, *125*, 1244.

- (12) Svedružić, D.; Jónsson, S.; Toyota, C. G.; Reinhardt, L. A.; Ricagno, S.; Lindqvist, Y.; Richards, N. G. J. *Arch. Biochem. Biophys.* **2005**, *433*, 176.
- (13) Tanner, A.; Bowater, L.; Fairhurst, S. A.; Bornemann, S. *J. Biol. Chem.* **2001**, *276*, 43627.
- (14) Wu, A. J.; Penner-Hahn, J. E.; Pecoraro, V. L. *Chem. Rev.* **2004**, *104*, 903.
- (15) Cotruvo, J. A.; Stubbe, J. *Biochemistry* **2010**, *49*, 1297.
- (16) Hearn, A. S.; Stroupe, M. E.; Cabelli, D. E.; Ramilo, C. A.; Luba, J. P.; Tainer, J. A.; Nick, H. S.; Silverman, D. N. *Biochemistry* **2003**, *42*, 2781.
- (17) Guan, Y.; Hickey, M. J.; Borgstahl, G. E. O.; Hallewell, R. A.; Lepock, J. R.; O'Connor, D.; Hsieh, Y. S.; Nick, H. S.; Silverman, D. N.; Tainer, J. A. *Biochemistry* **1998**, *37*, 4722.
- (18) Hsieh, Y. S.; Guan, Y.; Tu, C. K.; Bratt, P. J.; Angerhofer, A.; Lepock, J. R.; Hickey, M. J.; Tainer, J. A.; Nick, H. S.; Silverman, D. N. *Biochemistry* **1998**, *37*, 4731.
- (19) Lévêque, V. J.-P.; Stroupe, M. E.; Lepock, J. R.; Cabelli, D. E.; Tainer, J. A.; Nick, H. S.; Silverman, D. N. *Biochemistry* **2000**, *39*, 7131.
- (20) VanAtta, R. B.; Strouse, C. E.; Hanson, L. K.; Valentine, J. S. *J. Am. Chem. Soc.* **1987**, *109*, 1425.
- (21) Kitajima, N.; Komatsuzaki, H.; Hikichi, S.; Osawa, M.; Moro-oka, Y. *J. Am. Chem. Soc.* **1994**, *116*, 11596.
- (22) Singh, U. P.; Sharma, A. K.; Hikichi, S.; Komatsuzaki, H.; Moro-oka, Y.; Akita, M. *Inorg. Chim. Acta* **2006**, *359*, 4407.
- (23) Annaraj, J.; Cho, J.; Lee, Y.-M.; Kim, S. Y.; Latifi, R.; de Visser, S. P.; Nam, W. *Angew. Chem. Int. Ed.* **2009**, *48*, 4150.
- (24) Seo, M. S.; Kim, J. Y.; Annaraj, J.; Kim, Y.; Lee, Y.-M.; Kim, S.-J.; Kim, J.; Nam, W. *Angew. Chem. Int. Ed.* **2007**, *46*, 377.
- (25) Grapperhaus, C. A.; Mienert, B.; Bill, E.; Weyhermüller, T.; Wieghardt, K. *Inorg. Chem.* **2000**, *39*, 5306.
- (26) Groni, S.; Blain, G.; Guillot, R.; Policar, C.; Anxolabéhère-Mallart, E. *Inorg. Chem.* **2007**, *46*, 1951.
- (27) Groni, S.; Dorlet, P.; Blain, G.; Bourcier, S.; Guillot, R.; Anxolabéhère-Mallart, E. *Inorg. Chem.* **2008**, *47*, 3166.
- (28) Shook, R. L.; Gunderson, W. A.; Greaves, J.; Ziller, J. W.; Hendrich, M. P.; Borovik, A. S. *J. Am. Chem. Soc.* **2008**, *130*, 8888.
- (29) Geiger, R. A.; Chattopadhyay, S.; Day, V. W.; Jackson, T. A. *J. Am. Chem. Soc.* **2010**, *132*, 2821.
- (30) Shook, R. L.; Borovik, A. S. *Inorg. Chem.* **2010**, *49*, 3646.
- (31) Geiger, R. A.; Chattopadhyay, S.; Day, V. W.; Jackson, T. A. *Dalton Transactions* **2011**, *40*, 1707.
- (32) Emerson, J. P.; Kovaleva, E. G.; Farquhar, E. R.; Lipscomb, J. D.; Que, L., Jr. *Proc. Natl. Acad. Sci. USA* **2008**, *105*, 7347.
- (33) Whittaker, M. M.; Whittaker, J. W. *Biochemistry* **1996**, *35*, 6762.
- (34) Kirk, M. L.; Peariso, K. *Curr. Opin. Chem. Biol.* **2003**, *7*, 220.
- (35) Neese, F.; Solomon, E. I. *Inorg. Chem.* **1999**, *38*, 1847.
- (36) Nivorozhkin, A. L.; Anxolabéhère-Mallart, E.; Mialane, P.; Davydov, R.; Guilhem, J.; Cesario, M.; Audière, J.-P.; Girerd, J.-J.; Styring, S.; Schussler, L.; Seris, J.-L. *Inorg. Chem.* **1997**, *36*, 846.
- (37) Neese, F. *J. Biol. Inorg. Chem.* **2006**, *11*, 702.
- (38) Neese, F. *J. Chem. Phys.* **2003**, *119*, 9428.

- (39) Costas, M.; Mehn, M. P.; Jensen, M. P.; Que, L., Jr. *Chem. Rev.* **2004**, *104*, 939.
- (40) Girerd, J.-J.; Banse, F.; Simaan, A. J. *Struc. Bonding* **2000**, *97*, 143.
- (41) Koehntop, K. D.; Rohde, J.-U.; Costas, M.; Que Jr, L. *Dalton Transactions* **2004**, 3191.
- (42) Roelfes, G.; Vrajmasu, V.; Chen, K.; Ho, R. Y. N.; Rohde, J.-U.; Zondervan, C.; la Crois, R. M.; Schudde, E. P.; Lutz, M.; Spek, A. L.; Hage, R.; Feringa, B. L.; Münck, E.; Que, L. *J. Inorg. Chem.* **2003**, *42*, 2639.
- (43) Miller, A.-F. In *Comprehensive Coordination Chemistry II*; McCleverty, J. A., Meyer, T. J., Eds.; Elsevier Ltd.: Oxford, UK, 2004; Vol. 8, p 479.
- (44) Klopstra, M.; Hage, R.; Kellogg, R. M.; Feringa, B. L. *Tetrahedron Lett.* **2003**, *44*, 4581.
- (45) Roelfes, G.; Lubben, M.; Hage, R.; Que, J. L.; Feringa, B. L. *Chemistry – A European Journal* **2000**, *6*, 2152.
- (46) Roelfes, G.; Lubben, M.; Leppard, S. W.; Schudde, E. P.; Hermant, R. M.; Hage, R.; Wilkinson, E. C.; Que, L.; Feringa, B. L. *J. Mol. Catal. A: Chem.* **1997**, *117*, 223.
- (47) Van den Berg, T. A.; de Boer, J. W.; Browne, W. R.; Roelfes, G.; Feringa, B. L. *Chem. Commun.* **2004**, 2550.
- (48) Zhang, L.; Tang, H.; Tang, J.; Shen, Y.; Meng, L.; Radosz, M.; Arulsamy, N. *Macromolecules* **2009**, *42*, 4531.
- (49) Hage, R.; Lienke, A. *Angew. Chem. Int. Ed.* **2006**, *45*, 206.
- (50) Simaan, A. J.; Banse, F.; Mialane, P.; Boussac, A.; Un, S.; Kargar-Grisel, T.; Bouchoux, G.; Girerd, J.-J. *Eur. J. Inorg. Chem.* **1999**, 993.
- (51) Simaan, A. J.; Döpner, S.; Banse, F.; Bourcier, S.; Bouchoux, G.; Boussac, A.; Hildebrandt, P.; Girerd, J.-J. *Eur. J. Inorg. Chem.* **2000**, 1627.
- (52) Hazell, A.; McKenzie, C. J.; Nielsen, L. P.; Schindler, S.; Weitzer, M. *J. Chem. Soc., Dalton Trans.* **2002**, 310.
- (53) Bukowski, M. R.; Comba, P.; Limberg, C.; Merz, M.; Que Jr, L.; Wistuba, T. *Angew. Chem. Int. Ed.* **2004**, 43.
- (54) Neese, F.; Solomon, E. I. *J. Am. Chem. Soc.* **1998**, *120*, 12829.
- (55) Solomon, E. I.; Brunold, T. C.; Davis, M. I.; Kemsley, J. N.; Lee, S. K.; Lehnert, N.; Neese, F.; Skulan, A. J.; Yang, Y. S.; Zhou, J. *Chem. Rev.* **2000**, *100*, 235.
- (56) Neese, F., *ORCA - an ab initio, Density Functional and Semiempirical Program Package, Version 2.8*, University of Bonn, 2009.
- (57) Becke, A. D. *J. Chem. Phys.* **1986**, *84*, 4524.
- (58) Perdew, J. P. *Physical Review B* **1986**, *33*, 8822.
- (59) Schäfer, A.; Horn, H.; Ahlrichs, R. *J. Chem. Phys.* **1992**, *97*, 2571.
- (60) Schäfer, G.; Huber, C.; Ahlrichs, R. *J. Chem. Phys.* **1994**, *100*, 5829.
- (61) Neese, F. *J. Comput. Chem.* **2003**, *24*, 1740.
- (62) Becke, A. D. *J. Chem. Phys.* **1993**, *98*, 1372.
- (63) Becke, A. D. *J. Chem. Phys.* **1993**, *98*, 5648.
- (64) Lee, C.; Yang, W.; Parr, R. G. *Phys. Rev. B* **1988**, *37*, 785.
- (65) Weigend, F.; Ahlrichs, R. *PCCP* **2005**, *7*, 3297.
- (66) Neese, F. *J. Chem. Phys.* **2007**, *127*, 164112.
- (67) Bergman, D. L.; Laaksonen, L.; Laaksonen, A. *J. Mol. Graphics & Modelling* **1997**, *15*, 301.
- (68) Laaksonen, L. *J. Mol. Graphics* **1992**, *10*, 33.
- (69) Bauernschmitt, R.; Ahlrichs, R. *Chem. Phys. Lett.* **1996**, *256*, 454.
- (70) Casida, E. M.; Jamorski, C.; Casida, K. C.; Salahub, D. R. *J. Chem. Phys.* **1998**, *108*, 4439.

- (71) Stratman, R. E.; Scuseria, G. E.; Frisch, M. J. *J. Chem. Phys.* **1998**, *109*, 8218.
- (72) Neese, F.; Olbrich, G. *Chem. Phys. Lett.* **2002**, *362*, 170.
- (73) Neese, F.; Petrenko, T.; Ganyushin, D.; Olbrich, G. *Coord. Chem. Rev.* **2007**, *205*, 288.
- (74) Neese, F. *J. Inorg. Biochem.* **2006**, *100*, 716.

## **Chapter 6**

### **Geometric and Electronic Structure of a Peroxomanganese(III) Complex Supported by a Scorpionate Ligand**

## 6. 1 Introduction.

Monomeric peroxomanganese(III) species have been proposed to form in manganese containing enzymes, including manganese superoxide dismutase (MnSOD),<sup>1-6</sup> manganese-dependent homoprotocatechuate 2,3-dioxygenase (MndD),<sup>7,8</sup> and the oxalate-degrading enzymes oxalate oxidase<sup>9,10</sup> and oxalate decarboxylase.<sup>11-13</sup> These biological peroxomanganese(III) species are highly unstable and relatively little is known concerning their structural and electronic properties. In contrast, a variety of synthetic peroxomanganese(III) species have been generated and characterized, offering insights into the structural, electronic, and reactivity properties of this class of compound.

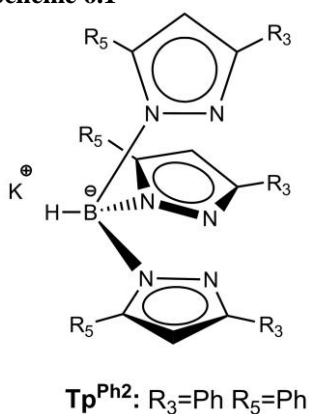
A monomeric  $\text{Mn}^{\text{III}}\text{-O}_2$  model complex supported by the monoanionic facially-coordinating  $\text{Tp}^{\text{iPr}_2}$  ligand ( $\text{Tp}^{\text{iPr}_2}$  = hydrotris(3,5-diisopropylpyrazol-1-yl)borate) was reported to be stable at room temperature for a few hours.<sup>14,15</sup> It was observed that the peroxo ligand is bound to the  $\text{Mn}^{\text{III}}$  ion in a side-on ( $\eta^2$ ) fashion, and the coordination sphere is completed by four other donors, leading to a six-coordinate  $\text{Mn}^{\text{III}}$  center. Three N-donors came from the pyrazole rings of the  $\text{Tp}^{\text{iPr}_2}$  ligand and the additional N-donor came from another coordinating ligand (3,5-isopropylpyrazole,  $\text{pz}^{\text{iPr}_2}$ ). It was observed that when the  $\text{Mn}^{\text{III}}\text{-O}_2$  complex was cooled down from 253 K to 193 K, the additional pyrazole ligand formed a hydrogen bond with the peroxo ligand and changed the electronic structure.<sup>14,15</sup> Because of the high stability of these complexes, as well as their solubility in solvents with low freezing points, they represent ideal systems for addressing the activation of the  $\text{Mn}^{\text{III}}\text{-O}_2$  unit.

Herein, we report the synthesis of a bulky scorpionate-based tridentate ligand hydrotris(3,5-diphenylpyrazol-1-yl)borate ( $\text{Tp}^{\text{Ph}_2}$ , Scheme 6.1), which was designed to stabilize a  $\text{Mn}^{\text{III}}\text{-O}_2$  complex at room temperature. We proposed that the bulky phenyl groups should shield



the peroxo ligand and form a weak hydrogen bonding network, thereby stabilizing a  $\text{Mn}^{\text{III}}\text{-O}_2$  intermediate allowing for characterization by XRD and permitting further studies examining  $\text{Mn}^{\text{III}}\text{-O}_2$  activation. Treatment of this  $\text{Mn}^{\text{II}}$  complex with  $\text{H}_2\text{O}_2$  or  $\text{KO}_2$  at room temperature resulted in the formation of a  $\text{Mn}^{\text{III}}\text{-O}_2$  complex that is stable for several days at ambient conditions. With the formation of a  $\text{Mn}^{\text{III}}\text{-O}_2$  complex, we sought to answer the two important questions: Is the peroxomanganese(III) complex five- or six-coordinate? What is the electronic structure of this  $\text{Mn}^{\text{III}}\text{-O}_2$  complex? On the basis of electronic absorption, EPR, MCD, VTVH MCD spectroscopies, as well as DFT computations, and XRD experiments, we conclude that this complex contains a six-coordinate  $\text{Mn}^{\text{III}}$  center with a side-on peroxo ligand with an additional solvent ligand bound (tetrahydrofuran, THF). This work thus lends further support to our major conclusion in chapter five; namely that there is a strong preference for a six-coordinate geometry for peroxomanganese(III) species. The electronic structure of the  $[\text{Mn}^{\text{III}}(\text{O}_2)(\text{Tp}^{\text{Ph}_2})(\text{THF})]$  was unique compared to the other peroxomanganese(III) complexes in Chapters, 2 and 5. It was observed that the *d-d* transitions are blue shifted in energy compared to the other peroxomanganese(III) complexes due to a large Jahn-Teller elongation.

Scheme 6.1



## 6.2 Results and Discussion.

**6.2.1 Structural properties of  $[\text{Mn}^{\text{II}}(\text{Tp}^{\text{Ph}_2})(\text{DMF})_3](\text{OTf})$ .** Figure 6.1 (left) displays an ORTEP diagram for  $[\text{Mn}^{\text{II}}(\text{Tp}^{\text{Ph}_2})(\text{DMF})_3](\text{OTf})$ . Selected bond distances and angles are given in Table 6.1. The tridentate  $\text{Tp}^{\text{Ph}_2}$  ligand is bound facially, creating three open coordination sites occupied by solvent ligands (dimethylformamide, DMF) that complete the coordination sphere to make a six-coordinate  $\text{Mn}^{\text{II}}$  ion in a distorted octahedral geometry. The Mn-ligand bond lengths range from  $\sim 2.1$  to  $2.3 \text{ \AA}$ , indicative of high-spin  $\text{Mn}^{\text{II}}$  ion. Figure 6.1 (right) displays an axial view of the space filling model for  $[\text{Mn}^{\text{II}}(\text{Tp}^{\text{Ph}_2})(\text{DMF})_3](\text{OTf})$  without the coordinated solvent molecules. This perspective highlights the open face of the metal ion that is shielded by the phenyl groups of the supporting ligand.

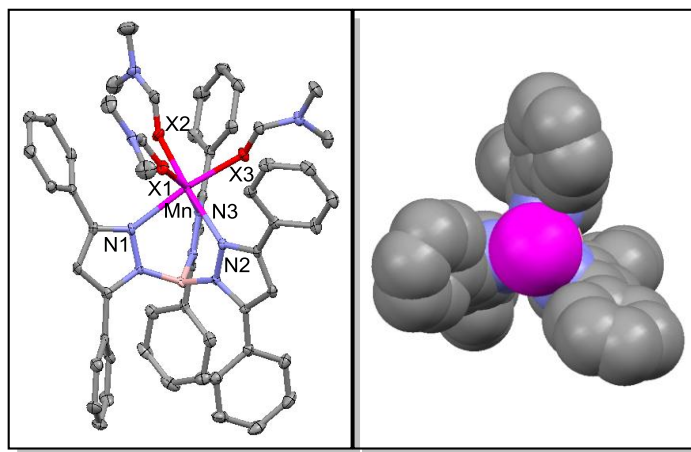


**Figure 6.1.** ORTEP diagram of  $[\text{Mn}^{\text{II}}(\text{Tp}^{\text{Ph}_2})(\text{DMF})_3](\text{OTf})$  (left) and space filling model (right). For the ORTEP diagram, hydrogen atoms and the counter anion have been removed for clarity. For the space filling model hydrogen atoms, coordinating solvents molecules, and the counter anion have been removed for clarity. The significant interatomic distances and angles are listed in Table 6.1.

**Table 6.1.** Selected Bond Lengths (Å) and Angles (°) for Mn<sup>II</sup> Complex.

[Mn <sup>II</sup> (Tp <sup>Ph2</sup> )(DMF)](OTf)			
Mn-N(1)	2.286(1)	N(1)-Mn-(X3)	169.1(5)
Mn-N(2)	2.250(3)	N(2)-Mn-(X2)	172.0(2)
Mn-N(3)	2.319(1)	N(3)-Mn-(X1)	171.6(2)
Mn-O(X1)	2.157(3)	N(1)-Mn-(N2)	83.3(4)
Mn-O(X2)	2.141(6)	N(1)-Mn-(N3)	86.5(2)
Mn-O(X3)	2.191(1)	N(2)-Mn-(N3)	86.7(9)
X=ONC <sub>3</sub> H <sub>7</sub>			

**6.2.2 Formation of a Mn<sup>III</sup> species.** No intense features are observed in the electronic absorption spectra of tetrahydrofuran (THF) solutions of [Mn<sup>II</sup>(Tp<sup>Ph2</sup>)(DMF)<sub>3</sub>](OTf) at energies below 33 000 cm<sup>-1</sup>, indicative of high spin Mn<sup>II</sup> center. A weak shoulder is observed at ~ 28 000 cm<sup>-1</sup>, this transition could be attributed to a Mn<sup>II</sup> to ligand (Tp<sup>Ph2</sup>) charged transfer transition. Treatment of [Mn<sup>II</sup>(Tp<sup>Ph2</sup>)(DMF)<sub>3</sub>](OTf) with 20 equivalents of H<sub>2</sub>O<sub>2</sub> or excess of KO<sub>2</sub> at ambient conditions results in the formation of a yellow intermediate with new absorption features in the visible region (Figure 6.2). The absorption spectrum is characterized by a prominent band at 26 320 cm<sup>-1</sup> and a weaker, broader band at 22 900 cm<sup>-1</sup> ( $\epsilon = 180$  and  $45 \text{ M}^{-1} \text{ cm}^{-1}$ , respectively). For the previously reported [Mn<sup>III</sup>(O<sub>2</sub>)(Ph<sup>iPr2</sup>)(Pz<sup>iPr2</sup>)] complex a weak, broad band was observed at 17 800 cm<sup>-1</sup> which shifted to 17 150 cm<sup>-1</sup> when a pyrazole-peroxo hydrogen bond was formed.<sup>14</sup> The extinction coefficient for this transition ( $\sim 50 \text{ M}^{-1} \text{ cm}^{-1}$ ) is the same as the lowest-energy band of the yellow intermediate. The formation of these absorption bands upon addition of H<sub>2</sub>O<sub>2</sub> or KO<sub>2</sub> is consistent with oxidation of the Mn<sup>II</sup> ion to higher Mn oxidation states (*i.e.* Mn<sup>III</sup> and Mn<sup>IV</sup>). EPR experiments were performed to further investigate the manganese oxidation state and determine the number of species formed upon oxidation.

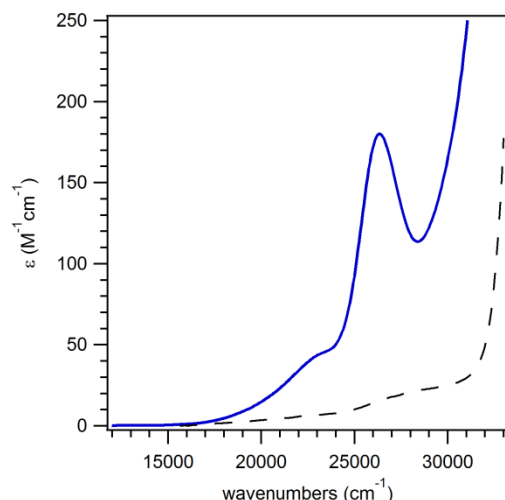


**Figure 6.2.** Electronic absorption spectra of yellow intermediate (solid blue) and  $[\text{Mn}^{\text{II}}(\text{Tp}^{\text{Ph}_2})(\text{DMF})_3](\text{OTf})$  (black dashes) at 298 K in THF.

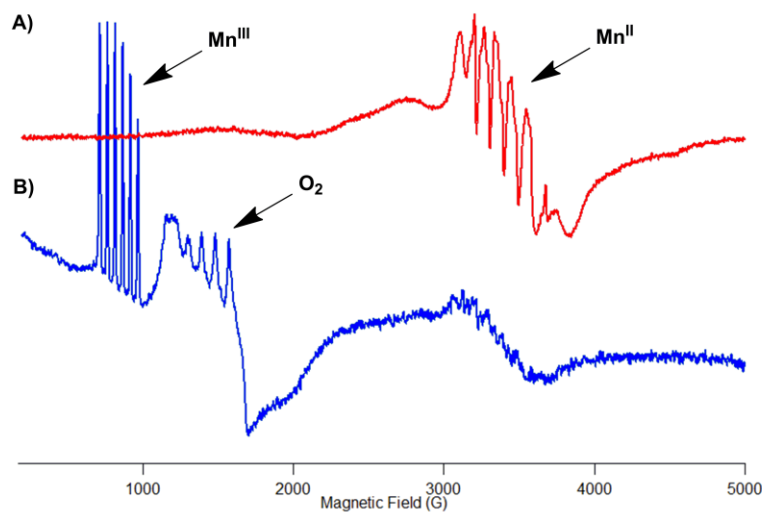


**Figure 6.3.** A) X-band EPR spectrum recorded in perpendicular mode for  $[\text{Mn}^{\text{II}}(\text{Tp}^{\text{Ph}_2})(\text{DMF})_3](\text{OTf})$  at 15 K in 75:25 2-Me-tetrahydrofuran:THF. B) X-band EPR spectrum recorded in parallel mode for the yellow intermediate at 5 K in 75:25 2-Me-tetrahydrofuran:THF. Conditions:  $\nu_{\text{mw}} = 9.4$  GHz, modulation amplitude 0.5 mT, microwave power 8 mW (a) and 2 mW (b).

The X-band EPR spectrum of  $[\text{Mn}^{\text{II}}(\text{Tp}^{\text{Ph}_2})(\text{DMF})_3](\text{OTf})$  in perpendicular mode exhibits a broad six line resonance over a wide magnetic field range centered around 3400 gauss (Figure 6.3), which is indicative of a mononuclear  $\text{Mn}^{\text{II}}$  system. After treatment with  $\text{H}_2\text{O}_2$ , this signal dramatically decreases in intensity. However, a six line signal at a low magnetic field (800 gauss) is observed in a parallel mode experiment, which is indicative of a mononuclear  $\text{Mn}^{\text{III}}$

species. In addition to this  $\text{Mn}^{\text{III}}$  species, molecular oxygen and a small amount of unreacted  $\text{Mn}^{\text{II}}$  are observed. Because the yellow intermediate persisted for approximately a week at ambient conditions, single crystals were isolated for XRD experiments.

**6.2.3 Structural properties of the  $\text{Mn}^{\text{III}}$  species.** The XRD structure of the yellow needles revealed a neutral monomeric six-coordinate  $\text{Mn}^{\text{III}}$  complex with a side-on peroxo ligand and coordination of a THF molecule (Figure 6.4). Selected bond distances and angles are given the Table 6.3. The  $\text{Mn}^{\text{III}}$  ion is in a distorted octahedral geometry with an apparent Jahn-Teller elongation along the (THF)O-Mn-N(1) axis (bond lengths of 2.313(7) Å and 2.375(2) Å, respectively). The other Mn-N bond distances are nearly identical, with Mn-N bond lengths of 2.09 Å. The peroxo ligand is nearly symmetrically bound to the  $\text{Mn}^{\text{III}}$  ion with Mn-O distances of 1.865(2) and 1.859(2). The O-O bond length is 1.432(3) Å, which is typical of a peroxo ligand bound to a transition-metal and in good agreement with other reported  $\text{Mn}^{\text{III}}$ -O<sub>2</sub> complexes (Table 6.2).<sup>14,15,16,26,28</sup> Figure 6.4 (right) displays axial and side views of the space filling model for  $[\text{Mn}^{\text{III}}(\text{O})_2(\text{Tp}^{\text{Ph}_2})(\text{THF})]$ . This shows that the peroxo ligand is shielded by the three phenyl groups of the  $\text{Tp}^{\text{Ph}_2}$  ligand. This shielding explains the high thermal stability of this complex. There are weak phenyl-peroxo hydrogen bonds (H(37)····O(2)····H(67) of 2.2 and 2.3 Å, respectively), which can be observed by the slightly elongated Mn-O(2) bond (Table 6.2).

**Table 6.2.** Selected Bond Lengths (Å) and for reported  $\text{Mn}^{\text{III}}$ -O<sub>2</sub> complexes

Complex	Mn-O(1)	Mn-O(2)	O-O	Mn-N (average)
$[\text{Mn}^{\text{III}}(\text{O})_2(\text{TPP})]^-$	1.888	1.901	1.42	2.184
$[\text{Mn}^{\text{III}}(\text{O})_2(\text{Tp}^{\text{iPr}_2})(3,5\text{-iPr}_2\text{pzH})]$	1.850	1.851	1.42	2.203
$[\text{Mn}^{\text{III}}(\text{O})_2(\text{Tp}^{\text{iPr}_2})(3,5\text{-iPr}_2\text{pzH})]$ H Bond	1.842	1.879	1.43	2.195
$[\text{Mn}^{\text{III}}(\text{O})_2(13\text{-TMC})]^+$	1.855	1.863	1.41	2.242
$[\text{Mn}^{\text{III}}(\text{O})_2(14\text{-TMC})]^+$	1.884	1.884	1.40	2.265
$[\text{Mn}^{\text{III}}(\text{O})_2(\text{Tp}^{\text{Ph}_2})(\text{THF})]^a$	1.859	1.865	1.43	2.187

<sup>a</sup> This work

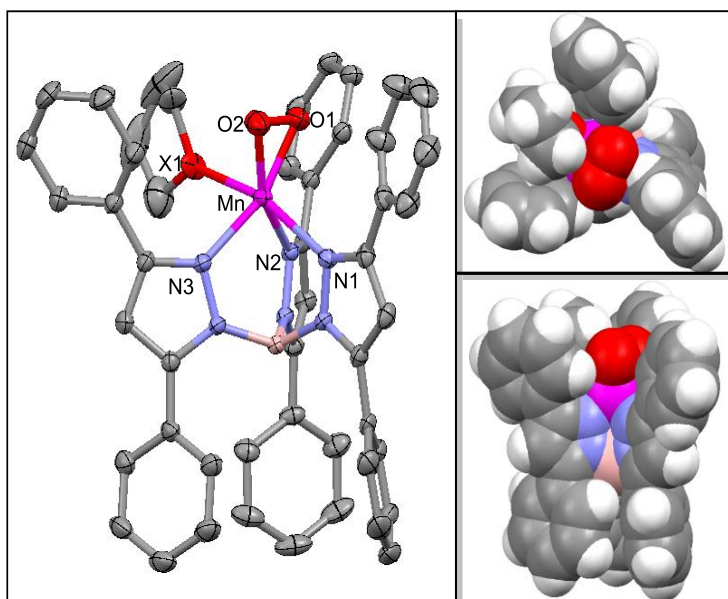


**Figure 6.4.** ORTEP diagram of  $[\text{Mn}^{\text{III}}(\text{O}_2)(\text{Tp}^{\text{Ph}_2})(\text{THF})]$  (left) and space filling models (right). For ORTEP diagrams hydrogen atoms have been removed for clarity. The significant interatomic distances and angles are listed in Table 6.3.

**Table 6.3.** Selected Bond Lengths (Å) and Angles (°) for  $\text{Mn}^{\text{III}}$  Complex.

$[\text{Mn}^{\text{III}}(\text{O}_2)(\text{Tp}^{\text{Ph}_2})(\text{THF})]$			
Mn-O(1)	1.865(2)	O(1)-O(2)	1.432(3)
Mn-O(2)	1.859(2)	N(2)-Mn-(O1)	109.1(2)
Mn-O(X1)	2.313(7)	N(3)-Mn-(O2)	111.9(9)
Mn-N(1)	2.375(2)	N(1)-Mn-(X1)	163.1(2)
Mn-N(2)	2.095(2)	N(1)-Mn-(N3)	84.5(1)
Mn-N(3)	2.091(2)	N(1)-Mn-(N2)	84.6(9)

X=OC<sub>4</sub>H<sub>8</sub>

**6.24 MCD and VTVH MCD Spectroscopy.** Figure 6.5 shows the 298 K absorption and 2 K, 7 T MCD spectra of  $[\text{Mn}^{\text{III}}(\text{O}_2)(\text{Tp}^{\text{Ph}_2})(\text{THF})]$ . The two prominent absorption bands at 26 320 and 22 900  $\text{cm}^{-1}$  correspond to positive features in the MCD spectrum, and additional negative bands are also resolved at 18 900, 23 385, and 24 090  $\text{cm}^{-1}$ . An iterative Gaussian deconvolution of the absorption and MCD data reveals a total of seven electronic transitions from 16 500 to 31 000  $\text{cm}^{-1}$  (Table A.6.1). The negative bands in the MCD spectrum make this complex unique compared to other peroxomanganese(III) complexes, which showed only positive MCD

features.<sup>17</sup> Given the unique nature of this MCD spectrum, we cannot assign these features on the basis of our previous work.<sup>18,19</sup> As discussed below, TD-DFT computations were thus performed to aid in assigning these transitions.

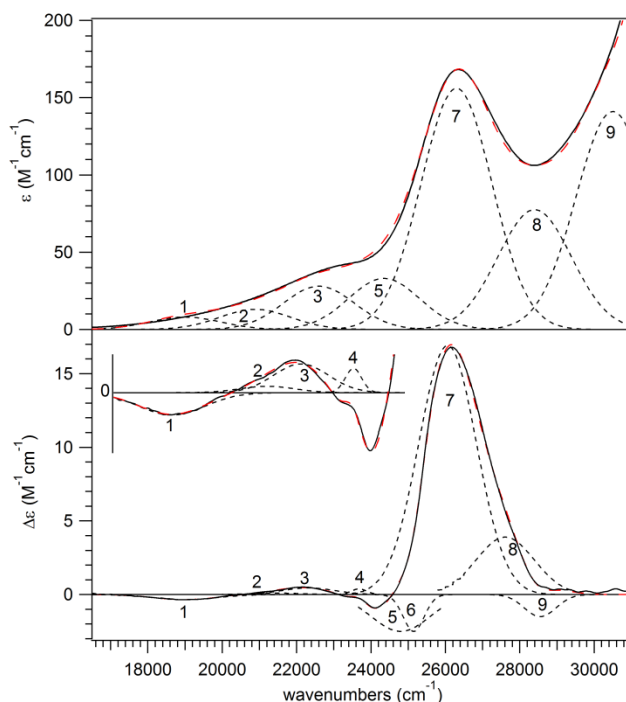


**Figure 6.5.** 298 K electronic absorption (top) and 2 K, 7 T MCD (bottom) spectra of  $[\text{Mn}^{\text{III}}(\text{O}_2)(\text{Tp}^{\text{Ph}_2})(\text{THF})]$ . Inset: An enhancement (15x) of the 2 K, 7 T MCD spectra from 17 500 to 25 000  $\text{cm}^{-1}$ . Individual Gaussian curves (black dotted lines) and their sums (red dashed lines) obtained from iterative fits of these data sets are displayed on their respective spectra. Conditions: Absorption data were collected for a 2.5 mM sample in THF. MCD data were collected for a 15 mM frozen glass sample in 75:25 solution of 2-Me-tetrahydrofuran:THF.

VTVH MCD spectroscopy was used to probe both the ZFS parameters and transition polarizations of  $[\text{Mn}^{\text{III}}(\text{O}_2)(\text{Tp}^{\text{Ph}_2})(\text{THF})]$ .<sup>20,21</sup> VTVH MCD curves obtained for  $[\text{Mn}^{\text{III}}(\text{O}_2)(\text{Tp}^{\text{Ph}_2})(\text{THF})]$  at 26 180  $\text{cm}^{-1}$  are nested, indicating that the  $\text{Mn}^{\text{III}}$  ion is subject to moderate ZFS (Figure 6.6). Since neither ZFS parameters nor transition polarization are known for  $[\text{Mn}^{\text{III}}(\text{O}_2)(\text{Tp}^{\text{Ph}_2})(\text{THF})]$ , the VTVH MCD data sets were systematically fitted to obtain these parameters. The best fits were obtained using an  $S = 2$  spin state, further confirming our

assignment of a high-spin  $\text{Mn}^{\text{III}}$  center. Excellent fits for  $[\text{Mn}^{\text{III}}(\text{O}_2)(\text{Tp}^{\text{Ph}_2})(\text{THF})]$  ( $\chi^2 < 0.04$ ) were obtained with  $D$  value of  $-2.0$  and  $E/D$  value of  $0.05 \text{ cm}^{-1}$  with  $z$ -polarization ( $<1\%$   $x$ ,  $<1\%$   $y$ -, and  $98\%$   $z$ -polarization). These ZFS splitting parameters fit in the range of those reported for other peroxomanganese(III) adducts ( $D = -1.5$  to  $-3.0$  and  $E/D = 0.05$  to  $0.30$ ).<sup>17,22-24</sup>

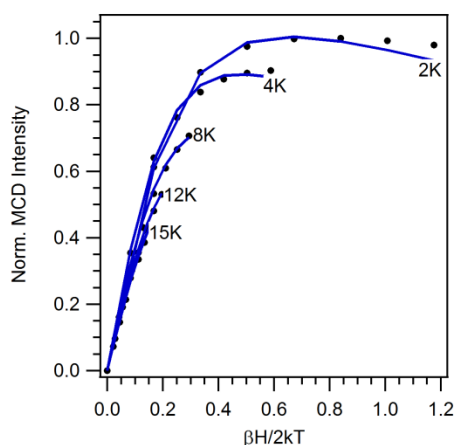


**Figure 6.6.** Experimental VTVH MCD data collected at  $26\,180 \text{ cm}^{-1}$  for  $[\text{Mn}^{\text{III}}(\text{O}_2)(\text{Tp}^{\text{Ph}_2})(\text{THF})]$  ( $\cdots$ ) and theoretical fit ( $\text{—}$ ) using the following parameters:  $D = -2.00$ ,  $E/D = 0.05$ ,  $g_{\text{iso}} = 2.00$ , and  $0.8\%$   $x$ ,  $0.8\%$   $y$ , and  $98.4\%$   $z$  polarization.

**6.2.5 DFT Optimized Geometry of  $[\text{Mn}^{\text{III}}(\text{O}_2)(\text{Tp}^{\text{Ph}_2})(\text{THF})]$ .** Using the crystallographic data collected for  $[\text{Mn}^{\text{III}}(\text{O}_2)(\text{Tp}^{\text{Ph}_2})(\text{THF})]$  as a starting point for a geometry optimization, a DFT optimized model was produced using COSMO to incorporate solvent effects (Figure 6.7). Important metric parameters of our DFT-optimized model of  $[\text{Mn}^{\text{III}}(\text{O}_2)(\text{Tp}^{\text{Ph}_2})(\text{THF})]$  are collected in Table A6.1. The  $\text{Mn}-\text{O}_{\text{peroxo}}$  bond lengths are symmetrical at  $1.861$  and  $1.866 \text{ \AA}$ , and in good agreement with the crystallographic data. The computations also reproduce the Jahn-Teller elongation ( $\text{Mn}-\text{X}(1)$  and  $\text{Mn}-\text{N}(1)$  distances of  $2.375$  and  $2.366 \text{ \AA}$ , respectively) and the  $\text{Mn}-\text{N}(2)$  and  $\text{Mn}-\text{N}(3)$  bond lengths ( $2.093$  and  $2.086 \text{ \AA}$ , respectively).



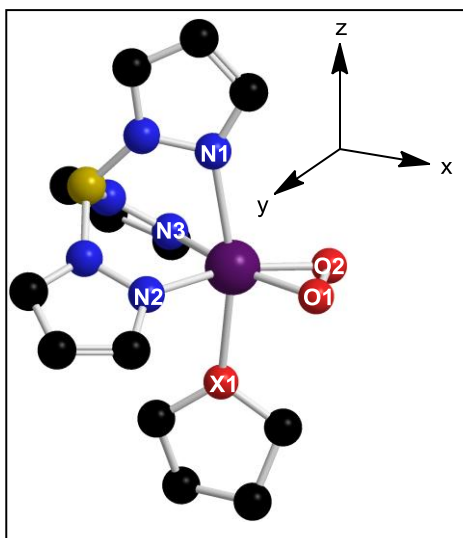


**Figure 6.7.** DFT-Optimized Model of [Mn<sup>III</sup>(O<sub>2</sub>)(Tp<sup>Ph2</sup>)(THF)]. Phenyl groups and hydrogen atoms are hidden for clarity.

The Mn *d* orbital splitting pattern for [Mn<sup>III</sup>(O<sub>2</sub>)(Tp<sup>Ph2</sup>)(THF)] is shown in Figure 6.8. For this calculation, we have used a coordinate system with the Mn<sup>III</sup>-O<sub>2</sub> unit sitting in the *xy* plane with the *x*-axis collinear with the Mn-O(2) bond vector. In this orientation the *z*-axis is the Jahn-Teller axis. With this coordinate system, the Mn  $d_{x^2-y^2}$  and  $d_z^2$  MOs are the  $\sigma$ -type orbitals (*i.e.*, the  $e_g$  set), whereas the  $d_{xz}$ ,  $d_{xy}$ , and  $d_{yz}$  MOs are the  $\pi$ -type orbitals (*i.e.*, the  $t_{2g}$  set).

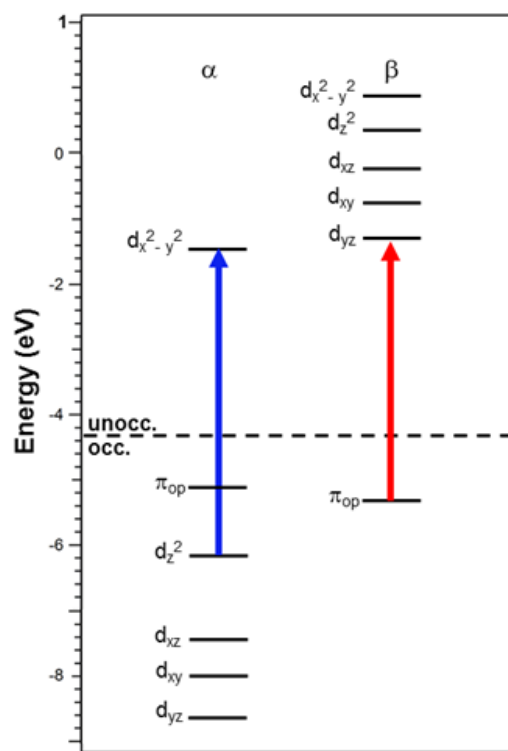


**Figure 6.8.** Molecular orbital (MO) energy-level diagram for  $[\text{Mn}^{\text{III}}(\text{O}_2)(\text{Tp}^{\text{Ph}_2})(\text{THF})]$  obtained from spin-unrestricted DFT calculations. MOs are labeled according to their principal contributors. For clarity only  $\text{Mn}^{\text{III}}$  d-based and  $\text{O}_2$   $\pi_{\text{op}}^*$ -based MOs are included.  $\text{Mn } d_z^2 \rightarrow d_x^2-y^2$  transition (blue arrow) and  $\text{O}_2 \pi_{\text{op}}^* \rightarrow \text{Mn } d_{xy}$  (red arrow)

**6.2.5 Electronic Structure and Spectral Assignments for  $[\text{Mn}^{\text{III}}(\text{O}_2)(\text{Tp}^{\text{Ph}_2})(\text{THF})]$ .** To simplify the calculation, a truncated model of  $[\text{Mn}^{\text{III}}(\text{O}_2)(\text{Tp}^{\text{Ph}_2})(\text{THF})]$  was used. The 5-phenyl groups were replaced with methyl groups. To validate that this truncation does not affect the electronic transition energies, calculations were performed on truncated (with H and Me groups) versus nontruncated models. It was observed that the electronic transition energies were not perturbed when the 5-phenyl group was replaced by a methyl group.

The bonding in side-on peroxometal adducts is dominated by a  $\sigma$ -interaction involving the  $\text{Mn } d_x^2-y^2$  orbital and the in-plane peroxo  $\pi$ -antibonding orbital ( $\pi_{\text{ip}}^*$ ), as discussed previously in chapter 2. The strength of the  $\text{Mn}-\text{O}_2$   $\sigma$ -interaction is evidenced by the relatively high percentage of peroxo character ( $\sim 48\%$ ) in this MO. In contrast to the high covalency of the Mn

$d_x^2 - y^2$  MO, the  $d_z^2$  MO carries only ~7% peroxo character and is predominantly Mn-Tp<sup>Ph2</sup>  $\sigma$ -antibonding (Table A.6.2). The Mn  $d_{xz}$  and Mn  $d_{xy}$  orbitals are involved in  $\pi$  antibonding interactions with the peroxo ligand (Figure 6.9). The strength of the Mn–O<sub>2</sub>  $\pi$ -interaction is evidenced by the percentage of peroxo character (Mn  $d_{xz}$  ~ 29 and Mn  $d_{xy}$  ~20% ) in these MOs. Also included among the orbitals are the doubly-occupied out-of-plane peroxo  $\pi$ -antibonding orbital ( $\pi_{op}^*$ ). This is the highest-occupied MO and carries a small percentage of Mn  $d_{yz}$  character (~ 5 %). To correlate this electronic structure description with the spectroscopic data collected, we next performed TD-DFT computations on the truncated model of [Mn<sup>III</sup>(O<sub>2</sub>)(Tp<sup>Ph2</sup>)(THF)] to predict electronic transition energies.

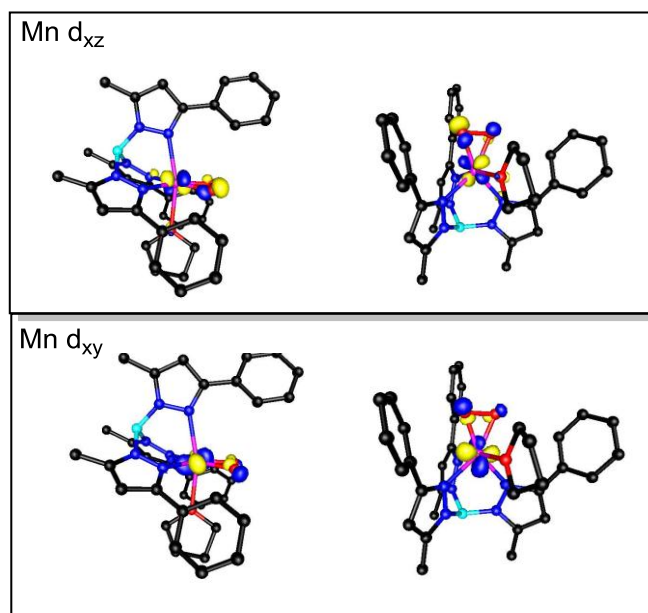


**Figure 6.9.** Surface contour plots (isodensity values of +/- 0.01 au) of the spin-up Mn  $d_{xz}$  (top) and Mn  $d_{xy}$  (bottom) MOs.

The TD-DFT computed absorption for [Mn<sup>III</sup>(O<sub>2</sub>)(Tp<sup>Ph2</sup>)(THF)] is similar to the experimental spectrum (Figure 6.10). A low-intensity band is predicted at 20 300 cm<sup>-1</sup> (band *i*) that is in good agreement with the experiment feature at ~ 19 000 cm<sup>-1</sup> (band 1; Figure 6.4). Band *i* is due solely to a Mn  $d_z^2 \rightarrow d_x^2 - y^2$  transition (Table A.2.3), which is the lowest-energy *d-d*

transition. This transition is highly blue-shifted compared to other reported  $\text{Mn}^{\text{III}}\text{-O}_2$  complexes, which is attributed to the large Jahn-Teller elongation of  $[\text{Mn}^{\text{III}}(\text{O}_2)(\text{Tp}^{\text{Ph}_2})(\text{THF})]$  that stabilizes the Mn  $d_z^2$  orbital. Band *ii* (Figure 6.10), is due to two weak peroxo-to-Mn<sup>III</sup> charge transfer (CT) transitions ( $\text{O}_2 \pi_{\text{op}}^* \rightarrow \text{Mn } d_{xy}$  and  $\text{O}_2 \pi_{\text{op}}^* \rightarrow \text{Mn } d_{yz}$ , respectively). These correspond well with the observed experimental bands at 20 800 and 22 600  $\text{cm}^{-1}$  (bands 2 and 3). In addition to allowing us to assign features in the absorption spectrum, the TD-DFT calculations allow us to make assignments for additional bands resolved in the low-temperature MCD spectrum. Specifically bands 5 and 7 (Figure 6.5) can be assigned as the next two Mn *d-d* transitions ( $d_{xy} \rightarrow d_x^2 - y^2$  and  $d_{xz} \rightarrow d_x^2 - y^2$ ), which are predicted at 27 000 and 28 800  $\text{cm}^{-1}$ , respectively. The high covalency of the peroxo ligand with the Mn  $d_{xz}$  and Mn  $d_{xy}$  orbitals explains the intensity of these combined transitions. At higher-energy, the TD-DFT calculations predict additional peroxo-to-Mn CT transitions as well as the fourth *d-d* band (Table A.6.3).

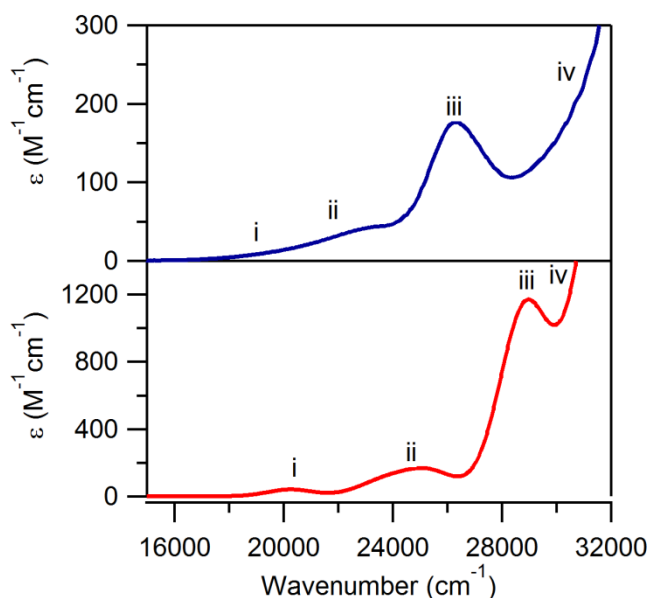


**Figure 6.10.** Experimental absorption spectra of  $[\text{Mn}^{\text{III}}(\text{O}_2)(\text{Tp}^{\text{Ph}_2})(\text{THF})]$  (top). Simulated absorption spectra of  $[\text{Mn}^{\text{III}}(\text{O}_2)(\text{Tp}^{\text{Ph}_2})(\text{THF})]$  based on TD-DFT computations employing the B3LYP functional (bottom).

### 6.3 Summary.

This chapter describes the generation and characterization of a room temperature stable peroxomanganese(III) complex supported by a tridentate scorpionate ligand ( $\text{Tp}^{\text{Ph}_2}$ ). The greater thermal stability allowed for the isolation of single crystals for XRD analysis. The peroxomanganese(III) crystal structure revealed a six coordinate  $\text{Mn}^{\text{III}}$  center with a symmetric peroxo ligand and coordinated solvent ligand. The increased thermal stability can be accounted for the shielding of the peroxo ligand with the bulky phenyl groups on the  $\text{Tp}^{\text{Ph}_2}$  ligand. The electronic structure of this complex revealed that the Mn  $d-d$  transitions are blue shifted compared to the peroxomanganese(III) complexes discussed in chapter 2 and 5. This difference is due to the Jahn-Teller elongation in the  $[\text{Mn}^{\text{III}}(\text{O}_2)(\text{Tp}^{\text{Ph}_2})(\text{THF})]$  complex. With  $[\text{Mn}^{\text{III}}(\text{O}_2)(\text{Tp}^{\text{Ph}_2})(\text{THF})]$  having a relatively large thermal stability, it will allow for investigation of peroxo activation with various substrates (*i.e.* acids, acylchlorides, and carbonate). In addition the THF ligand could be labile and able to be replaced by added substrates.

### 6.4 Material and Methods.

**6.4.1 Materials.** All chemicals were obtained from commercial vendors at ACS reagent-grade or better and were used without further purification. All solvents were dried by routine techniques under an inert argon atmosphere.<sup>25</sup>  $\text{Mn}^{\text{II}}$  complex synthesis was carried out under argon using a glovebox.

**6.4.2 Instrumentation.**  $^1\text{H}$  NMR spectra were obtained on a Bruker DRX 400 MHz NMR spectrometer. Electronic absorption spectra were recorded on a Cary 50 Bio spectrophotometer (Varian) interfaced with a Unisoku cryostat (USP-203-A). ESI-mass spectrometry experiments were performed using an LCT Primers MicroMass electrospray-ionization time-of-flight

instrument. EPR spectra were collected on Bruker EMXPlus instrument with a dual mode cavity. Magnetic circular dichroism (MCD) spectra were collected on a spectropolarimeter (Jasco J-815) interfaced with a magnetocryostat (Oxford Instruments SM-4000-8) capable of horizontal fields up to 8 T.

**6.4.4 Preparation of  $[\text{Mn}^{\text{II}}(\text{Tp}^{\text{Ph}_2})(\text{DMF})_3](\text{OTf})$  Complex.** Potassium tris(3,5-diphenylpyrazol)hydroborate ( $\text{Tp}^{\text{Ph}_2}$ ) was prepared as previously described by condensing 3 molar equivalents of 3,5-diphenylpyrazole with  $\text{KBH}_4$ .<sup>26,27</sup>  $\text{Mn}(\text{OTf})_2$  was prepared by a previously reported procedure by reacting equal molar amounts of  $(\text{CH}_3)_3\text{Si}(\text{OTf})$  and anhydrous  $\text{MnCl}_2$ .<sup>28</sup> The  $[\text{Mn}^{\text{II}}(\text{Tp}^{\text{Ph}_2})](\text{OTf})$  complex was prepared as follows. To a stirred solution of  $\text{Mn}(\text{OTf})_2$  (0.497 g, 1.411 mmol) in 20 mL of DMF was added  $\text{Tp}^{\text{Ph}_2}$  (1.0 g, 1.411 mmol) in 30 mL DMF. The colorless solution was stirred for 4 hours. Precipitation of the crude product was obtained by addition of diethyl ether.  $[\text{Mn}^{\text{II}}(\text{Tp}^{\text{Ph}_2})(\text{DMF})_3](\text{OTf})$  (1.39g, 90%)  $\text{M}^+$   $[\{[\text{Mn}(\text{Tp}^{\text{Ph}_2})]\}^+)$  724.2 requires  $\text{M}^+$ , 724.2].

**6.4.5 X-ray Crystallography.** Single needle crystals of  $[\text{Mn}^{\text{II}}(\text{Tp}^{\text{Ph}_2})(\text{DMF})_3](\text{OTf})$  were grown by layering heptane on a THF solution of the metal complex at ambient temperature. Single needle crystals of  $[\text{Mn}^{\text{III}}(\text{O}_2)(\text{Tp}^{\text{Ph}_2})(\text{THF})]$  were grown by vapor diffusion of diethyl ether into a 50:50 mixture of 2-Me-tetrahydrofuran:THF at -20 °C. Data collection and refinement parameters are summarized in the appendix in Tables A.6.4 and A.6.5.

**6.4.6 In Situ Preparation of  $[\text{Mn}^{\text{III}}(\text{O}_2)(\text{Tp}^{\text{Ph}_2})(\text{THF})]$  Complex.** The yellow peroxomanganese(III) intermediate was formed by treating a THF solution of  $[\text{Mn}^{\text{II}}(\text{Tp}^{\text{Ph}_2})(\text{DMF})_3](\text{OTf})$  with 20 equivalents  $\text{H}_2\text{O}_2$  or by adding excess  $\text{KO}_2$  at ambient

conditions. Purification of  $[\text{Mn}^{\text{III}}(\text{O}_2)(\text{Tp}^{\text{Ph}_2})(\text{THF})]$  sample was done by laying metal solution with diethyl ether at  $-20\text{ }^{\circ}\text{C}$ .

**6.4.7 EPR Experiments.** A frozen glass sample of  $[\text{Mn}^{\text{II}}(\text{Tp}^{\text{Ph}_2})(\text{DMF})_3](\text{OTf})$  (366  $\mu\text{m}$ ) was prepared in a 75:25 mixture of 2-Me-tetrahydrofuran:THF at ambient temperature. A frozen glass sample of  $[\text{Mn}^{\text{III}}(\text{O}_2)(\text{Tp}^{\text{Ph}_2})(\text{THF})]$  (5 mM) was prepared in 75:25 mixture of 2-Me-tetrahydrofuran:THF at ambient temperature. Once formation of the peroxomanganese(III) species was complete (as monitored by UV-visible spectroscopy), the sample was transferred to an EPR tube, and flash-frozen in liquid  $\text{N}_2$ .

**6.4.7 Magnetic Circular Dichroism Experiments.** A frozen glass sample of  $[\text{Mn}^{\text{III}}(\text{O}_2)(\text{Tp}^{\text{Ph}_2})(\text{THF})]$  (15 mM) was prepared in 75:25 mixture of 2-Me-tetrahydrofuran:THF at ambient temperature. Once formation of the peroxomanganese(III) species was complete (as monitored by UV-visible spectroscopy), the sample was transferred to MCD cells, and flash-frozen in liquid  $\text{N}_2$ . The obtained MCD spectra were measured in mdeg ( $\theta$ ) and converted to  $\Delta\epsilon$  ( $\text{M}^{-1}\text{cm}^{-1}$ ) using the standard conversion factor  $\Delta\epsilon = \theta/(32980 \cdot c \cdot d)$ , where  $c$  is the concentration of the sample and  $d$  is the path length. MCD spectra were collected at 2, 4, 8, and 15 K for positive and negative field strengths of 1 to 7 T in 1 T increments. VTVH data were fit using the general method developed by Neese and Solomon.<sup>20</sup> Fits were performed for an  $S = 2$  system with isotropic  $g$ -values of 2.00. Using a previously described protocol,<sup>3</sup> zero-field splitting (ZFS) parameters  $D$  and  $E/D$  were systematically varied while the transition moment products were optimized for a given set of ZFS parameters.

**6.4.8 Density Functional Theory Calculations.** The ORCA 2.7 software package was used for all DFT computations.<sup>29</sup> An initial model of  $[\text{Mn}^{\text{III}}(\text{O}_2)(\text{Tp}^{\text{Ph}_2})(\text{THF})]$  was built using the X-ray

coordinates of the  $[\text{Mn}^{\text{III}}(\text{O}_2)(\text{Tp}^{\text{Ph}_2})(\text{THF})]$  complex. Geometry optimization of this model was converged to the  $S = 2$  spin state. This calculation employed the Becke-Perdew (BP86) functional<sup>30,31</sup> and the SVP (Ahlrichs split valence polarized)<sup>32,33</sup> basis sets with the SV/C auxiliary basis sets for all atoms except for manganese, nitrogen, and oxygen, where the larger TZVP (Ahlrichs triple- $\zeta$  valence polarized)<sup>20</sup> basis sets in conjunction with the TZV/J auxiliary basis sets were used. The resolution of identity (RI) approximation, developed by Neese,<sup>34</sup> was used for all calculations. Solvation effects associated with THF (dielectric constant  $\epsilon = 7.58$ ) were incorporated using COSMO, as implemented in *ORCA*.<sup>35</sup>

Electronic transition energies and intensities were computed for  $[\text{Mn}^{\text{III}}(\text{O}_2)(\text{Tp}^{\text{Ph}_2})(\text{THF})]$  and using the TD-DFT method<sup>36-38</sup> within the Tamm-Dancoff approximation.<sup>39,40</sup> These calculations employed the B3LYP functional,<sup>41-43</sup> and TZVP (Mn, N, and O) and SVP (C and H) basis sets. In each calculation, 40 excited states were calculated by including all one-electron excitations within an energy window of  $\pm 3$  Hartrees with respect to the HOMO/LUMO energies. Isosurface plots of molecular orbitals and electron density difference maps (EDDMs) were generated using the gOpenMol program using isodensity values of 0.01 and 0.001  $\text{b}^{-3}$ , respectively.

## 6.6 References

- (1) Grove, L. E.; Brunold, T. C. *Comments Inorg. Chem.* **2008**, 29, 134.
- (2) Miller, A.-F. *Curr. Opin. Chem. Biol.* **2004**, 8, 162.
- (3) Jackson, T. A.; Karapetian, A.; Miller, A.-F.; Brunold, T. C. *Biochem.* **2005**, 44, 1504.
- (4) Bull, C.; Niederhoffer, E. C.; Yoshida, T.; Fee, J. A. *J. Am. Chem. Soc.* **1991**, 113, 4069.
- (5) Hearn, A. S.; Stroupe, M. E.; Cabelli, D. E.; Lepock, J. R.; Tainer, J. A.; Nick, H. S.; Silverman, D. N. *Biochem.* **2001**, 40, 12051.
- (6) Hearn, A. S.; Tu, C. K.; Nick, H. S.; Silverman, D. N. *J. Bio. Chem.* **1999**, 274, 24457.
- (7) Gunderson, W. A.; Zatsman, A. I.; Emerson, J. P.; Farquhar, E. R.; Que, L.; Lipscomb, J. D.; Hendrich, M. P. *J. Am. Chem. Soc.* **2008**, 130, 14465.



- (8) Vetting, M. W.; Wackett, L. P.; Que, L., Jr.; Lipscomb, J. D.; Ohlendorf, D. H. *J. Bacteriol.* **2004**, *186*, 1945.
- (9) Opaleye, O.; Rose, R.-S.; Whittaker, M. M.; Woo, E.-J.; Whittaker, J. W.; Pickersgill, R. W. *J. Biol. Chem.* **2006**, *281*, 6428.
- (10) Borowski, T.; Bassan, A.; Richards, N. G. J.; Siegbahn, P. E. M. *J. Chem. Theory Comput.* **2005**, *1*, 686.
- (11) Reinhardt, L. A.; Svedruzic, D.; Chang, C. H.; Cleland, W. W.; Richards, N. G. J. *J. Am. Chem. Soc.* **2003**, *125*, 1244.
- (12) Svedružić, D.; Jónsoon, S.; Toyota, C. G.; Reinhardt, L. A.; Ricagno, S.; Lindqvist, Y.; Richards, N. G. J. *Arch. Biochem. Biophys.* **2005**, *433*, 176.
- (13) Tanner, A.; Bowater, L.; Fairhurst, S. A.; Bornemann, S. *J. Biol. Chem.* **2001**, *276*, 43627.
- (14) Kitajima, N.; Komatsuzaki, H.; Hikichi, S.; Osawa, M.; Moro-oka, Y. *J. Am. Chem. Soc.* **1994**, *116*, 11596.
- (15) Singh, U. P.; Sharma, A. K.; Hikichi, S.; Komatsuzaki, H.; Moro-oka, Y.; Akita, M. *Inorg. Chim. Acta* **2006**, *359*, 4407.
- (16) VanAtta, R. B.; Strouse, C. E.; Hanson, L. K.; Valentine, J. S. *J. Am. Chem. Soc.* **1987**, *109*, 1425.
- (17) Geiger, R. A.; Chattopadhyay, S.; Day, V. W.; Jackson, T. A. *J. Am. Chem. Soc.* **2010**, *132*, 2821.
- (18) Costas, M.; Mehn, M. P.; Jensen, M. P.; Que, L. J. *Chem. Rev.* **2004**, *104*, 939.
- (19) Neese, F.; Solomon, E. I. *J. Am. Chem. Soc.* **1998**, *120*, 12829.
- (20) Neese, F.; Solomon, E. I. *Inorg. Chem.* **1999**, *38*, 1847.
- (21) Oganessian, V. S.; George, S. J.; Cheesman, M. R.; Thomson, A. J. *J. Chem. Phys.* **1999**, *110*, 762.
- (22) Shook, R. L.; Gunderson, W. A.; Greaves, J.; Ziller, J. W.; Hendrich, M. P.; Borovik, A. S. *J. Am. Chem. Soc.* **2008**, *130*, 8888.
- (23) Groni, S.; Blain, G.; Guillot, R.; Policar, C.; Anxolabéhère-Mallart, E. *Inorg. Chem.* **2007**, *46*, 1951.
- (24) Groni, S.; Dorlet, P.; Blain, G.; Bourcier, S.; Guillot, R.; Anxolabéhère-Mallart, E. *Inorg. Chem.* **2008**, *47*, 3166.
- (25) Armarego, W. L. F.; Perrin, D. D. *Purification of Laboratory Chemicals*; Butterworth-Heinemann: Oxford, U.K., 1997.
- (26) Pecoraro, V. L.; Baldwin, M. J.; Gelasco, A. *Chem. Rev.* **1994**, *94*, 807.
- (27) Vaska, L. *Acc. Chem. Res.* **1975**, *9*, 175.
- (28) Seo, M. S.; Kim, J. Y.; Annaraj, J.; Kim, Y.; Lee, Y.-M.; Kim, S.-J.; Kim, J.; Nam, W. *Angew. Chem. Int. Ed.* **2007**, *46*, 377.
- (29) Neese, F., *ORCA - an ab initio, Density Functional and Semiempirical Program Package, Version 2.8*, University of Bonn, 2009.
- (30) Becke, A. D. *J. Chem. Phys.* **1986**, *84*, 4524.
- (31) Perdew, J. P. *Phys. Rev. B* **1986**, *33*, 8822.
- (32) Schäfer, A.; Horn, H.; Ahlrichs, R. *J. Chem. Phys.* **1992**, *97*, 2571.
- (33) Schäfer, G.; Huber, C.; Ahlrichs, R. *J. Chem. Phys.* **1994**, *100*, 5829.
- (34) Neese, F. J. *Comput. Chem.* **2003**, *24*, 1740.
- (35) Sinnecker, S.; Rajendran, A.; Klamt, A.; Diedenhofen, M.; Neese, F. *J. Phys. Chem. A* **2006**, *110*, 2235.
- (36) Bauernschmitt, R.; Ahlrichs, R. *Chem. Phys. Lett.* **1996**, *256*, 454.

- (37) Casida, E. M.; Jamorski, C.; Casida, K. C.; Salahub, D. R. *J. Chem. Phys.* **1998**, *108*, 4439.
- (38) Stratman, R. E.; Scuseria, G. E.; Frisch, M. J. *J. Chem. Phys.* **1998**, *109*, 8218.
- (39) Hirata, S.; Head-Gordon, M. *Chem. Phys. Lett.* **1999**, *302*, 375.
- (40) Hirata, S.; Head-Gordon, M. *Chem. Phys. Lett.* **1999**, *314*, 291.
- (41) Becke, A. D. *J. Chem. Phys.* **1993**, *98*, 1372.
- (42) Becke, A. D. *J. Chem. Phys.* **1993**, *98*, 5648.
- (43) Lee, C.; Yang, W.; Parr, R. G. *Phys. Rev. B* **1988**, *37*, 785.

## Appendix

**Table A.2.1.** Crystal Data and Structure Refinement for [Mn(N<sub>4</sub>C<sub>17</sub>H<sub>22</sub>)(NCCH<sub>3</sub>)<sub>3</sub>][ClO<sub>4</sub>]<sub>2</sub> (**1-H**).

Empirical formula	C <sub>23</sub> H <sub>31</sub> Cl <sub>2</sub> MnN <sub>7</sub> O <sub>8</sub>	
Formula weight	659.39	
Temperature	100(2) K	
Wavelength	0.71073 Å	
Crystal system	Triclinic	
Space group	P $\bar{1}$ – C <sub>i</sub> <sup>1</sup> (No. 2)	
Unit cell dimensions	a = 10.4582(7) Å b = 11.9788(8) Å c = 12.9774(8) Å	$\alpha = 91.148(1)^\circ$ $\beta = 97.368(1)^\circ$ $\gamma = 111.967(1)^\circ$
Volume	1491.2(2) Å <sup>3</sup>	
Z	2	
Density (calculated)	1.469 Mg/m <sup>3</sup>	
Absorption coefficient	0.678 mm <sup>-1</sup>	
F(000)	682	
Crystal size	0.44 x 0.32 x 0.08 mm <sup>3</sup>	
Theta range for data collection	2.46° to 30.53°	
Index ranges	-14 ≤ h ≤ 14, -16 ≤ k ≤ 17, -18 ≤ l ≤ 18	
Reflections collected	17596	
Independent reflections	8675 [R <sub>int</sub> = 0.037]	
Completeness to theta = 30.53°	95.2 %	
Absorption correction	Multi-scan	
Max. and min. transmission	1.000 and 0.898	
Refinement method	Full-matrix least-squares on F <sup>2</sup>	
Data / restraints / parameters	8675 / 92 / 559	
Goodness-of-fit on F <sup>2</sup>	1.019	
Final R indices [I > 2sigma(I)]	R <sub>1</sub> = 0.047, wR <sub>2</sub> = 0.106	
R indices (all data)	R <sub>1</sub> = 0.065, wR <sub>2</sub> = 0.112	
Largest diff. peak and hole	0.41 and -0.32 e <sup>-</sup> /Å <sup>3</sup>	

$$R_1 = \Sigma ||F_O| - |F_C|| / \Sigma |F_O|$$

$$wR_2 = \{ \Sigma [w(F_O^2 - F_C^2)^2] / \Sigma [w(F_O^2)^2] \}^{1/2}$$

**Table A.2.2.** Crystal Data and Structure Refinement for  $[\text{Mn}(\text{N}_4\text{C}_{17}\text{H}_{20}\text{Br}_2)(\text{ClO}_4)(\text{CH}_3\text{COCH}_3)][\text{ClO}_4]$  (**1-Br**).

Empirical formula	$\text{C}_{20}\text{H}_{26}\text{Br}_2\text{Cl}_2\text{MnN}_4\text{O}_9$	
Formula weight	752.11	
Temperature	100(2) K	
Wavelength	0.71073 Å	
Crystal system	Monoclinic	
Space group	$\text{P2}_1/\text{c} - \text{C}_{2\text{h}}^5$ (No. 14)	
Unit cell dimensions	$a = 9.801(1)$ Å $b = 17.980(1)$ Å $c = 15.157(1)$ Å	$\alpha = 90.000^\circ$ $\beta = 96.511(1)^\circ$ $\gamma = 90.000^\circ$
Volume	$2653.8(2)$ Å <sup>3</sup>	
Z	4	
Density (calculated)	$1.882 \text{ Mg/m}^3$	
Absorption coefficient	$3.767 \text{ mm}^{-1}$	
F(000)	1500	
Crystal size	$0.16 \times 0.10 \times 0.06 \text{ mm}^3$	
Theta range for data collection	$2.38^\circ$ to $30.52^\circ$	
Index ranges	$-13 \leq h \leq 13, -24 \leq k \leq 25, -21 \leq l \leq 21$	
Reflections collected	30806	
Independent reflections	7991 [ $R_{\text{int}} = 0.042$ ]	
Completeness to theta = $30.52^\circ$	98.7 %	
Absorption correction	Multi-scan	
Max. and min. transmission	1.000 and 0.758	
Refinement method	Full-matrix least-squares on $F^2$	
Data / restraints / parameters	7991 / 102 / 590	
Goodness-of-fit on $F^2$	1.017	
Final R indices [ $I > 2\sigma(I)$ ]	$R_1 = 0.040, wR_2 = 0.085$	
R indices (all data)	$R_1 = 0.060, wR_2 = 0.091$	
Largest diff. peak and hole	$0.79$ and $-0.49 \text{ e}^-/\text{\AA}^3$	

$$R_1 = \Sigma ||F_O| - |F_C|| / \Sigma |F_O|$$

$$wR_2 = \{ \Sigma [w(F_O^2 - F_C^2)^2] / \Sigma [w(F_O^2)^2] \}^{1/2}$$

**Table A.2.3.** Crystal Data and Structure Refinement for [Mn(N<sub>4</sub>C<sub>19</sub>H<sub>26</sub>)(NCCH<sub>3</sub>)(ClO<sub>4</sub>)](ClO<sub>4</sub>) (**1-Me**).

Empirical formula	C <sub>21</sub> H <sub>29</sub> Cl <sub>2</sub> MnN <sub>5</sub> O <sub>8</sub>	
Formula weight	605.33	
Temperature	100(2) K	
Wavelength	0.71073 Å	
Crystal system	Monoclinic	
Space group	P2 <sub>1</sub> /c – C <sub>2h</sub> <sup>5</sup> (No. 14)	
Unit cell dimensions	a = 18.169(2) Å	α = 90.000°
	b = 9.879(1) Å	β = 104.277(2)°
	c = 14.545(2) Å	γ = 90.000°
Volume	2530.1(6) Å <sup>3</sup>	
Z	4	
Density (calculated)	1.589 Mg/m <sup>3</sup>	
Absorption coefficient	0.789 mm <sup>-1</sup>	
F(000)	1252	
Crystal size	0.44 x 0.12 x 0.11 mm <sup>3</sup>	
Theta range for data collection	2.31° to 29.20°	
Index ranges	-24 ≤ h ≤ 24, -13 ≤ k ≤ 13, -19 ≤ l ≤ 19	
Reflections collected	23041	
Independent reflections	6423 [R <sub>int</sub> = 0.054]	
Completeness to theta = 29.20°	93.8 %	
Absorption correction	Multi-scans	
Max. and min. transmission	1.000 and 0.901	
Refinement method	Full-matrix least-squares on F <sup>2</sup>	
Data / restraints / parameters	6423 / 0 / 450	
Goodness-of-fit on F <sup>2</sup>	1.043	
Final R indices [I>2sigma(I)]	R <sub>1</sub> = 0.048, wR <sub>2</sub> = 0.100	
R indices (all data)	R <sub>1</sub> = 0.062, wR <sub>2</sub> = 0.107	
Largest diff. peak and hole	0.82 and -0.50 e <sup>-</sup> /Å <sup>3</sup>	

$$R_1 = \sum ||F_O| - |F_C|| / \sum |F_O|$$

$$wR_2 = \{ \sum [w(F_O^2 - F_C^2)^2] / \sum [w(F_O^2)^2] \}^{1/2}$$

**Table A.2.4.** Crystal Data and Structure Refinement for [Mn(N<sub>4</sub>C<sub>19</sub>H<sub>28</sub>O<sub>2</sub>)(ClO<sub>4</sub>)<sub>2</sub>] (**1-MeO**).

Empirical formula	C <sub>19</sub> H <sub>28</sub> Cl <sub>2</sub> MnN <sub>4</sub> O <sub>10</sub>	
Formula weight	598.29	
Temperature	100(2) K	
Wavelength	0.71073 Å	
Crystal system	Monoclinic	
Space group	C2/c – C <sub>2h</sub> <sup>6</sup> (No. 15)	
Unit cell dimensions	a = 13.631(1) Å b = 10.755(1) Å c = 17.202(2) Å	α = 90.000° β = 109.022(1)° γ = 90.000°
Volume	2384.0(4) Å <sup>3</sup>	
Z	4	
Density (calculated)	1.667 Mg/m <sup>3</sup>	
Absorption coefficient	0.842 mm <sup>-1</sup>	
F(000)	1236	
Crystal size	0.40 x 0.32 x 0.30 mm <sup>3</sup>	
Theta range for data collection	2.47° to 29.10°	
Index ranges	-18 ≤ h ≤ 17, -14 ≤ k ≤ 14, -23 ≤ l ≤ 23	
Reflections collected	10685	
Independent reflections	2995 [R <sub>int</sub> = 0.057]	
Completeness to theta = 29.10°	93.6 %	
Absorption correction	Multi-scan	
Max. and min. transmission	1.000 and 0.815	
Refinement method	Full-matrix least-squares on F <sup>2</sup>	
Data / restraints / parameters	2995 / 0 / 178	
Goodness-of-fit on F <sup>2</sup>	1.107	
Final R indices [I > 2σ(I)]	R <sub>1</sub> = 0.053, wR <sub>2</sub> = 0.125	
R indices (all data)	R <sub>1</sub> = 0.054, wR <sub>2</sub> = 0.126	
Largest diff. peak and hole	0.69 and -0.67 e <sup>-</sup> /Å <sup>3</sup>	

$$R_1 = \sum ||F_O| - |F_C|| / \sum |F_O|$$

$$wR_2 = \{ \sum [w(F_O^2 - F_C^2)^2] / \sum [w(F_O^2)^2] \}^{1/2}$$

**Table A.2.5.** Selected Bond Lengths (Å) and Angles (°) for Low-Occupancy Forms of **1-H**, and **1-Br**.

Complex <b>1-H</b>			
Mn-N(1)	2.299(13)	N(1)-Mn-N(2)	158.4(10)
Mn-N(2)	2.329(13)	N(1)-Mn-N(3)	73.4(6)
Mn-N(3)	2.352(15)	N(2)-Mn-N(4)	70.3(5)
Mn-N(4)	2.377(14)	N(3)-Mn-N(4)	68.8(5)
Mn-X(1)	2.323(7)	X(1)-Mn-X(2)	159.8(3)
Mn-X(2)	2.257(7)	X(1)-Mn-X(3)	78.5(2)
Mn-X(3)	2.479(6)	X(2)-Mn-X(3)	81.8(2)
Complex <b>1-Br</b>			
Mn-N(1)	2.292(11)	N(1)-Mn-N(2)	154.5(5)
Mn-N(2)	2.248(12)	N(1)-Mn-N(3)	71.4(4)
Mn-N(3)	2.320(12)	N(2)-Mn-N(4)	73.5(4)
Mn-N(4)	2.340(11)	N(3)-Mn-N(4)	69.1(3)
Mn-X(1)	2.211(4)	X(1)-Mn-X(2)	153.1(2)
Mn-X(2)	2.290(4)	X(1)-Mn-X(3)	89.2(3)
Mn...X(3)	2.671(3)	X(2)-Mn-X(3)	73.8(3)



**Table A.2.6.** Cartesian coordinates (Å) for DFT energy-minimized model of  $[\text{Mn}^{\text{III}}(\text{O}_2)(\text{L}^7\text{py}_2^{\text{H}})]^+$  (isomer **P**).

<b>Atom</b>	<b>x</b>	<b>y</b>	<b>z</b>
Mn	-0.0503	-0.0136	0.5891
N	-1.8556	-1.0878	-0.1123
N	-0.8691	1.4379	-0.8658
N	1.5472	1.5782	0.2308
N	1.6120	-1.1033	-0.1119
C	-2.3394	-2.1916	0.5013
C	-3.6942	-2.5445	0.4627
H	-4.0395	-3.4606	0.9657
C	-4.5866	-1.7002	-0.2196
H	-5.6629	-1.9344	-0.2592
C	-4.0886	-0.5473	-0.8473
H	-4.7592	0.1390	-1.3882
C	-2.7118	-0.2766	-0.7821
C	-2.0818	0.8742	-1.5387
H	-1.7674	0.4795	-2.5286
H	-2.8303	1.6715	-1.7387
C	-1.2364	2.6460	-0.0352
H	-1.8267	2.2822	0.8313
H	-1.9061	3.2976	-0.6438
C	-0.0343	3.4962	0.4111
H	0.3205	4.1007	-0.4516
H	-0.4123	4.2371	1.1494
C	1.1577	2.7615	1.0440
H	0.9126	2.3967	2.0636
H	2.0151	3.4738	1.1257
C	1.5729	-2.3590	-0.6142
C	2.7336	-3.0906	-0.8896
H	2.6551	-4.1082	-1.2999
C	3.9788	-2.4917	-0.6364
H	4.9146	-3.0343	-0.8448
C	4.0180	-1.1842	-0.1259
H	4.9773	-0.6801	0.0689
C	2.8146	-0.5112	0.1330
C	2.7655	0.8957	0.7044
H	3.6974	1.4527	0.4472
H	2.7096	0.8370	1.8146
C	1.5966	1.8887	-1.2199
H	2.2729	1.1563	-1.7027
H	2.0451	2.8947	-1.3857
C	0.1891	1.7729	-1.8705
H	-0.0852	2.7043	-2.4162
H	0.1993	0.9489	-2.6108
O	0.1025	-0.5927	2.3578

O	-0.8414	0.4898	2.2121
H	-1.6034	-2.8045	1.0471
H	0.5714	-2.7771	-0.8011

**Table A.2.7.** Cartesian coordinates (Å) for DFT energy-minimized model of  $[\text{Mn}^{\text{III}}(\text{O}_2)(\text{L}^7\text{py}_2^{\text{H}})]^+$  (isomer **E**).

Atom	x	y	z
Mn	0.0244	-0.0460	-0.0257
O	-0.1289	-1.7802	-0.7025
O	-0.1628	-1.7463	0.7369
N	-2.0225	0.6529	-0.5992
N	0.3060	0.7871	-2.0596
N	2.2147	0.6757	-0.2563
N	0.5673	0.7816	1.8746
C	-3.1031	0.8476	0.1884
C	-4.3684	1.1650	-0.3218
C	-4.5151	1.2919	-1.7126
C	-3.3965	1.0863	-2.5352
C	-2.1650	0.7569	-1.9462
C	-0.9404	0.4265	-2.7775
C	0.4764	2.2811	-2.0512
C	1.8880	2.7288	-1.6717
C	2.4062	2.1505	-0.3552
C	-0.2748	1.1890	2.8509
C	0.1560	1.4608	4.1551
C	1.5184	1.3044	4.4564
C	2.3966	0.8924	3.4413
C	1.8916	0.6346	2.1583
C	2.7722	0.1682	1.0103
C	2.6231	-0.0381	-1.4876
C	1.5142	0.0853	-2.5876
H	-2.9456	0.7369	1.2732
H	-5.2163	1.3136	0.3642
H	-5.4909	1.5507	-2.1541
H	-3.4739	1.1763	-3.6305
H	-0.9272	-0.6709	-2.9542
H	-0.9963	0.9252	-3.7719
H	0.2388	2.6706	-3.0694
H	-0.2775	2.7014	-1.3501
H	1.8810	3.8371	-1.5844
H	2.5945	2.4986	-2.4978
H	1.8783	2.6166	0.5033
H	3.4934	2.3868	-0.2488
H	-1.3326	1.3039	2.5698
H	-0.5699	1.7921	4.9129
H	1.8970	1.5110	5.4701

H	3.4738	0.7728	3.6372
H	3.8264	0.4940	1.1766
H	2.7666	-0.9444	0.9752
H	2.7526	-1.1052	-1.2205
H	3.6023	0.3357	-1.8656
H	1.8943	0.6013	-3.4963
H	1.1933	-0.9286	-2.8920

**Table A.2.8.** Cartesian coordinates (Å) for DFT energy-minimized model of  $[\text{Mn}^{\text{III}}(\text{O}_2)(\text{L}^7\text{py}_2^{\text{Me}})^6]$ .

Atom	x	y	z
Mn	-0.0108	0.0953	0.4954
O	-0.6883	0.2814	2.2681
O	0.5173	-0.5233	2.1750
N	-1.9737	-0.8909	-0.1724
N	-0.8237	1.5287	-0.8814
N	1.4410	1.8519	0.4785
N	1.8530	-0.7460	-0.2524
C	-2.5954	-1.8840	0.5267
C	-3.9879	-2.0677	0.4241
C	-4.7524	-1.2295	-0.4026
C	-4.0953	-0.2176	-1.1235
C	-2.7110	-0.0833	-0.9802
C	-1.8959	0.9379	-1.7477
C	-1.4234	2.5881	0.0288
C	-0.4002	3.5187	0.6924
C	0.8143	2.8707	1.3718
C	-1.7485	-2.8055	1.3728
C	2.0560	-1.9119	-0.9346
C	3.3423	-2.4730	-1.0246
C	4.4316	-1.8395	-0.4077
C	4.2156	-0.6280	0.2588
C	2.9141	-0.1043	0.3096
C	2.6556	1.2319	0.9984
C	1.5667	2.3506	-0.9109
C	0.2865	2.0662	-1.7372
C	0.8770	-2.5773	-1.5862
H	-4.4703	-2.8757	0.9958
H	-5.8430	-1.3677	-0.4776
H	-4.6405	0.4665	-1.7927
H	-1.3850	0.4531	-2.6054
H	-2.5464	1.7425	-2.1596
H	-2.0375	2.0485	0.7784
H	-2.1073	3.2152	-0.5877
H	-0.0556	4.2684	-0.0509
H	-0.9405	4.1082	1.4655

H	0.5444	2.3493	2.3112
H	1.5501	3.6755	1.6168
H	-1.0510	-2.2419	2.0273
H	-1.1306	-3.4610	0.7195
H	-2.4045	-3.4404	2.0038
H	3.4858	-3.4092	-1.5847
H	5.4326	-2.2950	-0.4721
H	5.0338	-0.0665	0.7360
H	3.5560	1.8747	0.8447
H	2.5303	1.0667	2.0878
H	2.4388	1.8658	-1.3927
H	1.7924	3.4403	-0.9152
H	-0.0542	2.9903	-2.2573
H	0.4829	1.2873	-2.4985
H	0.1347	-2.9177	-0.8316
H	1.2003	-3.4639	-2.1681
H	0.3410	-1.8896	-2.2756

**Table A.2.9.** Room-temperature effective magnetic moments ( $\mu_{\text{eff}}$  BM) for  $[\text{Mn}^{\text{II}}(\text{L}^7\text{py}_2^{\text{R}})]^{2+}$  complexes in deuterated MeCN solution, as measured by the  $^1\text{H}$ -NMR method of Evans.

Compound	$\mu_{\text{eff}}$
$[\text{Mn}^{\text{II}}(\text{L}^7\text{py}_2^{\text{H}})](\text{ClO}_4)_2$	5.99
$[\text{Mn}^{\text{II}}(\text{L}^7\text{py}_2^{5\text{-Br}})](\text{ClO}_4)_2$	5.88
$[\text{Mn}^{\text{II}}(\text{L}^7\text{py}_2^{6\text{-Me}})](\text{ClO}_4)_2$	5.80
$[\text{Mn}^{\text{II}}(\text{L}^7\text{py}_2^{6\text{-MeO}})](\text{ClO}_4)_2$	6.15

**Table A.2.10.** Electronic transition energies ( $\text{cm}^{-1}$ ), oscillator strengths ( $f_{\text{exp}}$ ), and bandwidths (fwhm;  $\text{cm}^{-1}$ ) from Gaussian deconvolutions of 233 K absorption and 4.5, 7 T MCD data of  $[\text{Mn}^{\text{III}}(\text{O}_2)(\text{L}^7\text{py}_2^{\text{H}})]^+$ .

band	energy	$f_{\text{exp}}$	fwhm
1	Abs: 16 000	0.00127	Abs: 3247
	MCD: 16 300		MCD: 3164
2	Abs: 22 170	0.00500	Abs: 2498
	MCD: 21 830		MCD: 2248
3	Abs: 24 632	0.00201	Abs: 2248
	MCD: 24 430		MCD: 2248
4	Abs: 26 912	0.00177	Abs: 2248
	MCD: 26 650		MCD: 2248
5	Abs: 29 226	0.00273	Abs: 2248
	MCD: 28 735		MCD: 2248
6	Abs: 31 428	0.00626	Abs: 2248
	MCD: 30 100		MCD: 2248

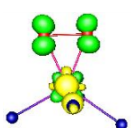
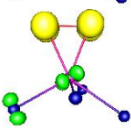
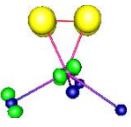
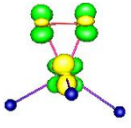
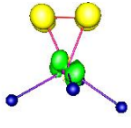
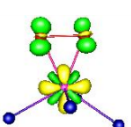
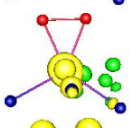
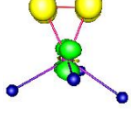
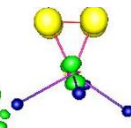
**Table A.2.11.** Electronic transition energies ( $\text{cm}^{-1}$ ), oscillator strengths ( $f_{exp}$ ), and bandwidths (fwhm;  $\text{cm}^{-1}$ ) from Gaussian deconvolutions of 233 K absorption and 4.5, 7 T MCD data of  $[\text{Mn}^{\text{III}}(\text{O}_2)(\text{L}^7\text{py}_2^{6-\text{Me}})]^+$ .

band	energy	$f_{exp}$	fwhm
1	Abs: 14 400 MCD: 13 650	0.00020	Abs: 4163 MCD: 3330
2	Abs: 17 600 MCD: 18 800	0.00097	Abs: 4163 MCD: 3330
3	Abs: 21 000 MCD: 21 665	0.00152	Abs: 4163 MCD: 2248
4	Abs: 23 900 MCD: 24 000	0.00358	Abs: 3330 MCD: 2248
5	Abs: 28 780 MCD: 28 720	0.00244	Abs: 3330 MCD: 2248
6	Abs: 30 800 MCD: 30 860	0.00440	Abs: 3330 MCD: 2248

**Table A.2.12.** Energies (eV) and Compositions (%) of the O 2p-based MOs and the Mn 3d-based MOs Based on Spin-Unrestricted B3LYP DFT Computations for  $[\text{Mn}^{\text{III}}(\text{O}_2)(\text{L}^7\text{py}_2^{\text{H}})]^+$ .

orbital	occup	spin	energy	Mn 3d	O <sup>A</sup> 2p	O <sup>B</sup> 2p	L <sup>7</sup> py <sub>2</sub> <sup>H</sup>
88 (Mn yz)	1.0	↑	-11.735	54.4	1.5 (z)	1.9 (z/x)	5.9
90 (Mn yz / py)	1.0	↑	-11.270	29.4	1.3 (z)	2.2 (x)	19.0
93 (Mn xy/x <sup>2</sup> -y <sup>2</sup> )	1.0	↑	-10.416	27.2	23.7 (x)	2.6 (x)	21.4
94 (Mn x <sup>2</sup> -y <sup>2</sup> )	1.0	↑	-10.364	38.9	1.8 (z)	16.0 (x)	9.4
95 (Mn xz)	1.0	↑	-10.130	46.7	7.3 (z)	11.1 (z)	19.6
96 (Mn z <sup>2</sup> )	1.0	↑	-8.835	42.6	2.0 (x)	3.4 (x)	32.9
97 (O <sub>2</sub> π <sub>op</sub> <sup>*</sup> )	1.0	↑	-8.402	5.3 (yz)	46.6 (z)	46.6 (z)	0.2
98 (N py π)	0.0	↑	-4.908	5.7 (xy)	1.5 (x)	2.7 (x)	22.0
99 (Mn xy)	0.0	↑	-4.757	33.0	25.8 (x)	22.2 (x)	6.4
100 (N py π)	0.0	↑	-4.522	1.5 (z <sup>2</sup> )	0.2 (x)	0.9 (x)	81.0
101 (N py π)	0.0	↑	-4.293	0.1 (yz)	0	0	88.4
93 (O <sub>2</sub> π <sub>op</sub> <sup>*</sup> )	1.0	↓	-8.521	7.1 (yz)	44.0 (z)	46.3 (z)	0.2
94 (py π)	0.0	↓	-5.128	12.6 (x <sup>2</sup> -y <sup>2</sup> )	0.5 (x/y)	0.7 (x/y)	74.9
95 (py π)	0.0	↓	-4.722	12.8 (yz)	0.2 (z)	1.5 (z)	61.1
96 (py π)	0.0	↓	-4.309	3.9 (yz)	0.5 (z)	0.1 (z)	84.2
97 (py π)	0.0	↓	-4.012	9.4 (yz)	0.8 (z)	0.4 (z)	77.7
98 (Mn yz)	0.0	↓	-3.772	71.2	2.8 (z)	2.8 (z)	3.7
99 (Mn x <sup>2</sup> -y <sup>2</sup> )	0.0	↓	-3.450	66.4	1.2 (y)	1.9 (x)	6.8
100 (Mn xz)	0.0	↓	-3.411	83.1	3.4 (z)	1.3 (z)	2.8
101 (Mn z <sup>2</sup> )	0.0	↓	-2.694	72.6	1.7 (x)	0.6 (y)	7.5
102 (Mn xy)	0.0	↓	-2.600	66.5	9.6 (x)	10.8 (x)	3.0

**Table A.2.13.** TD-DFT Calculated Energies, Percent Contributions from Dominant One-electron Excitations, and Oscillator Strengths for the Major Electronic Transitions of  $[\text{Mn}^{\text{III}}(\text{O}_2)(\text{L}^7\text{py}_2^{\text{H}})]^+$  (**2-H**).

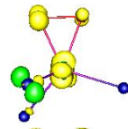
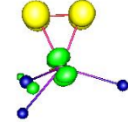
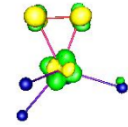
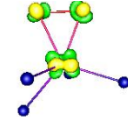
band	state	energy ( $\text{cm}^{-1}$ ) <sup>a</sup>	$f_{osc}$	transition <sup>b</sup>	%	donor MO	acceptor MO	comments	EDDM <sup>c</sup>
<i>i</i>	2	17 300	0.000882	96 $\alpha$ $\rightarrow$	79	Mn $d_z^2$	Mn $d_{xy}$	Mn d $\rightarrow$ d	
				99 $\alpha$	13	Mn $d_z^2$	py $\pi$		
				96 $\alpha$ $\rightarrow$					
				98 $\alpha$					
<i>ii</i>	4	22 600	0.001901	97 $\alpha$ $\rightarrow$	46	O <sub>2</sub> $\pi_{op}^*$	py $\pi$	O <sub>2</sub> $\rightarrow$ Mn / py $\pi$ CT	
				98 $\alpha$					
				93 $\beta$ $\rightarrow$	33	O <sub>2</sub> $\pi_{op}^*$	Mn $d_{yz}$		
				95 $\beta$					
<i>iii</i>	5	22 700	0.001292	97 $\alpha$ $\rightarrow$	42	O <sub>2</sub> $\pi_{op}^*$	py $\pi$	O <sub>2</sub> $\rightarrow$ Mn CT	
				98 $\alpha$					
				93 $\beta$ $\rightarrow$	32	O <sub>2</sub> $\pi_{op}^*$	Mn $d_{yz}$		
				95 $\beta$					
	6	24 600	0.000030	95 $\alpha$ $\rightarrow$	65	Mn $d_{xz}$	Mn $d_{xy}$	Mn d $\rightarrow$ d	
				99 $\alpha$					
				95 $\alpha$ $\rightarrow$	10	Mn $d_{xz}$	py $\pi$		
				98 $\alpha$					
	9	26 000	0.001851	93 $\beta$ $\rightarrow$	29	O <sub>2</sub> $\pi_{op}^*$	Mn $d_{yz}$	O <sub>2</sub> $\rightarrow$ Mn / py $\pi$ CT	
				98 $\beta$					
				93 $\beta$ $\rightarrow$	17	O <sub>2</sub> $\pi_{op}^*$	py $\pi$		
				96 $\beta$	13	O <sub>2</sub> $\pi_{op}^*$	py $\pi$		
				93 $\beta$ $\rightarrow$					
				95 $\beta$					
				93 $\beta$ $\rightarrow$	13	O <sub>2</sub> $\pi_{op}^*$	py $\pi$		
				99 $\beta$	10	O <sub>2</sub> $\pi_{op}^*$	Mn $d_{xz}$		
				93 $\beta$ $\rightarrow$					
				100 $\beta$					
	10	26 400	0.006583	94 $\alpha$ $\rightarrow$	46	Mn $d_x^2 - d_y^2$	Mn $d_{xy}$	Mn d $\rightarrow$ d	
				99 $\alpha$					
	11	27 500	0.017751	96 $\alpha$ $\rightarrow$	92	Mn $d_z^2$	py $\pi$	Mn $\rightarrow$ py CT	
				100 $\alpha$					
	13	28 700	0.002082	93 $\beta$ $\rightarrow$	38	O <sub>2</sub> $\pi_{op}^*$	Mn $d_{xz}$	O <sub>2</sub> $\rightarrow$ Mn CT	
				100 $\beta$	25	O <sub>2</sub> $\pi_{op}^*$	py $\pi$		
				93 $\beta$ $\rightarrow$					
				96 $\beta$					
	15	29 400	0.003336	93 $\beta$ $\rightarrow$	53	O <sub>2</sub> $\pi_{op}^*$	py $\pi$	O <sub>2</sub> $\rightarrow$ Mn CT	
				96 $\beta$					
				93 $\beta$ $\rightarrow$	32	O <sub>2</sub> $\pi_{op}^*$	Mn $d_{xz}$		
				100 $\beta$					

18	31 500	0.002318	93 $\beta$ $\rightarrow$ 102 $\beta$	45	O <sub>2</sub> $\pi_{op}^*$	Mn d <sub>xy</sub>	O <sub>2</sub> $\rightarrow$ Mn CT	
25	33 800	0.003753	90 $\alpha$ $\rightarrow$ 99 $\alpha$	14	Mn d <sub>yz</sub>	Mn d <sub>xy</sub>	Mn d $\rightarrow$ d	
			88 $\alpha$ $\rightarrow$ 99 $\alpha$	13	Mn d <sub>yz</sub>	Mn d <sub>xy</sub>		

<sup>a</sup>Electronic transition energies have been rounded to the nearest 100 cm<sup>-1</sup>. Included in this table are all Mn *d-d* transitions, as well as charge-transfer (CT) transitions with  $f_{osc} > 0.001$ . <sup>b</sup>Composition of molecular orbitals (MOs) involved in these electronic transitions are listed in Table S12. Spin-up and spin-down MOs are designated by  $\alpha$  and  $\beta$ , respectively. <sup>c</sup>Electron density difference maps (EDDMs) showing surface contour plots of loss (yellow) and gain (green) of electron density for a given electronic transition. For clarity, only the Mn, N, and O atoms are shown in these plots.

**Table A.2.14.** TD-DFT Calculated Energies, Percent Contributions from Dominant One-electron Excitations, and Oscillator Strengths for the Major Electronic Transitions of [Mn<sup>III</sup>(O<sub>2</sub>)(L<sup>7</sup>py<sub>2</sub><sup>6-</sup>Me)]<sup>+</sup> (**2-Me**).

band	state	energy (cm <sup>-1</sup> ) <sup>a</sup>	$f_{osc}$	transition <sup>b</sup>	%	donor MO	acceptor MO	comments	EDDM <sup>c</sup>
<i>i</i>	2	16 000	0.002124	104 $\alpha$ $\rightarrow$ 106 $\alpha$	90	Mn d <sub>z</sub> <sup>2</sup>	Mn d <sub>xy</sub>	Mn d $\rightarrow$ d	
<i>ii</i>	4	23 300	0.001474	101 $\beta$ $\rightarrow$ 103 $\beta$	63	O <sub>2</sub> $\pi_{op}^*$	Mn d <sub>xz</sub>	O <sub>2</sub> $\rightarrow$ Mn CT	
	5	24 600	0.000792	103 $\alpha$ $\rightarrow$ 106 $\alpha$ 100 $\alpha$ $\rightarrow$ 106 $\alpha$	41 32	Mn d <sub>xz</sub> Mn d <sub>x</sub> <sup>2-y</sup> <sup>2</sup> / yz	Mn d <sub>xy</sub> Mn d <sub>xy</sub>	Mn d $\rightarrow$ d	
<i>iii</i>	7	26 300	0.010058	100 $\alpha$ $\rightarrow$ 106 $\alpha$ 99 $\alpha$ $\rightarrow$ 106 $\alpha$	35 24	Mn d <sub>x</sub> <sup>2-y</sup> <sup>2</sup> / yz Mn d <sub>xy</sub> / d <sub>x</sub> <sup>2-y</sup> <sup>2</sup>	Mn d <sub>xy</sub> Mn d <sub>xy</sub>	Mn d $\rightarrow$ d	
	8	26 900	0.002456	105 $\alpha$ $\rightarrow$ 108 $\alpha$	90	O <sub>2</sub> $\pi_{op}^*$	py $\pi$	Mn $\rightarrow$ py CT	
	10	27 700	0.001323	101 $\beta$ $\rightarrow$ 107 $\beta$	44	O <sub>2</sub> $\pi_{op}^*$	Mn d <sub>yz</sub>	O <sub>2</sub> $\rightarrow$ Mn CT	

11	28 100	0.007111	104 $\alpha$ $\rightarrow$ 108 $\alpha$	80	Mn d <sub>z</sub> <sup>2</sup>	py $\pi$	Mn $\rightarrow$ py CT	
12	29 300	0.003792	101 $\beta$ $\rightarrow$ 106 $\beta$	31	O <sub>2</sub> $\pi_{op}^*$	Mn d <sub>xz</sub>	O <sub>2</sub> $\rightarrow$ Mn CT	
			101 $\beta$ $\rightarrow$ 107 $\beta$	23	O <sub>2</sub> $\pi_{op}^*$	Mn d <sub>yz</sub>		
			101 $\beta$ $\rightarrow$ 103 $\beta$	13	O <sub>2</sub> $\pi_{op}^*$	Mn d <sub>xz</sub>		
15	31 300	0.004872	101 $\beta$ $\rightarrow$ 106 $\beta$	17	O <sub>2</sub> $\pi_{op}^*$	Mn d <sub>xy</sub>	O <sub>2</sub> $\rightarrow$ Mn CT	
22	33 200	0.001915	95 $\alpha$ $\rightarrow$ 106 $\alpha$	13	Mn d <sub>xz</sub>	Mn d <sub>xy</sub>	Mn d $\rightarrow$ d	
			98 $\alpha$ $\rightarrow$ 106 $\alpha$	11	Mn d <sub>xz</sub>	Mn d <sub>xy</sub>		

<sup>a</sup>Energies have been rounded to the nearest 100 cm<sup>-1</sup>. Included in this table are all Mn *d-d* transitions, as well as charge-transfer (CT) transitions with  $f_{osc} > 0.001$ . <sup>b</sup>Composition of molecular orbitals (MOs) involved in these electronic transitions are listed in Table S15. Spin-up and spin-down MOs are designated by  $\alpha$  and  $\beta$ , respectively. <sup>c</sup>Electron density difference maps (EDDMs) showing surface contour plots of loss (yellow) and gain (green) of electron density for a given electronic transition. For clarity, only the Mn, N, and O atoms are shown in these plots.

**Table A.2.15.** Energies (eV) and Compositions (%) of the O 2p-based MOs and the Mn 3d-based MOs Based on Spin-Unrestricted B3LYP DFT Computations for [Mn<sup>III</sup>(O<sub>2</sub>)(L<sup>7</sup>py<sub>2</sub><sup>6-Me</sup>)]<sup>+</sup>.

orbital	occup	spin	energy	Mn 3d	O <sup>A</sup> 2p	O <sup>B</sup> 2p	L <sup>7</sup> py <sub>2</sub> <sup>Me</sup>
95 (Mn xz)	1.0	↑	-11.738	55.3	2.3 (z)	0.4 (z)	11.1
98 (Mn xz)	1.0	↑	-11.152	18.4	2.8 (y)	0.9 (y)	23.4
99 (Mn xy / x <sup>2</sup> -y <sup>2</sup> )	1.0	↑	-10.696	32.8	0.7 (y)	22.2 (y)	18.7
100 (Mn x <sup>2</sup> -y <sup>2</sup> / yz)	1.0	↑	-10.453	44.3	16.1 y)	4.2 (z)	14.8
103 (Mn xz)	1.0	↑	-10.132	29.6	12.2 (z/y)	4.2 (z/x)	25.7
104 (Mn z <sup>2</sup> )	1.0	↑	-8.806	36.7	9.1 (y)	1.4 (z/y)	34.0
105 (O <sub>2</sub> $\pi_{op}^*$ )	1.0	↑	-8.515	5.9 (xz)	46.8 (z)	44.2 (z)	0.9
106 (Mn xy)	0.0	↑	-5.019	35.1	23.4 (y)	25.8 (y)	5.2
107 (py $\pi$ )	0.0	↑	-4.610	2.4 (x <sup>2</sup> -y <sup>2</sup> )	1.4 (y)	2.9 (y)	81.5
108 (py $\pi$ )	0.0	↑	-4.450	0.8 (xz)	0.7 (y)	0.1 (y)	84.2
101 (O <sub>2</sub> $\pi_{op}^*$ )	1.0	↓	-8.640	5.2 (xz)	48.8 (z)	42.0 (z)	0.6
103 (Mn xz / py $\pi$ )	0.0	↓	-4.687	19.6	1.6 (z)	0.5 (z)	63.0
105 (Mn xz / py $\pi$ )	0.0	↓	-3.826	32.8	0.6 (z)	0.8 (z)	51.8
106 (Mn xz / py $\pi$ )	0.0	↓	-3.754	43.3	1.8 (z)	1.0 (z)	35.6
107 (Mn yz)	0.0	↓	-3.620	82.9	1.4 (z)	2.8 (z)	3.1
108 (Mn x <sup>2</sup> -y <sup>2</sup> )	0.0	↓	-3.517	53.7	1.2 (y)	1.7 (x)	5.6
109 (Mn z <sup>2</sup> / xy)	0.0	↓	-2.868	74.6	6.9 (y)	3.0 (y)	4.5
110 (Mn xy / z <sup>2</sup> )	0.0	↓	-2.684	70.2	4.2 (y/x)	8.0 (y)	6.1



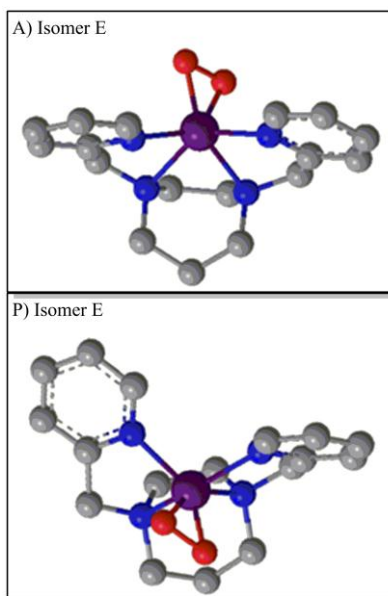


**Figure A.2.1.** Molecular structures of isomers of  $[\text{Mn}^{\text{III}}(\text{O}_2)(\text{L}^7\text{py}_2^{\text{H}})]^+$  based on BP86 DFT geometry optimizations.

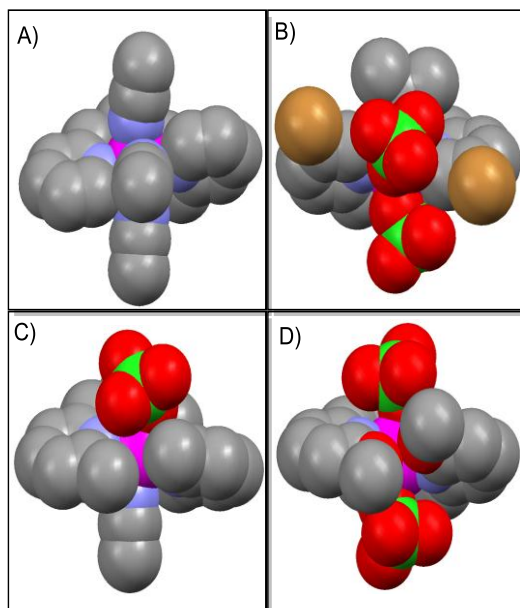


**Figure A.2.2.** Space-filling diagrams of A)  $[\text{Mn}^{\text{II}}(\text{L}^7\text{py}_2^{\text{H}})(\text{NCMe})_3](\text{ClO}_4)_2$  (**1-H**), B)  $[\text{Mn}^{\text{II}}(\text{L}^7\text{py}_2^{5\text{-Br}})(\text{OCMe}_2)(\text{ClO}_4)](\text{ClO}_4)$  (**1-Br**), C)  $[\text{Mn}^{\text{II}}(\text{L}^7\text{py}_2^{6\text{-Me}})(\text{NCMe})_2](\text{ClO}_4)_2$  (**1-Me**), and D)  $[\text{Mn}^{\text{II}}(\text{L}^7\text{py}_2^{6\text{-MeO}})(\text{ClO}_4)_2]$  (**1-MeO**) based on X-ray crystal structure data. Hydrogen atoms and non-coordinating perchlorate counter anions have been removed for clarity.

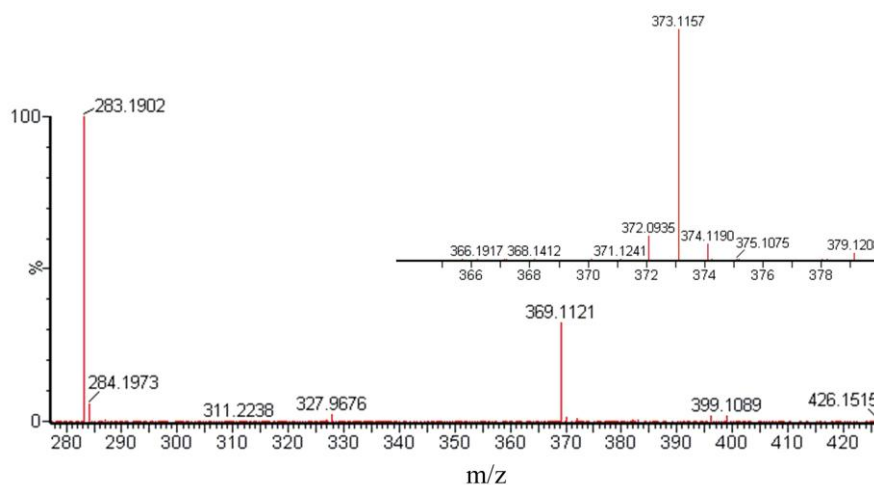


**Figure A.2.3.** ESI-MS data for  $[\text{Mn}^{\text{III}}(\text{O}_2)(\text{L}^7\text{py}_2\text{H})]^+$  prepared with  $\text{H}_2^{16}\text{O}_2$ . The peak observed at 283.1902  $m/z$  corresponds to  $[\text{L}^7\text{py}_2\text{H}]^+$ , which is observed in ESI-MS experiments of  $[\text{Mn}^{\text{II}}(\text{L}^7\text{py}_2\text{H})]^{2+}$  and  $[\text{Mn}^{\text{III}}(\text{O}_2)(\text{L}^7\text{py}_2\text{H})]^+$ . Inset: Corresponding data collected for a sample prepared with  $\text{H}_2^{18}\text{O}_2$ .

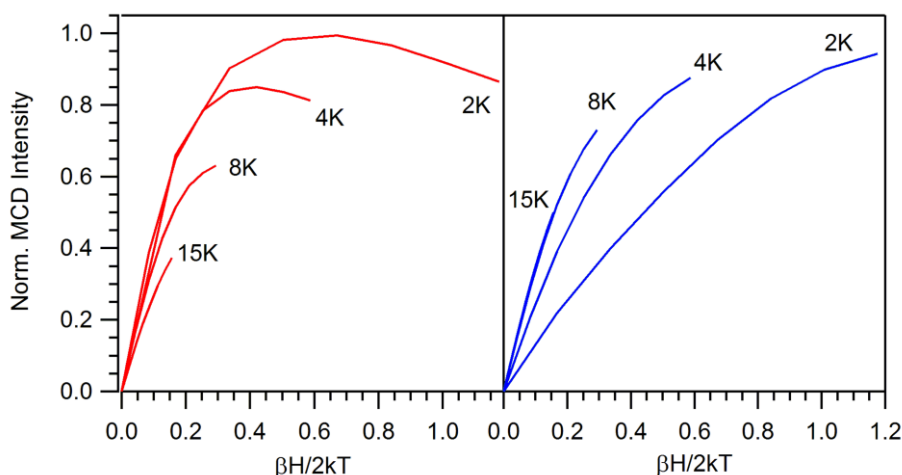


**Figure A.2.4.** Simulated VTVH MCD curves demonstrating the effect of an increase in 9%  $z$  polarization. Specific parameters used to simulated these curves are as follows. Left:  $g_{\text{iso}} = 2.00$ ,  $D = -3.0$ ,  $E/D = 0.5$ , and 5.1%  $x$ , 4.3%  $y$  and 90.6 %  $z$  polarization. Right:  $g_{\text{iso}} = 2.00$ ,  $D = -3.0$ ,  $E/D = 0.5$ , and 0.001%  $x$ , 0.002%  $y$  and 99.997%  $z$  polarization.

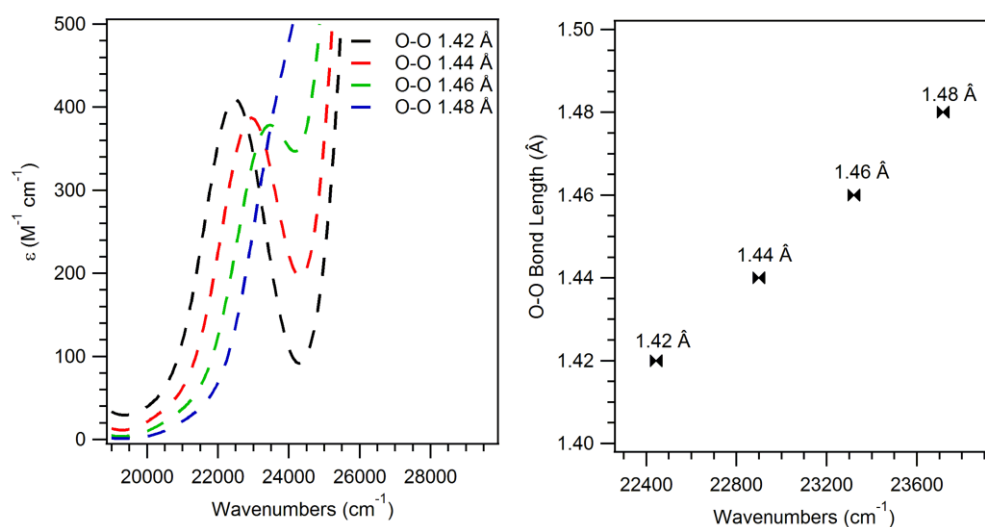


**Figure A.2.5.** Left: Simulated absorption spectra for models of  $[\text{Mn}^{\text{III}}(\text{O}_2)(\text{L}^7\text{py}_2\text{H})]^+$  (**2-H**) where the O-O bond lengths are systematically varied from 1.42 to 1.48 Å in 0.02 Å increments. Right: Plot of TD-DFT-computed  $\text{O}_2 \pi_{\text{op}}^* \rightarrow \text{Mn } d_{yz}$  transition energy as a function of the O-O distance.

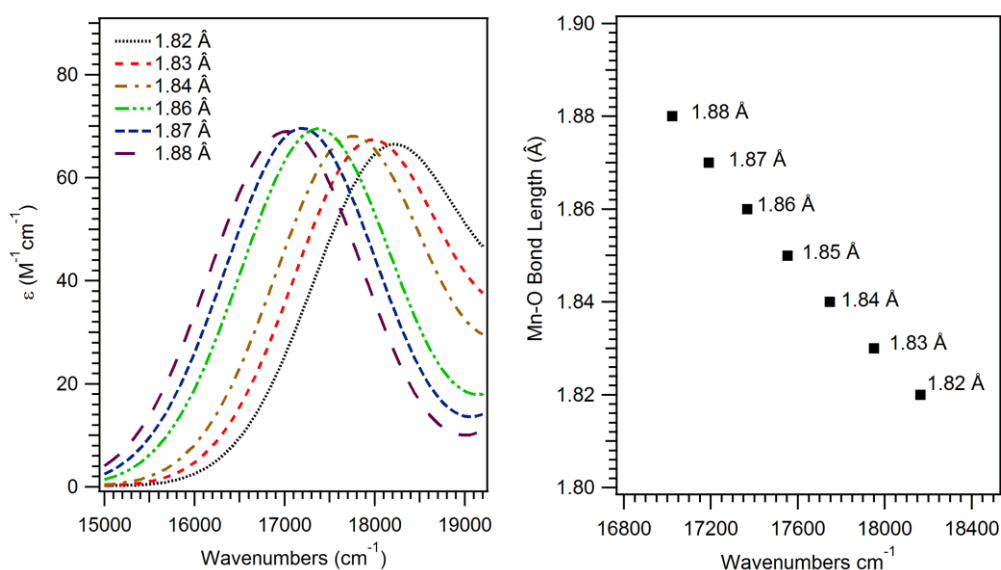


**Figure A.2.6.** Left: Simulated absorption spectra for models of  $[\text{Mn}^{\text{III}}(\text{O}_2)(\text{L}^7\text{py}_2\text{H})]^+$  (**2-H**) where the Mn-O bond lengths are systematically varied from 1.88 to 1.82 Å in 0.01 Å increments. Right: Plot of TD-DFT-computed  $\text{Mn } d_{z^2} \rightarrow d_{xy}$  transition energy as a function of the Mn-O distance.

**Table A.3.1.** Crystal data and structure refinement for  $[\text{Mn}(\text{L}^6\text{py}_2)(\text{NCCH}_3)_3](\text{ClO}_4)_2 \cdot \text{CH}_3\text{CN}$ .

Empirical formula	$\text{C}_{24}\text{H}_{32}\text{Cl}_2\text{MnN}_8\text{O}_8$	
Formula weight	686.42	
Temperature	173(2) K	
Wavelength	0.71073 Å	
Crystal system	Triclinic	
Space group	$\text{P}\bar{1} - \text{C}_i^1$ (No. 2)	
Unit cell dimensions	$a = 11.618(2)$ Å	$\alpha = 88.508(2)^\circ$
	$b = 11.666(2)$ Å	$\beta = 71.869(2)^\circ$
	$c = 13.214(3)$ Å	$\gamma = 69.296(2)^\circ$
Volume	$1585.0(5)$ Å <sup>3</sup>	
Z	2	
Density (calculated)	$1.438 \text{ Mg/m}^3$	
Absorption coefficient	$0.642 \text{ mm}^{-1}$	
F(000)	710	
Crystal size	$0.18 \times 0.14 \times 0.09 \text{ mm}^3$	
Theta range for data collection	$3.72^\circ$ to $27.84^\circ$	
Index ranges	$-15 \leq h \leq 15, -15 \leq k \leq 15, -17 \leq l \leq 17$	
Reflections collected	15336	
Independent reflections	7423 [ $R_{\text{int}} = 0.029$ ]	
Completeness to $\theta = 27.84^\circ$	98.3 %	
Absorption correction	Multi-scans	
Max. and min. transmission	1.000 and 0.872	
Refinement method	Full-matrix least-squares on $F^2$	
Data / restraints / parameters	7423 / 0 / 392	
Goodness-of-fit on $F^2$	1.071	
Final R indices [ $I > 2\sigma(I)$ ]	$R_1 = 0.059, wR_2 = 0.161$	
R indices (all data)	$R_1 = 0.073, wR_2 = 0.170$	
Largest diff. peak and hole	$0.84$ and $-0.71 \text{ e}^-/\text{Å}^3$	
$R_1 = \Sigma   F_O  -  F_C   / \Sigma  F_O $ $wR_2 = \{ \Sigma [w(F_O^2 - F_C^2)^2] / \Sigma [w(F_O^2)^2] \}^{1/2}$		

**Table A.3.2.** Crystal data and structure refinement for  $[\text{Mn}(\text{L}^7\text{py}_2^{4-\text{Me}})(\text{OTf})_2]$ .

Empirical formula	$\text{C}_{21}\text{H}_{26}\text{F}_6\text{MnN}_4\text{O}_6\text{S}_2$	
Formula weight	663.52	
Temperature	100(2) K	
Wavelength	0.71073 Å	
Crystal system	Monoclinic	
Space group	$\text{P2}_1/\text{c} - \text{C}_{2\text{h}}^5$ (No. 14)	
Unit cell dimensions	$a = 16.801(7)$ Å $b = 8.582(4)$ Å $c = 19.054(8)$ Å	$\alpha = 90.000^\circ$ $\beta = 99.020(7)^\circ$ $\gamma = 90.000^\circ$
Volume	$2713(2)$ Å <sup>3</sup>	
Z	4	
Density (calculated)	$1.624 \text{ Mg/m}^3$	
Absorption coefficient	$0.726 \text{ mm}^{-1}$	
F(000)	1356	
Crystal size	$0.50 \times 0.34 \times 0.18 \text{ mm}^3$	
Theta range for data collection	$2.31^\circ$ to $29.15^\circ$	
Index ranges	$-22 \leq h \leq 22, -11 \leq k \leq 11, -25 \leq l \leq 25$	
Reflections collected	24171	
Independent reflections	6823 [ $R_{\text{int}} = 0.041$ ]	
Completeness to $\theta = 29.15^\circ$	93.3 %	
Absorption correction	Multi-scans	
Max. and min. transmission	1.000 and 0.810	
Refinement method	Full-matrix least-squares on $F^2$	
Data / restraints / parameters	6823 / 0 / 363	
Goodness-of-fit on $F^2$	1.082	
Final R indices [ $I > 2\sigma(I)$ ]	$R_1 = 0.043, wR_2 = 0.115$	
R indices (all data)	$R_1 = 0.050, wR_2 = 0.118$	
Largest diff. peak and hole	$1.464$ and $-0.673 \text{ e}^-/\text{\AA}^3$	

$$R_1 = \sum ||F_O| - |F_C|| / \sum |F_O|$$

$$wR_2 = \{ \sum [w(F_O^2 - F_C^2)^2] / \sum [w(F_O^2)^2] \}^{1/2}$$

**Table A.3.3.** Crystal data and structure refinement for  $[\text{Mn}(\text{L}^7\text{q}_2)(\text{ClO}_4)_2]$ .

Empirical formula	$\text{C}_{25}\text{H}_{26}\text{Cl}_2\text{MnN}_4\text{O}_8$	
Formula weight	636.34	
Temperature	100(2) K	
Wavelength	0.71073 Å	
Crystal system	Monoclinic	
Space group	$\text{P2}_1/\text{c} - \text{C}_{2\text{h}}^5$ (No. 14)	
Unit cell dimensions	$a = 9.0119(17)$ Å	$\alpha = 90.000^\circ$
	$b = 8.3049(15)$ Å	$\beta = 92.618(3)^\circ$
	$c = 34.494(6)$ Å	$\gamma = 90.000^\circ$
Volume	$2578.9(8)$ Å <sup>3</sup>	
Z	4	
Density (calculated)	$1.639$ Mg/m <sup>3</sup>	
Absorption coefficient	$0.778$ mm <sup>-1</sup>	
F(000)	1308	
Crystal size	$0.28 \times 0.26 \times 0.24$ mm <sup>3</sup>	
Theta range for data collection	$2.50^\circ$ to $29.18^\circ$	
Index ranges	$-12 \leq h \leq 12, -10 \leq k \leq 10, -45 \leq l \leq 46$	
Reflections collected	23188	
Independent reflections	6423 [ $R_{\text{int}} = 0.048$ ]	
Completeness to $\theta = 29.18^\circ$	92.0 %	
Absorption correction	Multi-scans	
Max. and min. transmission	1.000 and 0.900	
Refinement method	Full-matrix least-squares on $F^2$	
Data / restraints / parameters	6423 / 0 / 493	
Goodness-of-fit on $F^2$	1.041	
Final R indices [ $I > 2\sigma(I)$ ]	$R_1 = 0.044, wR_2 = 0.109$	
R indices (all data)	$R_1 = 0.053, wR_2 = 0.113$	
Largest diff. peak and hole	$0.56$ and $-0.47$ e <sup>-</sup> /Å <sup>3</sup>	
$R_1 = \sum   F_O  -  F_C   / \sum  F_O $ $wR_2 = \{ \sum [w(F_O^2 - F_C^2)^2] / \sum [w(F_O^2)^2] \}^{1/2}$		

**Table A.3.4.** Crystal data and structure refinement for  $[\text{Mn}(\text{L}^{\text{H}}\text{py}_2)(\text{ClO}_4)_2]$ .

Empirical formula	$\text{C}_{18}\text{H}_{24}\text{Cl}_2\text{MnN}_4\text{O}_8$	
Formula weight	550.25	
Temperature	173(2) K	
Wavelength	0.71073 Å	
Crystal system	Monoclinic	
Space group	$\text{P2}_1/\text{c} - \text{C}_{2\text{h}}^5$ (No. 14)	
Unit cell dimensions	$\mathbf{a} = 14.731(2)$ Å $\mathbf{b} = 17.692(2)$ Å $\mathbf{c} = 8.752(1)$ Å	$\alpha = 90.000^\circ$ $\beta = 95.547(1)^\circ$ $\gamma = 90.000^\circ$
Volume	$2270.1(5)$ Å <sup>3</sup>	
Z	4	
Density (calculated)	$1.610$ Mg/m <sup>3</sup>	
Absorption coefficient	$0.870$ mm <sup>-1</sup>	
F(000)	1132	
Crystal size	$0.27 \times 0.24 \times 0.22$ mm <sup>3</sup>	
Theta range for data collection	$3.97^\circ$ to $29.57^\circ$	
Index ranges	$0 \leq h \leq 20, -24 \leq k \leq 0, -12 \leq l \leq 12$	
Reflections collected	18486	
Independent reflections	6352 [ $R_{\text{int}} = 0.036$ ]	
Completeness to $\theta = 29.57^\circ$	99.7 %	
Absorption correction	Multi-scans	
Max. and min. transmission	0.8317 and 0.7991	
Refinement method	Full-matrix least-squares on $F^2$	
Data / restraints / parameters	6352 / 0 / 298	
Goodness-of-fit on $F^2$	1.057	
Final R indices [ $I > 2\sigma(I)$ ]	$R_1 = 0.037, wR_2 = 0.092$	
R indices (all data)	$R_1 = 0.043, wR_2 = 0.095$	
Largest diff. peak and hole	$0.45$ and $-0.36$ e <sup>-</sup> /Å <sup>3</sup>	

---


$$R_1 = \Sigma ||F_{\text{O}}| - |F_{\text{C}}|| / \Sigma |F_{\text{O}}|$$

$$wR_2 = \{ \Sigma [w(F_{\text{O}}^2 - F_{\text{C}}^2)^2] / \Sigma [w(F_{\text{O}}^2)^2] \}^{1/2}$$

**Table A.3.5.** Crystal data and structure refinement for [Mn(L<sup>8</sup>py<sub>2</sub><sup>6-Me</sup>)(OTf)<sub>2</sub>].

Empirical formula	C <sub>22</sub> H <sub>28</sub> F <sub>6</sub> MnN <sub>4</sub> O <sub>6</sub> S <sub>2</sub>	
Formula weight	677.54	
Temperature	100(2) K	
Wavelength	0.71073 Å	
Crystal system	Monoclinic	
Space group	C2/c - C <sub>2h</sub> <sup>6</sup> (No. 15)	
Unit cell dimensions	<b>a</b> = 13.546(3) Å <b>b</b> = 10.324(2) Å <b>c</b> = 19.340(4) Å	<b>α</b> = 90.000° <b>β</b> = 99.912(3)° <b>γ</b> = 90.000°
Volume	2664.4(8) Å <sup>3</sup>	
Z	4	
Density (calculated)	1.689 Mg/m <sup>3</sup>	
Absorption coefficient	0.741 mm <sup>-1</sup>	
F(000)	1388	
Crystal size	0.52 x 0.48 x 0.33 mm <sup>3</sup>	
Theta range for data collection	2.49° to 29.10°	
Index ranges	-18 ≤ h ≤ 18, -13 ≤ k ≤ 13, -25 ≤ l ≤ 25	
Reflections collected	11982	
Independent reflections	3356 [R <sub>int</sub> = 0.052]	
Completeness to theta = 29.10°	93.7 %	
Absorption correction	Multi-scans	
Max. and min. transmission	1.000 and 0.815	
Refinement method	Full-matrix least-squares on F <sup>2</sup>	
Data / restraints / parameters	3356 / 0 / 242	
Goodness-of-fit on F <sup>2</sup>	1.052	
Final R indices [I > 2σ(I)]	R <sub>1</sub> = 0.030, wR <sub>2</sub> = 0.084	
R indices (all data)	R <sub>1</sub> = 0.031, wR <sub>2</sub> = 0.085	
Largest diff. peak and hole	0.50 and -0.33 e <sup>-</sup> /Å <sup>3</sup>	

$$R_1 = \frac{\sum ||F_O| - |F_C||}{\sum |F_O|}$$

$$wR_2 = \left\{ \frac{\sum [w(F_O^2 - F_C^2)^2]}{\sum [w(F_O^2)^2]} \right\}^{1/2}$$



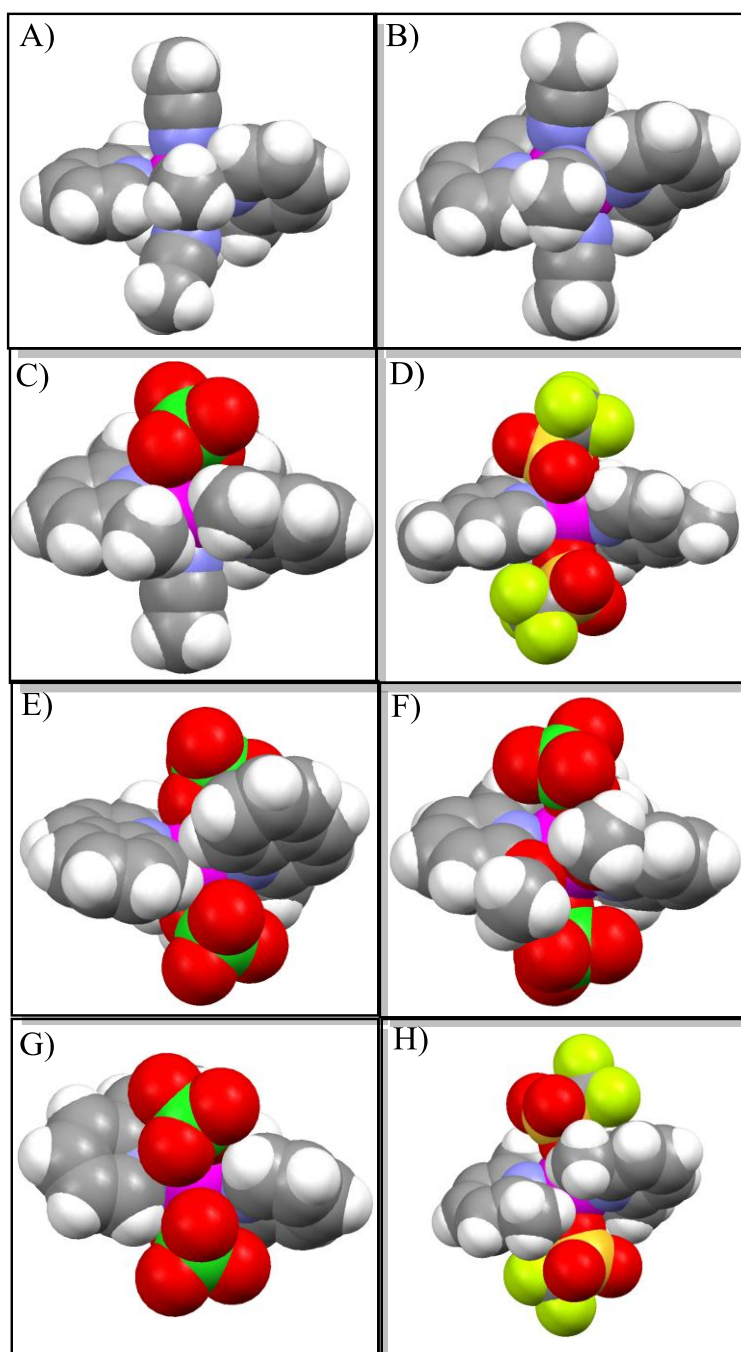


**Figure A.3.1.** Space-filling diagrams of A)  $[\text{Mn}^{\text{II}}(\text{L}^6\text{py}_2^{\text{H}})(\text{NCMe})_3](\text{ClO}_4)_2$ , B)  $[\text{Mn}^{\text{II}}(\text{L}^7\text{py}_2^{\text{H}})(\text{CH}_3\text{CN})_3](\text{ClO}_4)_2$  (reference<sup>20</sup>), C)  $[\text{Mn}^{\text{II}}(\text{L}^7\text{py}_2^{6-\text{Me}})(\text{ClO}_4)(\text{CH}_3\text{CN})](\text{ClO}_4)$  (reference<sup>20</sup>), D)  $[\text{Mn}^{\text{II}}(\text{L}^7\text{py}_2^{4-\text{Me}})(\text{OTf})_2]$ , and E)  $[\text{Mn}^{\text{II}}(\text{L}^7\text{q}_2)(\text{ClO}_4)_2]$  F)  $[\text{Mn}^{\text{II}}(\text{L}^7\text{py}_2^{6-\text{MeO}})(\text{ClO}_4)_2]$  (reference<sup>20</sup>), G)  $[\text{Mn}^{\text{II}}(\text{L}^8\text{py}_2^{\text{H}})(\text{ClO}_4)_2]$ , and H)  $[\text{Mn}^{\text{II}}(\text{L}^8\text{py}_2^{6-\text{Me}})(\text{OTf})_2]$  based on X-ray crystal structure data. Non-coordinating perchlorate counter anions or triflate counter anions have been removed for clarity.

**Table A.3.6.** Cartesian coordinates (Å) for DFT optimized model of  $[\text{Mn}^{\text{III}}(\text{O}_2)(\text{L}^7\text{py}_2^{\text{H}})]^+$ .

Atom	x	y	z
Mn	-0.278039	3.034828	1.014223
O	-0.530305	4.859658	0.740655
O	-0.465168	4.514143	2.141256
N	-2.317116	2.194425	0.577825
N	-0.078869	2.390066	-1.093472
N	1.927974	2.504719	0.632849
N	0.268396	1.650337	2.593571
C	-3.322184	2.010708	1.463726
C	-4.503722	1.331376	1.140523
C	-4.641411	0.811159	-0.157280
C	-3.613618	1.026398	-1.088321
C	-2.471888	1.743733	-0.691357
C	-1.425796	2.186651	-1.690302
C	0.648120	3.432208	-1.906270
C	2.155548	3.503896	-1.646692
C	2.577884	3.573907	-0.177665
C	1.900181	1.194508	-0.073690
C	0.675030	1.101141	-1.030678
C	-0.590734	0.961349	3.380083
C	-0.179480	0.238707	4.505421
C	1.186704	0.221011	4.828353
C	2.084240	0.915868	4.004365
C	1.595669	1.625589	2.896411
C	2.511141	2.411294	1.982433
H	-1.650313	0.987444	3.088341
H	-0.924374	-0.301387	5.108938
H	1.552324	-0.336729	5.705353
H	3.166225	0.909450	4.211218
H	2.616851	3.448600	2.374032
H	3.531738	1.960528	1.972863
H	-3.172322	2.441754	2.466748
H	-5.293985	1.210349	1.897455
H	-5.546270	0.252723	-0.446125
H	-3.696845	0.654605	-2.121462
H	-1.376148	1.493387	-2.560048
H	-1.759925	3.171551	-2.085078
H	0.490980	3.207261	-2.987450
H	0.157694	4.404307	-1.687563
H	2.536410	4.413640	-2.159475
H	2.663571	2.651322	-2.145422
H	2.295474	4.548807	0.276252
H	3.689178	3.474600	-0.115001
H	1.820144	0.397089	0.690882
H	2.857508	1.023183	-0.615632

H	0.983031	0.792755	-2.055881
H	-0.035488	0.334608	-0.657343

**Table A.3.7.** Cartesian coordinates (Å) for DFT optimized model of  $[\text{Mn}^{\text{III}}(\text{O}_2)(\text{L}^7\text{py}_2^{6-\text{Me}})]^+$ .

Atom	x	y	z
Mn	-0.010842	0.095253	0.495449
O	-0.688271	0.281369	2.268111
O	0.517331	-0.523306	2.175018
N	-1.973742	-0.890898	-0.172400
N	-0.823722	1.528735	-0.881397
N	1.440974	1.851885	0.478487
N	1.852991	-0.745970	-0.252437
C	-2.595424	-1.884041	0.526700
C	-3.987895	-2.067748	0.424103
C	-4.752404	-1.229497	-0.402558
C	-4.095348	-0.217583	-1.123466
C	-2.710950	-0.083283	-0.980245
C	-1.895894	0.937875	-1.747728
C	-1.423382	2.588126	0.028798
C	-0.400180	3.518720	0.692445
C	0.814257	2.870690	1.371788
C	-1.748460	-2.805510	1.372782
C	2.056048	-1.911850	-0.934629
C	3.342309	-2.473030	-1.024592
C	4.431553	-1.839473	-0.407691
C	4.215612	-0.627952	0.258826
C	2.914129	-0.104306	0.309603
C	2.655641	1.231888	0.998374
C	1.566742	2.350614	-0.910856
C	0.286457	2.066187	-1.737239
C	0.877047	-2.577344	-1.586203
H	-4.470292	-2.875712	0.995789
H	-5.842984	-1.367715	-0.477574
H	-4.640539	0.466492	-1.792721
H	-1.385005	0.453085	-2.605428
H	-2.546363	1.742461	-2.159594
H	-2.037461	2.048531	0.778364
H	-2.107293	3.215161	-0.587725
H	-0.055564	4.268386	-0.050870
H	-0.940540	4.108162	1.465520
H	0.544432	2.349278	2.311182
H	1.550080	3.675469	1.616764
H	-1.050952	-2.241883	2.027278
H	-1.130551	-3.460962	0.719501
H	-2.404493	-3.440418	2.003846
H	3.485822	-3.409171	-1.584697

H	5.432584	-2.295011	-0.472075
H	5.033808	-0.066525	0.736042
H	3.556036	1.874714	0.844743
H	2.530258	1.066665	2.087786
H	2.438841	1.865799	-1.392672
H	1.792432	3.440273	-0.915224
H	-0.054208	2.990317	-2.257335
H	0.482937	1.287316	-2.498476
H	0.134737	-2.917651	-0.831608
H	1.200277	-3.463907	-2.168069
H	0.340955	-1.889571	-2.275607

**Table A.3.8.** Cartesian coordinates (Å) for DFT optimized model for  $[\text{Mn}^{\text{III}}(\text{O}_2)(\text{L}^7\text{py}_2^{4-\text{Me}})]^+$

Atom	x	y	z
Mn	-0.469549	2.634620	1.182838
O	-0.956405	4.398556	0.781838
O	-0.841302	4.156933	2.200683
N	-2.492751	1.846130	0.743326
N	-0.149251	1.726470	-0.810429
N	1.783775	2.613029	0.783718
N	0.317168	1.512035	2.769293
C	-3.591431	2.197368	1.446931
C	-4.875042	2.215736	0.889940
C	-5.050996	1.880034	-0.469302
C	-3.892410	1.523062	-1.195500
C	-2.642529	1.509732	-0.563662
C	-1.389496	1.022023	-1.261995
C	-6.404388	1.912006	-1.130775
H	-3.423776	2.482705	2.498462
H	-5.734074	2.502201	1.516954
H	-3.964287	1.249262	-2.260635
H	-1.274765	-0.054768	-1.012237
H	-1.502009	1.084712	-2.367630
H	-6.615525	0.951417	-1.651092
H	-6.441991	2.711638	-1.905824
H	-7.214089	2.103240	-0.396669
C	0.156418	2.897320	-1.714091
C	1.574764	3.471854	-1.547624
C	2.063717	3.761537	-0.118743
C	2.149525	1.314621	0.164349
C	1.006517	0.779608	-0.743802
H	0.050717	2.559023	-2.772356
H	-0.622487	3.666675	-1.531657
H	1.611762	4.422447	-2.122173
H	2.297525	2.796482	-2.054432
H	1.555014	4.650022	0.309111

H	3.161225	3.968781	-0.151680
H	2.326072	0.586930	0.980220
H	3.107650	1.409318	-0.394850
H	1.373798	0.553968	-1.770489
H	0.620294	-0.166867	-0.319831
C	-0.381628	0.676439	3.573144
C	0.167294	0.111074	4.725786
C	1.501567	0.407455	5.083860
C	2.219879	1.266758	4.224330
C	1.608836	1.808257	3.086836
C	2.326615	2.762686	2.146235
C	2.124667	-0.155513	6.333123
H	-1.416191	0.458284	3.265744
H	-0.448214	-0.565542	5.339435
H	3.271391	1.516933	4.438343
H	2.133084	3.809766	2.472848
H	3.430043	2.599824	2.190569
H	3.232797	-0.180140	6.263054
H	1.750060	-1.178744	6.546916
H	1.856623	0.480314	7.208920

---

**Table A.4.1.** Crystal data and structure refinement for  $[\text{Mn}(\text{L}^7\text{py}_2^{4-\text{Cl}})(\text{OTf})_2]$ .

Empirical formula	$\text{C}_{19} \text{H}_{20} \text{Cl}_2 \text{F}_6 \text{Mn} \text{N}_4 \text{O}_6 \text{S}_2$	
Formula weight	704.35	
Temperature	100(2) K	
Wavelength	1.54178 Å	
Crystal system	Monoclinic	
Space group	P2(1)	
Unit cell dimensions	$a = 14.2345(5) \text{ Å}$ $b = 9.0034(3) \text{ Å}$ $c = 42.1864(14) \text{ Å}$	$a = 90^\circ$ . $b =$ $97.8430(10)^\circ$ . $g = 90^\circ$ .
Volume	$5356.0(3) \text{ Å}^3$	
Z	8	
Density (calculated)	$1.747 \text{ Mg/m}^3$	
Absorption coefficient	$8.102 \text{ mm}^{-1}$	
F(000)	2840	
Crystal size	$0.14 \times 0.13 \times 0.04 \text{ mm}^3$	
Theta range for data collection	1.06 to $69.29^\circ$ .	
Index ranges	$-17 \leq h \leq 16$ , $-10 \leq k \leq 10$ , $-50 \leq l \leq 43$	
Reflections collected	35226	
Independent reflections	16487 [R(int) = 0.0430]	
Completeness to $\theta = 69.29^\circ$	96.1 %	
Absorption correction	Multi-scan	
Max. and min. transmission	1.000 and 0.681	
Refinement method	Full-matrix least-squares on $F^2$	
Data / restraints / parameters	16487 / 79 / 1442	
Goodness-of-fit on $F^2$	1.051	
Final R indices [I > 2sigma(I)]	$R_1 = 0.0884$ , $wR_2 = 0.2158$	
R indices (all data)	$R_1 = 0.0931$ , $wR_2 = 0.2199$	
Absolute structure parameter	0.0(4)	
Largest diff. peak and hole	3.069 and $-1.250 \text{ e.Å}^{-3}$	
$R_1 = \sum   F_O  -  F_C   / \sum  F_O $ $wR_2 = \{ \sum [w(F_O^2 - F_C^2)^2] / \sum [w(F_O^2)^2] \}^{1/2}$		

**Table A.4.2.** Crystal data and structure refinement for [Mn(L<sup>7</sup>isoq<sub>2</sub>)(OTf)<sub>2</sub>].

Empirical formula	C <sub>29</sub> H <sub>29</sub> F <sub>6</sub> MnN <sub>5</sub> O <sub>6</sub> S <sub>2</sub>	
Formula weight	776.63	
Temperature	100(2) K	
Wavelength	1.54178 Å	
Crystal system	Orthorhombic	
Space group	Pbca	
Unit cell dimensions	a = 19.2491(7) Å	α = 90°.
	b = 17.1888(5) Å	β = 90°.
	c = 19.4207(5) Å	γ = 90°.
Volume	6425.7(3) Å <sup>3</sup>	
Z	8	
Density (calculated)	1.606 Mg/m <sup>3</sup>	
Absorption coefficient	5.334 mm <sup>-1</sup>	
F(000)	3176	
Crystal size	0.12 x 0.11 x 0.05 mm <sup>3</sup>	
Theta range for data collection	4.13 to 69.21°.	
Index ranges	-16 ≤ h ≤ 22, -20 ≤ k ≤ 20, -	
	20 ≤ l ≤ 22	
Reflections collected	26827	
Independent reflections	5825 [R(int) = 0.0356]	
Completeness to theta = 69.21°	97.0 %	
Absorption correction	Multi-scan	
Max. and min. transmission	1.000 and 0.730	
Refinement method	Full-matrix least-squares on F <sup>2</sup>	
Data / restraints / parameters	5825 / 57 / 501	
Goodness-of-fit on F <sup>2</sup>	1.112	
Final R indices [I > 2σ(I)]	R1 = 0.1353, wR2 = 0.2788	
R indices (all data)	R1 = 0.1417, wR2 = 0.2814	
Largest diff. peak and hole	1.309 and -1.297 e.Å <sup>-3</sup>	
$R_1 = \sum   F_O  -  F_C   / \sum  F_O $ $wR_2 = \{ \sum [w(F_O^2 - F_C^2)^2] / \sum [w(F_O^2)^2] \}^{1/2}$		

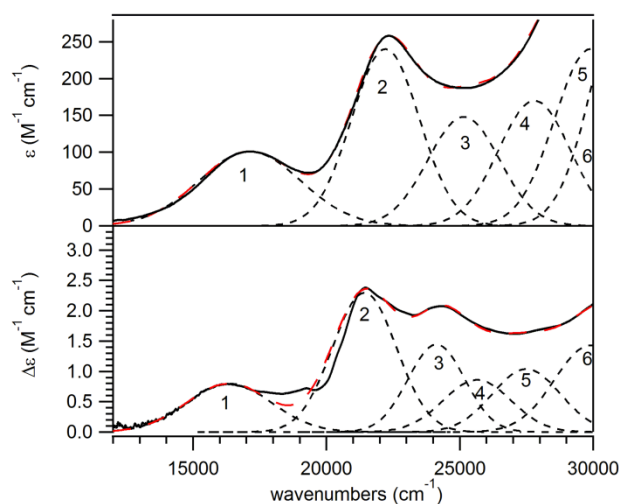


**Figure A.4.1.** 233 K electronic absorption (top) and 2 K, 7 T MCD (bottom) spectra of  $[\text{Mn}^{\text{III}}(\text{O}_2)(\text{L}^7\text{py}_2^{4-\text{Me}})]^+$ . Individual Gaussian curves (black dotted lines) and their sums (red dashed lines) obtained from iterative fits of these data sets are displayed on their respective spectra. Conditions: Absorption data were collected for a 2.5 mM sample in  $\text{CH}_3\text{CN}$ . MCD data were collected for a 10 mM frozen glass sample in butyronitrile.

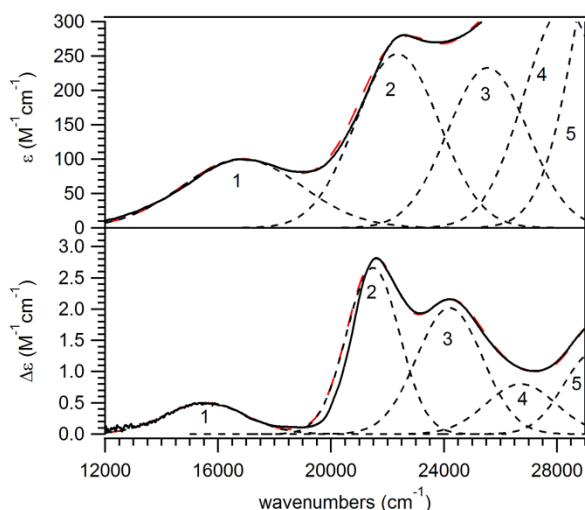


**Figure A.4.2.** 233 K electronic absorption (top) and 2 K, 7 T MCD (bottom) spectra of  $[\text{Mn}^{\text{III}}(\text{O}_2)(\text{L}^7\text{iso-q}_2)]^+$ . Individual Gaussian curves (black dotted lines) and their sums (red dashed lines) obtained from iterative fits of these data sets are displayed on their respective spectra. Conditions: Absorption data were collected for a 2.5 mM sample in  $\text{CH}_3\text{CN}$ . MCD data were collected for a 10 mM frozen glass sample in butyronitrile.



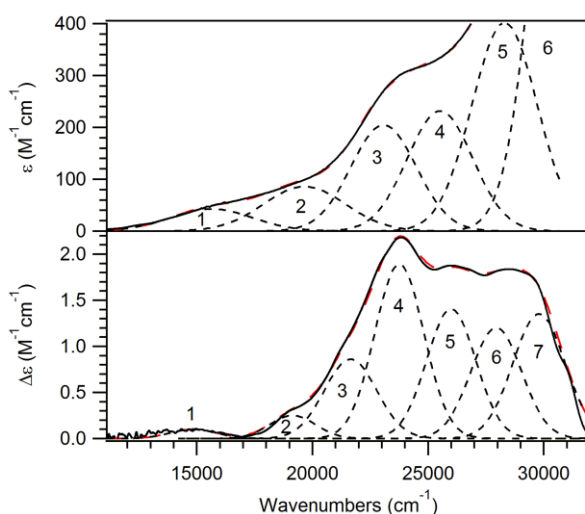


**Figure A.4.3.** 233 K electronic absorption (top) and 2 K, 7 T MCD (bottom) spectra of  $[\text{Mn}^{\text{III}}(\text{O}_2)(\text{L}^7\text{q}_2)]^+$ . Individual Gaussian curves (black dotted lines) and their sums (red dashed lines) obtained from iterative fits of these data sets are displayed on their respective spectra. Conditions: Absorption data were collected for a 2.5 mM sample in  $\text{CH}_3\text{CN}$ . MCD data were collected for a 15 mM frozen glass sample in butyronitrile.

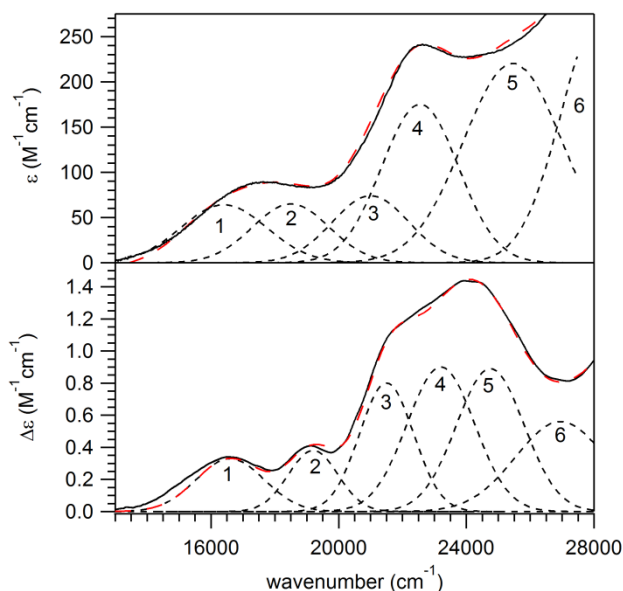


**Figure A.4.4.** 233 K electronic absorption (top) and 2 K, 7 T MCD (bottom) spectra of  $[\text{Mn}^{\text{III}}(\text{O}_2)(\text{L}^7\text{py}_2^{4-\text{Cl}})]^+$ . Individual Gaussian curves (black dotted lines) and their sums (red dashed lines) obtained from iterative fits of these data sets are displayed on their respective spectra. Conditions: Absorption data were collected for a 2.5 mM sample in  $\text{CH}_3\text{CN}$ . MCD data were collected for a 15 mM frozen glass sample in butyronitrile.

**Table A.4.3.** Cartesian coordinates (Å) for DFT optimized model of  $[\text{Mn}^{\text{III}}(\text{O}_2)(\text{L}^7\text{py}_2^{\text{H}})]^+$ .

Atom	x	y	z
Mn	-0.278039	3.034828	1.014223
O	-0.530305	4.859658	0.740655
O	-0.465168	4.514143	2.141256
N	-2.317116	2.194425	0.577825
N	-0.078869	2.390066	-1.093472
N	1.927974	2.504719	0.632849
N	0.268396	1.650337	2.593571
C	-3.322184	2.010708	1.463726
C	-4.503722	1.331376	1.140523
C	-4.641411	0.811159	-0.157280
C	-3.613618	1.026398	-1.088321
C	-2.471888	1.743733	-0.691357
C	-1.425796	2.186651	-1.690302
C	0.648120	3.432208	-1.906270
C	2.155548	3.503896	-1.646692
C	2.577884	3.573907	-0.177665
C	1.900181	1.194508	-0.073690
C	0.675030	1.101141	-1.030678
C	-0.590734	0.961349	3.380083
C	-0.179480	0.238707	4.505421
C	1.186704	0.221011	4.828353
C	2.084240	0.915868	4.004365
C	1.595669	1.625589	2.896411
C	2.511141	2.411294	1.982433
H	-1.650313	0.987444	3.088341
H	-0.924374	-0.301387	5.108938
H	1.552324	-0.336729	5.705353
H	3.166225	0.909450	4.211218
H	2.616851	3.448600	2.374032
H	3.531738	1.960528	1.972863
H	-3.172322	2.441754	2.466748
H	-5.293985	1.210349	1.897455
H	-5.546270	0.252723	-0.446125
H	-3.696845	0.654605	-2.121462
H	-1.376148	1.493387	-2.560048
H	-1.759925	3.171551	-2.085078
H	0.490980	3.207261	-2.987450
H	0.157694	4.404307	-1.687563
H	2.536410	4.413640	-2.159475
H	2.663571	2.651322	-2.145422
H	2.295474	4.548807	0.276252
H	3.689178	3.474600	-0.115001
H	1.820144	0.397089	0.690882
H	2.857508	1.023183	-0.615632

H	0.983031	0.792755	-2.055881
H	-0.035488	0.334608	-0.657343

**Table A.4.4.** Cartesian coordinates (Å) for DFT optimized model of  $[\text{Mn}^{\text{III}}(\text{O}_2)(\text{L}^7\text{py}_2^{6-\text{Me}})]^+$ .

Atom	x	y	z
Mn	-0.010842	0.095253	0.495449
O	-0.688271	0.281369	2.268111
O	0.517331	-0.523306	2.175018
N	-1.973742	-0.890898	-0.172400
N	-0.823722	1.528735	-0.881397
N	1.440974	1.851885	0.478487
N	1.852991	-0.745970	-0.252437
C	-2.595424	-1.884041	0.526700
C	-3.987895	-2.067748	0.424103
C	-4.752404	-1.229497	-0.402558
C	-4.095348	-0.217583	-1.123466
C	-2.710950	-0.083283	-0.980245
C	-1.895894	0.937875	-1.747728
C	-1.423382	2.588126	0.028798
C	-0.400180	3.518720	0.692445
C	0.814257	2.870690	1.371788
C	-1.748460	-2.805510	1.372782
C	2.056048	-1.911850	-0.934629
C	3.342309	-2.473030	-1.024592
C	4.431553	-1.839473	-0.407691
C	4.215612	-0.627952	0.258826
C	2.914129	-0.104306	0.309603
C	2.655641	1.231888	0.998374
C	1.566742	2.350614	-0.910856
C	0.286457	2.066187	-1.737239
C	0.877047	-2.577344	-1.586203
H	-4.470292	-2.875712	0.995789
H	-5.842984	-1.367715	-0.477574
H	-4.640539	0.466492	-1.792721
H	-1.385005	0.453085	-2.605428
H	-2.546363	1.742461	-2.159594
H	-2.037461	2.048531	0.778364
H	-2.107293	3.215161	-0.587725
H	-0.055564	4.268386	-0.050870
H	-0.940540	4.108162	1.465520
H	0.544432	2.349278	2.311182
H	1.550080	3.675469	1.616764
H	-1.050952	-2.241883	2.027278
H	-1.130551	-3.460962	0.719501
H	-2.404493	-3.440418	2.003846
H	3.485822	-3.409171	-1.584697

H	5.432584	-2.295011	-0.472075
H	5.033808	-0.066525	0.736042
H	3.556036	1.874714	0.844743
H	2.530258	1.066665	2.087786
H	2.438841	1.865799	-1.392672
H	1.792432	3.440273	-0.915224
H	-0.054208	2.990317	-2.257335
H	0.482937	1.287316	-2.498476
H	0.134737	-2.917651	-0.831608
H	1.200277	-3.463907	-2.168069
H	0.340955	-1.889571	-2.275607

**Table A.4.5.** Cartesian coordinates (Å) for DFT optimized model for  $[\text{Mn}^{\text{III}}(\text{O}_2)(\text{L}^7\text{py}_2^{4-\text{Me}})]^+$

Atom	x	y	z
Mn	-0.469549	2.634620	1.182838
O	-0.956405	4.398556	0.781838
O	-0.841302	4.156933	2.200683
N	-2.492751	1.846130	0.743326
N	-0.149251	1.726470	-0.810429
N	1.783775	2.613029	0.783718
N	0.317168	1.512035	2.769293
C	-3.591431	2.197368	1.446931
C	-4.875042	2.215736	0.889940
C	-5.050996	1.880034	-0.469302
C	-3.892410	1.523062	-1.195500
C	-2.642529	1.509732	-0.563662
C	-1.389496	1.022023	-1.261995
C	-6.404388	1.912006	-1.130775
H	-3.423776	2.482705	2.498462
H	-5.734074	2.502201	1.516954
H	-3.964287	1.249262	-2.260635
H	-1.274765	-0.054768	-1.012237
H	-1.502009	1.084712	-2.367630
H	-6.615525	0.951417	-1.651092
H	-6.441991	2.711638	-1.905824
H	-7.214089	2.103240	-0.396669
C	0.156418	2.897320	-1.714091
C	1.574764	3.471854	-1.547624
C	2.063717	3.761537	-0.118743
C	2.149525	1.314621	0.164349
C	1.006517	0.779608	-0.743802
H	0.050717	2.559023	-2.772356
H	-0.622487	3.666675	-1.531657
H	1.611762	4.422447	-2.122173
H	2.297525	2.796482	-2.054432
H	1.555014	4.650022	0.309111

H	3.161225	3.968781	-0.151680
H	2.326072	0.586930	0.980220
H	3.107650	1.409318	-0.394850
H	1.373798	0.553968	-1.770489
H	0.620294	-0.166867	-0.319831
C	-0.381628	0.676439	3.573144
C	0.167294	0.111074	4.725786
C	1.501567	0.407455	5.083860
C	2.219879	1.266758	4.224330
C	1.608836	1.808257	3.086836
C	2.326615	2.762686	2.146235
C	2.124667	-0.155513	6.333123
H	-1.416191	0.458284	3.265744
H	-0.448214	-0.565542	5.339435
H	3.271391	1.516933	4.438343
H	2.133084	3.809766	2.472848
H	3.430043	2.599824	2.190569
H	3.232797	-0.180140	6.263054
H	1.750060	-1.178744	6.546916
H	1.856623	0.480314	7.208920

**Table A.4.6.** Cartesian coordinates (Å) for DFT optimized model for  $[\text{Mn}^{\text{III}}(\text{O}_2)(\text{L}^7\text{q}_2)]^+$

<b>Atom</b>	<b>x</b>	<b>y</b>	<b>z</b>
Mn	1.79435	2.03519	4.03841
O	3.11685	2.56043	2.83348
O	1.79892	2.88061	2.35231
N	0.76604	0.21111	3.07714
N	-0.26100	2.18523	4.81093
N	1.68034	3.88006	5.39698
N	3.22000	1.65364	5.58195
C	1.25884	-0.51150	2.00851
C	0.38373	-1.29710	1.17098
C	-1.00870	-1.28790	1.46936
C	-1.47440	-0.54930	2.54631
C	-0.54680	0.18497	3.33371
C	-0.99760	0.90984	4.58354
C	-0.88680	3.30268	4.00462
C	-0.46050	4.71521	4.44166
C	1.04419	4.97270	4.61647
C	3.77532	0.42902	5.91014
C	4.96988	0.35007	6.71402
C	5.54395	1.56764	7.17660
C	4.93793	2.77494	6.86692
C	3.77146	2.78486	6.05810

C	3.10352	4.09966	5.69260
C	0.89445	3.53172	6.60744
C	-0.23420	2.51963	6.26840
C	2.65520	-0.49840	1.72842
C	3.16306	-1.23630	0.66445
C	2.30300	-2.01160	-0.16340
C	0.93635	-2.04030	0.08500
C	3.16081	-0.77290	5.46297
C	3.71686	-2.00650	5.78659
C	4.90445	-2.08890	6.56541
C	5.51905	-0.93010	7.02255
H	-1.70470	-1.86650	0.83959
H	-2.54520	-0.52420	2.80140
H	-2.09720	1.08361	4.56730
H	-0.78580	0.24146	5.44634
H	-0.64590	3.11400	2.93725
H	-1.99430	3.23135	4.11717
H	-0.99330	4.97895	5.38067
H	-0.84580	5.42458	3.67753
H	1.56034	5.02202	3.63575
H	1.18346	5.95243	5.13703
H	6.45854	1.53903	7.79120
H	5.34552	3.72857	7.23550
H	3.26237	4.84573	6.50810
H	3.58503	4.50606	4.77569
H	1.58268	3.06682	7.33990
H	0.49134	4.45312	7.08443
H	-0.05180	1.57215	6.81204
H	-1.23240	2.89488	6.58887
H	3.31833	0.11574	2.35700
H	4.24603	-1.21830	0.45735
H	2.72630	-2.58610	-1.00350
H	0.25932	-2.63400	-0.55160
H	2.23586	-0.71230	4.86747
H	3.22908	-2.93100	5.43819
H	5.33047	-3.07530	6.80845
H	6.43608	-0.97970	7.63199

**Table A.4.7.** Cartesian coordinates (Å) for DFT optimized model for  $[\text{Mn}^{\text{III}}(\text{O}_2)(\text{L}^{\text{7isoq}_2})]^+$

Atom	x	y	z
Mn	0.014061	4.706862	4.263822
O	-0.943589	4.012901	2.822009

O	-0.735252	5.438607	2.716255
N	2.087124	4.021932	3.814563
N	0.503136	6.616996	5.168026
N	-1.378322	4.939972	6.056464
N	0.201849	2.883569	5.492165
C	2.456282	2.860508	4.363826
C	4.257291	4.276291	2.781534
C	3.777280	2.321452	4.197397
C	2.966027	4.707514	3.014548
C	4.203834	1.088280	4.780509
C	6.418195	1.366739	3.784235
C	4.711056	3.067593	3.386389
C	5.498111	0.623862	4.576154
C	6.033042	2.566914	3.199468
C	-0.453882	8.603361	6.190483
C	1.661188	7.312188	4.925017
C	0.758845	9.335003	5.910265
C	1.825812	8.637666	5.274271
C	-1.420403	10.623337	7.173539
C	-0.514341	7.225252	5.800025
C	0.850308	10.709053	6.280112
C	-1.537443	9.281956	6.830665
C	-0.221098	11.340454	6.900117
C	-1.735955	6.368308	6.072953
C	-1.043742	2.038352	5.391872
C	0.422857	3.394700	6.880113
C	1.361132	2.064150	5.047300
C	-2.580624	4.074021	5.885149
C	-0.560330	4.546070	7.237949
C	-2.255995	2.600552	6.140451
H	-2.215733	6.650241	7.039047
H	-2.491967	6.540251	5.273691
H	-1.259408	1.920064	4.309531
H	-0.818771	1.027704	5.805823
H	1.466468	3.768835	6.917870
H	0.345363	2.554034	7.607549
H	0.987552	1.333152	4.295747
H	1.748963	1.467577	5.901005
H	-2.953951	4.230394	4.849923
H	-3.383160	4.394292	6.593118
H	-1.219572	4.273444	8.091871
H	0.024467	5.430102	7.555596

H	-2.137754	2.424461	7.231037
H	-3.138621	1.995739	5.839412
H	4.926856	4.859526	2.129802
H	2.573286	5.622479	2.544725
H	3.512236	0.493956	5.396650
H	7.440728	0.983745	3.634077
H	5.815179	-0.328100	5.031054
H	6.739834	3.144909	2.581838
H	2.469713	6.748353	4.439959
H	2.777185	9.148518	5.059182
H	-2.263694	11.137213	7.662852
H	1.780968	11.259030	6.064660
H	-2.476270	8.751103	7.048679
H	-0.145813	12.402609	7.184535

**Table A.4.8.** Cartesian coordinates (Å) for DFT optimized model for  $[\text{Mn}^{\text{III}}(\text{O}_2)(\text{L}^7\text{py}_2^{4\text{Cl}})]^+$

Atom	x	y	z
Mn	-0.163963	2.339919	15.727912
O	-0.026490	3.635682	17.063521
O	-1.178977	3.830345	16.220065
N	0.729456	3.386768	13.988730
N	-1.324005	1.460025	14.071261
N	1.323453	1.078586	16.527637
N	-1.330320	0.575303	16.577716
Cl	0.830426	6.559307	10.744698
Cl	4.307957	-1.328989	18.936626
C	0.894900	0.287244	17.550019
C	3.160545	-0.400122	18.006117
C	1.519382	4.476091	14.112435
C	1.600366	5.477352	13.138286
C	-0.037497	4.215839	11.852811
C	-0.035589	3.256520	12.876363
C	0.798145	5.335383	11.994058
C	1.791221	-0.474329	18.311098
C	-1.260002	-0.548702	15.609864
C	-0.816444	1.964069	12.756734
C	-0.599381	0.292329	17.826028
C	-2.743894	1.924568	14.306993
C	-1.224173	-0.032208	14.143606
C	-2.726634	1.049119	16.786803
C	-3.467770	1.189676	15.448230



C	2.642803	1.130743	16.235850
C	3.605131	0.409452	16.947305
H	2.108198	4.551148	15.041040
H	2.263810	6.343023	13.280121
H	-0.675685	4.087613	10.965690
H	1.421626	-1.114357	19.125995
H	-2.104170	-1.255368	15.776302
H	-0.328154	-1.112274	15.810949
H	-1.646019	2.069596	12.023699
H	-0.119419	1.201945	12.346126
H	-0.911886	-0.667593	18.300969
H	-0.830095	1.108560	18.546707
H	-3.325520	1.754950	13.370525
H	-2.707024	3.020460	14.480670
H	-0.255132	-0.311170	13.685538
H	-2.026738	-0.497449	13.527718
H	-3.284979	0.327132	17.431385
H	-2.669880	2.020180	17.321349
H	-4.417936	1.734833	15.637581
H	-3.776630	0.184252	15.091014
H	2.934731	1.776885	15.393136
H	4.667581	0.480022	16.673051

**Table A.5.1.** Cartesian coordinates (Å) for DFT energy minimized  $[\text{Mn}^{\text{III}}(\text{O}_2)(\text{mL}_5^2)\text{-N}(1)]^+$  model.

Atom	x	y	z
Mn	-0.040375	-0.009896	-0.015145
O	1.838127	-0.035004	-0.018102
O	1.318816	1.277773	-0.011925
N	0.113550	-2.365762	0.043816
N	-0.071852	-0.551423	2.199579
N	-2.505980	-0.978628	0.016108
N	-1.510896	1.598319	0.058151
N	-0.032341	-0.700254	-2.187726
C	-2.784574	1.410643	0.495131
C	0.385704	-1.791954	2.486335
C	0.968683	-2.667165	-1.131570
C	0.565244	-2.225529	3.811734
C	-3.691658	2.477969	0.598031
C	-0.139820	-0.038384	4.560249
C	0.817232	-2.656361	1.315160
C	0.528691	-1.918960	-2.376356

C	-0.316196	0.305136	3.213860
C	-2.345650	-2.317403	0.608932
C	-0.332294	0.052516	-3.265885
C	0.459329	-1.642619	-4.781729
C	-3.153059	-0.003516	0.900868
C	-3.278129	3.771591	0.246918
C	0.771690	-2.429827	-3.663084
C	0.300785	-1.336135	4.863604
C	-1.195731	-3.067170	-0.065550
C	-1.114013	2.849486	-0.283558
C	-1.963079	3.959441	-0.204838
C	-0.099119	-0.371088	-4.580881
C	-3.190647	-1.022357	-1.287880
H	1.023829	-3.761049	-1.336858
H	1.996502	-2.321720	-0.895606
H	0.924228	-3.245923	4.013240
H	-4.716647	2.287511	0.949364
H	-0.346592	0.697880	5.349904
H	1.893101	-2.433369	1.154062
H	0.745602	-3.735511	1.585774
H	-0.662393	1.309416	2.922803
H	-3.275846	-2.931366	0.521407
H	-2.144912	-2.198292	1.690894
H	-0.776038	1.038649	-3.057979
H	0.651589	-2.018130	-5.797945
H	-2.788206	-0.178971	1.935225
H	-4.264737	-0.110531	0.929568
H	-3.975704	4.619631	0.319172
H	1.213533	-3.430134	-3.782877
H	0.443349	-1.651905	5.908065
H	-1.119980	-4.098160	0.350569
H	-1.421431	-3.181196	-1.144271
H	-0.071981	2.940474	-0.625385
H	-1.591111	4.951615	-0.497041
H	-0.354812	0.284024	-5.425685
H	-3.199754	-0.012637	-1.740584
H	-4.245361	-1.375475	-1.188650
H	-2.657027	-1.693353	-1.985019

**Table A.5.2.** Cartesian coordinates (Å) for DFT energy minimized  $[\text{Mn}^{\text{III}}(\text{O}_2)(\text{mL}_5^2)\text{-N}(4)]^+$  model.

Atom	x	y	z
Mn	0.083111	-0.272717	0.325625
O	1.870545	-0.622704	0.636999
O	1.625567	0.749040	0.304688

N	0.083375	-0.935365	-1.947538
N	-0.879343	-2.245026	0.532424
N	-0.362437	-0.487010	2.556998
N	-1.482469	0.877692	-0.457337
C	-0.324536	-1.793758	2.914704
C	-0.565736	0.197379	-2.644784
C	-0.248496	-2.194059	4.258183
C	-1.629437	0.884157	-1.811519
C	-0.490935	-3.009380	-0.690313
C	-2.365306	1.563837	0.309454
C	-3.602539	2.287804	-1.623901
C	-0.280682	-2.799210	1.774818
C	-0.171323	-1.211230	5.256619
C	-2.694426	1.574108	-2.417727
C	-0.723959	-2.185847	-1.961104
C	-0.281877	0.455315	3.520195
C	-0.180615	0.141436	4.881741
C	-3.432676	2.286938	-0.229434
C	-2.356488	-2.180899	0.677899
C	1.492883	-1.137833	-2.366232
C	1.748447	-1.615954	-3.793760
N	0.722372	-1.607043	-4.668866
C	3.047986	-2.031531	-4.155618
C	3.284618	-2.442099	-5.473900
C	2.218308	-2.433531	-6.388239
C	0.961706	-2.009872	-5.933673
H	-0.968117	-0.098842	-3.635735
H	0.225551	0.950912	-2.846326
H	-0.235823	-3.263676	4.516129
H	-1.051916	-3.968949	-0.750119
H	0.583736	-3.262074	-0.595470
H	-2.196783	1.518555	1.395803
H	-4.436358	2.836180	-2.087671
H	0.784686	-3.031136	1.563080
H	-0.774568	-3.751928	2.073220
H	-0.099576	-1.499757	6.316086
H	-2.796804	1.552199	-3.513268
H	-0.501009	-2.801159	-2.857951
H	-1.792740	-1.902812	-2.039874
H	-0.285185	1.501991	3.176744
H	-0.111083	0.944786	5.628934
H	-4.117634	2.832833	0.434701
H	-2.619275	-1.561957	1.555392
H	-2.781371	-3.200619	0.815270
H	-2.813836	-1.723959	-0.217524
H	1.966124	-1.838065	-1.649098

H	2.020109	-0.176813	-2.188049
H	3.860558	-2.029134	-3.412205
H	4.288275	-2.770263	-5.784338
H	2.355132	-2.752054	-7.431751
H	0.095280	-1.990292	-6.617006

**Table A.5.3.** Cartesian coordinates (Å) for DFT energy minimized  $[\text{Mn}^{\text{III}}(\text{O}_2)(\text{mL}_5^2)\text{-N}(3)]^+$  model.

Atom	x	y	z
Mn	0.057307	-0.006508	-0.031598
O	1.917927	-0.112338	-0.041800
O	1.460732	1.233520	-0.063578
N	-2.125883	-0.937872	-0.614383
N	-1.348433	1.571041	0.668170
N	-0.098867	-0.048982	-2.269989
C	-1.977693	-1.561339	-1.944630
C	-1.092942	-0.746150	-2.867731
C	-2.772997	1.122890	0.595367
C	0.793691	0.618559	-3.035298
C	-0.319086	-0.077149	-5.059588
C	-1.243631	-0.771426	-4.264223
C	-3.022246	0.241962	-0.626948
C	0.723549	0.625120	-4.434239
C	-1.138735	2.776384	-0.181537
C	-0.908290	1.838882	2.090321
C	-1.689911	2.900593	2.847199
N	-2.886862	2.509907	3.343817
C	-1.176021	4.198378	3.039091
C	-1.934535	5.126037	3.771767
C	-3.605770	3.408779	4.038338
C	-3.177064	4.725714	4.282396
H	-2.965298	-1.763580	-2.421844
H	-1.489551	-2.549775	-1.797032
H	-0.190202	4.473981	2.634557
H	-3.461233	1.994637	0.579648
H	-3.007810	0.585591	1.534607
H	1.574905	1.159750	-2.479158
H	-0.413416	-0.084004	-6.156465
H	0.164730	2.106806	2.033505
H	-1.000424	0.880719	2.640613
H	-1.555964	6.144566	3.945856
H	-2.072256	-1.334210	-4.719817
H	-4.098051	-0.052021	-0.666571
H	-2.811247	0.805039	-1.558202
H	-4.574721	3.054831	4.429703

H	-3.804953	5.415169	4.865859
H	1.473565	1.177741	-5.018207
H	-0.072889	3.067428	-0.152989
H	-1.763545	3.625314	0.171416
H	-1.408620	2.546409	-1.229128
C	-2.482693	-1.935701	0.410440
C	-1.255007	-2.651307	0.938371
N	-0.100180	-1.936389	0.940936
C	-1.314968	-3.953782	1.458242
C	-0.159418	-4.525645	2.011589
C	1.027818	-3.777188	2.023194
C	1.017446	-2.490770	1.473115
H	-3.237487	-2.669582	0.044874
H	-2.957449	-1.409630	1.264793
H	-2.263452	-4.510756	1.428346
H	-0.185772	-5.544788	2.424726
H	1.958745	-4.181869	2.444536

**Table A.5.4.** Cartesian coordinates (Å) for DFT energy minimized  $[\text{Mn}^{\text{III}}(\text{O}_2)(\text{ImL}_5^2)\text{-N(1)}]^+$  model.

Atom	x	y	z
Mn	-0.257761	-0.194416	0.101153
O	1.594084	-0.112451	0.179465
O	1.070249	1.194263	0.123799
N	-2.415551	-0.979318	-0.032528
N	-1.699081	1.837890	-0.016451
N	-0.701535	0.471240	2.302838
N	-0.938537	0.981178	4.459138
C	-1.312097	2.631688	1.175141
C	-3.320813	0.044173	-0.625174
C	-2.355763	-2.184104	-0.913384
C	-3.112627	1.413282	0.027666
C	-2.943338	-1.408237	1.290616
C	-0.562020	0.032864	3.549470
C	-1.182439	1.767787	2.400475
C	-1.347148	2.093236	3.737800
C	-0.894085	0.865170	5.915853
C	0.862969	-3.205636	0.259156
C	-0.858402	-4.356665	-0.549088
C	1.209942	-5.699592	0.071698
C	-1.174146	-3.011050	-0.500777
N	-0.094128	-2.313878	0.008759
N	0.441879	-4.461092	-0.066796
H	-2.017697	3.478668	1.365002

H	-0.313906	3.067777	0.959154
H	-4.392296	-0.260881	-0.519356
H	-3.098884	0.105977	-1.708429
H	-2.216269	-1.824147	-1.956216
H	-3.306607	-2.769141	-0.882008
H	-3.781932	2.160511	-0.467450
H	-3.417707	1.370956	1.094311
H	-2.246012	-2.137431	1.750092
H	-3.948541	-1.885846	1.179843
H	-3.025599	-0.540036	1.969802
H	-0.198084	-0.958543	3.845937
H	-1.687818	3.007381	4.236954
H	-0.174932	1.597253	6.340883
H	-0.565370	-0.158076	6.184332
H	-1.901110	1.045351	6.347991
H	1.855163	-2.977068	0.665833
H	-1.420361	-5.237211	-0.878585
H	0.689786	-6.399230	0.759776
H	2.207428	-5.457399	0.486801
H	1.338940	-6.183399	-0.919235
C	-1.310967	2.508473	-1.278571
C	-1.057884	1.549979	-2.413725
N	-0.550150	0.283592	-2.176406
C	-1.110355	1.771025	-3.780998
N	-0.608511	0.623239	-4.377563
C	-0.288045	-0.241951	-3.369838
C	-0.429467	0.403713	-5.812130
H	-0.355189	3.036923	-1.074695
H	-2.061328	3.281205	-1.582054
H	0.138687	-1.235419	-3.555091
H	-1.430026	2.633369	-4.376864
H	-1.397885	0.516634	-6.343434
H	-0.048585	-0.624117	-5.972246
H	0.304284	1.128088	-6.225378

**Table A.5.5.** Cartesian coordinates (Å) for DFT energy minimized  $[\text{Mn}^{\text{III}}(\text{O}_2)(\text{ImL}_5^2)\text{-N}(4)]^+$  model.

Atom	x	y	z
Mn	-0.287018	0.022922	-0.250008
O	1.240344	0.900957	-0.831297
O	0.436576	0.404006	-1.906050
N	-2.251208	-0.939480	-0.715037
N	-1.738257	1.938627	-0.202692
N	-0.497315	0.379307	1.792199
N	-0.734328	0.385592	3.997797

C	-1.473854	2.581922	1.105116
C	-3.136320	0.149721	-1.224406
C	-1.913443	-1.944484	-1.766072
C	-3.114687	1.375767	-0.304654
C	-2.870474	-1.625575	0.446309
C	-0.257967	-0.294280	2.920485
C	-1.157436	1.549865	2.154146
C	-1.314726	1.556930	3.528287
C	-0.643675	-0.026310	5.400018
C	1.163770	-3.087586	-0.304669
C	-0.296480	-4.029096	-1.680969
C	1.778931	-5.393066	-1.139879
C	-0.736299	-2.769698	-1.313563
N	0.181797	-2.200477	-0.443855
N	0.919020	-4.213092	-1.037085
C	-1.404167	2.858548	-1.343850
C	-2.098339	4.192049	-1.333946
N	-3.468811	4.310688	-1.524244
C	-1.534977	5.454600	-1.182614
N	-2.580892	6.354659	-1.287298
C	-3.718621	5.611196	-1.488835
C	-2.482356	7.811020	-1.239936
H	-2.305189	3.247550	1.438118
H	-0.580521	3.231177	0.967285
H	-4.184233	-0.219132	-1.341695
H	-2.768544	0.430883	-2.232468
H	-1.641996	-1.379420	-2.685085
H	-2.793014	-2.587662	-2.009796
H	-3.828969	2.142088	-0.686607
H	-3.446182	1.095162	0.717322
H	-2.183548	-2.409594	0.823411
H	-3.837085	-2.100737	0.150053
H	-3.061189	-0.902155	1.263049
H	0.241273	-1.266845	2.992803
H	-1.766712	2.285883	4.209782
H	-0.033869	0.703057	5.973670
H	-0.160780	-1.021351	5.451208
H	-1.658526	-0.091034	5.844667
H	2.070001	-2.956236	0.299759
H	-0.715038	-4.794881	-2.343620
H	1.240308	-6.294826	-0.780192
H	2.679477	-5.235832	-0.514851
H	2.094236	-5.545807	-2.192925
H	-1.643025	2.308200	-2.276975
H	-0.302779	2.991980	-1.335487
H	-0.501500	5.789508	-1.034398

H	-4.703955	6.081513	-1.612484
H	-2.020384	8.138817	-0.284255
H	-3.501010	8.240764	-1.309467
H	-1.874107	8.190715	-2.089158

**Table A.5.6.** Cartesian coordinates (Å) for DFT energy minimized  $[\text{Mn}^{\text{III}}(\text{O}_2)(\text{ImL}_5^2)\text{-N}(3)]^+$  model.

Atom	x	y	z
Mn	0.081726	0.052508	0.161156
O	1.936538	0.207479	0.231334
O	1.377275	0.810851	-0.936575
N	0.137189	-2.150398	-0.623972
N	-2.318735	-1.002797	0.667319
N	-0.149326	-0.199644	2.229644
N	0.290926	-0.533711	4.374547
C	-2.598237	-0.602420	2.058137
C	-1.218391	-2.751640	-0.724007
C	-2.100869	-2.450941	0.490178
C	0.986677	-2.910473	0.336439
C	0.803295	-0.179268	3.166627
C	-1.326257	-0.579255	2.857142
C	-1.061939	-0.796803	4.197231
C	1.027668	-0.634551	5.636237
C	-3.257003	-0.402789	-0.296196
C	-2.797465	0.985562	-0.650785
N	-1.438859	1.264320	-0.630214
C	-3.470266	2.103193	-1.110993
N	-2.499131	3.060061	-1.378106
C	-1.291338	2.516487	-1.074710
C	-2.741785	4.412526	-1.884207
C	0.802936	-2.102528	-1.979183
C	0.829913	-3.386383	-2.762261
N	1.505391	-4.517343	-2.327742
C	1.347082	-5.415000	-3.288502
C	0.261692	-3.629701	-4.008838
C	0.268969	-5.630923	-5.573116
N	0.604092	-4.929456	-4.337667
H	-3.368807	-1.243818	2.548696
H	-3.014957	0.427465	2.025380
H	-1.152845	-3.854858	-0.861700
H	-1.692237	-2.354565	-1.645841
H	-3.063304	-3.009758	0.395846
H	-1.613430	-2.826908	1.411627
H	1.965906	-2.402524	0.412947
H	1.148102	-3.953803	-0.007437



H	0.513327	-2.910386	1.336736
H	1.853762	0.078191	2.993094
H	-1.702161	-1.100448	5.030772
H	0.590767	0.051120	6.387218
H	2.080756	-0.353209	5.461022
H	0.988572	-1.672886	6.018269
H	-4.311973	-0.398873	0.065923
H	-3.248287	-1.024821	-1.215491
H	-4.532776	2.298980	-1.284196
H	-0.333664	3.037677	-1.181127
H	-3.253843	4.364544	-2.864112
H	-1.773816	4.928173	-2.008531
H	-3.367047	4.981287	-1.169035
H	1.829908	-1.729703	-1.798797
H	0.282270	-1.326028	-2.574256
H	1.750524	-6.435102	-3.289246
H	-0.319514	-3.000566	-4.691288
H	-0.829438	-5.682533	-5.707100
H	0.668782	-6.659135	-5.520758
H	0.718667	-5.119671	-6.446767

**Table A.5.7.** Gaussian fitting parameters.

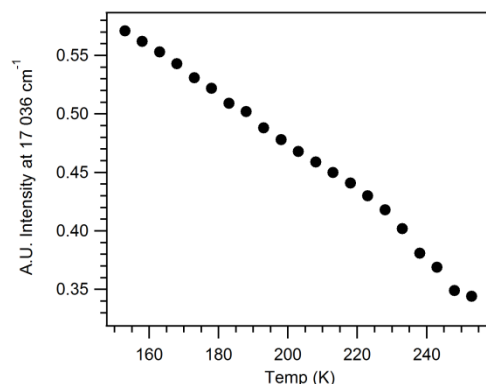
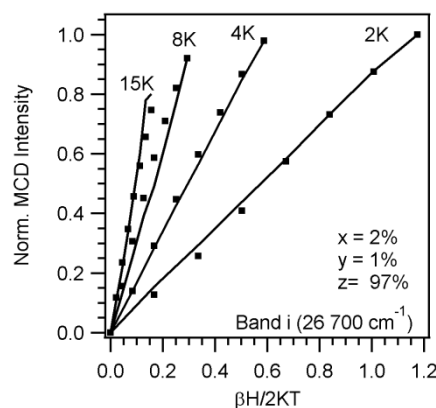
band	$[\text{Mn}^{\text{III}}(\text{O}_2)(\text{imL}_5^2)]^+$			$[\text{Mn}^{\text{III}}(\text{O}_2)(\text{mL}_5^2)]^+$		
	energy ( $\text{cm}^{-1}$ )	fwhm ( $\text{cm}^{-1}$ )	$f_{\text{exp}} \times 10^3$	energy ( $\text{cm}^{-1}$ )	fwhm ( $\text{cm}^{-1}$ )	$f_{\text{exp}} \times 10^3$
1	Abs: 17 200	4496	3.58	Abs: 17 120	4496	1.84
	MCD: 16 720	4163		MCD: 15 325	4163	
2	Abs: 22 800	4163	0.883	Abs: 23 000	4163	1.38
	MCD: 23 800	4496		MCD: 21 500	4496	
3	Abs: 27 000	4163	3.53	Abs: 26 900	4163	2.68
	MCD: 26 400	4995		MCD: 25 900	4995	
4	Abs: 32 200	4163	13.8	Abs: 31 000	4163	14.39
	MCD: 32 800	4995		MCD: 30 900	4995	

**Table A.5.8.** Transition Polarizations and ZFS Parameters determined from fits of VTVH MCD Data Collected for  $[\text{Mn}^{\text{III}}(\text{O}_2)(\text{mL}_5^2)]^+$  and  $[\text{Mn}^{\text{III}}(\text{O}_2)(\text{imL}_5^2)]^+$  at the Energies Indicated.

	band	energy ( $\text{cm}^{-1}$ )	$D$ ( $\text{cm}^{-1}$ )	$E/D$	Polarization (%)		
					$x$	$y$	$z$
$[\text{Mn}^{\text{III}}(\text{O}_2)(\text{mL}_5^2)]^+$	1	15 300	-2.9	0.075	15	81	4
		16 700			5	89	6
	2	26 600			2	1	97
	3	30 800			<1	<1	100
$[\text{Mn}^{\text{III}}(\text{O}_2)(\text{imL}_5^2)]^+$	1	16 700	-2.0	0.30	33	40	27
	2	25 600			100	<1	<1
	3	32 800			11	2	87

**Table A.5.9.** Metric parameters for  $\text{ImL}_5^2$  structures from surface scan.

Mn-N(1) <sup>a</sup>	Relative Energy	Mn-O	O-O	Mn-N(2)	Mn-N(3)	Mn-N(4)	Mn-N(5)
2.70	0	1.858	1.429	2.342	5.393	2.099	2.095
		1.862					
2.60	0.11	1.861	1.428	2.410	5.410	2.103	2.097
		1.865					
2.50	0.73	1.864	1.426	2.359	5.432	2.112	2.101
		1.869					
2.40	1.96	1.866	1.424	2.373	5.451	2.133	2.100
		1.871					
2.30	3.91	1.865	1.422	2.392	5.480	2.175	2.089
		1.874					
2.20	5.38	1.843	1.432	2.438	5.558	2.312	2.066
		1.863					
2.10	7.04	1.844	1.433	2.445	5.571	2.346	2.072
		1.859					
2.00	10.42	1.843	1.435	2.450	5.582	2.371	2.078
		1.860					

**Figure A.5.1.** Absorption intensity of  $[\text{Mn}^{\text{III}}(\text{O}_2)(\text{ImL}_5^2)]^+$  at  $17\,036\text{ cm}^{-1}$  as a function of temperature from 280 K – 150 K in 5 K increments.**Figure A.5.2.** VTVH MCD data collected for  $[\text{Mn}^{\text{III}}(\text{O}_2)(\text{mL}_5^2)]^+$  (dots) and fits (solid lines) at  $26\,700\text{ cm}^{-1}$  using  $D = -2.9\text{ cm}^{-1}$ ,  $E/D = 0.075$ ,  $g_{\text{iso}} = 2.0$ , and polarizations listed in the inset.

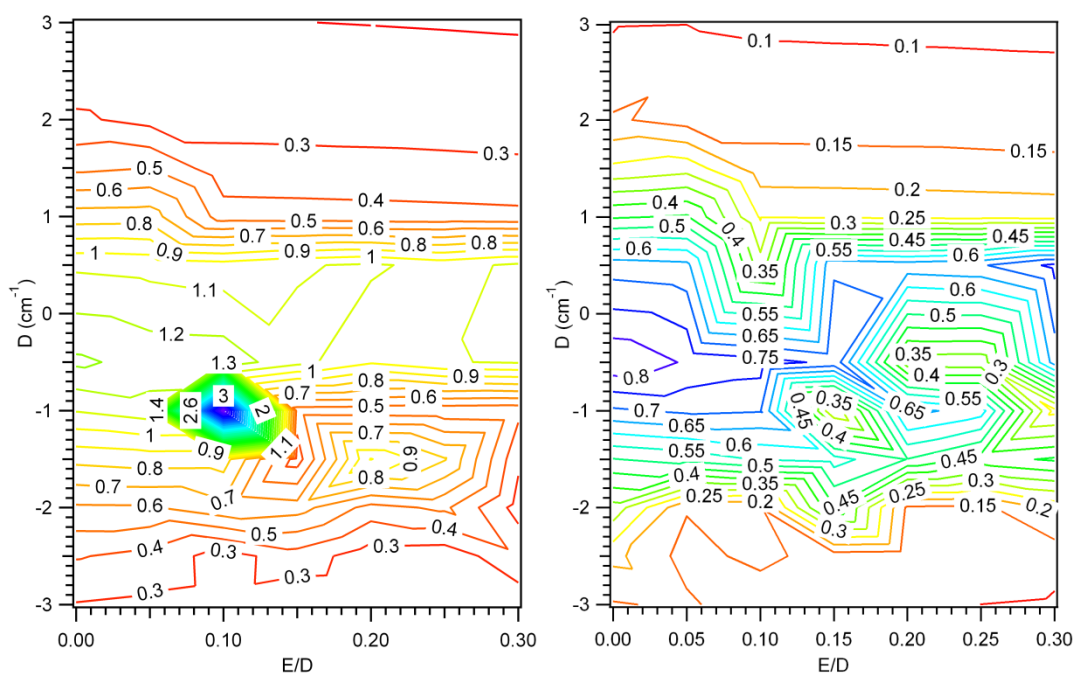


**Figure A.5.3.** Contour plot of  $\chi^2$  values as a function of ZFS parameters  $D$  and  $E/D$  for fits of VTVH MCD data collected for  $[\text{Mn}^{\text{III}}(\text{O}_2)(\text{mL}_5^2)]^+$  at 26 667 (left) and 30 800 (right)  $\text{cm}^{-1}$ .

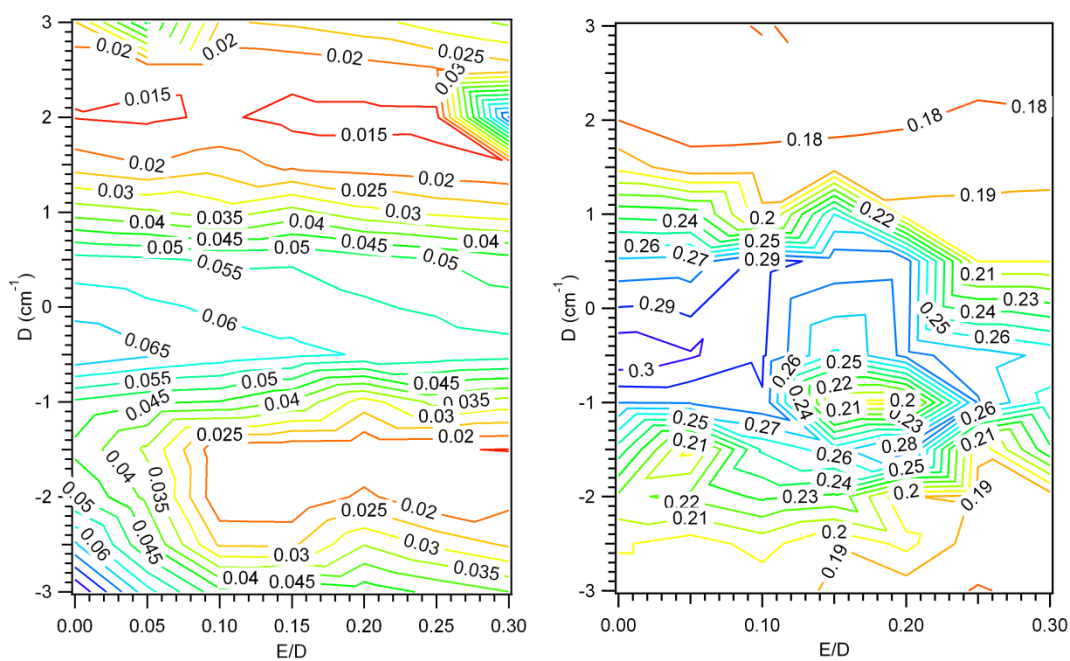


**Figure A.5.4.** Contour plot of  $\chi^2$  values as a function of ZFS parameters  $D$  and  $E/D$  for fits of VTVH MCD data collected for  $[\text{Mn}^{\text{III}}(\text{O}_2)(\text{imL}_5^2)]^+$  at 16 700 (left) and 25 600 (right)  $\text{cm}^{-1}$ .

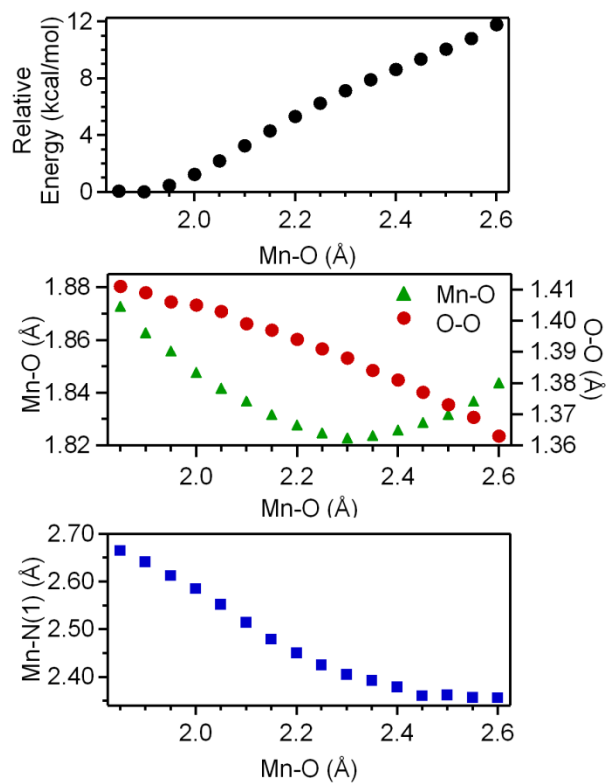


**Figure A.5.5.** Relative energy (top), Mn-O and O-O bond lengths (center), and Mn-N(1) bond lengths (bottom) as a function of the Mn-O distance for  $[\text{Mn}^{\text{III}}(\text{O}_2)(\text{mL}_5^2)]^+$  determined by a relaxed surface scan using DFT computations.

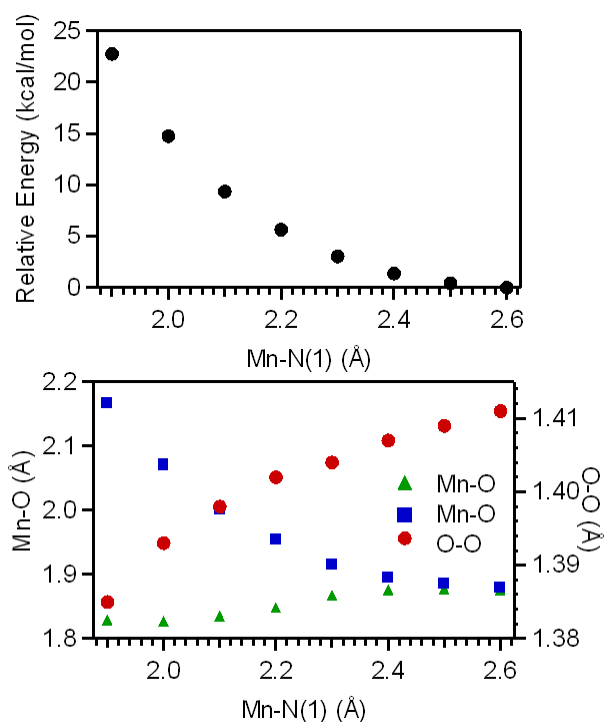


**Figure A.5.6.** Total energy and Mn-O and O-O bond lengths as a function of the Mn-N(1) distance of  $[\text{Mn}^{\text{III}}(\text{O}_2)(\text{mL}_5^2)]^+$  determined by a relaxed surface scan using DFT computations.

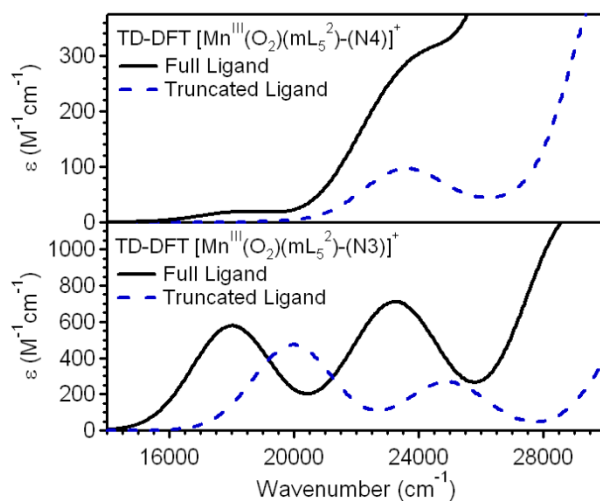


**Figure A.5.7.** TD-DFT-computed electronic absorption spectra for  $[\text{Mn}^{\text{III}}(\text{O}_2)(\text{mL}_5^2)\text{-N(4)}]^+$  (top) and  $[\text{Mn}^{\text{III}}(\text{O}_2)(\text{mL}_5^2)\text{-N(3)}]^+$  (bottom) using for models including the full  $\text{mL}_5^2$  ligand (solid lines) and four  $\text{NH}_3$  groups (dashed lines).

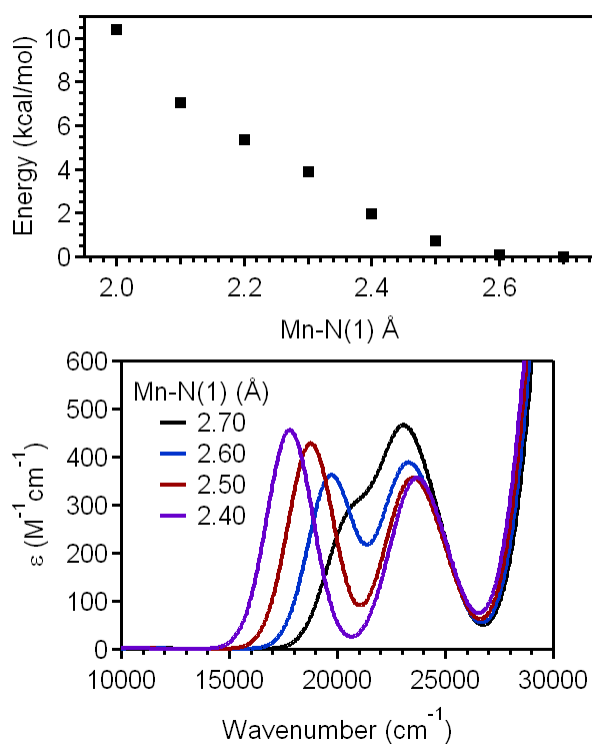


**Figure A.5.8.** Top: Total energy of  $[\text{Mn}^{\text{III}}(\text{O}_2)(\text{ImL}_5^2)\text{-N}(3)]^+$  as a function of Mn-N(1) distance. Bottom: TD-DFT-computed absorption spectra for  $[\text{Mn}^{\text{III}}(\text{O}_2)(\text{ImL}_5^2)\text{-N}(3)]^+$  models with Mn-N(1) distances from 2.70 to 2.40 Å.

**Table A.6.1.** Crystal data and structure refinement for [Mn(Tp<sup>Ph2</sup>)(DMF)<sub>3</sub>](OTf).

Empirical formula	C <sub>59</sub> H <sub>63</sub> BF <sub>3</sub> MnN <sub>9</sub> O <sub>7</sub> S	
Formula weight	1164.99	
Temperature	100(2) K	
Wavelength	1.54178 Å	
Crystal system	Monoclinic	
Space group	P2(1)/n	
Unit cell dimensions	a = 17.6441(10) Å b = 14.8052(8) Å c = 21.9441(11) Å	α = 90°. β = 93.243(4)°. γ = 90°.
Volume	5723.2(5) Å <sup>3</sup>	
Z	4	
Density (calculated)	1.352 Mg/m <sup>3</sup>	
Absorption coefficient	2.805 mm <sup>-1</sup>	
F(000)	2436	
Crystal size	0.22 x 0.01 x 0.01 mm <sup>3</sup>	
Theta range for data collection	10.74 to 66.71°.	
Index ranges	-20 ≤ h ≤ 20, -17 ≤ k ≤ 16, -24 ≤ l ≤ 25	
Reflections collected	19229	
Independent reflections	9144 [R(int) = 0.1286]	
Completeness to theta = 66.71°	90.2 %	
Absorption correction	Multi-scan	
Max. and min. transmission	1.000 and 0.793	
Refinement method	Full-matrix least-squares on F <sup>2</sup>	
Data / restraints / parameters	9144 / 0 / 709	
Goodness-of-fit on F <sup>2</sup>	0.928	
Final R indices [I > 2σ(I)]	R1 = 0.0638, wR2 = 0.1504	
R indices (all data)	R1 = 0.0984, wR2 = 0.1649	
Largest diff. peak and hole	1.402 and -0.894 e.Å <sup>-3</sup>	

---


$$R_1 = \sum ||F_O| - |F_C|| / \sum |F_O|$$

$$wR_2 = \{ \sum [w(F_O^2 - F_C^2)^2] / \sum [w(F_O^2)^2] \}^{1/2}$$

**Table A.6.2.** Crystal data and structure refinement for [Mn(O<sub>2</sub>)(Tp<sup>Ph2</sup>)(THF)].

Empirical formula	C <sub>58</sub> H <sub>62</sub> BMnN <sub>6</sub> O <sub>5</sub>	
Formula weight	988.89	
Temperature	100(2) K	
Wavelength	1.54178 Å	
Crystal system	Monoclinic	
Space group	P2(1)/n	
Unit cell dimensions	a = 12.928(2) Å b = 21.642(4) Å c = 18.633(3) Å	α = 90°. β = 103.572(4)°. γ = 90°.
Volume	5067.5(15) Å <sup>3</sup>	
Z	4	
Density (calculated)	1.296 Mg/m <sup>3</sup>	
Absorption coefficient	2.562 mm <sup>-1</sup>	
F(000)	2088	
Crystal size	0.23 x 0.20 x 0.06 mm <sup>3</sup>	
Theta range for data collection	3.18 to 66.52°.	
Index ranges	-15 ≤ h ≤ 15, -25 ≤ k ≤ 19, - 21 ≤ l ≤ 21	
Reflections collected	45183	
Independent reflections	8594 [R(int) = 0.0482]	
Completeness to theta = 66.52°	96.2 %	
Absorption correction	Multi-scan	
Max. and min. transmission	1.000 and 0.810	
Refinement method	Full-matrix least-squares on F <sup>2</sup>	
Data / restraints / parameters	8594 / 30 / 693	
Goodness-of-fit on F <sup>2</sup>	1.077	
Final R indices [I > 2σ(I)]	R1 = 0.0514, wR2 = 0.1460	
R indices (all data)	R1 = 0.0528, wR2 = 0.1474	
Largest diff. peak and hole	0.944 and -0.535 e.Å <sup>-3</sup>	

---


$$R_1 = \sum ||F_O| - |F_C|| / \sum |F_O|$$

$$wR_2 = \{ \sum [w(F_O^2 - F_C^2)^2] / \sum [w(F_O^2)^2] \}^{1/2}$$



**Table A.6.3.** Cartesian coordinates (Å) for DFT energy minimized [Mn<sup>III</sup>(O<sub>2</sub>)(Tp<sup>Ph2</sup>)(THF)] model.

Atom	x	y	z
Mn	2.311278	5.168113	8.572887
O	3.759224	4.994203	7.408479
O	3.702012	3.944327	8.39639
O	3.642094	6.494182	10.025693
N	0.531187	4.095032	7.443028
N	1.29661	6.924038	8.086569
N	1.148728	4.746492	10.261434
N	-0.182102	5.072468	10.203946
N	-0.675955	4.675571	7.737045
N	0.002915	7.007179	8.533482
B	-0.777242	5.703335	8.899954
C	-1.695933	4.029288	7.074486
C	-1.115549	2.982868	6.349993
C	0.278409	3.060868	6.59728
C	-0.446171	8.298971	8.418836
C	0.597253	9.057491	7.86571
C	1.672346	8.164192	7.669132
C	-0.75983	4.883731	11.434879
C	0.246276	4.439276	12.307237
C	1.423074	4.346505	11.533707
C	-3.122816	4.41319	7.087925
C	-3.54652	5.755614	6.936598
C	-4.913374	6.0725	6.883498
C	-5.883315	5.057732	6.973848
C	-5.475734	3.718441	7.116625
C	-4.108853	3.39927	7.172456
C	1.30298	2.165797	6.016736
C	2.617277	2.598687	5.724944
C	3.542085	1.72037	5.134432
C	3.177311	0.397649	4.823422
C	1.871992	-0.04476	5.110218
C	0.945819	0.829963	5.700579
C	-1.782401	8.793367	8.814209
C	-2.36368	8.482828	10.065985
C	-3.606851	9.02433	10.429283
C	-4.289297	9.888691	9.554043
C	-3.71636	10.213329	8.310792
C	-2.473499	9.67219	7.944217

C	2.987638	8.483451	7.077143
C	3.620911	9.706662	7.406037
C	4.844505	10.061323	6.815830
C	5.45373	9.201693	5.882800
C	4.827141	7.989516	5.541610
C	3.603509	7.632058	6.130691
C	-2.188855	5.066142	11.768434
C	-2.529037	5.709462	12.984204
C	-3.871567	5.841674	13.374697
C	-4.898018	5.33189	12.558414
C	-4.571156	4.683966	11.353178
C	-3.22971	4.547236	10.961781
C	2.73614	3.843311	11.987691
C	3.221705	4.221099	13.263644
C	4.440482	3.716821	13.745588
C	5.192825	2.821935	12.961949
C	4.712988	2.431209	11.698561
C	3.493368	2.933361	11.214475
C	3.214411	7.534751	10.950286
C	4.458382	7.897943	11.769279
C	5.597298	7.621325	10.769254
C	5.096992	6.365083	10.052628
H	-1.633772	2.301757	5.664913
H	0.573997	10.127612	7.630868
H	0.117627	4.134897	13.352104
H	-2.798897	6.558025	6.835146
H	-5.222622	7.123673	6.760456
H	-6.956171	5.310218	6.927996
H	-6.227323	2.914172	7.187294
H	-3.795155	2.348989	7.294857
H	2.918763	3.630836	5.962713
H	4.561822	2.077277	4.912743
H	3.907777	-0.287954	4.361568
H	1.573301	-1.080472	4.877377
H	-0.067449	0.466800	5.937741
H	-1.830297	7.827967	10.772099
H	-4.042706	8.770735	11.409456
H	-5.266041	10.310907	9.842117
H	-4.242647	10.890437	7.617011
H	-2.034985	9.920592	6.963872
H	3.152575	10.380976	8.142642
H	5.326333	11.015049	7.088299

H	6.414766	9.479021	5.419004
H	5.291717	7.314972	4.803005
H	3.108311	6.694600	5.835317
H	-1.728767	6.118134	13.622552
H	-4.117554	6.347139	14.323221
H	-5.952724	5.435496	12.864199
H	-5.367271	4.272972	10.711187
H	-2.989236	4.012554	10.029806
H	2.638872	4.927288	13.878533
H	4.804938	4.026285	14.738921
H	6.149941	2.424872	13.338375
H	5.289454	1.720031	11.083498
H	3.111419	2.594062	10.240319
H	2.377791	7.134522	11.563455
H	2.839901	8.401869	10.357583
H	4.548801	7.229166	12.652852
H	4.433434	8.948472	12.128501
H	6.581008	7.462723	11.259597
H	5.697716	8.464468	10.05032
H	5.441171	6.266887	9.00275
H	5.355249	5.434518	10.608295
H	-1.937045	5.988601	9.095838

**Table A.6.4.** Cartesian coordinates (Å) for DFT energy minimized  $[\text{Mn}^{\text{III}}(\text{O}_2)(\text{Tp}^{\text{Ph,Me}})(\text{THF})]$  model.

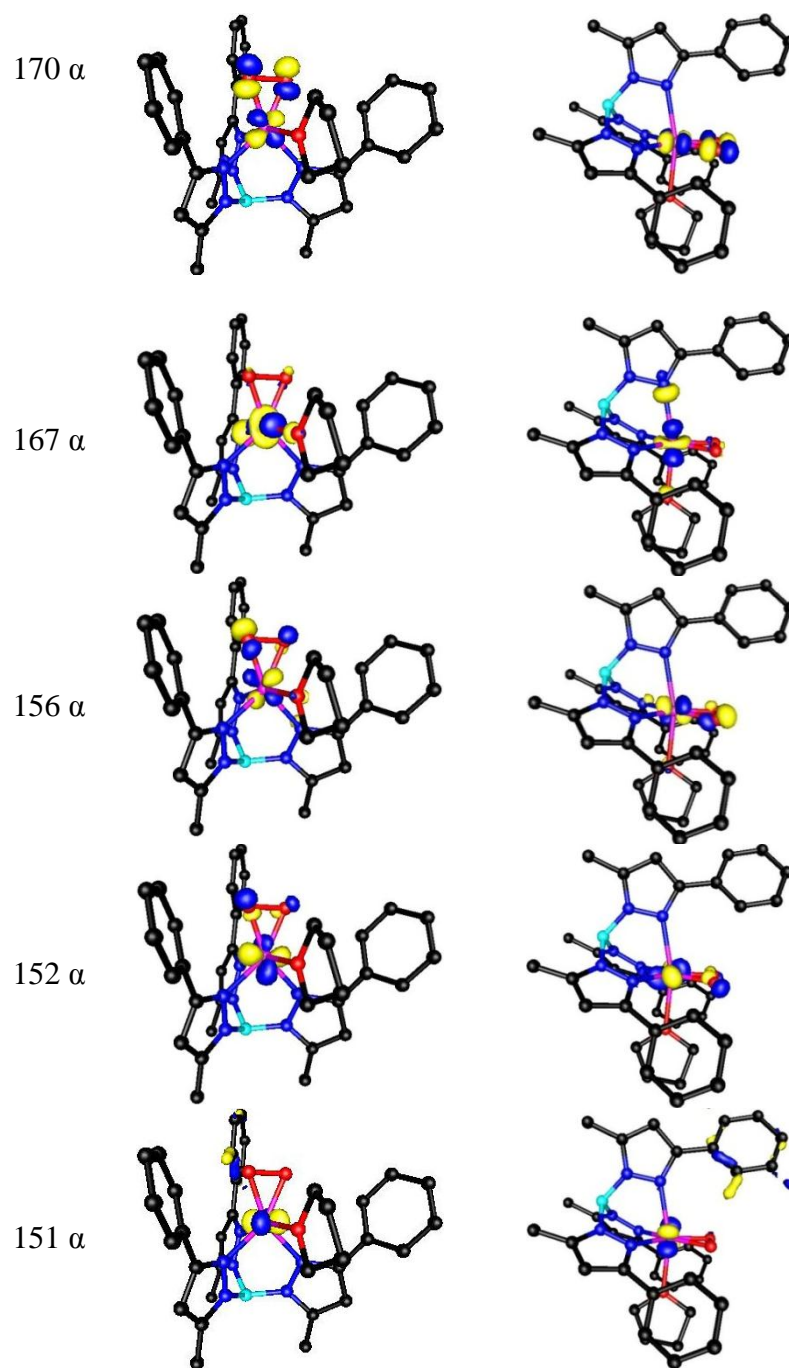
Atom	x	y	z
Mn	0.000000	0.000000	0.000000
O	-1.854526	-0.208260	0.000000
O	-1.146840	-1.465504	0.000000
O	-0.005152	0.023431	-2.374784
N	0.554751	0.222984	2.288960
N	0.422438	2.040054	-0.095163
N	1.996603	-0.607940	-0.156403
N	2.941567	0.180790	0.448265
N	1.645044	1.035517	2.467048
N	1.679688	2.407126	0.310880
B	2.503175	1.458400	1.240795
H	1.965103	0.401315	-2.965131
H	0.811331	1.778758	-3.177974
H	1.094151	-0.767126	-4.910694
H	0.826253	0.924577	-5.468045
H	-1.346370	-0.758565	-5.322228

H	-1.507980	0.897011	-4.630129
H	-2.023934	-0.417048	-2.630224
H	-0.879026	-1.733182	-3.114965
C	1.952702	1.143215	3.805244
C	1.035736	0.348942	4.501687
C	0.171948	-0.203017	3.522113
C	1.934412	3.698883	-0.076457
C	0.790612	4.170579	-0.739223
C	-0.136448	3.106179	-0.731116
C	4.197678	-0.263296	0.117264
C	4.041581	-1.362002	-0.742549
C	2.650747	-1.560981	-0.875946
C	-0.976385	-1.094036	3.796608
C	-2.144382	-1.100905	2.999333
C	-3.225688	-1.936912	3.326875
C	-3.165543	-2.779826	4.451711
C	-2.007546	-2.782201	5.252257
C	-0.925333	-1.948628	4.927554
C	-1.507375	3.126127	-1.281144
C	-1.753936	3.779178	-2.513289
C	-3.055885	3.861944	-3.032318
C	-4.134627	3.297766	-2.326143
C	-3.901288	2.656452	-1.096238
C	-2.600070	2.571823	-0.574954
C	1.985969	-2.652351	-1.617856
C	2.486468	-3.035666	-2.886368
C	1.910216	-4.104372	-3.591907
C	0.826309	-4.811774	-3.039042
C	0.330039	-4.446494	-1.774390
C	0.904071	-3.377344	-1.066210
C	3.214759	4.419824	0.225905
C	3.086361	1.970499	4.335954
C	5.460792	0.367289	0.624043
C	0.933721	0.674864	-3.277404
C	0.565863	0.184153	-4.682396
C	-0.949525	-0.062209	-4.553541
C	-1.062399	-0.634444	-3.138688
H	3.492381	2.046726	1.615276
H	0.957352	0.250788	5.590734
H	0.649626	5.168311	-1.169924
H	4.840432	-1.993399	-1.147665
H	-2.207079	-0.447402	2.115160

H	-4.128744	-1.926589	2.693807
H	-4.016544	-3.435210	4.703125
H	-1.943596	-3.441719	6.133777
H	-0.016637	-1.972864	5.550875
H	-0.911633	4.216276	-3.075513
H	-3.228510	4.369022	-3.996197
H	-5.157363	3.361839	-2.732977
H	-4.742160	2.221369	-0.530538
H	-2.432990	2.092598	0.401633
H	3.331422	-2.480029	-3.326602
H	2.309877	-4.384938	-4.580270
H	0.372393	-5.651080	-3.591267
H	-0.510326	-5.003867	-1.327723
H	0.531657	-3.124044	-0.063106
H	3.369838	4.549662	1.319588
H	3.194452	5.427419	-0.239545
H	4.101007	3.875328	-0.167488
H	3.068625	1.962994	5.445390
H	3.021343	3.029507	4.001104
H	4.079329	1.584314	4.012533
H	5.570631	1.418656	0.277484
H	6.337323	-0.204244	0.255003
H	5.502460	0.379169	1.734679

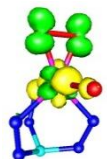
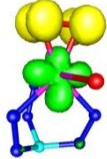
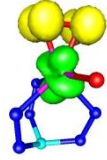
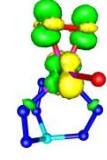
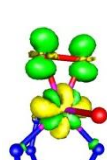
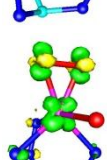
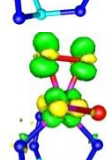
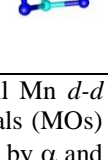
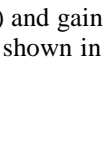
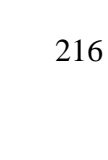

**Table A.6.5.** Energies (eV) and Compositions (%) of the O 2p-based MOs and the Mn 3d-based MOs Based on Spin-Unrestricted B3LYP DFT Computations for  $[\text{Mn}^{\text{III}}(\text{O}_2)(\text{Tp}^{\text{Ph}_2})]^+$ .

orbital	occup	spin	energy	Mn 3d	O <sup>A</sup> 2p	O <sup>B</sup> 2p	O 2p (THF)	Tp <sup>2Ph</sup>
151(Mn yz)	1.0	↑	-8.6471	48.0	1.8(z)	0.0	1.3(z)	6.1
152(Mn xy)	1.0	↑	-8.0123	51.4	12.3(x)	7.5(y)	1.9(z)	11.1
156(Mn xz)	1.0	↑	-7.4612	42.7	7.5(z)	21.2(z)	3.7(y)	9.0
158 (THF $\pi^*$ )	1.0	↑	-7.0722	2.5 (yz)	0.9(x)	1.3(x)	47.7(y)	4.7
167 (Mn $z^2$ )	1.0	↑	-6.1688	48.4	3.1 (x)	3.9(x/y)	4.4 (z)	15.9
168 (N/C $\pi^*$ )	1.0	↑	-5.7493	0.6	0.6(z)	0.0	0.0	99.04
169 (O <sub>2</sub> $\pi_{\text{op}}^*$ )	1.0	↑	-5.2063	5.3 (yz)	44.2(z)	46.6(z)	0.0	0.0
170 (Mn $x^2-y^2$ )	1.0	↑	-1.4551	41.2	23.9(x)	24.0(x)	0.0	5.7
165 (O <sub>2</sub> $\pi_{\text{op}}^*$ )	1.0	↓	-5.3216	6.1(yz)	43.3(z)	44.8(z)	0.4(y)	0.7
166(Mn yz)	0.0	↓	-1.3335	26.7	0.4(x)	0.7(y)	0.1(x)	16.6
168(Mn xy)	0.0	↓	-0.7335	25.3	1.9(z)	2.0(z)	0.1(y)	17.3
173 (Mn xz)	0.0	↓	-0.2259	29.7	1.4(z)	0.2(z)	0.1(y)	7.0
177(Mn $z^2$ )	0.0	↓	0.3684	76.0	0.9(x)	1.0(x)	3.0 ( $\sigma$ )	4.4
179 (Mn $x^2-y^2$ )	0.0	↓	0.8850	27.1	4.1(y)	4.6(x)	0.0	7.3



**Figure A.6.1.** Surface contour plots (isodensity values of  $\pm 0.01$  au) of the spin-up Mn d-MOs for  $[\text{Mn}^{\text{III}}(\text{O}_2)(\text{Tp}^{\text{Ph}_2})(\text{THF})]$ .

**Table A.6.6.** TD-DFT Calculated Energies, Percent Contributions from Dominant One-electron Excitations, and Oscillator Strengths for the Major Electronic Transitions of  $[\text{Mn}^{\text{III}}(\text{O}_2)(\text{Tp}^{\text{Ph}_2})]^+$ .

band	state	energy ( $\text{cm}^{-1}$ ) <sup>a</sup>	$f_{osc}$	transition <sup>b</sup>	%	donor MO	acceptor MO	comments	EDDM <sup>c</sup>
i	2	20 300	0.0003749	$167\alpha \rightarrow 170\alpha$	88	$\text{Mn } d_z^2$	$\text{Mn } d_{x^2-y^2}^2$	Mn d $\rightarrow$ d	
	3	23 200	0.0004766	$165\beta \rightarrow 166\beta$	69	$\text{O}_2 \pi_{op}^*$	$\text{Mn } d_{xy}$	$\text{O}_2 \rightarrow \text{Mn CT}$	
				$165\beta \rightarrow 168\beta$	23	$\text{O}_2 \pi_{op}^*$	$\text{Mn } d_{yz}$	$\text{O}_2 \rightarrow \text{Mn CT}$	
ii	5	25 600	0.0011298	$165\beta \rightarrow 168\beta$	15	$\text{O}_2 \pi_{op}^*$	$\text{Mn } d_{xy}$	$\text{O}_2 \rightarrow \text{Mn CT}$	
				$165\beta \rightarrow 168\beta$	66	$\text{O}_2 \pi_{op}^*$	$\text{Mn } d_{yz}$	$\text{O}_2 \rightarrow \text{Mn CT}$	
	6	27 000	0.0000013	$156\alpha \rightarrow 170\alpha$	30	$\text{Mn } d_{xz}$	$\text{Mn } d_{x^2-y^2}^2$	Mn d $\rightarrow$ d	
				$161\alpha \rightarrow 170\alpha$	21	pyr $\pi$	$\text{Mn } d_{x^2-y^2}^2$		
iii	9	28 800	0.0055239	$152\alpha \rightarrow 170\alpha$	31	$\text{Mn } d_{xz}$	$\text{Mn } d_{x^2-y^2}^2$	Mn d $\rightarrow$ d	
	12	29 200	0.0032213	$168\alpha \rightarrow 170\alpha$	10	pyr $\pi$	$\text{Mn } d_{x^2-y^2}^2$		
				$168\alpha \rightarrow 170\alpha$	24	$\text{O}_2 \pi_{op}^*$	$\text{Mn } d_{x^2-y^2}^2$	$\text{O}_2 \rightarrow \text{Mn CT}$	
iv	16	31 200	0.0048239	$151\alpha \rightarrow 170\alpha$	26	$\text{Mn } d_{yz}$	$\text{Mn } d_{x^2-y^2}^2$	Mn d $\rightarrow$ d	

<sup>a</sup>Electronic transition energies have been rounded to the nearest  $100 \text{ cm}^{-1}$ . Included in this table are all Mn  $d$ - $d$  transitions, as well as charge-transfer (CT) transitions with  $f_{osc} > 0.001$ . <sup>b</sup>Composition of molecular orbitals (MOs) involved in these electronic transitions are listed in Table S12. Spin-up and spin-down MOs are designated by  $\alpha$  and  $\beta$ , respectively. <sup>c</sup>Electron density difference maps (EDDMs) showing surface contour plots of loss (yellow) and gain (green) of electron density for a given electronic transition. For clarity, only the Mn, N, and O atoms are shown in these plots.

**Table A.6.7.** Electronic transition energies ( $\text{cm}^{-1}$ ), oscillator strengths ( $f_{\text{exp}}$ ), and bandwidths (fwhm;  $\text{cm}^{-1}$ ) from Gaussian deconvolutions of 298 K absorption and 2 K, 7 T MCD data of  $[\text{Mn}^{\text{III}}(\text{O}_2)(\text{Tp}^{\text{Ph}_2})(\text{THF})]$ .

band	energy	$f_{\text{exp}} \times 10^3$	fwhm
1	Abs: 19 000 MCD: 19 000	0.083	Abs: 2248 MCD: 1998
2	Abs: 20 890 MCD: 21 455	0.135	Abs: 2248 MCD: 1665
3	Abs: 22 600 MCD: 22 325	0.290	Abs: 2248 MCD: 1665
4	Abs: NA MCD: 23 675		Abs: NA MCD: 500
5	Abs: 24 350 MCD: 24 800	34.20	Abs: 2248 MCD: 1832
6	Abs: NA MCD: 25 150		Abs: NA MCD: 666
7	Abs: 26 300 MCD: 26 060	167.64	Abs: 2331 MCD: 1832
8	Abs: 28 400 MCD: 27 609	83.28	Abs: 2331 MCD: 1832
9	Abs: NA MCD: 28 350		Abs: NA MCD: 999

**Table A.6.8.** Metric parameters for  $[\text{Mn}^{\text{III}}(\text{O}_2)(\text{Tp}^{\text{Ph}_2})(\text{THF})]$  from DFT optimized geometry. Bond Lengths ( $\text{\AA}$ ) and Angles ( $^\circ$ ) for  $\text{Mn}^{\text{III}}$  Complex computed.

$[\text{Mn}^{\text{III}}(\text{O}_2)(\text{Tp}^{\text{Ph}_2})(\text{THF})]$			
Mn-O(1)	1.866	O(1)-O(2)	1.443
Mn-O(2)	1.861	N(2)-Mn-(O1)	108.1
Mn-O(X1)	2.375	N(3)-Mn-(O2)	111.1
Mn-N(1)	2.366	N(1)-Mn-(X1)	165.3
Mn-N(2)	2.093	N(1)-Mn-(N3)	84.5
Mn-N(3)	2.086	N(1)-Mn-(N2)	82.9